FACULTY OF SCIENCES

Cold gas and baryon-induced dark matter cores in nearby galaxies

Flor Allaert

Supervisors: Prof. Dr. Maarten Baes, Dr. Gianfranco Gentile

A dissertation submitted to Ghent University in partial fulfilment of the requirements for the degree of Doctor of Science: Astronomy

September 2017

GHENT UNIVERSITY

fwo

Supervisors:

Prof. Dr. Maarten Baes
Vakgroep Fysica en Sterrenkunde
Universiteit Gent

Dr. Gianfranco Gentile
Vakgroep Fysica en Sterrenkunde
Vrije Universiteit Brussel

Jury members:

Prof. Dr. Dirk Poelman (President)
Vakgroep Vastestofwetenschappen
Universiteit Gent

Dr. Karel Van Acoleyen (Secretary)
Vakgroep Fysica en Sterrenkunde
Universiteit Gent

Prof. Dr. Sven De Rijcke
Vakgroep Fysica en Sterrenkunde
Universiteit Gent

Prof. Dr. Herwig Dejonghe
Vakgroep Fysica en Sterrenkunde
Universiteit Gent

Prof. Dr. Uli Klein
Argelander-Institut für Astronomie
Universität Bonn

Prof. Dr. Erwin de Blok
Netherlands Institute for Radio Astronomy

Contents

List of Figures

List of Tables

Acknowledgements

Over the past five years, I have been very fortunate to experience life as an astronomer, using real telescopes to do real research. In this thesis, I present the results of that research. However, there is no I in astronomy. None of the work described in this document would have been possible without the help and support of many others. Before proceeding to the astronomy, I wish to express my gratitude to all these people and give them the credit that they deserve.

First of all, I want to thank my two supervisors: Maarten and Gianfranco. You guys are not only brilliant scientists, but also wonderful people (and laudable football players) and I greatly admire both of you. Gianfranco, you taught me everything I know about radio astronomy and were always available to answer questions or help me out if I had a problem. I know very well that this is not obvious and that I have been incredibly lucky to have such a committed supervisor. Maarten, I would not know how to define good leadership, but I can give you as a prime example. Your door is always open, for scientific questions and for personal matters, and your unrestrained enthusiasm is inspiring. I want to thank you for the confidence and freedom that you gave me and for the opportunity to conduct (and occasionally screw up) observations all across the world.

Next, a big thanks to my office mates (Steven, Waad, Marjorie and Michiel) and all the other members of the astronomy team who I have come to consider as friends rather than colleagues. The pleasant lunch and coffee breaks, summer barbecues and occasional astrodrinks all contributed to a work atmosphere that I will always remember. Never once have I dreaded going to work. Despite the recurring defeats, I also deeply enjoyed the after-lunch ping pong sessions with Steven, Sébastien and Michiel. Special thanks further go to the supporting staff, Inge and Gerbrand, who made my life a whole lot easier. The department is very lucky to have both of you.

I also want to thank the members of the jury for taking the time to read this thesis and provide comments that helped to improve it. Furthermore, I am very grateful to M. Verheijen, S. Peters, E. de Blok, D. Hunter, S.H. Oh, J. Simon, K. Yim, S. Garcia-Burillo and M. Dumke for kindly sharing their data products with me. This work would not have been possible without their generosity. As a PhD fellow of the Research Foundation - Flanders (FWO - Vlaanderen), I acknowledge and am grateful for their financial support over the past years.

Astronomy is nice, but so are other things. I am surrounded by a fantastic group of friends and family, and although they may not have had a direct impact on this work, I would like to use this opportunity to emphasise how much they mean to me.

Tom, you and I go way back. Our friendship was forged in the stench of Amylum many years ago and has always been obvious, without any reservations or awkwardness. Marlies, my cheerful room-mate in the Ommegangstraat, we don't see each other as often as I would like to any more, but you mean a lot to me and you will always be one of my closest friends. Sam, it's amazing how much we have in common. I consider the time we lived together as some of the best years in my life and I hope we will continue to disagree with the tactics of de Duivels until we are grey and incontinent. Daan, Jeroen, Charlotte, Joachim, William, Bieke, Francis, Eva, Eline, Sacha, Camille, Jana, Hannah, Matthias, Alexander, Mitja, Nena and the others, thank you all for the lovely times. I would be miserable without you. Finally, I cannot go without mentioning Jeu de Boules, the football team that I am proudly part of. Hopefully we can keep whooping Charlie ass for many years to come.

I have the incredible privilege to be part of an extended, warm and dedicated family and family-in-law. Mama, papa, Leo, Inge, Ellen, Jesse, Sil, Astrid, Inti, and all the others, thank you for always being there for me, taking me as I am and supporting me, regardless of the stupid things I do or the surprises that I bring. I may not say it that often, but I love you all and praise myself lucky to have you. Also a special mention for de Mannen van de Vierschaar, the extraordinary gentlemen that are my cousins. Screw Lieven Scheire, I have a much better crew.

Finally, a special mention for the two girls that I happily come home to every day. Two beautiful, fun, smart and strong women that help me to enjoy life and put things in the right perspective. Gitte and Febe, you are truly amazing. I'm incredibly proud of both of you and I love you with all my heart. And someday, Gitte, perhaps, someday ...

Flor

1 Introduction

1.1 Galaxies - building blocks of the Universe

Astronomy is the oldest of all sciences and dates back to the ancient civilisations that first looked at the heavens and attempted to make sense of what they saw. Despite this long history, our current knowledge of the structure of the Universe was established only recently. The first great leap in this process came in the 16th and 17th century, with the revolutionary and courageous insights of Copernicus and later Galilei that the Earth revolves around the Sun, and not vice versa. How the Universe looks beyond our own Solar System, however, remained unclear for many more centuries. Even at the beginning of the 20th century, the Sun was still generally considered as the center of the Milky Way. This notion changed with the pioneering work of Harlow Shapley, Jan Oort and Bertil Lindblad, who placed the center of our Galaxy thousands of light years away from the Sun. On the other hand, Shapley, as many others, did still believe that the Milky Way comprised the entire Universe. Others, led by Heber Curtis, believed the opposite. In 1920 this discussion climaxed in the Great Debate about the nature of the 'spiral nebulae' that had been observed throughout the night sky. It was only after Edwin Hubble established that the Andromeda nebula was located much further away than anything else measured until then (Hubble 1925), that these nebulae were generally accepted as distant and independent structures: galaxies, just like our own Milky Way.

While only a handful of nearby galaxies are visible with the naked eye, telescope observations show that these fascinating objects cover the entire sky around us. Looking deeper into seemingly empty patches of the sky continues to reveal new, fainter and more distant galaxies (Fig. 1.1). With an estimated total of 2 trillion galaxies in the observable Uni-

Figure 1.1: The Hubble Ultra Deep Field, showing a Universe filled with galaxies. Credit: NASA/ESA/S, Beckwith(STScl) and the HUDF Team.

verse (up to $z < 8$; Conselice et al. 2016), these systems can truly be called the building blocks of the Universe.

1.1.1 Classification

Galaxies come in a large variety of shapes, colors, masses and sizes. In order to understand these systems, we must start by seeing the galactic forest through the trees and classify the galaxies into groups of similar systems. The first and still most commonly used classification scheme for galaxies was invented by Edwin Hubble in 1926 (Hubble 1926) and is depicted in Figure 1.2. It arranges galaxies in three main categories, based on their optical morphology: ellipticals, spirals and irregulars.

Elliptical galaxies are spheroidal, pressure supported systems. They do not actively form stars and primarily contain old stellar populations and a hot and ionised interstellar medium. The ellipticals are located on the left side of the diagram and are further subdivided based on their *apparent* ellipticity on the sky, going from almost round (E0) to highly flattened (E7). The number in the notation corresponds to the ellipticity $(1 - b/a)$ multiplied by 10, where b/a is the projected minor to major axis ratio.

The right side of the Hubble diagram shows two parallel arms containing the spiral galaxies. These consist of flat, rotating disks with active star formation and a clear spiral pattern. A more spheroidal concentration of older stars (called the bulge) is generally present in the center. In addition to the bulge, spirals can also have a bar-shaped structure in their center. These barred spirals are grouped on the lower arm of the Hubble tuning

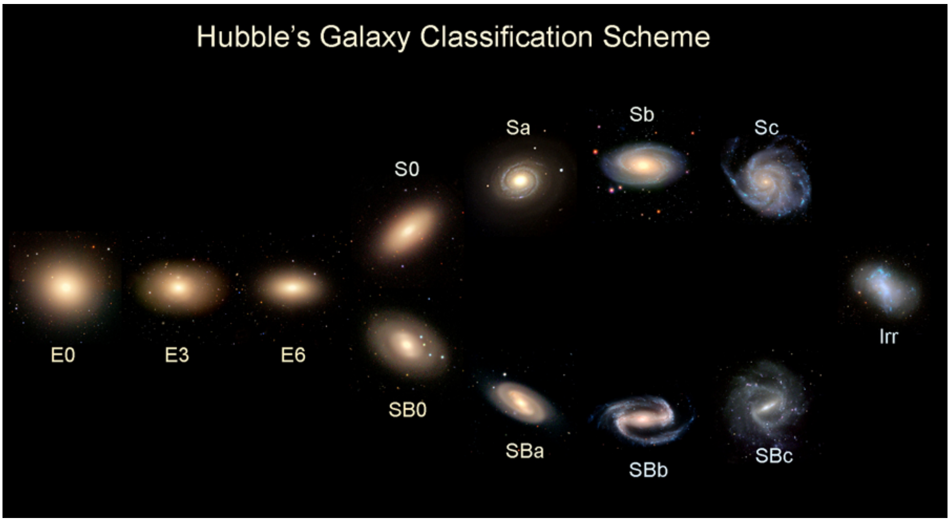

Figure 1.2: The Hubble sequence. Credit: Galaxy Zoo Blog.

fork. Spirals without a clear bar are located on the upper arm. Both arms are further subdivided according to the shape of the spiral arms and the strength of the bulge, going from a prominent bulge and tightly wound spiral arms on the left (S(B)a) to little or no bulge and loosely wound spiral arms on the right (S(B)c).

The lenticular galaxies form the transition between the ellipticals and the spirals. These bulge dominated systems still contain a significant disk, but show no spiral structure or active star formation.
The last category is formed by the irregular galaxies. These are neither elliptical nor spiral galaxies, but, unsurprisingly, have irregular shapes. They are generally considered to be the remnants of recent galaxy-galaxy interactions.

Although the Hubble diagram is based purely on optical morphology, it is now believed that it also roughly represents an (inverse) evolutionary sequence. When primordial gas falling into a dark matter halo collapses under its own gravity, conservation of angular momentum and the dissipative nature of the gas eventually lead to the formation of a rotationally supported disk (e.g. Fall & Efstathiou 1980; Dalcanton et al. 1997). Once the gas has sufficiently cooled, stars begin to form in this disk. Elliptical galaxies are generally thought to form from spirals in violent galaxy-galaxy interactions. These break up the rotationally supported structure and induce a massive starburst (e.g. Joseph et al. 1984; Mihos & Hernquist 1996), causing the galaxy to rapidly consume its available gas reservoir. What is left is a passively evolving system that has no fuel left to form new stars and is dominated by random motions (e.g. Negroponte & White 1983; De Lucia et al. 2006; Naab et al. 2006).
Somewhat confusingly, however, ellipticals are generally called *early* type galaxies (or

ETGs), while the spirals on the right side are called *late* type galaxies. This misleading nomenclature is essentially a relic from the common misconception that Hubble originally devised his classification as an evolutionary sequence, with ellipticals evolving into spirals. As stated explicitly in Hubble (1927), however, this is not true: "The entire classification is purely empirical and without prejudice to theories of evolution – comparison with theories will be the more significant for this reason."

Hubble's classification has a number of shortcomings. For example, it is based on the 2D morphology of galaxies on the plane of the sky. This is particularly problematic for elliptical galaxies, where the apparent ellipticity of a system depends strongly on its orientation on the sky. An apparently elliptical system could, for example, actually be a moderately inclined lenticular that still contains a rotating disk. Additionally, the classification criteria for spirals are subjective and not based on measurable quantities. As a consequence, the same galaxy is often classified differently by different observers (e.g. Lintott et al. 2008). Since different wavelengths emphasize different stellar populations, the classification of a galaxy might also change with the wavelength at which it is observed. This is particularly an issue for galaxies at high redshift (large distances), where the stellar emission is shifted to longer wavelengths.

As an alternative to the Hubble diagram, the ATLAS^{3D} consortium recently developed a classification scheme that is based on the kinematics of galaxies in addition to their morphology (Cappellari et al. 2011b). Spiral galaxies, identified by their spiral arms, remain a class of their own. Early type galaxies are kinematically divided into fast rotators (rotation dominated) and slow rotators (dominated by random motions). It turns out that only the 'round' ellipticals from the Hubble scheme (E0 to E4) are slow rotators and hence genuine spheroidal systems. Other ellipticals (E5 and flatter) are in fact rotation dominated fast rotators. While this classification is more robust, as it is less affected by projection effects, it is not yet widely used, because of the need for 3D spectroscopy. In the rest of this thesis, we shall use the original classification by Hubble.

1.1.2 Chemical evolution

In the beginning there was gas...

Despite their static and majestic appearance in images, spiral galaxies are in fact vibrant and dynamic environments that are in constant evolution. The fundamental starting point and fuel of this evolution is gas, in the form of single hydrogen and helium atoms, that fills the entire galaxy and reaches far beyond the extent of the stars. It is the primordial leftover of the Big Bang Nucleosynthesis and typically spans a huge range in temperature and density (Thronson & Shull 1990). In most of its volume, this gas is in an extremely hot and low density state, with temperatures of the order of a million K and densities as low as 1 particle per 1000 cm^3. It is in fact so hot that the atoms are fully ionised. Closer to the midplane of the galaxy, the temperatures are lower and the ionisation fraction drops, going from still mostly ionised at $T \sim 8000$ K to a predominantly neutral medium at

$T \sim 6000$ K. In this temperature range, the gas is typically called "warm", although it is still extremely hot by human standards. As the gas cools down even further, it condenses closer to the midplane to form a heterogeneous cold neutral medium, consisting of clouds and filaments with $T \sim 30 - 100$ K. Finally, in the coldest and densest regions of this medium, single atoms can combine and form clouds of molecular (essentially H_2) gas.

... and then it said, let there be light...

Molecular clouds are not uniform, but consist of dense filaments slicing through regions of lower density (André et al. 2010). If the densities become high enough, certain areas in these filaments can collapse under their own gravity, and stars are born. In rare cases, at very low metallicities (small concentrations of elements heavier than helium), the gravitational collapse even overtakes the formation of molecules, and stars form directly from the cold atomic medium (Krumholz 2012).

Stars, in their turn, are the engines behind the chemical evolution in galaxies, fusing light atoms into heavier elements (or 'metals' in the astronomical jargon) in their extremely hot and dense cores. This process releases huge amounts of energy, which they emit as electromagnetic radiation, or light, making galaxies visible to us. Massive stars, with masses of a few to a few ten times that of the Sun ($M_\odot$), do this violently and burn up their fuel in several to about 100 million years. The lightest stars ($M \sim 0.1 - 0.5\ M_\odot$) live much longer and can carry on their nuclear fusion for $\sim 10^{11}$ to 10^{12} years, far beyond the current age of the Universe. At the end of their life, stars cast off their outer layers or explode violently as a supernova, finally releasing the newly formed metals back into the interstellar medium (ISM). Here they either mix with the interstellar gas, or condense to form tiny solid grains of dust.

... until it returned to dust

Interstellar dust is essentially composed of silicates (i.e. sand), amorphous carbon (soot) and aromatic molecules. Its existence has been accepted for many decades (Trumpler 1930a,b), but how and where exactly these grains form is still a matter of debate and active research. Various mechanisms and formations sites have been proposed, such as the metal-rich, cool and dense winds from evolved asymptotic giant branch stars and the cooling ejecta from novae and supernovae. A third option is that dust grains simply grow directly through the coagulation of metals in the ISM. All these formation mechanisms are probably active in real galaxies, but their relative importance is still debated and has been found to depend on the evolutionary state of the galaxy at hand (e.g. Dwek & Scalo 1980; Kozasa et al. 1991; Dwek 1998; Zhukovska & Henning 2013; Zhukovska 2014; Rowlands et al. 2014).

In the ISM dust grains are constantly bombarded by energetic UV and X-ray photons, hot electrons and cosmic rays (a process called sputtering), which can eventually lead to their destruction. In addition, the same supernovae that create new grains are also a major source of dust destruction. In the shock waves generated by these violent explosions, sputtering and grain-grain collisions can shatter and vaporise dust grains (Jones 2004; Micelotta et al. 2010; Jones & Nuth 2011; Bocchio et al. 2012; Slavin et al. 2015).

Dust grains efficiently scatter and absorb ultra-violet (UV), optical and near-infrared (NIR) radiation and reprocess this energy to mid and far-infrared (MIR, FIR) and submillimetre (submm) wavelengths. As a result, they effectively redden or even block the light from the stars as it is travelling towards us. Since dust typically constitutes less than 1 percent of the total baryonic mass of a galaxy (e.g. Cortese et al. 2012; Rémy-Ruyer et al. 2014), it was long considered as an insignificant and annoying component that only hindered our observations of the stars. After several decades of misappreciation, it is now recognised that dust too plays a vital role in the evolution of a galaxy. Dust grains are crucial in regulating star formation. On the one hand, inelastic collisions of gas particles with dust grains allow the gas to cool and reach densities high enough to form and conserve molecules (Dalgarno & McCray 1972; Ostriker & Silk 1973). On the other hand, dust grains catalyse the formation of H_2 molecules by bringing hydrogen atoms together on their sticky surface and absorbing the excess energy. Finally, the macroscopic grains also act as a shield, protecting the newly formed molecules from the destructive UV radiation from the stars (Gould & Salpeter 1963; Hollenbach & Salpeter 1971; Cazaux & Tielens 2002).

Star formation does not only create and destroy dust grains, but also affects the gas. Massive stars emit strongly in the UV, and their energetic photons heat and partly ionise the surrounding gas, creating so called Hii regions. More dramatically, the shock waves from supernova explosions sweep up the surrounding gas, creating giant bubbles and massive outflows of hot, ionised gas. If the ambient ISM is compressed, this can stimulate further star formation. On the other hand, if enough material is expelled from the galaxy, star formation is suppressed (e.g. Kereš et al. 2009a; Alatalo et al. 2011; Newton & Kay 2013; Lagos et al. 2013). As explained later, the combined effect of many supernovae can even alter the shape of the dark matter halo.

The various components of a galaxy thus strongly interact with each other, and influence each other's state and evolution. As a consequence, they cannot be considered separately from the others. To fully understand one, we must study them all.

1.1.3 Accretion and mergers

In addition to the 'closed-box' evolution that was explained in the previous section, galaxies also undergo influences from outside. In fact, accretion of substantial amounts of external gas is crucial for a galaxy to replenish its fuel reservoir and to keep forming stars over the course of its life. This happens in two ways. On the one hand, primordial gas is continuously accreted directly from intergalactic medium (Sancisi et al. 2008; Ocvirk

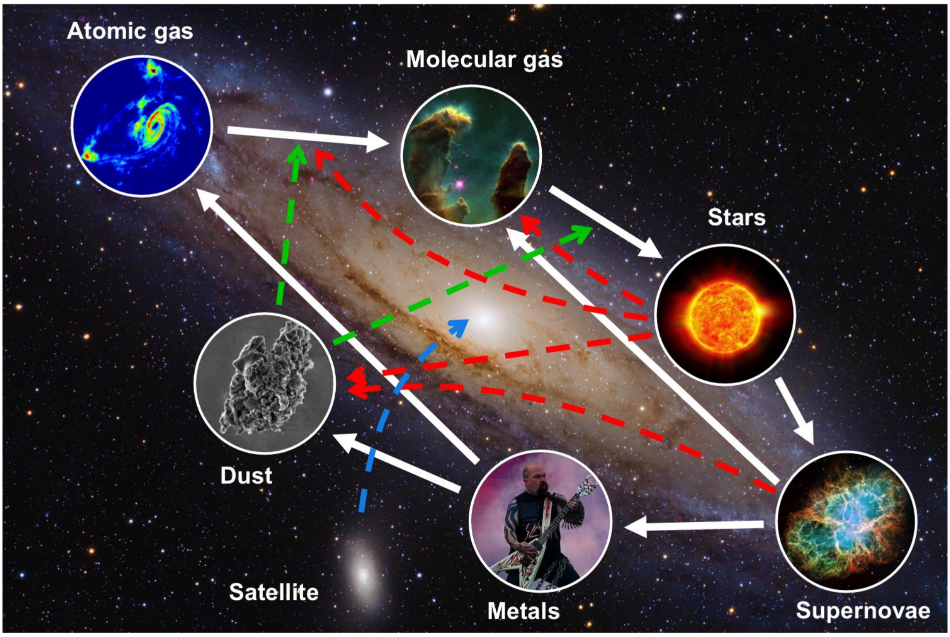

Figure 1.3: Schematic overview of the chemical evolution of galaxies. Atomic gas condenses into clouds of molecular gas, which collapse to form stars. Stars produce heavier elements and release these in the ISM at the end of their life, where they enrich the gas or form dust grains. Dust catalyses molecular cloud and star formation, while the radiation from young stars heats the gas and destroys molecules and dust grains. Supernova shock waves also destroy dust. Mergers are vital to replenish the gas reservoir for further evolution.

et al. 2008; Kereš et al. 2009b). On the other hand, galaxies can also 'collide' and merge with each other. This is essentially the way in which small dwarf galaxies grow to massive systems like our own Milky Way (e.g. Toomre & Toomre 1972; Woods & Geller 2007; Lambas et al. 2012; Di Teodoro & Fraternali 2014).

The most common type of galaxy-galaxy encounters happen between massive systems and their low-mass companions (so-called minor mergers), because the latter are far more abundant than massive galaxies. When considered individually, the main effect of minor mergers on their massive participants is to temporarily and moderately enhance the star formation rate in spiral galaxies (Kaviraj 2014a), or reignite star formation in ETGs (Kaviraj et al. 2011; Shabala et al. 2012). In spirals, individual minor mergers can also induce asymmetries and warps in the disk, or generate radial gas flows, but otherwise the shape, size and state of the galaxy are typically not significantly affected. Although the star formation associated to a single minor merger is moderate, the accumulation of these frequently occurring events over cosmic time does make minor mergers a major driver of cosmic star formation (Kaviraj 2014b,a). In addition, consensus is growing that these events are also responsible for the observed 3–5 fold increase of the sizes of massive ETGs over the lifetime of the Universe. (Trujillo et al. 2006; Buitrago et al. 2008; Newman et al. 2012; Oser et al. 2012).

Major mergers between equal mass systems have a much larger impact on the merging galaxies, but occur far less frequently than minor mergers. Major mergers can induce strong starbursts in their remnants (e.g. Joseph et al. 1984; Mihos & Hernquist 1996), and simulations have shown that mergers between massive disk galaxies can even destroy the disks and produce pressure supported spheroidal galaxies (e.g. Negroponte & White 1983; De Lucia et al. 2006; Naab et al. 2006). However, due to the paucity of these events, even at high redshift, it is still a matter of debate whether major mergers are the main driver behind the fraction of early type galaxies we observe today (e.g. Lofthouse et al. 2017).

1.2 Observing the different components

After being confined to the surface of the Earth for many thousands of years, mankind is now cautiously taking its first steps in outer space. Visiting the Moon has proven feasible (although that flag was waving vigorously), but it is still far beyond our reach to travel to another planet, let alone a different galaxy. And even with a space ship travelling at the speed of light, it would take 2.54 million years to reach the Andromeda galaxy, our closest large neighbour. Therefore, our only means of empirically studying galaxies and the components inside them is to observe the electromagnetic radiation (and gravitational waves) that they emit.

1.2.1 Stars

Stars can, to a good approximation, be considered as blackbodies that emit radiation according to Planck's law. Solar mass stars, with an effective temperature of $\sim$ 5000 K, radiate most of their energy at optical wavelengths, i.e. in 'visible' light. For more massive stars ($M >$ a few $M_{\odot}$) this peak shifts to the UV, while low mass stars ($M \lesssim 0.5$ $M_{\odot}$) emit mostly in the NIR. Since the Earth's atmosphere is largely transparent at these wavelengths (Fig. 1.4), most of the radiation from the different stellar populations can be observed with telescopes on Earth.

The stars were the first, and for a very long time the only, galaxy component to be observed with telescopes. These observations were initially performed by eye and with a sketch book, and later with photographic plates. In modern times, stellar observations are typically conducted with a CCD detector, where the incoming photons generate free electrons through the photoelectric effect. After a certain integration time, the accumulated charge in each pixel is then translated to an intensity in the image. For modern optical telescopes, the theoretical angular resolution is typically so high that the resolution of the images is in practice determined by the turbulence of the atmosphere (an effect called seeing). At good observing sites, this is typically less than one arcsecond. Moreover, when

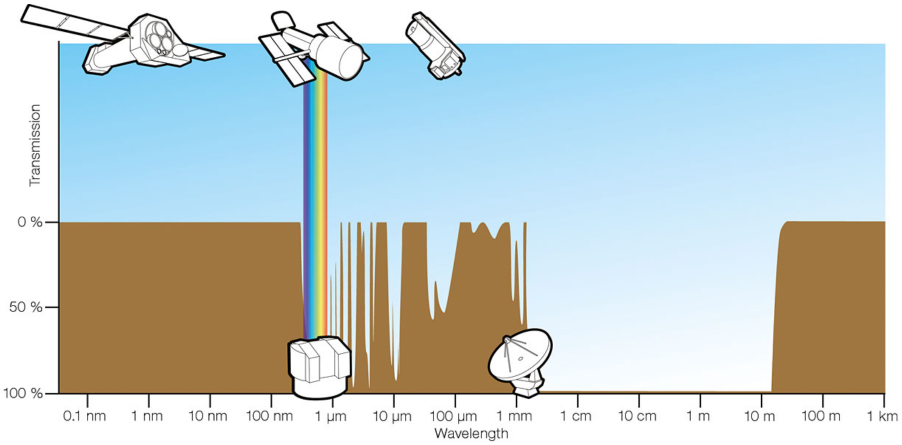

Figure 1.4: The opacity of the Earth's atmosphere as a function of wavelength. The brown regions are opaque and the blue areas are transparent. Credit: ESO.

the adaptive optics technique is used to correct for the turbulence of the atmosphere in real-time, angular resolutions of the order of 0.05 arcseconds can even be achieved. This is about 500 times better than the human eye[1] and means that we can distinguish details comparable to the width of a human hair at a distance of 300 m.

While not hampered by the atmosphere of the Earth, star light is typically affected to some degree by interstellar dust grains. However, the efficiency of this extinction strongly decreases with increasing wavelength and is already low in the NIR. Observations at a wavelength of 3.6 μm are therefore often used as an approximately dust-free tracer of the distribution of the stars in a galaxy (e.g. Meidt et al. 2014; Querejeta et al. 2015).

1.2.2 Gas

Observational studies of the gas in galaxies typically focus on the molecular and neutral atomic media, since these provide the direct fuel for future star formation. Warm ionised gas is also often observed to trace the star formation rate. Unlike the stars, gas atoms and molecules radiate primarily through discrete spectral lines.

Atomic gas is typically traced by the 21-cm hyperfine line of the neutral hydrogen (HI) atom. As can be seen in Figure 1.4, the Earth's atmosphere is also completely transparent in this wavelength range (called the radio domain). The 21-cm line is emitted when the quantum mechanical spins of the electron and the proton flip from parallel to antiparallel, bringing the atom in a slightly lower energy state. While this transition has an extremely large half-life time of 1.11×10^7 years (meaning that a single HI atom takes on average about 11 million years to decay spontaneously), the large abundance of hydrogen atoms

---

[1] http://www.physics.mcgill.ca/~moore/P101/Lectures/Lecture-16.pdf

makes the 21-cm line observable. The low efficiency of this transition means that, at the typical densities in the neutral ISM, the relative population of the hyperfine levels is determined only by collisions between atoms. Assuming no self-absorption, the observed intensity in the 21-cm line can then be translated directly into a HI column density (Wilson et al. 2009).

Molecular gas in galaxies consists mostly of molecular hydrogen, or H_2. These molecules, however, are linear and homonuclear. As a result, they have no permanent dipole moment and no rotational dipole transitions. The lowest lying transitions are rotational quadrupole transitions, at infrared wavelengths. These are not only weak, but also have high excitation energies (Bolatto et al. 2013). At typical molecular cloud temperatures of a few 10 K, collisions between molecules are to weak to significantly excite these transitions. Consequently, the H_2 in molecular clouds is not observable in emission. The molecular gas content in galaxies is therefore generally studied through the rotational J=1-0 and J=2-1 transitions of the ^{12}CO molecule, at 2.6 mm (115 GHz) and 1.3 mm (230 GHz) respectively. At these wavelengths, the Earth's atmosphere is also fairly transparent. The observed CO line intensities are then converted to H_2 column densities via the famous X_{CO} conversion factor. While this has been shown to depend on metallicity (e.g. Schruba et al. 2012; Rémy-Ruyer et al. 2014), extragalactic studies of 'normal' galaxies generally assume the same value as for the Milky Way (e.g. Bolatto et al. 2013).

Warm ionised gas is typically traced via the Balmer-α (Hα) transition of the hydrogen atom, between the $n = 3$ and $n = 2$ states. When a proton and an electron recombine, the electron is initially typically in a high energy state. When it subsequently cascades down the energy ladder, it can emit a Hα photon. The Hα line has a wavelength of 656 nm and can therefore easily be observed with optical telescopes.

Single dish telescopes

The angular resolution of a telescope at wavelength λ is approximately given by $1.22\,\lambda/D$, where D is the diameter of the mirror (or lens). At the millimetre and especially centimetre wavelengths used to trace the molecular and atomic gas, this means that we need very large telescopes to reach a usable angular resolution. However, self-supporting and steerable dishes are technically limited to a diameter of about 100 m. For larger dishes, the reflecting surface will deform under its own weight. At 21 cm, the angular resolution of a 100 m telescope is only about 9 arcminutes (about 20 times worse than the human eye). This easily encompasses the entire atomic gas disk of a typical nearby spiral galaxy. Larger dishes have been built in natural cavities in Puerto Rico (Arecibo telescope, 305 m diameter) and China (FAST telescope, 500 m diameter, Fig. 1.5), but these are no longer steerable and still only reach angular resolutions of the order of a few arcminutes for the HI line.

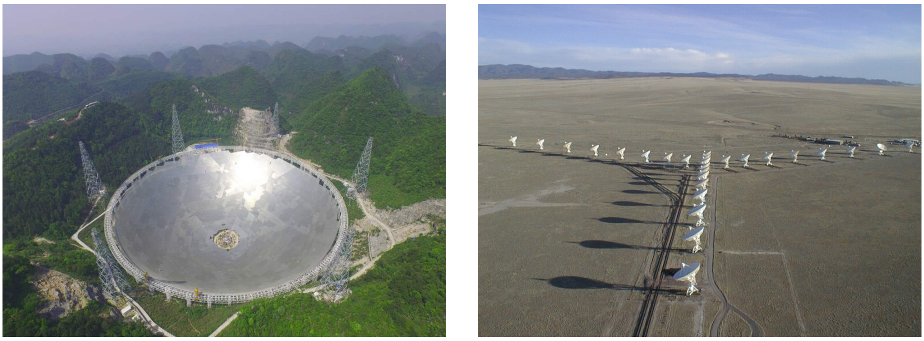

Figure 1.5: Left: the 500-m FAST telescope in China. Right: the Very Large Array in New Mexico. Credit: www.gbtimes.com / www.aoc.nrao.edu

Interferometers

The answer to this problem is interferometry, where a large collection of single dish telescopes (also called antennas) work together to effectively mimic one very large telescope. An example of this is the Very Large Array in New Mexico (shown in Fig. 1.5). The basic entity of an interferometric array is a two-element interferometer or antenna pair, formed by every antenna with every other antenna in the array. The vector connecting the two antennas in an antenna pair is called the baseline. Optical CCD detectors count the incoming photons by the photoelectric effect. This no longer works at radio wavelengths, because the energy of the photons is too low. Instead, radio telescopes measure the oscillating electric field of the incoming waves. For a source not perpendicular to the baseline, the two antennas of an antenna pair detect these waves with a slight offset in phase, because of the different path length that is travelled. By cross-correlating the signals measured by the two antennas, one can define a complex quantity (called visibility), characterized by an amplitude and a phase. The amplitude is related to the intensity of the source, while the phase of the visibility is related to the position of the source on the sky. Visibilities are registered by each antenna pair at regular sampling times, and essentially sample the Fourier transform of the sky brightness distribution. They populate a plane, called the *uv* plane, where their location corresponds to the tip of the vector connecting the associated antennas. An image of the sky brightness distribution of the source can be constructed by taking the Fourier transform of the visibilities in the *uv* plane. The angular resolution of the image is determined by the largest antenna spacing (or baseline). At 21 cm wavelength, the frequently used C configuration of the VLA gives a beam FWHM of approximately $15''$. In addition, the shortest baseline sets the largest angular size (LAS) that is visible to the array. This property is unique to interferometers and means that structures, or spatial frequencies, larger than the LAS are filtered out by the array.

For more information about radio interferometry, we refer the reader to Taylor et al. (1999).

Kinematics

A nice benefit of the spectral line observations that are conducted to study the interstellar gas, is that they can also be used to trace the kinematics of the galaxy. Indeed, for a particle moving at a certain velocity in a galaxy, the observed spectral line is Doppler shifted to a slightly different frequency or wavelength than at which it was emitted. From the central frequency and width of the line observed in different regions of a galaxy, we can thus reconstruct the rotational velocities and velocity dispersion of the gas.

On top of this Doppler shifting, the light from distant objects also undergoes an effect called cosmological redshift. Because the Universe is expanding, space and the light waves travelling through it are constantly stretched further and further. As a result, by the time it reaches an observer on Earth, the light from a distant galaxy will have a longer wavelength than when it was emitted. In other words, the light is shifted more towards the red part of the electromagnetic spectrum. Hence the term ‘redshift’. In combination with a cosmological model, this effect can be used to estimate the distance of far away objects.

1.2.3 Dust

Dust grains scatter and absorb the radiation from the stars at UV/optical wavelengths and re-emit the absorbed energy in the MIR/FIR/submm. Unfortunately, the atmosphere of the Earth is largely opaque in this wavelength range. To observe the emission from interstellar dust, we must therefore bring our telescopes into space, above the atmosphere. The first infrared space telescope, IRAS, was launched in 1983 (Neugebauer et al. 1984). It was later followed by the ISO (Kessler et al. 1996), Spitzer (Werner et al. 2004) and AKARI (Murakami et al. 2007) missions. The technical difficulties of mounting a telescope on a space craft limited the mirror sizes of these missions, resulting in relatively poor sensitivities and angular resolutions. For all but the most nearby galaxies, they therefore only allowed global, unresolved studies of the dust content. In addition, they also had limited wavelength coverage, operating at maximum wavelengths of 100, 240, 160 and 180 μm, respectively. However, the bulk of the dust in galaxies is typically cold, with temperatures of $\sim$ 20 K (Smith et al. 2012c; Rowlands et al. 2012; di Serego Alighieri et al. 2013), and emits significantly at higher wavelengths as well.
This situation was improved substantially with the launch of the Herschel Space Observatory (Pilbratt et al. 2010). With significantly better sensitivity and resolution than the previous missions, and extending the observable wavelength range to 500 μm, Herschel first enabled spatially resolved studies of the full dust content in nearby galaxies.

Complete observational studies of interstellar dust have thus become possible only recently, in stark contrast to the gas and stars. The first radio interferometers were built already in the 1970s, and CCD detectors replaced photographic plates for optical telescopes in the 1980s. As a consequence, our knowledge of dust is still very limited in comparison to the stars and gas. Many unknowns concerning the exact composition, shape and optical properties of interstellar dust grains remain. This is also amplified by the fact that the macroscopic grains primarily radiate continuum emission rather than spectral lines, which impedes identification. Our current knowledge of (or assumptions about) the properties of dust grains is essentially limited to the Milky Way and some local galaxies, and is based on a combination of theoretical modelling, lab experiments and analysis of extinction curves (e.g. Tielens & Allamandola 1986; Zubko et al. 2004; Draine & Li 2007; Jones et al. 2013).

1.3 Panchromatic SED modelling and dust radiative transfer

The interstellar gas in galaxies is traced via discrete spectral lines that are generally well understood. With modern observing facilities, good angular resolutions can be achieved in such studies. In addition, the photons corresponding to these spectral lines do not significantly interact with the other components. Hence, the interstellar gas can be observationally distinguished from the other components and studied on its own. For the stars, whose photons are absorbed and scattered by dust, and the dust, for which the optical properties are still uncertain and the observational resolution is still rather poor, the situation is more complicated.

The most complete way to study the stars and interstellar dust in galaxies is to consider the extinction of the stellar light and the thermal emission from the dust at the same time. Indeed, neglecting background sources, the energy emitted by the dust in the FIR/submm should be exactly equal to the energy that is absorbed from the stars at UV and optical wavelengths (a property called dust energy balance).

1.3.1 SED fitting

One way to perform this type of study is based purely on the spectral energy distribution (SED) of the galaxy, which gives the observed energy density (in units W m^{-2}) as a function of wavelength. While the emission of galaxies ranges from X-rays to deep into the radio, SEDs typically only cover the UV-submm range ($\sim 0.1 - 1000\ \mu$m) where the emission is dominated by the stars and dust. An example of such an SED is shown in Fig. 1.7.

To extract information from an observed SED, synthetic SEDs are created by combining emission models of different stellar populations with parametrised dust models under the condition of dust energy balance, and optimised until the observed SED is reproduced. This panchromatic (= multi-wavelength) SED fitting yields not only the mass and temperature of the dust, but also an intrinsic, unattenuated view of the stars. The technique can be applied globally, for the galaxy as a whole, or separately for each pixel in the images. A big advantage of this approach is that it is computationally fast, making it excellently suited for statistical studies of large samples of galaxies. Various tools to model the SEDs of galaxies have recently been developed (e.g. Silva et al. 1998; da Cunha et al. 2008;

Noll et al. 2009; Serra et al. 2011; Silva et al. 2011).
A major downside of the SED fitting technique is that is yields very little information about the spatial distribution of the dust and stars in galaxies. Even when the SED of each pixel is modelled separately, the spatial information is limited to projected two-dimensional distributions. In addition, the angular resolution is determined by the coarsest image in the data set. Given that Herschel-SPIRE images at 500 μm have a FWHM of $36''$, this is not very high. An additional downside of SED fitting is that it ignores non-local effects such as the heating of dust in one pixel by the radiation from stars in other pixels.

1.3.2 Dust radiative transfer

An alternative, but computationally very demanding approach is to perform 3D radiative transfer (RT) simulations. This technique does not use SEDs, but is based on the 3D distributions of the stars and dust and explicitly simulates the scattering, absorption and reprocessing of photons by the dust in the entire galaxy and at many wavelengths. Two approaches are broadly used for this purpose. Monte Carlo (MC) radiative transfer simulates a large number of photon packages and follows their individual paths through the dusty medium until they are absorbed or eventually leave the galaxy (e.g. Gordon et al. 2001; Jonsson 2006; Chakrabarti et al. 2007; Bianchi 2008; Baes et al. 2011). Ray-tracing radiative transfer starts from a fixed set of directions, or rays, and calculates the variation of the radiation field along these directions (e.g. Steinacker et al. 2006; Natale et al. 2014).

The first RT simulations were performed mainly for theoretical purposes in the form of forward radiative transfer. Starting from an artificial distribution of stellar sources and dust, the main question here is how this system would look to an outside observer and how the star light is attenuated along different lines of sight. Initially, this was done with analytical distributions of varying complexity for the stars and dust (e.g. Witt et al. 1992; Byun et al. 1994; Baes & Dejonghe 2001; Misiriotis & Bianchi 2002; Gadotti et al. 2010; Pastrav et al. 2013a,b). More recently, the technique has been extended to post-process hydrodynamical simulations of galaxies (e.g. Jonsson 2006; Domínguez-Tenreiro et al. 2014; Saftly et al. 2015; Camps et al. 2016; Trayford et al. 2017). This is still an active field of research today.

More interesting from an observational point of view is to start from a set of images of a real galaxy and build RT models with different combinations of stellar and dust distributions until the observed images can be reproduced. This type of modelling is called inverse radiative transfer and ultimately yields constraints on the full three-dimensional distributions of the stars and dust, the intrinsic stellar luminosities and the dust masses. Because the dust distribution can, in principle, be derived from attenuation effects in the UV/optical, inverse RT has the advantage that it is not limited by the poor resolution of the FIR and submm images. On the other hand, it is computationally much more expensive

Figure 1.6: The edge-on spiral galaxy NGC 4565. The dust is clearly visible as a dark lane. Credit: http://cs.astronomy.com.

than SED fitting. Inverse radiative transfer is therefore typically used to analyse small samples of nearby galaxies.

1.3.3 The energy balance problem

For a long time, inverse radiative transfer studies of galaxies have targeted edge-on systems, for a number of reasons. First, the dust in edge-ons often forms dark lanes in optical images (Fig. 1.6) and is therefore clearly visible both in emission and in extinction. Second, edge-ons are the only systems where both the radial and the vertical distribution of the stars and dust can be studied. Third, due to the line of sight projection, these distributions can often be approximated by smooth analytical profiles such as exponential disks, rings or (flattened) Sérsic bulges. Up to very recently, these analytical approximations were the only way to make radiative transfer studies computationally feasible.

The first applications of inverse radiative transfer to edge-on galaxies focused only on the extinction in the optical (Kylafis & Bahcall 1987; Xilouris et al. 1997, 1998, 1999; Bianchi 2007). These studies consistently showed that the dust in massive spirals is distributed in a thinner, but generally more extended disk than the stars. Later studies also included the thermal dust emission at FIR/submm wavelengths in the modelling (e.g. Alton et al. 2004; Dasyra et al. 2005; Baes et al. 2010; De Looze et al. 2012b,a). Interestingly, these studies revealed a discrepancy. For models that correctly reproduced the extinction in the optical, the predicted thermal dust emission consistently underestimated the observed FIR/submm fluxes by up to a factor of 3 (Fig. 1.7). This discrepancy has been named the dust energy balance problem. Several explanations were proposed for this problem. First, the emissivity of the interstellar dust could simply have been underestimated (Alton et al. 2004; Dasyra et al. 2005). Second, a significant fraction of the dust could reside in dense and compact clumps instead of a smooth distribution. Such clumps would have little influence on the overall extinction of stellar radiation, but would contribute significantly to the FIR/submm emission (Popescu et al. 2000; Misiriotis et al. 2001; Bianchi 2008; Saftly et al. 2015). Finally, obscured star forming regions might be embedded in the dust (e.g. Knapen et al. 1991). The UV radiation from the newly formed stars would be completely absorbed by the surrounding dust, hence contributing significantly to the heating of the dust, but not to the observed UV/optical emission. However, this last explanation was refuted by De Looze et al. (2012b).

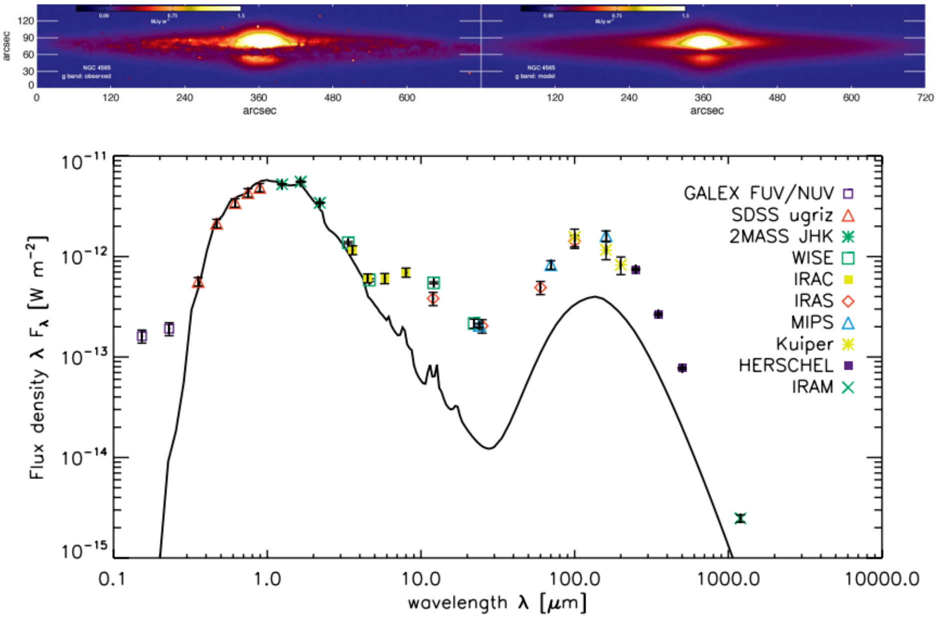

Figure 1.7: Top: observed *g*-band image of the edge-on galaxy NGC 4565 (left) and image derived from the radiative transfer model of De Looze et al. (2012a) in the same band (right). Bottom: observed (points) and modelled (solid black line) SED of the same galaxy. If the extinction in the optical is reproduced, the model underestimates the observed FIR/submm fluxes by a factor of three.

One drawback of the studies mentioned above is that they were performed by hand, i.e. the parameters of the RT models were adjusted manually until a satisfactory agreement with the data was achieved. This makes them hard to compare and hampers a systematic investigation of the energy balance problem. A significant improvement to this situation was brought by the FitSKIRT tool that was developed by De Geyter et al. (2013, 2014). FitSKIRT is an automatic fitting tool built around the MC radiative transfer code SKIRT (Baes et al. 2011; Camps & Baes 2015). In addition to providing reproducible and unbiased fits, it also allows to fit images at multiple wavelengths at the same time. The latter significantly increases the power of the fits, as it combines important information on the stellar distributions from NIR bands with constraints on the dust attenuation from images at bluer (shorter) wavelengths. An analysis of two edge-on spiral galaxies with FitSKIRT (De Geyter et al. 2015) still found a discrepancy between the observed and predicted FIR/submm fluxes.

1.4 FRIEDL, HEROES and NHEMESES

In order to thoroughly and systematically investigate the energy balance problem, an ensemble of three Herschel programmes was set up by the nearby galaxy group of the UGent astronomy team, in collaboration with other institutes. Each project targets a sample of nearby edge-on galaxies of a different Hubble type. All the galaxies were imaged with the PACS and SPIRE instruments of the Herschel telescope.
The first objective of the projects was to use SKIRT and FitSKIRT to construct radiative transfer models of all the sample galaxies in a systematic and unbiased way, in order to gain insights in the energy balance crisis. The second major objective was to map the interstellar gas in these systems as well, and to investigate the distributions of the gas, dust and stars with respect to each other, radially and vertically, and for different Hubble types. Since the evolution of the various components is so closely connected, studying them together is vital to correctly interpret the observations. Due to the line of sight projection, the dust can be traced out to large radii in edge-on galaxies. This allows to study the gas-to-dust ratio also in the outskirts of the sample galaxies, in regions where face-on studies often no longer detect dust.

The Far-infraRed Investigation of Early-type galaxies with Dust Lanes (or FRIEDL) project focuses on a sample of 11 early-type galaxies with dust lanes. The selection of the FRIEDL sample is described in section 4.1. The Herschel observations of these systems were performed on UGent guaranteed time in 2012. Dust lane ETGs are an interesting class of galaxies. They often show signs of recent star formation (unexpected for ETGs) and morphological disturbances, indicating a merger in their recent past. Given the paucity of major mergers at low redshift (i.e. in the recent history of the Universe), dust lane ETGs are most likely the remnants of recent gas-rich minor mergers (Kaviraj et al. 2011). Moreover, since early type galaxies have generally long lost their own cold ISM, the dust and neutral gas in dust lane ETGs holds information about the low-mass progenitors of the recent mergers.

The HERschel Observations of Edge-on Spirals (or HEROES) project targets 7 massive early-type spiral galaxies. The dust in these systems typically forms a thin lane and was observed with Herschel in 2010 and 2011, also on UGent guaranteed time. The details of the sample selection are given in section 2.1.

Finally, NHEMESES (New HErschel Multi-wavelength Extragalactic Survey of Edge-on Spirals) targets 12 less massive, later type spiral galaxies. The Herschel observations of the dust content were conducted as OT1 priority 2 and OT2 priority 1 programme in 2011 and 2012 (with B. Holwerda as principle investigator). While the dust in massive spirals typically forms a thin lane, it was found to have a more flocculant and vertically extended distribution in less massive spiral galaxies (Dalcanton et al. 2004). One of the goals of NHEMESES is to investigate whether there is indeed a sharp phase change in the vertical structure of the ISM with disk mass. In this thesis, however, the NHEMESES project is not considered. For more information about NHEMESES, we refer the reader to Holwerda et al. (2012a,b).

1.4.1 The energy balance problem revisited

Detailed radiative transfer models of the HEROES galaxies were recently constructed with FitSKIRT by Mosenkov et al. (2016) and Mosenkov et al. (in prep.). In summary, they find that the energy balance problem in edge-on galaxies still persists, even with more sophisticated stellar distributions (young superthin disk + thin disk + thick disk + bulge), or when the original dust models from Zubko et al. (2004) or Draine & Li (2007) are replaced by the more accurate THEMIS dust model (Jones et al. 2013; Köhler et al. 2014, 2015).

In the same period, however, a giant leap forward in 3D radiative transfer modelling was taken by De Looze et al. (2014). With increased computing power, they were able to model the *face-on* galaxy M51 in extreme detail by using the exact stellar and dust geometries from observed images. In particular, the distribution of the dust was derived at high resolution through the FUV attenuation, and multiple stellar components (old, young non-ionising and young ionising) were used based on images in multiple bands. The two-dimensional face-on images were supplemented with exponential profiles for the vertical direction, based on previous RT studies of edge-on systems, and deprojected to obtain the three-dimensional geometries. In contrast with the previous works, De Looze et al. (2014) found no discrepancy in the energy balance for M51. A similar result was later also obtained for M31 (Andromeda) by Viaene et al. (2017).
Whether or not these studies resolve the dust energy budget crisis, is, however, not clear. On the one hand, face-on galaxies offer a clear advantage over edge-ons. The FIR emission from dust at a certain location in a galaxy depends on how much dust there is and how that dust is heated, which, in turn, is determined by the interstellar radiation field at that location. To correctly reconstruct both these aspects, it is crucial to know how the different stellar populations and the dust are distributed with respect to each other. In face-on systems, the locations of individual star forming regions and the asymmetries in the dust and stellar distributions can be discerned. At high inclinations, the projected view washes away these details. On the other hand, the energy balance problem is intrinsically less apparent in face-on galaxies, because the attenuation by the dust at optical wavelengths is much weaker than in edge-on systems. This provides more freedom to vary the amount of dust and hence makes it easier to find a model that reproduces the observed emission at all wavelengths.

1.5 Dark matter

Up to know, we have only discussed the baryonic matter in galaxies. This comprises everything we can see or detect through the emission or absorption of radiation in some part of the electromagnetic spectrum. According to the standard cosmological model, however, this ordinary matter only makes up about 16 percent of the total amount of mass in the Universe. The remaining 84 percent is thought to be made up of a dissipationless and collisionless form of matter that interacts only through gravity: the infamous dark matter. While it adds to the mysterious aura, the term 'dark' is in fact somewhat infelicitous. It refers to the fact that dark matter does not interact electromagnetically, i.e. it doesn't absorb, scatter or emit any light. As such, dark matter is in fact completely *transparent* and cannot be observed with any telescope, on Earth or in space.

1.5.1 History

The first notion of a mass deficiency in astronomical systems came in the beginning of the 20th century. In 1915, the Estonian astronomer Ernst Öpic first attempted to infer the total mass density in the Solar neighbourhood by measuring the motions of nearby stars perpendicular to the Galactic disk. He came to the conclusion that the combined masses of the visible stars in the vicinity of the Sun were sufficient to explain the observed stellar velocities (Öpic 1915). This result was later confirmed by Jacobus Kapteyn, who found that little or no "dark matter" was needed to account for the observations (Kapteyn 1922). A different conclusion was reached by James Jeans and Jan Oort. Based on similar analyses, they concluded that the observed stellar motions could only be explained by a significant amount of additional mass, up to a factor of 2 or more (Jeans 1922; Oort 1932). They proposed that this missing mass consisted of faint (undetected) stars, or stars hiding behind other stars. In the following decades, the mass density in the Solar neighbourhood was reanalysed several times, with some studies confirming the results of Öpic and Kapteyn (e.g. Kuzmin 1952, 1955; Jõeveer 1972, 1974) and others backing the conclusions from Jeans and Oort (e.g. Oort 1960; Bahcall & Soneira 1980; Bahcall 1984).

On a completely different scale, the flamboyant Swiss astronomer Fritz Zwicky (Fig. 1.8) applied the virial theorem to the galaxies of the Coma cluster and found that the velocities of these galaxies were much too high to be held together by the gravity of the visible matter alone (Zwicky 1937). He estimated that the total mass of "Dunkle Materie" in the Coma cluster should be at least an order of magnitude larger than the visible mass of the stars and gas. In addition to a brilliant astrophysicist, Zwicky was also an unusual character and regularly referred to his own colleagues as spherical bastards, because "no matter how you look at them, they are just bastards".
Several other works later also found mass deficiencies in systems of galaxies, for example by analysing the relative motions of the Milky Way and Andromeda in the Local Group (e.g. Kahn & Woltjer 1959; Einasto & Lynden-Bell 1982).

Alternative evidence for the existence of dark matter on galactic scales came from the analysis of the rotational velocities of disk galaxies as a function of their radius (so-called rotation curves). For a spherical distribution of mass, the rotational velocity that is needed

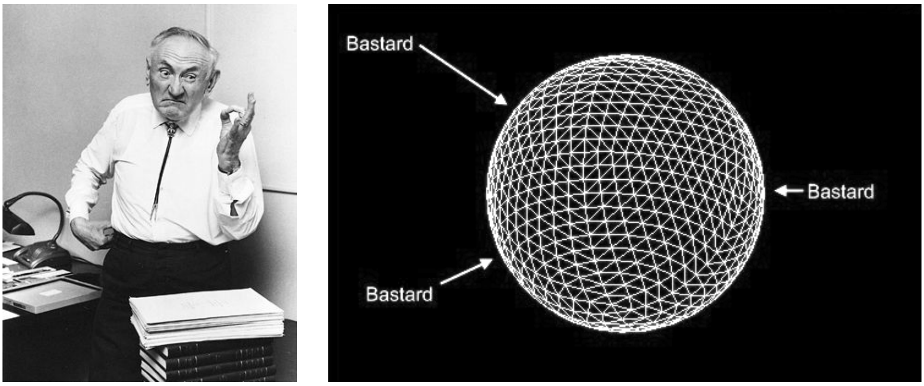

Figure 1.8: Fritz Zwicky, one of the first to propose the existence of dark matter. He regularly called his colleagues "spherical bastards", because "no matter how you look at them, they are just bastards". Credit: www.scienceblogs.com

to resist the inward gravitational pull from the enclosed mass $M(r)$ at radius r is:

$$V(r) = \sqrt{\frac{G\,M(r)}{r}}, \tag{1.1}$$

where G is the gravitational constant. This relation changes somewhat for mass distributed in a disk (like the stars and gas in spiral galaxies), but the main principle remains the same. In the outskirts of stellar disks, where the density of stars is low, the enclosed visible mass does not significantly increase any more with increasing radius. As a consequence, the ratio $M(r)/r$, and therefore also $V(r)$, is expected to decrease with radius. When Babcock (1939) and Oort (1940) measured the rotational velocities of the stars in M31 (Andromeda) and NGC 3115, however, they found that these were much higher than expected at large radii. This indicated that either the stellar mass-to-light ratios in the outskirts of galaxies were orders of magnitude higher than in the solar neighbourhood, or that significant amounts of invisible matter were present. More detailed observations of the stellar velocities in M31 and other galaxies later also found flat, non-declining rotation curves (e.g. Rubin & Ford 1970; Rubin et al. 1980, 1985, Fig. 1.9). Rotation curves derived from radio observations of the HI gas provided even stronger evidence for the presence of invisible matter. These rotation curves were found to remain flat even well beyond the stellar disks (e.g. Freeman 1970; Roberts & Whitehurst 1975; Rubin et al. 1978; Bosma 1978). Since essentially no stars are present at these large radii, even an anomalously high mass-to-light ratio could not explain the lack of decline in the observed rotation curves.

By the 1980s, the need for a significant amount of invisible or dark matter in galaxies and clusters of galaxies was firmly established. The nature of this dark matter, however, is still a mystery today.

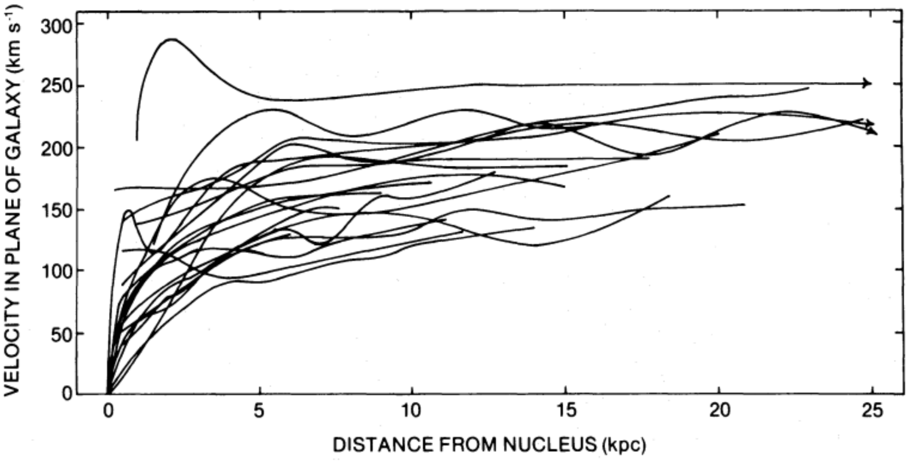

Figure 1.9: Rotation curves of 21 galaxies as measured by Rubin et al. (1980). The curves do not show the decline that is expected for visible matter only. Credit: Rubin et al. (1980).

1.5.2 Dark matter in cosmology

Modern cosmology started in the 1920s, when Alexander Friedmann and Georges Lemaître independently proposed solutions for Einstein's general relativistic field equations (Friedmann 1922; Lemaître 1927). In contrast to Einstein himself, who introduced an additional term to obtain a static Universe, Friedmann and Lemaître suggested that the Universe is expanding. This was later confirmed observationally by Edwin Hubble, who found that galaxies move away from the Milky Way at velocities that are proportional to their distance (Hubble 1929).

Two alternative cosmological theories emerged from this finding. On the one hand, Lemaître suggested that the Universe must have had a starting point and that it was created from a singularity. This theory was further developed by Ralph Alpher in collaboration with George Gamow (Alpher et al. 1948) and Robert Herman (Alpher & Herman 1948a,b). On the other hand, Fred Hoyle's Steady State theory proposed that the Universe had always existed and that matter was continuously created as the Universe expanded, keeping the total density constant. During a radio broadcast on the BBC, Hoyle contemptuously called the initial singularity from Lemaître's model the "Big Bang", thus unwillingly naming the theory that he opposed. Both theories existed side by side until the discovery of the cosmic microwave background (CMB) in 1965 (Penzias & Wilson 1965). The existence of the CMB had already been predicted from the Big Bang model in 1948 by Alpher and Herman, but could not be explained by the Steady State theory.

The Big Bang theory thus emerged as the correct model, but an important issue still remained. If the matter in the Universe consisted only of baryons (as was still the general idea at that time), the cosmic structure in the Universe must have formed directly from

the fluctuations in the CMB. Although not observed explicitly, upper limits on these fluctuations dictated that they could only be very small. Much too small to explain the large density fluctuations (e.g. galaxies) we observe today. At the start of the 1980s, it was realised that the observationally established dark matter could resolve this problem and that the total matter content of the Universe must even be heavily dominated by this dark matter. Indeed, unaffected by the photons in the early Universe, dark matter could already develop overdensities well before the epoch of recombination.
While firmly establishing its existence, observational studies did not provide any insights in the nature of the dark matter. In the beginning of the 1980s, it was proposed that dark matter could be 'hot' and consist of fast moving particles (generally thought to be massive neutrinos). However, it was soon realised that such relativistic particles would wash away all but the most extended density fluctuations in the Early Universe. Structure formation would therefore happen top-down, with very large structures forming first. It was generally thought that these would then collapse asymmetrically into flat 'pancakes'. Denser filaments would occur at the intersect of such pancakes. These large structures would only fragment into smaller structures (clusters and galaxies) later on. This scenario has several problems. First, it predicts that galaxies should only start forming relatively late on. This is in contradiction with the old stellar populations found in galaxies (with ages close to that of the Universe) and with high redshift observations that have revealed galaxies forming at very early epochs. Second, if galaxies form by fragmentation of large filaments, their large-scale distribution should still have a strongly filamentary structure, much stronger than what is actually observed in the real Universe. For cold dark matter (CDM), consisting of slowly moving particles, structure formation is hierarchical, with small structures forming first and merging into larger structures later on. As a consequence, it does not have the problems faced by hot dark matter.

Around the same time, the cosmic inflation theory (Guth 1981; Linde 1982; Albrecht & Steinhardt 1982) suggested that the Universe had experienced a short and very rapid expansion just after the big bang. This implied that the Universe should be flat, with a total density close to the critical density, which was also confirmed by measurements of the CMB fluctuations by the COBE satellite in 1992 (Smoot et al. 1992; Wright et al. 1992). However, if baryons and cold dark matter alone accounted for this total density (referred to as the Standard CDM or SCDM model), several tensions with the observational data arose. When normalised to the reproduce the large scale CMB fluctuations observed by COBE, SCDM overpredicts the number of galaxy clusters (at scales of a few Mpc White et al. 1993) and underpredicts their correlations on larger scales (Olivier et al. 1993; Borgani et al. 1997). Several modifications to the SCDM model were therefore proposed, including CHDM (Cold Hot Dark Matter) and ΛCDM (Lambda Cold Dark Matter). In the former, about 20% of the dark matter is hot (e.g Primack et al. 1995). In the latter, the majority of the total density of the Universe is accounted for by a cosmological constant, interpreted as vacuum or dark energy, which has a negative pressure. As opposed to matter and its associated gravity, dark energy would accelerate the expansion of the Universe at the current epoch. With the empirical confirmation of this accelerated expansion from observations of type Ia supernovae in other galaxies (Riess et al. 1998), ΛCDM finally became the standard cosmological model.

1.5.3 Cosmological simulations

By the late 1980s, computers had become powerful enough to perform large scale simulations of structure formation in the Universe within the CDM framework. Since gravity is the only interaction that is still relevant at large spatial scales, and collisionless dark matter was known to make up the bulk of the total mass, such simulations were typically performed as gravitational N-body simulations of a large number of dark matter particles (e.g. Efstathiou et al. 1985). Structure formation in these simulations occurs hierarchically through the gravitational collapse of small overdensities, forming individual (virialised) dark matter haloes. Larger structures subsequently form through the accretion of matter from the surroundings, or merging with neighbouring haloes, but retain substructure in the form of smaller subhaloes. If the CDM framework is indeed correct, the structures in a simulated Universe (or at least a representative part of the Universe) should have the same statistical properties as observed in the real Universe.

The first simulations gave promising results, but were often still based on the SCDM model and suffered from the problems explained in the previous section (e.g. Blumenthal et al. 1984; Davis et al. 1985). Later simulations, based on the ΛCDM model, excellently reproduce the observed large scale structure of the Universe, up to the scales of individual large galaxies (e.g. Klypin et al. 1999a, 2011; Springel et al. 2005). On smaller scales, however, several issues still remain.

While the number of massive galaxies is correctly reproduced, dark matter-only simulations also predict that these should have numerous smaller scale satellites, much more than are actually observed around the Milky Way or other galaxies (e.g. Klypin et al. 1999b; Moore et al. 1999a; Diemand et al. 2008; Springel et al. 2008). This discrepancy is known as the ‘missing satellites problem’. A plausible solution to this problem is that these low mass haloes are simply not visible, because they were at some point inhibited to form or keep forming stars, for example due to the UV background radiation or because they lost their gas through stripping or supernova feedback (e.g. Hambrick et al. 2011; Verbeke et al. 2015; Nierenberg et al. 2016; Vandenbroucke et al. 2016).

A related issue is that, for the satellite galaxies that are observed, the inferred dark matter halo masses are on average much smaller than predicted by ΛCDM simulations (Boylan-Kolchin et al. 2011, 2012; Ferrero et al. 2012; Tollerud et al. 2014; Papastergis et al. 2015). In other words, if these smaller haloes are present and support observable dwarf galaxies, the larger ones that are predicted by ΛCDM could not have failed to form galaxies of their own. This is known as the ‘too big to fail problem’. A potential solution for this issue was recently proposed by Verbeke et al. (2017), who found that basic Hɪ rotation curves can severely underestimate the true circular velocities in turbulent low-mass dwarf galaxies. As a consequence, the observationally inferred dark matter halo masses

are also severely underestimated.
Additionally, zoom-in dark matter-only simulations of individual haloes at different scales have consistently found steep inner density profiles for the dark matter, in stark contrast with observational constraints. This issue, known as the ‘cusp-core controversy’, is the subject of some of the work done in this thesis.

1.5.4 The cusp-core controversy

The analysis of a number of extended optical and HI rotation curves in the 1970s and early 1980s firmly established the existence of extended dark matter haloes around galaxies. Soon, various works took this analysis a step further and decomposed the rotation curves of spiral galaxies into the contributions of the stars, gas and dark matter to derive the radial distribution of the dark matter (e.g. van Albada et al. 1985; Athanassoula et al. 1987; Begeman et al. 1991). Most interesting for this type of study are dwarf and low surface brightness (LSB) galaxies, for which the uncertain contribution of the stars (due to their uncertain mass-to-light ratio) is limited even in the inner regions. From the rotation curves of such galaxies, it was found that, after subtraction of the baryonic contributions, the velocity curve of the dark matter rises almost linearly in the central regions. For a spherical distribution, this implies that the enclosed mass goes as $M(r) \propto r^3$ (eq. 1.1), and hence that the dark matter density is approximately constant in the inner regions of disk galaxies.

Various analytic profiles for the dark matter distribution were proposed in the 1980s and 1990s. These profiles, including the pseudo-isothermal sphere (e.g. van Albada et al. 1985; Begeman 1987), the Burkert halo (Burkert 1995) and the Universal Rotation Curve (Persic et al. 1996), all have a central core of constant density and were found to give excellent fits to the rotation curves of both dwarf galaxies and massive spirals (e.g. Begeman et al. 1991; Broeils 1992; de Blok et al. 2001a; Gentile et al. 2004). The pseudo-isothermal sphere in particular soon became the standard way to describe the dark matter distribution in disk galaxies. It should be noted, though, that these density profiles are purely empirical and were not derived from first principles. In fact, the pseudo-isothermal sphere model is highly unphysical since its enclosed mass diverges for $r \to \infty$.

At the same time, high-resolution N-body simulations of individual dark matter haloes were also used to investigate the distribution of dark matter. Surprisingly, these studies found no trace of finite density cores. Instead, Dubinski & Carlberg (1991) found that their haloes were better described by a cuspy density profile, behaving as $\rho(r) \propto r^{-1}$ for $r \to 0$. The central (log) slope of dark matter density profiles is typically noted as γ, such that

$$\gamma = -\frac{\mathrm{d}\ln\rho}{\mathrm{d}\ln r}, \ \ r \to 0. \tag{1.2}$$

Dubinski & Carlberg (1991) thus found a density profile with a central slope of $\gamma = 1$. Navarro et al. (1996b) reached a similar conclusion and found that haloes of very different scales all had central cusps and were well described by a single universal profile:

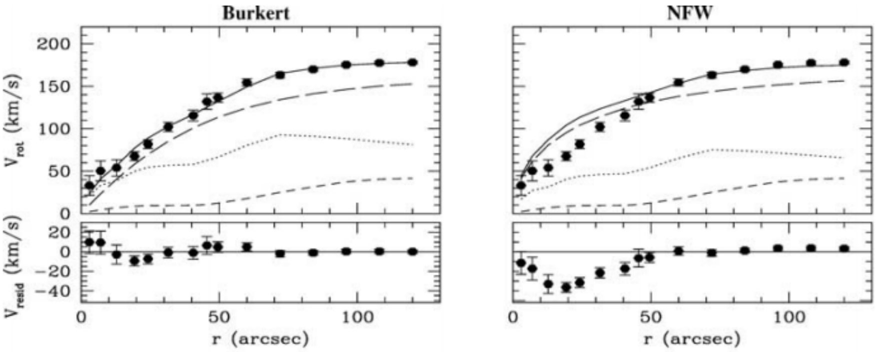

Figure 1.10: Dynamical models for the spiral galaxy ESO 79-G14 from Gentile et al. (2004). The observed rotation curve is represented by the data points with error bars. The model curve is shown by the solid black line and the various contributions to the model are shown by the dashed and dotted lines. The cored Burkert halo (left) provides a good fit, while the cuspy NFW halo (right) fails to reproduce the data. Credit: Gentile et al. (2004).

the famous Navarro-Frenk-White (NFW) halo. These studies still relied on the SCDM model, but this makes little difference for individual haloes. Later dark matter-only simulations, based on ΛCDM cosmology, also consistently found dark matter cusps, albeit with varying central slopes. Moore et al. (1999b), Fukushige & Makino (2001) and Klypin et al. (2001), for example, found a somewhat steeper central slope of 1.5, while Taylor & Navarro (2001) found weaker cusps with $\gamma \sim 0.7$ and Colín et al. (2004) confirmed the NFW profile ($\gamma = 1$). A vast body of other works also conducted similar analyses. In summary, these studies all found central (or near central) slopes of the order of $\gamma = 1$ or steeper.

When used to fit observed rotation curves of dwarf or LSB galaxies, these cuspy profiles generally either require halo parameters that are in strong conflict with those predicted by the simulations, or fail to reproduce the rotation curves altogether (e.g. de Blok et al. 2001b; Gentile et al. 2004, 2007, see also Fig. 1.10). This discrepancy has become known as the cusp-core controversy. In more massive spirals, where the significant stellar contribution allows more freedom in the dark matter, the rotation curves are generally represented equally well by cored and cuspy dark matter halo models (e.g. de Blok et al. 2008). Again, it is important to note that the cuspy dark matter profiles inferred from simulations are merely extrapolations of analytical fits to the simulated haloes. As such, they are not actual predictions of the ΛCDM model.

At the onset of the cusp-core discussion, both the observational studies and the simulations actually had significant flaws. The initial simulations often had rather low resolution ($\sim$ 1 kpc) and the relatively large spread in the reported central slopes indicates that the conclusions could be influenced by the initial conditions, numerical convergence and analysis techniques of the simulations (de Blok 2010). The rotation curves, on the other hand, often suffered from various observational biases or uncertainties. For example, they often did not account for non-circular motions or internal pressure support of the interstellar gas. In addition, due to the poor angular resolution of the observations, HI based rotation curves were often biased by beam smearing (averaging of all the velocities in the observational beam, weighted by the associated intensities). Optical rotation curves had significantly higher resolution, but were derived from long-slit spectra measured along the major axis of the galaxy. These contained only limited information about the kinematics and could be severely biased if the slit was not placed correctly.

In the years that followed, however, the observations and analysis techniques improved significantly. Interferometric HI observations attained much higher resolutions, up to the point that beam smearing was no longer an issue for nearby galaxies. With the advent of integral field spectroscopy, optical observations were no longer limited to one dimensional slits, but could also obtain 2D velocity fields. More accurate techniques were further developed to quantify and correct for pressure support and non-circular motions. In addition, astronomers became more aware of the potential biases and used stricter selection criteria to avoid them. With the ever increasing computing power, N-body dark matter-only simulations also attained increasingly higher resolutions, up to and beyond those of the observations (e.g. Stadel et al. 2009). With these significant advancements, consensus is growing that the rotation curves of galaxies do truly trace their gravitational potentials, at least for properly selected systems, and that the conclusions from both sides are now trustworthy (although some remain sceptical, e.g. Valenzuela et al. 2014; Baushev et al. 2016; Amorisco 2017; Pineda et al. 2017).

The discrepancy between observations and dark matter-only simulations, however, essentially remains. Observational studies continue to find a strong preference for cored dark matter distributions in dwarf and LSB galaxies (e.g. Gentile et al. 2007; de Blok et al. 2008; Kuzio de Naray et al. 2008; Bottema & Pestaña 2015; Oh et al. 2015; Karukes & Salucci 2017) and perhaps even in higher mass spirals as well (Spano et al. 2008; Rodrigues et al. 2017). For the simulations, Navarro et al. (2004) found that the simulated haloes are in fact not universal (i.e. they cannot be made identical after rescaling) and have inner slopes that monotonically become less steep towards the center, rather than converging to a fixed value as in the NFW case. However, these haloes still consistently show slopes of around $\gamma \sim 1$ or steeper at radii comparable to the innermost regions probed by the observations (e.g. Merritt et al. 2006; Gao et al. 2008; Stadel et al. 2009; Navarro et al. 2010). For dwarf and LSB galaxies, the dark matter-only simulations therefore remain in conflict with the observed rotation curves.

1.5.5 Baryons to the rescue?

One important aspect that we have not yet considered is baryonic physics. The simulations that were discussed in the previous sections were purely gravitational N-body simulations of only dark matter particles, and essentially ignored the formation and evolution of galaxies inside the dark matter haloes. It has been know for a long time, however, that baryons can indirectly have a significant impact on the distribution of the dark matter as well.

This can happen in multiple ways and with multiple outcomes. For example, when hot gas cools down in a forming galaxy, it loses angular momentum and falls towards the center of the halo, gravitationally dragging the dark matter along with it. This adiabatic contraction would therefore make a primordial cusp even steeper (e.g. Blumenthal et al. 1986; Jesseit et al. 2002; Gnedin et al. 2004; Katz et al. 2014).
Alternatively, El-Zant et al. (2001) proposed a dynamical friction scenario in which purely baryonic clumps of primordial gas that fall into a dark matter halo gravitationally transfer their angular momentum to the dark matter. The latter is thus dynamically heated and puffs up. El-Zant et al. (2001) argued that this process could be efficient at transforming initial dark matter cusps into cores if it occurs in the early Universe, when dark matter haloes still had low masses. The viability of this mechanism was later confirmed by Jardel & Sellwood (2009), but based on Kaufmann et al. (2006) they did note that the required masses of the infalling clumps are about two orders of magnitude higher than what is expected for purely baryonic gas clouds. Similar scenarios were also investigated by other works, but their efficiency remains questionable (for an elaborate discussion, see de Blok 2010).
Feedback from supernovae (and possibly AGN activity in high mass galaxies) can induce massive gas outflows that can also cause the dark matter halo to expand. Navarro et al. (1996a) already investigated this scenario using a highly simplified outflow model and concluded that supernova feedback could have flattened the dark matter cusps in dwarf irregular galaxies, but is unlikely to be effective in more massive systems. In a more detailed study, Read & Gilmore (2005) found that repeated bursts of star formation and the associated supernovae, alternated by epochs of gas contraction can indeed gradually transform dark matter cusps into cores in simulated dwarf galaxies. This result was later confirmed and extended to somewhat higher mass galaxies by numerous studies (e.g. Governato et al. 2010; Cloet-Osselaer et al. 2012; Macciò et al. 2012; Teyssier et al. 2013; Di Cintio et al. 2014b; Oñorbe et al. 2015). Important to note here is the (halo) mass dependence of this process. Cusps can only be turned into cores if sufficient feedback energy is available. In tiny dwarf galaxies that form little stars, too few supernovae go off to alter the distribution of the dark matter. In very massive galaxies, significant feedback does occur, but the gravitational field is too strong for this feedback to be effective, and the dark matter halo also retains its cusp. The details of this mass dependence are still a matter of debate. For example, while Governato et al. (2012) found that supernova feedback can only expand dark matter haloes in galaxies with $M_{*} \gtrsim 10^{7}\ M_{\odot}$, Read et al. (2016a) concluded that cores also form in lower mass systems if star formation proceeds for long enough. There is, however, consensus that cusps are efficiently transformed into cores in the intermediate-mass galaxies that are generally the subject of observational rotation curve studies.

Hydrodynamical simulations therefore seem to suggest that stellar feedback effects can solve the cusp-core controversy. However, this remains at the level of simulations. To really test this solution, the simulated haloes must be compared to real observed rotation curves. For this purpose, two new analytic dark matter density profiles were recently proposed. The DC14 profile was derived by Di Cintio et al. (2014a) from their simulated galaxies in the mass range $10^{10} < M_{\rm halo}/M_{\odot} < 8 \times 10^{11}$ and was recently tested on samples of observed rotation curves by Katz et al. (2017) and Pace (2016). Both studies concluded that the DC14 profile can indeed reproduce the observed rotation curves. Katz et al. (2017) also found that the derived dark matter halo parameters are in excellent agreement with the cosmological stellar mass-halo mass and halo mass-concentration relations. Pace (2016), on the other hand, concluded the opposite. He found halo masses significantly below the cosmological prediction for galaxies with stellar masses $M_* \lesssim 10^9$ $M_{\odot}$, and a huge scatter of almost two orders of magnitude in the derived halo concentrations. The coreNFW model was derived by Read et al. (2016a) from simulations of tiny dwarf galaxies in the mass range $M_{\rm halo} \sim 10^7 - 10^9$ $M_{\odot}$. Read et al. (2017) also recently tested this profile on a set of dwarf galaxy rotation curves extracted from the LITTLE THINGS sample (Hunter et al. 2012; Iorio et al. 2017), with halo masses ranging from a few 10^8 $M_{\odot}$ to about 2×10^{10} $M_{\odot}$. They also found good fits to the observed rotation curves and good agreement with the stellar mass-halo mass relation.

While both models seem to agree with observed rotation curves, the agreement of the DC14 model with cosmological scaling relations therefore remains an open question. In addition, the simulations of Read et al. (2016a) and Di Cintio et al. (2014a) are valid in different, complementary mass ranges. It remains to be seen if their predictions are actually consistent with each other and the combination of both works therefore offers a global picture of core formation over a large mass range.

1.5.6 Alternatives to dark matter

Up to now we have only presented dark matter as solution for the missing mass problem in galaxies and galaxy clusters. Beyond this problem, cold dark matter (in the frame of the ΛCDM model) has indeed also led to a number of successful cosmological predictions on much larger scales, such as the power spectrum of the CMB fluctuations. However, since the dark matter particle, whatever it may be, is yet to be detected, we still have no solid proof of its existence.

The need for dark matter comes from a discrepancy between observations and the expected gravitational effects of the visible baryonic matter. Instead of assuming that the Universe is filled with a hypothetical, invisible form of matter, an alternative solution could therefore be that our notion of gravity is simply wrong or incomplete. From a philosophical point of view, this is as plausible or implausible as the dark matter hypothesis.

The first and most famous modification of gravity as alternative to dark matter was MOND (MOdified Newtonian Dynamics), developed by Mordehai Milgrom in 1983 (Milgrom

1983). Milgrom suggested a modification of the classical r^{-2} behaviour of gravity in the limit of small accelerations. In this formalism, the gravitational acceleration a resulting from a point mass M at radius r would be given by:

$$\frac{G\,M}{r^2} = a\,\mu\!\left(\frac{a}{a_0}\right), \tag{1.3}$$

where a_0 is a constant and $\mu(x)$ is a function that satisfies $\mu(x) \rightarrow 1$ for $x \gg 1$ and $\mu(x) \rightarrow x$ for $x \ll 1$. At accelerations below a_0 (found to be $\sim 10^{-10}$ m s^{-2} from fits to galaxy rotation curves), the gravitational acceleration would therefore only decrease as r^{-1} rather than r^{-2}. MOND provides a natural explanation for the rotation curves of galaxies and other observations, such as the empirical baryonic Tully-Fisher relation (e.g. McGaugh 2012). However, it is not a self-consistent theory, but merely a phenomenological modification of classical mechanics. A relativistic generalisation of MOND, called Tensor-Vector-Scalar theory (or TeVeS), was developed by Bekenstein (2004). This was later followed by other alternative relativistic theories of gravity, such as John Moffat's Scalar-Tensor-Vector Gravity (or STVG, Moffat 2006), of which the classical phenomenology (i.e. the MOND analog) is called MOdifiet Gravity (MOG), and Erik Verlinde's Emergent Gravity (Verlinde 2011, 2016). A complete overview and comparison of these theories is beyond the scope of this introduction and can be found in Famaey & McGaugh (2013).

Both dark matter and modified gravity have their strengths and weaknesses, and pass or fail different observational tests (a very good overview is again given by Famaey & McGaugh 2013). For example, tidal dwarf galaxies that form in the tidal tails of larger interacting galaxies are expected to be almost free of dark matter. In the rotation curves of three such systems, however, significant mass discrepancies were found nonetheless (Bournaud et al. 2007). While this is naturally explained by MOND, it poses a problem for CDM (Gentile et al. 2007). On the other hand, modified gravity struggles to explain the CMB power spectrum, while this is well reproduced by ΛCDM (e.g. Dodelson 2011; Shafieloo & Hazra 2017). Which of the two hypotheses is ultimately correct remains an open question and the subject of a heated debate, in which we remain neutral. While some of the work in this thesis assumes the ΛCDM framework, this does not mean we dismiss modified gravity.

1.6 This thesis

The evolution of galaxies is a tale of different components that are closely connected and can only be fully understood if considered together. The work performed in this thesis fits within this general consideration, but is otherwise hard to place under one common heading. It essentially consists of two major parts.

The start of our work is situated just after the introduction of the HEROES and FRIEDL (and NHEMESES) projects. With extensive experience in dust radiative transfer modelling and the analysis and interpretation of FIR data, the UGent nearby galaxies group had ample expertise to analyse the Herschel data of these programmes and to systematically investigate the dust energy balance problem. In this context, an initial study of the Herschel observations of the HEROES galaxies was presented by Verstappen et al. (2013). The first goal of the work in this thesis is to complementarily investigate the neutral gas content of the galaxies in the HEROES and FRIEDL samples (NHEMESES falls beyond our scope). Since gas makes up the bulk of the ISM mass and forms the fuel for the evolution of galaxies, knowledge of this component is crucial for a correct understanding and interpretation of the other components as well.

HEROES targets massive spiral galaxies that still contain a large reservoir of neutral gas. For these systems, our aim is to thoroughly investigate the details and peculiarities of the neutral gas disks in three dimensions. Since atomic gas in particular is the most extended of the visible components in a galaxy disk, it can be used to investigate the recent history of a galaxy and identify potential disruptions due to external sources. In chapter 2 we present new interferometric HI observations of two HEROES systems and complement these with archival data for the others. Due to the edge-on orientation of the target galaxies, the observed gas disks are strongly projected along the line of sight. To correctly interpret the observations, we build kinematical tilted-ring models of the HI disks using the TiRiFiC code (Józsa et al. 2007). The kinematical information that comes with the 21-cm spectral line observations allows to transform the intrinsically two-dimensional images into full three-dimensional models of the gas disks. We retrieve the main properties of the atomic gas and identify several indications of recent interactions with companion galaxies.

In chapter 3 we investigate the dark matter content of the HEROES systems. The rotation curves and atomic gas distributions from chapter 2 are combined with preliminary stellar distributions from Mosenkov et al. (2016) and Mosenkov et al. (in prep). Molecular gas data are used to investigate the influence of the central bars in NGC 5907 and NGC 4013 on their kinematics. A Markov Chain Monte Carlo (MCMC) technique is then used in combination with a general dark matter halo profile to construct mass models of the HEROES galaxies.

The FRIEDL project investigates dust lane early type galaxies. Since such systems generally do not contain large amounts of ISM, our primary aim for this project is to constrain how much atomic and molecular gas is present in the FRIEDL galaxies in comparison to their dust mass. In chapter 4, the limited literature data are complemented with new single-dish observations of the molecular gas and single-dish and interferometric observations of the atomic gas in the northern systems. The results are discussed and we investigate in particular the unusual gas-to-dust ratio found for NGC 5485.

The second (smaller) part of this thesis is related to the cusp-core controversy of the ΛCDM model. Hydrodynamical simulations offer an attractive solution to this problem in the form of stellar feedback effects. Two recently proposed dark matter halo profiles incorporate these feedback effects to allow transformations of primordial cusps into shallower cores. Both models were found to provide good fits to observed rotation curves (although they were tested on different samples). For the DC14 halo, however, conflicting conclusions were reached regarding the agreement of the derived haloes with cosmological scaling relations.

In addition, although the physical mechanism that drives core formation is essentially the same for both halo models, they do follow a somewhat different approach. In the DC14 model the stellar mass is used as a measure for the amount of supernova feedback energy that has become available and the shape of the dark matter halo is fully determined by M_*/M_{halo}. In the coreNFW model, on the other hand, the core strength is regulated by the total time that the galaxy has been forming stars, while the radial extent of the core is linked to the radial distribution of the stars.

The cNFW and DC14 models also probe different mass ranges. An overall comparison is therefore not meaningful, but the two models should both be appropriate for halo masses of the order $5 \times 10^9\ M_\odot \lesssim M_{\text{halo}} \lesssim 5 \times 10^{10}\ M_\odot$. Therefore, if DC14 and coreNFW both correctly describe dark matter core formation, their predictions should agree in this overlapping mass range. In chapter 5 we apply the coreNFW and DC14 models to a selection of 13 galaxy rotation curves with halo masses of $4 \times 10^9\ M_\odot$ to $7 \times 10^{10}\ M_\odot$, and compare their predictions. The DC14 halo is further applied to an additional 7 rotation curves with halo masses up to $9 \times 10^{11}\ M_\odot$ to investigate the agreement with the cosmological scaling relations.

The atomic gas content of the HEROES galaxies

2

Atomic gas is the most fundamental baryonic component in the Universe and forms the raw material for the formation and evolution of galaxies. Beyond the amount and distribution of this primordial component, interferometric HI data cubes furthermore contain a wealth of additional information about a galaxy. Since it is the most extended visible component in a galaxy, past or ongoing interactions between galaxies are often most clearly, or even solely, visible in the atomic gas. Examples of this are large-scale warps, a disrupted HI morphology, tidal structures and the presence of companion galaxies in the same velocity range. In addition to this morphological information, interferometric HI observations also enable us to constrain the kinematics of a galaxy out to large galactocentric distances. This, in turn, is crucial for constraining the distribution of the dark matter.

In this chapter we perform a detailed analysis of the atomic gas content of six of the HEROES galaxies. The atomic gas of the seventh HEROES galaxy was studied in another work according to the same strategy. Section 2.2 describes the HI observations and the data reduction process. Our strategy for modelling the data cubes is explained in section 2.3 and the results are discussed in section 2.4. We briefly compare our results to theoretical expectations of the thickness of the gas disks in section 2.5 and discuss the influence of the environment on our galaxies in section 2.6. Finally, the conclusions are summarised in section 2.8. This chapter was also published as the second paper in the HEROES series (Allaert et al. 2015).

Table 2.1: General properties of the HEROES galaxies

Galaxy	RA (J2000)	Dec (J2000)	Type	M_V (mag)	D (Mpc)	Scale (pc/arcsec)
NGC 973	02:34:20	+32:30:20	Sbc	13.6	63.5	308
UGC 4277	08:13:57	+52:38:54	Sc	14.9	76.5	371
IC 2531	09:59:56	-29:37:04	Sc	12.9	36.8	178
NGC 4013	11:58:31	+43:56:48	Sb	12.1	18.6	90
NGC 4217	12:15:51	+47:05:30	Sb	12.0	19.6	95
NGC 5529	14:15:34	+36:13:36	Sc	12.9	49.5	240
NGC 5907	15:15:54	+56:19:44	Sc	11.1	16.3	79

2.1 The HEROES sample

The HEROES project targets a sample of seven massive, edge-on spiral galaxies. As mentioned in section 1.4, one of the goals of the project is to map the dust emission in the FIR/submm and to compare this with the predictions from detailed radiative transfer models. Such a comparison is interesting mainly if the dust emission is sufficiently spatially resolved in all the images. To make sure that the dust emission is sufficiently spatially resolved even in the SPIRE 500 μm band, the galaxies were selected to have an optical diameter of at least $4'$. The galaxies were further selected to have a well-defined and regular dust lane, such that it could be approximated by smooth analytic profiles (a requirement for RT modelling at that time).
The starting point of the HEROES sample were the combined samples of Xilouris et al. (1997, 1999) and Bianchi (2007), who had previously modelled the optical/NIR extinction in edge-on spirals with their respective RT codes. After applying the aforementioned selection criteria, 8 galaxies remained. NGC 891 was further omitted from the sample due to overlap with a different Herschel programme. An overview of the HEROES sample is given in Table 2.1. The distances we use here are taken from NED, as explained in section 2.1 of Verstappen et al. (2013) (paper I in the HEROES series).

2.2 Observations and data reduction

2.2.1 HI Observations

We have observed the atomic gas content of NGC 973 with the Giant Metrewave Radio Telescope (GMRT) in August 2011. UGC 4277 was observed with the same telescope by Dr. G. De Geyter in July 2012. The GMRT consists of 30 45-m antennas located at a fixed position, yielding only one possible antenna configuration. A central area of approximately one square kilometre contains 14 antennas, with the shortest baselines measuring about 100 m. The other antennas are placed in a roughly Y-shaped configuration with three arms of about 14 km long, giving a maximum baseline of 25 km. In L band (1000-1500 MHz), each GMRT antenna provides two orthogonal, linearly polarised signals. Both galaxies were observed for about eight hours, including the observation of standard flux and phase calibrator sources. NGC 973 was observed with a bandwidth of 4.2 MHz, divided into 256 channels. The original plan was to use a bandwidth of 8.4 MHz, but this setup had to be changed due to technical problems with the telescope. UGC 4277 was observed with a bandwidth of 16.7 MHz divided into 512 channels.

For the remaining galaxies analysed here, we use literature data from the Very Large Array (VLA), Westerbork Synthesis Radio Telescope (WSRT), and Australia Telescope Compact Array (ATCA). A brief overview of these observations is given in Table 2.2. We refer the reader to the original papers for further details on the data.

The data for NGC 5907 and NGC 5529 were obtained from the VLA and WSRT archives, respectively. For IC 2531, S. Peters kindly shared the flagged and calibrated HI data that were used in the series of papers by O'Brien et al. (2010d,b,a,c) and in his own work (Peters et al. 2013). These consist of a combination of data sets obtained between 1992 and 2002 with different configurations of the ATCA. Upon inspection of the individual data sets, however, it became evident that two of them were severely corrupted, so we did not include them in our final data cube. Part of these data were also used by Kregel et al. (2004) and Kregel & van der Kruit (2004). Finally, M. Verheijen was kind enough to provide a fully reduced and deconvolved data cube of NGC 4217 from his WSRT observations (Verheijen & Sancisi 2001).

2.2.2 Data reduction

The output of a radio interferometer is a collection of complex visibilities that form (at each observed frequency) the Fourier transform of the surface brightness distribution on the plane of the sky. Typically some fraction of the visibilities is affected by e.g. malfunctioning hardware of the telescope, or interference from other radio sources such as mobile phones, radar or GPS signals, wifi, etc. (this is called radio frequency interference or RFI). In addition, the raw telescope data need to be calibrated against standard sources of known intensity before they truly represent the intensity of the target source. The process of removing bad data, calibrating the visibilities and Fourier transforming them to produce truthful images of the target source is called data reduction.

The reduction of the GMRT and VLA data (NGC 973, UGC 4277, and NGC 5907) was performed in the AIPS software package (Greisen 2003) following the standard procedure. Radio interferometric data sets can become quite large, of the order of tens or in extreme cases even hundreds of gigabytes. To save time in handling these large volumes of data, the initial part of the reduction was performed on the so-called 'channel-0' data set, the average of the central 75% of the frequency channels. This data set was visually inspected, and corrupted data were flagged (marked as bad). Next, the flux and phase

Table 2.2: Hɪ observations

Galaxy	Telescope	Array	Date	Bandwidth (MHz)	Number of channels	Time on source (h)	Reference
NGC 973	GMRT		Aug 2011	4.2	256	5.7	1
UGC 4277	GMRT		Jul 2012	16.7	512	6.2	1
IC 2531	ATCA	6.0A	Apr 1996	8.0	512	9.9	2
IC 2531	ATCA	6.0B	Sep 1996	8.0	512	10.0	3
IC 2531	ATCA	1.5D	Mar 1997	8.0	512	9.1	3
IC 2531	ATCA	750A	Jan 2002	8.0	512	9.6	4
NGC 4217	WSRT	Not mentioned	Aug 1990	5.0	63	12.0	5
NGC 5529	WSRT	Maxi-Short	May 2001	10.0	128	11.9	3
NGC 5907	VLA	Modified C	Aug 1997	2×3.1	2×32	4.7	6

References. (1) This work; (2) Bureau & Freeman (1997); (3) Kregel et al. (2004); (4) O'Brien et al. (2010d); (5) Verheijen & Sancisi (2001); (6) Shang et al. (1998).

calibration was performed for the channel-0 data. Calibration of VLA or GMRT data in AIPS is based on the observation of a flux calibrator at the start and/or the end of the observing run and periodic observations of a phase calibrator during the run. First, the observed flux calibrator was used to set the absolute flux scale. Next, the antenna gain amplitude and phase solutions were determined for both calibrator sources and the absolute flux information from the flux calibrator was transferred to the phase calibrator. Finally, the antenna gain solutions from the phase calibrator were interpolated to obtain the antenna gains for the target source. After the initial reduction of the channel-0 data, the antenna gains and bad data flags were copied to the spectral line data, which were finally bandpass-calibrated. Typically, several iterations of flagging and calibrating were needed to achieve a satisfactory result.

The WSRT data of NGC 5529 were reduced with the Miriad software package (Sault et al. 1995). Although the global strategy of the data reduction is the same as in AIPS (flagging, calibrating, and imaging the data), the exact calibration procedure is somewhat different. The observations of NGC 5529 did not include periodic observations of a phase calibrator. Only a flux calibrator source was observed at the start and the end of the observing run. This was used to set the absolute flux scale and obtain initial antenna gain solutions, as well as to determine the bandpass corrections to be applied. To take the strong variations of the antenna gain phases during the observing run into account, the quality of the initial calibration was improved through several iterations of self-calibration. This was performed on the continuum emission to increase the signal-to-noise ratio, and the derived antenna gains were subsequently copied to the spectral line data.

To suppress potential Gibbs ringing in the spectra, a data set is usually Hanning-smoothed. For NGC 4217 this step was already performed online, i.e. during the observations. For the remaining galaxies this was not the case, and the data had to be Hanning-smoothed manually during the data reduction. The inevitable downside of this smoothing, however, is that adjacent channels are no longer independent. One usually accounts for this by dropping every second channel, thereby reducing the spectral resolution of the final data cube by a factor of 2. However, fitting 3D tilted-ring models to the HI data cubes requires a good constraint on the kinematics, and hence a sufficiently high velocity resolution, preferably below 20 km s^{-1}. For NGC 5907 and NGC 5529, Hanning-smoothing would lead to a resolution of 41 km s^{-1} and 33 km s^{-1}, respectively. We therefore decided to perform the Hanning-smoothing only for NGC 973, UGC 4277, and IC 2531 and not for NGC 5529 and NGC 5907. For NGC 4217 the resolution is also 33 km s^{-1}, but unfortunately nothing could be done about this since the smoothing was already applied during the observations.

After subtracting the continuum emission from the visibilities in the *uv* plane, the data were imaged using a robust parameter of 0. This provides a good compromise between a high signal-to-noise ratio on the one hand and a better resolution with lower sidelobes on the other hand. The maximum baseline of the GMRT is approximately 25 km, which corresponds to a maximum *uv* distance of 119 kλ at a wavelength of 21 cm. Using this entire *uv* range to image the data results in a very narrow synthesised beam and produces a data cube where the emission is effectively resolved out. To image the data of NGC 973, the *uv* range was therefore limited to 40 kλ, and a Gaussian taper with a width of 10 kλ at the 30 % level was applied. For UGC 4277, a better result was obtained by limiting the *uv* range to 15 kλ and not applying any taper.

The deconvolution of the dirty beam was generally done using the CLEAN task in Miriad. This task offers a choice between the Högbom (Högbom 1974), Clark (Clark 1980), and Steer (Steer et al. 1984) *clean* algorithms and by default determines by itself which algorithm is the most appropriate. After an initial *clean* of the data cube down to three times the rms noise (σ), the data cube was smoothed to a beam size of 60″, and 2σ masks were defined in the resulting cube. The original data cube was subsequently *cleaned* down to 1σ in the masked regions and the resulting *clean* model was then used as input model for a final *cleaning* of the original cube down to 3σ. Finally, the *clean* components were convolved with a Gaussian beam fitted to the central lobe of the synthesised beam and restored to the residual image. A different strategy was used for the deconvolution of the cube of NGC 5907, the closest and by far the largest (in terms of angular size) galaxy in our sample. Ordinary *clean* algorithms typically represent a source by a collection of point sources, which is a poor approximation for extended sources like NGC 5907. To overcome this problem, we used the multi-scale *cleaning* option in AIPS (Greisen et al. 2009) with an enhanced version by Bill Cotton and Fred Schwab (Schwab 1984) of the Clark *clean* algorithm. Multi-scale *cleaning* essentially uses a set of circular 2D Gaussians as model components instead of point sources. In the current case three such Gaussian components, with widths of 40″, 120″, and 360″, were used in combination with a point source component, and the channel maps were *cleaned* down to twice the rms noise at each resolution.

Finally, each data cube was corrected for the primary beam and the spectral axis was transformed to barycentric radio velocities. An overview of the properties of the final data cubes is presented in Table 2.3.

The primary beam corrected cubes were then used to derive a total intensity map (also called zeroth moment map) of the H I in each galaxy. For this purpose we first smoothed each cube to a resolution of twice the original (*clean*) beam size. Masks were then defined in the smoothed cubes by excluding all emission that does not exceed 2σ in three or more consecutive channels. If the velocity resolution of a data cube is low, however, three consecutive channels can already span a wide velocity range. For NGC 5529, NGC 5907, and especially NGC 4217, the latter criterion was therefore somewhat relaxed. After applying the masks to the original data cubes, the intensities in the masked channel maps were multiplied by the appropriate channel width and added pixel by pixel to produce the moment-0 maps.
Total H I 21-cm fluxes were determined from the moment-0 maps by simply summing all the pixels. These fluxes can then be converted to total H I masses as (e.g. Rohlfs & Wilson

Table 2.3: Main properties of the final reduced data cubes

Galaxy	Synthesised beam FWHM (arcsec)	(kpc)	Velocity resolution (km s^{-1})	RMS noise (mJy/beam)	mJy/beam to Kelvin (K)
NGC 973	24.5 × 15.3	7.5 × 4.7	6.9	1.6	1.62
UGC 4277	15.6 × 9.8	5.8 × 3.6	6.9	1.0	3.96
IC 2531	16.0 × 9.2	2.8 × 1.6	6.6	1.1	4.12
NGC 4217	18.0 × 13.0	1.7 × 1.2	33.0	1.0	2.59
NGC 5529	23.6 × 14.0	5.7 × 3.4	16.5	0.6	1.83
NGC 5907	14.8 × 13.3	1.2 × 1.1	20.6	0.3	3.08

2013):

$$\frac{M_{\text{H}\,\textsc{i}}}{M_\odot} = 2.36 \times 10^5 \left(\frac{S_{\text{tot}}}{\text{Jy km s}^{-1}}\right)\left(\frac{D}{\text{Mpc}}\right)^2, \tag{2.1}$$

where S_{tot} is the total flux and D is the distance to the galaxy. The total atomic gas mass, finally, can be obtained from this value by including a correction factor of 1.36 for the contribution of helium and heavier elements.

2.3 Modelling strategy

2.3.1 Tilted-ring models

An interferometric HI data cube contains a wealth of information about a galaxy. Extracting and correctly interpreting this information is, however, not straightforward and the edge-on orientation of the HEROES galaxies makes this even more difficult. For example, for a low or moderately inclined galaxy one can derive the surface density distribution from the moment-0 map by subdividing the latter in a set of concentric rings and averaging the observed surface densities within each ring. This strategy breaks down for edge-on systems where each line of sight (LOS) cuts through the entire disk and shows the added contributions of gas at a range of galactocentric distances.

Instead we adopted a more complete approach and used the tilted-ring fitting software TiRiFiC (Józsa et al. 2007) to model the entire data cube of each HEROES galaxy. This essentially means that we constructed a virtual three-dimensional replica of the atomic gas disk of each galaxy, composed of a set of concentric rings. Every ring of the model is characterized by a number of parameters that can be tuned for each ring independently (orientation in the sky, gas density, rotational and radial velocity of the gas, etc.) Based on this model, a data cube is created that exactly matches all the properties of the observational data (pixel and beam size, velocity width, number of channels, etc.). The parameters of the different rings can then be optimised to give the best possible agreement with the data. By comparing not only the channel maps of the data cubes, but also the derived total intensity maps, position-velocity diagrams, etc., one can resolve the degeneracies between different representations of the gas disk that are especially present for an edge-on geometry. An additional advantage of this method is that it automatically takes into account the effect of beam smearing (bias of the observed velocities towards higher-density regions due to the averaging inside the beam) because the model is convolved with the same beam as the observational data.

2.3.2 General strategy

For each galaxy the width of the rings that make up the model was taken to be half the size of the beam minor axis. This provides a good compromise between angular resolution and efficiency. A sech^2 profile was assumed for the vertical gas distribution. This profile was originally devised for stellar disks (Spitzer 1942), but is also often used to model gas disks (see e.g. Moster et al. 2010; Gentile et al. 2013).

Initial guesses for the relevant parameters were derived as follows. The inclination was taken over from the literature. The (central) position angle and systemic velocity were estimated by eye from the observed data cube. With these values as inputs, we then used the task *rotcur* from the GIPSY software package (van der Hulst et al. 1992) to construct a model of the observed velocity field. Although this task is actually not well-suited to an edge-on galaxy (for the same reason as explained in Section 2.3.1), it did provide a rough initial guess of the central position and the rotation curve. The radial surface density profile was estimated with the GIPSY task *radial*, which essentially applies the method described by Warmels (1988) and Lucy (1974). An initial value of 0.3 kpc was used for the vertical scale height, and finally the overall velocity dispersion was estimated as the squared sum of the velocity resolution of the observations and an intrinsic velocity dispersion of 10 km s^{-1} (Leroy et al. 2008). For NGC 4217 we used the results from the analysis by Verheijen & Sancisi (2001) as starting point.

With these initial estimates as input we performed a first TiRiFiC fit of the data cube. A very basic geometry was imposed here, consisting of a simple disk with a constant scale height and inclination. The first fit was performed with the central position, the systemic velocity, the velocity dispersion, and the position angle as free global parameters, and the rotational velocity was free for each ring. For warped galaxies, the position angles were then adjusted to match the warp. Subsequently, the results were used as input in a second fit, this time leaving the inclination and vertical scale height free as global parameters and fitting the surface brightness for each ring. The resulting 'basic' model was then refined further by investigating different geometries and gradually adding extra features, each time optimising the column densities and rotational velocities (if necessary) to obtain the best possible fit to the data. The approaching and receding halves were modelled separately with the (obvious) constraint that the central position, the systemic velocity, and the velocity dispersion should be the same for both sides. In the basic geometry, the inclination and scale height were also required to be the same on both sides. The detailed strategy followed for each galaxy depends on the specific features encountered and is described in the sections below.

An automated χ^2 minimisation is included in the TiRiFiC code, which is performed after convolving the model cube with the observational beam. Although this greatly expedites the optimisation of the parameters, its results should not be trusted blindly. With an approximately constant noise across the maps, this minimisation scheme will by construction assign more weight to regions of higher surface brightness. However, low surface brightness features often impose the strongest constraints and are most important to distinguish between models. Also, TiRiFiC does not consider whether a model is realistic or not. The mathematically best-fitting model will often contain unphysical values and unrealistically strong radial variations of the parameters. Therefore, the geometry of the models was generally imposed by hand, and the parameter values obtained from a TiRiFiC fit were also refined further by manual adjustment.

The edge-on orientation of the HEROES galaxies brings along with it a number of potential degeneracies between different models. A prime example of this is the vertical thickness of the gas disks, as seen in projection on the plane of the sky. This can be modelled by adjusting either the vertical scale height or the inclination of the disk, or a combination of both. A second important example is the interpretation of the column density peaks observed in a zeroth moment map, where each LOS contains the sum of multiple rings at different galactocentric radii. To resolve these degeneracies, it is important to use all the information provided by the observations and to compare the models to the data in different projections of the data cube. Scale height and inclination effects, for example, can be disentangled by studying the shape of the emission contours in the different channel maps. Increasing the scale height simply makes the emission thicker in all the channel maps. On the other hand, decreasing the inclination moves the emission away from the major axis and gives it a V-like shape in the channel maps (see e.g. Fig. 2.32 later in this chapter for an example). The strength of this effect also strongly varies within the data cube, going from hardly visible at high LOS velocities to clearly visible close to the systemic velocity. Density peaks in a total HI map can be understood by inspecting the associated major axis position-velocity diagram. The addition of the kinematical information allows the correct surface density to be assigned to each ring and to potentially identify additional features that do not belong to the axisymmetric disk (see e.g. Figs. 2.27 and 2.28 later in this chapter).

2.3.3 Uncertainties

Following standard practice, the modelling strategy that we use here is a combination of χ^2 minimisation and the personal judgement of the modeller (e.g. Zschaechner et al. 2012; Gentile et al. 2013; Kamphuis et al. 2013). As a consequence it is not possible to determine the errors on the parameters of the final models in a statistical way. We therefore estimated the uncertainty on each parameter by keeping all the other parameters fixed to their best fit values and varying the parameter in question until the model clearly deviated from the observed cube. The uncertainties are generally restricted to one global value for the entire radial range. For the rotation curves that will later be used to determine the distribution of the dark matter, we did determine error bars at every radius. For each parameter, there are usually certain regions of the disk and/or certain projections of the data that are especially sensitive to variations in that parameter. We focussed on these regions and projections to assess the deviation of the model from the observed cube. Errors on the central position and the position angle were determined based on the moment-0 maps. For the inclination and the scale height, we focussed both on the moment-0 maps and on the channel maps near the systemic velocity (inclination) and at high rotational velocities (scale height). For the systemic velocity, we focussed on the central part of the major axis position-velocity (XV) diagrams, and the uncertainties on the velocity dispersion were determined from the spacing between the contours on the terminal edges of the XV-diagrams. Finally, the errors on the rotation curve were also derived from the major axis XV-diagrams, by varying the rotational velocity for each ring individually.

2.4 Modelling results

2.4.1 NGC 973

NGC 973 (UGC 2048) is located at a distance of 63.5 Mpc. The structure and kinematics of the atomic gas disk of NGC 973 have not been investigated before.

The HI data

Our GMRT data of NGC 973 have a total integration time of 5.7 hours, which is rather limited for a galaxy at a distance of 63.5 Mpc. Consequently, the signal-to-noise ratio in the channel maps of our data cube is generally on the low side. As a result, the shape of the observed low surface brightness emission is affected significantly by noise peaks and sometimes varies significantly from one channel map to another. This limits the level of detail that can be achieved in the modelling and the focus should lie on reproducing the main trends in the data. It is unrealistic, and in fact unphysical, to expect a model to match the shape of the emission in each channel map.

The zeroth-moment map of the HI disk of NGC 973 is compared to a V-band image in Fig. 2.1. The NE side of the disk is the approaching half, the SW side the receding half. Both the stellar and the HI disks are remarkably flat, even in the outer regions, but some asymmetry is visible in the high surface brightness contours in the total HI map. This is also visible in Fig. 2.2. Indeed, only one density peak is observed on the approaching side (at a major axis offset of +1′ in Fig. 2.2). This peak is mirrored on the receding

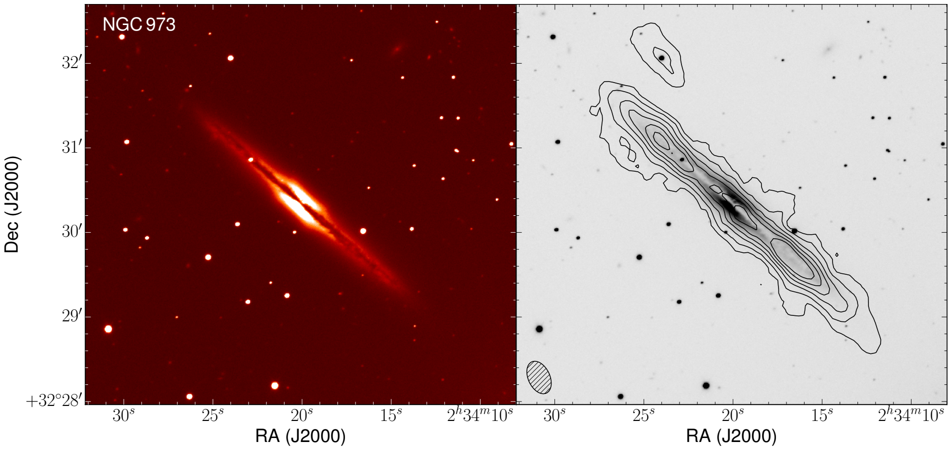

Figure 2.1: Left: False colour V-band image of NGC 973 based on observations made with the Italian Telescopio Nazionale Galileo (TNG). Right: HI contours overlaid on the same V-band image. The contours start at 1.76×10^{20} atoms cm^{-2} and increase as 3, 6, 9, 12, and 15 times this value. The HI beam is shown in the bottom left corner. North is up, east to the left.

side at an offset of -1′, but additionally a second, more central peak is also present on this side. The maximum (integrated) surface density is also significantly higher on the receding side.

We further detect (to our knowledge for the first time) a small satellite galaxy that is located slightly above the NE edge of the disk, at a distance of 36 kpc from the centre of NGC 973 (as determined from our models). We estimate its central position as RA $02^{\mathrm{h}}34^{\mathrm{m}}23.9^{\mathrm{s}}$, Dec 32°32′5.0″ and find no optical counterpart. The satellite appears in nine consecutive (independent) channels in the data cube between 4517 and 4572 km s^{-1}, although often only at the 3σ level, and it has a total HI flux of 0.36 Jy km s^{-1}. This translates to a HI mass of 3.39×10^{8} M$_{\odot}$.

For the disk of NGC 973 we find an integrated HI flux of 9.32 Jy km s^{-1}, corresponding to a total atomic hydrogen mass of 8.87×10^{9} M$_{\odot}$. Huchtmeier & Richter (1989) report a single-dish flux of 8.83 Jy km s^{-1}, while Springob et al. (2005) give a corrected[1] single-dish flux of 13.9 Jy km s^{-1}. Although these flux measurements are of the same order, they show a relatively large spread, which is caused by a combination of different effects. The dominant factor, in general, is the uncertainty in the flux calibration of the different observations, which can cause differences of up to a few ten percent. Secondly, given the limited observing time, a significant reservoir of low column density gas might still be hidden in the noise in our channel maps. In addition, single-dish observations often have a half power beam width (HPBW) that is smaller than the HI disk of the galaxy, causing them to miss some of the emission from the gas. To correct for this effect, Springob et al. (2005) assume a smooth Gaussian distribution for the HI, scaled according to the optical

---

[1] Corrected for pointing offsets and source extent, not HI self-absorption.

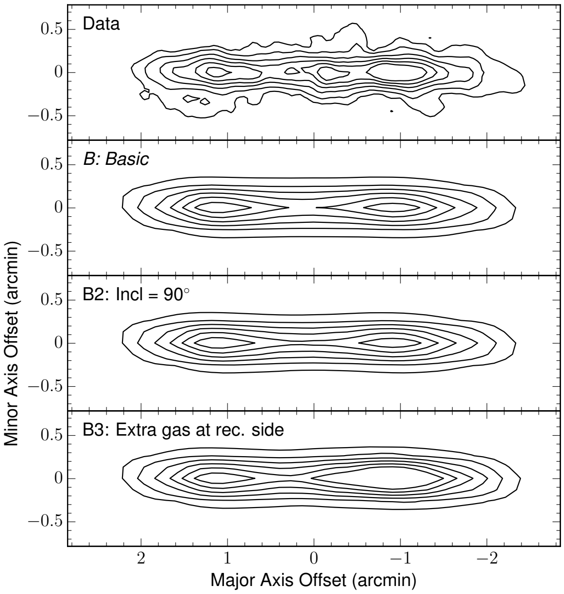

Figure 2.2: Total HI maps of the various models discussed here as compared to the observed total HI map of NGC 973. The *B* model is our best model. Contour levels are the same is in Fig. 2.1.

radius. Given the variety of morphologies shown by the atomic gas disks of galaxies, such a general correction can also be rather inaccurate for a specific galaxy.

Models

For modelling the data cube, we focus on the HI disk of NGC 973. The satellite galaxy is not included in the models. The best-fitting model in the basic geometry (which we refer to as the basic or *B* model) has a constant inclination of 88° and scale height of 0.2 kpc, although the latter is very ill constrained, with values up to 1.1 kpc giving only marginally different models. A single, constant position angle of 228° proved sufficient to reproduce the orientation of the disk on the plane of the sky. If we compare the zeroth-moment map of this model to the observations (Fig. 2.2) we see that the agreement is generally very good, apart from the observed central density peak on the receding side, which is not present in the model. The main trend in the channel maps is also reproduced well by the model (Fig. 2.3), although (as expected) it often does not match the exact shape of the observed emission. Additionally, at intermediate velocities, the model often underestimates the surface densities and thus lacks the high surface brightness contours. This effect can, for example, be seen in the channel maps at 4565, 4703, 4840, and 4909 km s^{-1} and is also visible in the major axis position-velocity (XV) diagram (Fig. 2.4). The latter is modelled well at the terminal sides (i.e. at the maximal velocities) and in the very central region, but lacks high surface brightness emission at intermediate velocities,

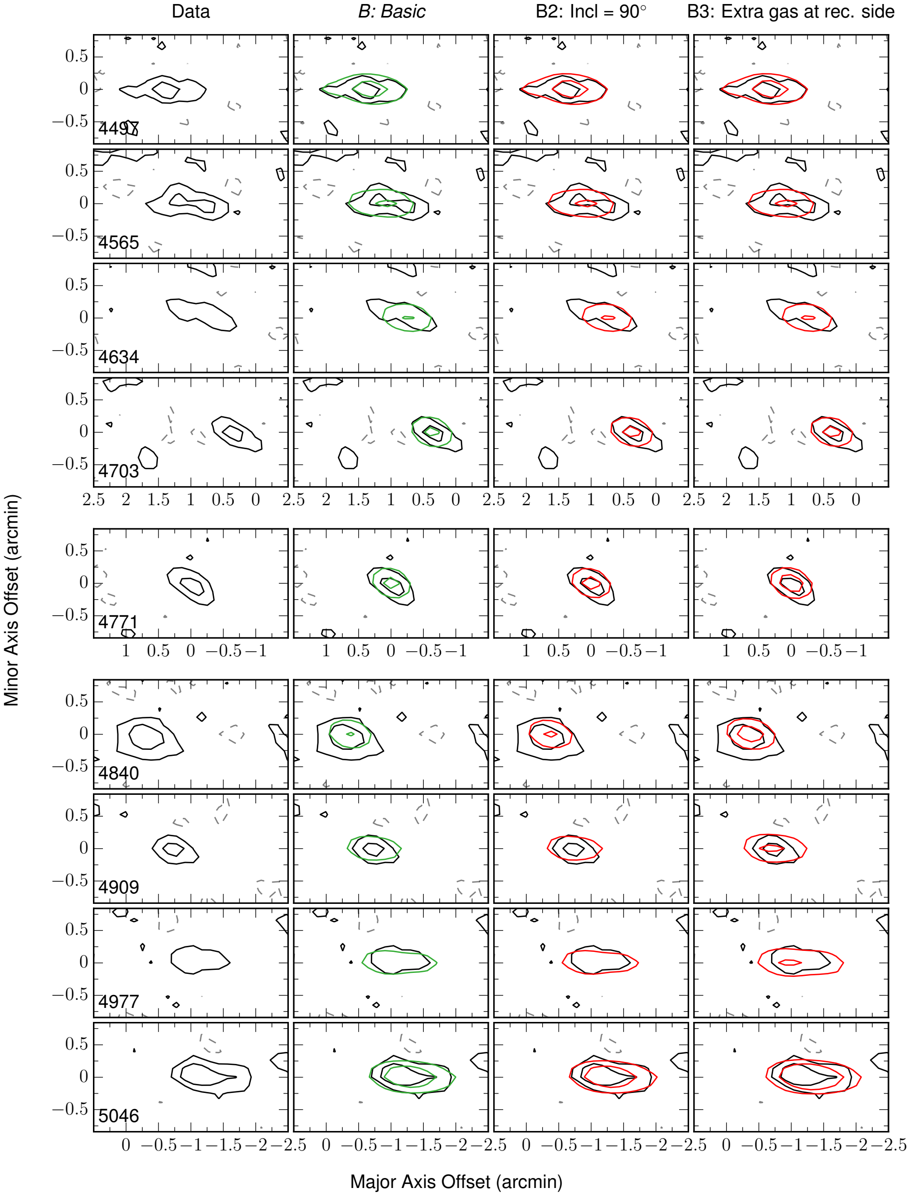

Figure 2.3: Representative channel maps from the observed data cube of NGC 973 and the various models. Contour levels are -2.3, 2.3 (1.5σ), and 6.2 mJy beam^{-1}. The observations are shown as black contours with the negative contours as dashed grey. The green contours show the final (*B*) model. Other models are shown as red contours. The line-of-sight velocity is indicated in km s^{-1} in the bottom left corner of the first panel of each row. The systemic velocity is 4770 ± 8 km s^{-1}. The horizontal axis is slightly shifted between the three blocks composing the figure.

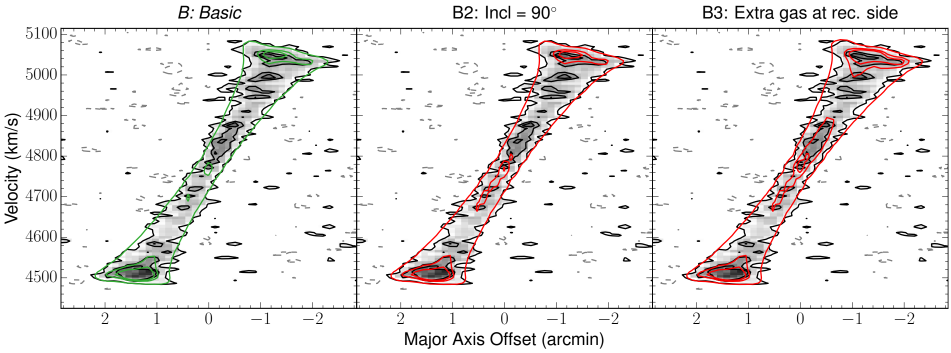

Figure 2.4: Observed major axis position-velocity diagram of NGC 973 (black and grey contours) overlaid with different models. The green contours show the final (*B*) model. Other models are shown as red contours. Contour levels are -2.3, 2.3 (1.5σ), 7.0, and 9.3 mJy beam^{-1}. The greyscale corresponds to the observations.

especially on the receding side. In a regularly rotating, axisymmetric disk that is viewed edge-on, the emission that is seen at these intermediate velocities is simply the projection along the major axis of the emission at the terminal velocities. As a result, the only ways to significantly enhance this emission are either to increase the inclination of the disk or to increase the surface brightness in some or all of the rings that make up the model.

The first option was tested by constructing a second basic model, the *B2* model, with a constant inclination of 90°. The corresponding optimal scale height is 0.4 kpc. With the surface brightnesses optimised to match the terminal sides of the XV-diagram, this model offers little improvement on the receding side (Fig. 2.4). On the approaching side, the problem is almost solved, but at the cost of then overestimating the emission close to the systemic velocity.

In a second attempt to improve our basic model, we manually scaled up the surface brightness distribution on the receding half of the *B2* model until we could reproduce the high brightness contours at intermediate velocities in Fig. 2.4. With an increase of 35 percent (*B3* model), this is almost achieved, but the XV-diagram is now clearly too wide on the receding side. This effect can also be seen in the channel maps at 4909, 4977, and 5046 km s^{-1} in Fig. 2.3, where the left and right edges of the model extend well beyond those of the observed emission. In addition, the emission at the terminal and systemic velocities in the XV-diagram is strongly overestimated (note, for example, the 6σ contour near the systemic velocity that only appears for the *B3* model in Fig. 2.4). In the total HI map (Fig. 2.2), the *B3* model overestimates the peak density on the receding side and shows one big peak instead of two separate peaks.

From the *B2* and *B3* models, it is clear that the HI disk of NGC 973 cannot be modelled simply as an axisymmetric disk. Either we underestimate the amount of gas moving at intermediate velocities or we overestimate the amount of gas moving at the terminal velocities. The reason for this is most probably that the disk of NGC 973 is far from smooth and has a clumpy structure with high-density regions alternating with regions with a lower density. Alternatively, a projected spiral arm might also cause this behaviour. In either case, although TiRiFiC allows different areas of a gas disk to be modelled individually, and to include spiral arms, the problem at hand in an edge-on disk is much too degenerate to attempt such a thing.

Apart from the arbitrary jumps of the observed emission in the channel maps, we do not see a clear trend that indicates that the shape of the model emission is systematically wrong. Although a moderate flare or a small warp along the line of sight cannot be excluded, we therefore stick to the basic geometry and use the *B* model as our final model for NGC 973. The uncertainty concerning the exact morphology of the disk does not strongly affect our results and is primarily restricted to the geometric parameters, i.e. the inclination and the scale height. Slight adjustments in the surface density profile can be necessary when adding a flare or a LOS warp to a model, but these are typically only of the order of 10% or less. In principle a LOS warp also affects the rotational velocities, but for small warps of only a few degrees (as would be the case here), these changes are negligible.

Figure 2.5 compares the model data cube to the observations. The satellite galaxy is indicated by arrows in the relevant channel maps. The main parameters describing the final model are given in Table 2.4 and Fig. 2.35 at the end of this chapter. The inclination and the position angle have errors of 2.0° and 3.0°, respectively. The scale height has a value of $0.2^{+0.9}_{-0.2}$ kpc. We note that this result seems to be consistent with a scale height of 0 kpc, which is of course unphysical. Unfortunately, the large observational beam means that it is not possible to determine a meaningful lower limit for the scale height of NGC 973.

2.4.2 UGC 4277

With a distance of 76.5 Mpc, UGC 4277 is the most distant of the HEROES galaxies. Like NGC 973, the details of its atomic gas content have not been investigated before.

The HI data

The total integration time of the GMRT observations is of the same order as for NGC 973. As a consequence, the signal-to-noise ratio in the data cube is again on the low side and the shape of the low surface brightness emission in the channel maps is significantly affected by the noise. This is also reflected in the major axis position-velocity diagram (see Fig. 2.9 later), where chunks of emission seem to be missing. However, the higher brightness contours in this diagram, that should be less affected by the noise, are also very irregular. This suggests that UGC 4277 has a clumpy HI disk. It is interesting to note that

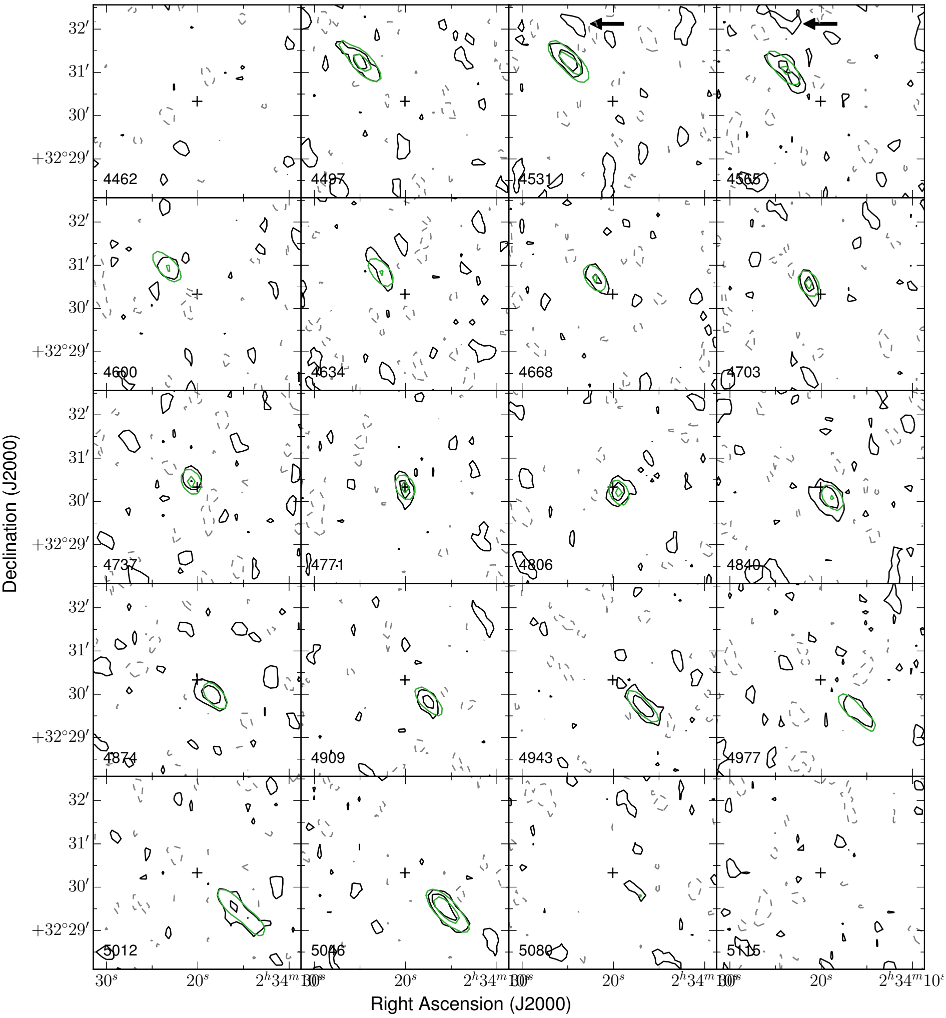

Figure 2.5: Channel maps from the observed data cube of NGC 973 (black and gray contours) and our final (*B*) model (green). Contour levels are -2.3, 2.3 (1.5σ) and 6.2 mJy beam^{-1}. The black cross indicates the centre of the galaxy. The companion galaxy is indicated by arrows at 4531 and 4565 km s^{-1}.

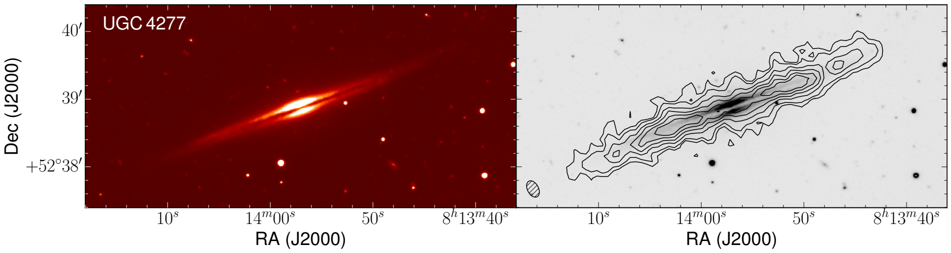

Figure 2.6: Left: False colour TNG V-band image of UGC 4277 from Bianchi (2007). Right: HI contours overlaid on the same V-band image. Contours start at 3.61×10^{20} atoms cm^{-2} and increase as 2, 4, 6, 8, and 10 times this value. North is up, east to the left.

the FIR morphology, especially in the PACS bands, similarly suggests that the dust disk of UGC 4277 is also irregular (Verstappen et al. 2013).

Fig. 2.6 shows that both the stellar disk and the atomic gas disk of UGC 4277 are slightly warped. From the zeroth-moment map we measure a total HI flux of 14.7 Jy km s^{-1}, corresponding to an atomic hydrogen mass of 2.03×10^{10} M$_{\odot}$. Huchtmeier & Richter (1989) report a single-dish flux of 17.9 Jy km s^{-1}, which was corrected to 18.9 Jy km s^{-1} by Springob et al. (2005).

Models

Following the standard procedure we first constructed a basic model that consists of a single disk with a constant inclination and scale height. This *B* model has an inclination of 87.3° and a rather large scale height of 1.8 kpc (but see last paragraph of this section). In the slightly warped outer edges of the disk, the position angle deviates at most 3.6° from the value in the inner disk. This model matches the observed total HI map rather well (Fig. 2.7), although it does not reproduce the highest brightness contours. If we compare the model channel maps (Fig. 2.8) and major axis XV-diagram (Fig. 2.9) to the observations, we see the same problems as we encountered for NGC 973. The model often does not match the exact shape of the observed emission in the channel maps and lacks the observed high surface brightness contours at intermediate velocities.

We therefore followed the same modelling strategy and constructed a *B2* model by imposing a constant inclination of 90°. TiRiFiC found the optimal corresponding scale height to be 2.2 kpc. As can be seen in Fig. 2.9, this model does not solve the problems mentioned in the previous paragraph. The higher contours at intermediate velocities are still not reproduced, and additionally the contours in the central region of the XV-diagram are now overestimated. In the channel maps in Fig. 2.8, this model also brings no improvement. Finally we note that the zeroth-moment map of the *B2* model now includes the highest contours from the observed moment-0 map (Fig. 2.7), but they are located too far towards the centre of the galaxy. This is actually the direct consequence of underestimating the

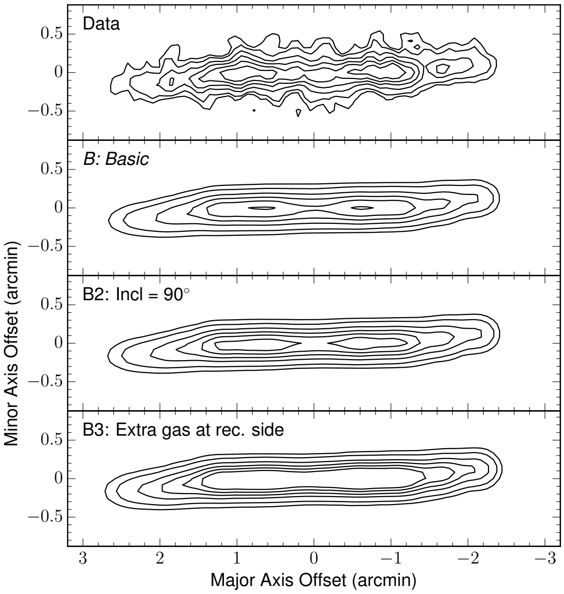

Figure 2.7: Total HI maps of the various models discussed here as compared to the observed total HI map of UGC 4277. The *B* model is our best model. Contour levels are the same as in Fig. 2.6.

emission at intermediate velocities and overestimating the emission close to the systemic velocity, as we described for the XV-diagram.

Next, we again manually scaled up the surface brightness distribution of the *B2* model to match the high brightness emission at intermediate velocities. In the end, an increase of 25 percent on the approaching side and 35 percent on the receding side was needed to more or less achieve this (*B3* model). However, from Fig. 2.9, it is clear that the shape of the model contours is quite different from the observed contours, which are clumpy and follow an irregular pattern. Additionally, the model now strongly overestimates the emission near the systemic velocity and at the terminal edges. We note that the innermost contour of the *B3* model between 5540 and 5620 km s^{-1} is actually a hole in the 3σ-contour and not a 6σ-contour. The agreement with the observations in the total HI map (Fig. 2.7) and in the channel maps (Fig. 2.8) is also clearly a lot worse than for the *B* model.

Similar to NGC 973, the combination of a low signal-to-noise ratio and an irregular gas disk means that little can be done to improve the model. Since the shape of the model emission in the channel maps again does not differ from that of the observed emission in a systematic way (on top of the irregular jumps of the latter), there is no reason to alter the geometry of the model, and we take the *B* model as our final model. The observed data cube is compared to the model cube in Fig. 2.10, and the main parameters of the model are shown in Fig. 2.35 and listed in Table 2.4. The inclination, position angle, and scale height have an uncertainty of 1.5°, 2.0°, and 1.0 kpc, respectively.

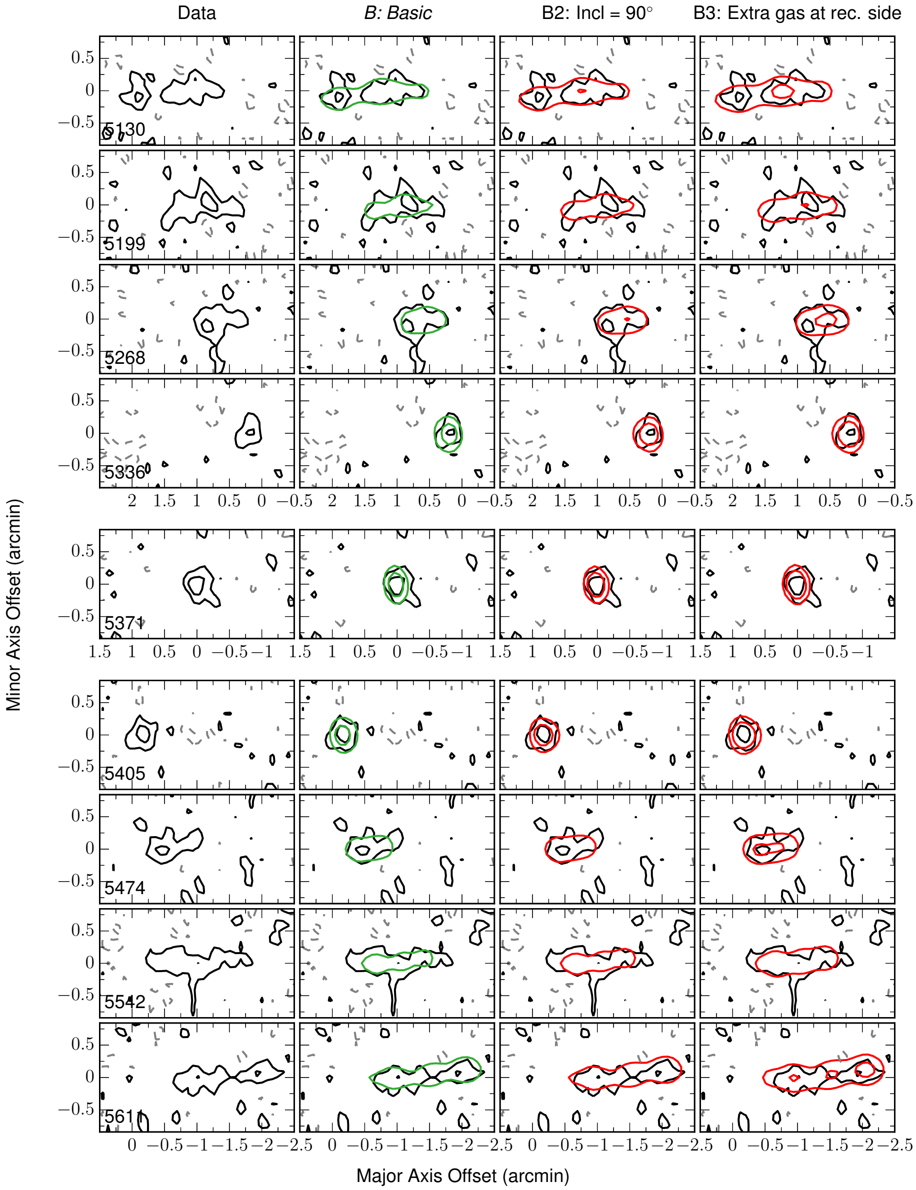

Figure 2.8: Representative channel maps from the observed data cube of UGC 4277 and the various models. Contour levels are -1.5, 1.5 (1.5σ), and 4.0 mJy beam^{-1}. The black contours show the observations with negative contours as dashed grey. The green contours represent the final (*B*) model. Other models are shown as red contours. The systemic velocity is 5370 ± 6 km s^{-1}.

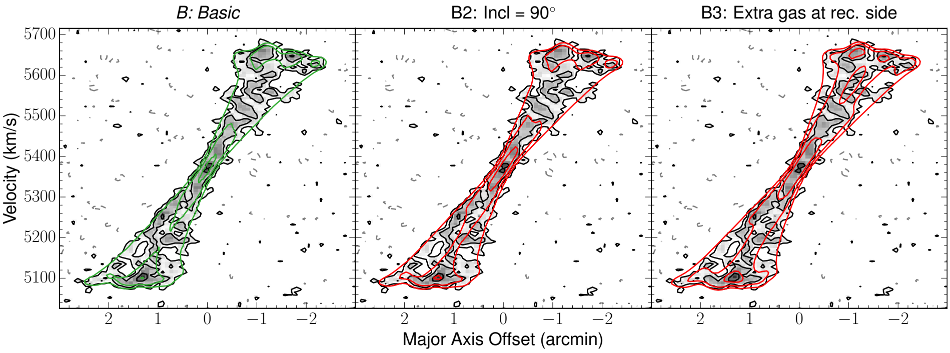

Figure 2.9: Observed major axis position-velocity diagram of UGC 4277 (black and grey contours) overlaid with different models. The green contours represent the final (*B*) model. Other models are shown as red contours. Contour levels are -1.5, 1.5 (1.5σ), 3.0, and 6.0 mJy beam^{-1}. The greyscale corresponds to the observations.

The scale height of the final model is remarkably high. However, the large uncertainty on this value indicates that it should not be trusted blindly and still allows a lower, more common value of the scale height as well. In addition, a flaring gas disk, with a large scale height in the outer regions but a significantly lower scale height in the inner disk, also agrees with the data. The low signal-to-noise ratio and irregular shape of the observed emission in the channel maps unfortunately make it impossible to distinguish between these options and put more stringent constraints on the scale height. We again note that this uncertainty does not strongly affect the other parameters.

2.4.3 IC 2531

IC 2531 is the only southern galaxy in our sample and is located at a distance of 36.8 Mpc. A false colour V-band image taken with the Faulkes Telescope South is shown in the top panel of Fig. 2.11. The stellar disk shows a slight warp and is more extended on the approaching (NE) side, where it is also slightly misaligned with the dust lane. On the receding (SW) side, the dust lane shows a weak bump. The HI content of IC 2531 has already been studied in the series of papers by Kregel et al. (Kregel et al. 2004; Kregel & van der Kruit 2004). They focussed mainly on deriving the HI rotation curves, with the ultimate goal of analysing the contribution of the stellar disk to the (inner) rotation curve of a spiral galaxy. IC 2531 was also part of the sample of O'Brien et al. (2010d,b,a,c) and later Peters et al. (2017a,b,c), who studied the rotation and flaring of the HI disks of a number of edge-on galaxies to derive the three-dimensional shape of their dark matter halos. These studies, however, did not yet include the possibility of a radially varying inclination. As we will see below, this feature proves to be important. Kregel et al. (2004) discovered two companion galaxies at projected distances of 12′ (128 kpc) and 14′ (150 kpc) and with velocity separations of 200 km s^{-1} and 182 km s^{-1} in their study of the HI content of IC 2531.

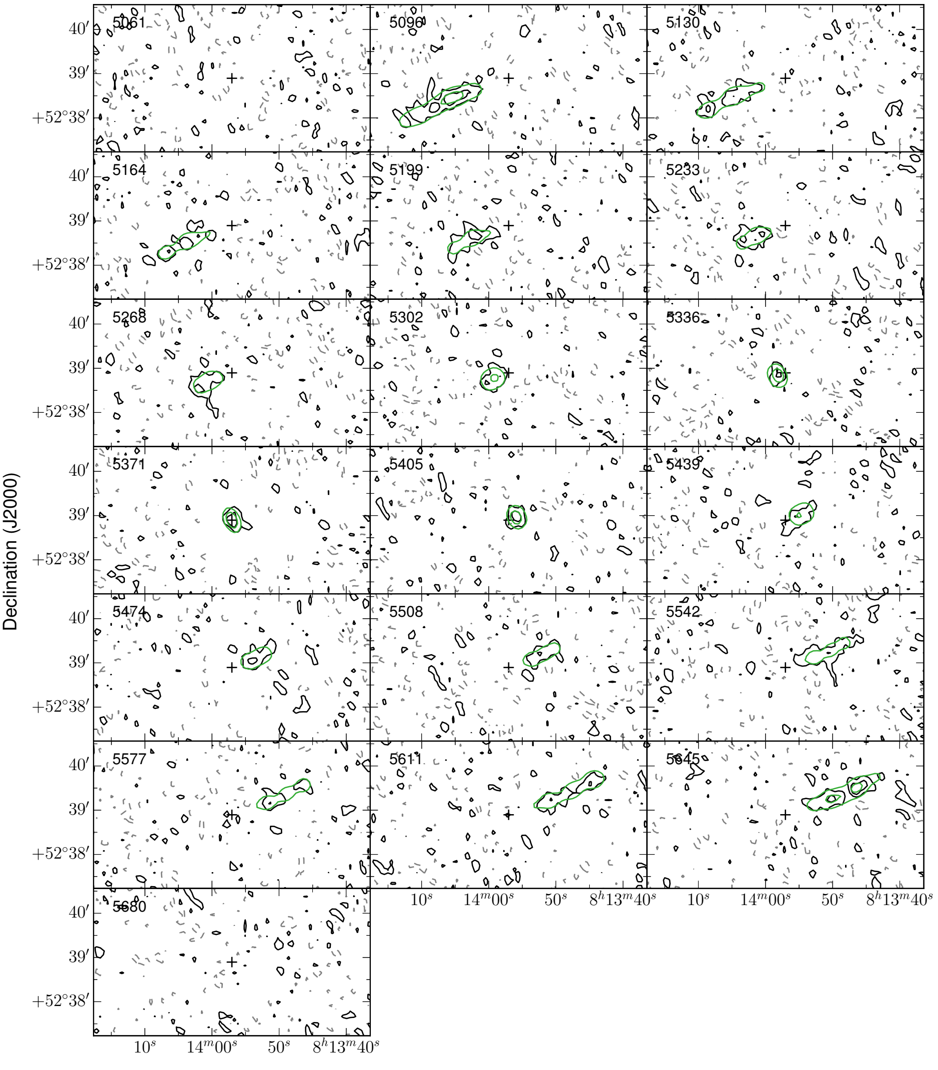

Figure 2.10: Channel maps from the observed data cube of UGC 4277 (black and gray contours) and our final (*B*) model (green). Contour levels are -1.5, 1.5 (1.5σ) and 4.0 mJy beam^{-1}. The black cross indicates the centre of the galaxy.

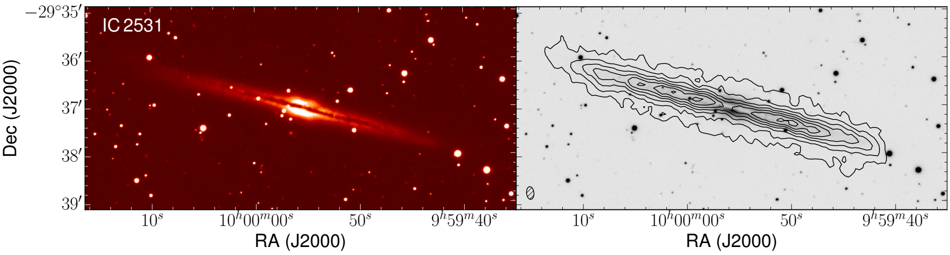

Figure 2.11: Left: False colour V-band image of IC 2531 taken with the Faulkes Telescope South. The data were cleaned and combined using standard data reduction techniques. Right: HI contours overlaid on the same V-band image. Contours start at 2.98×10^{20} atoms cm^{-2} and increase as 4, 8, 12, 16, 20, and 24 times this value. North is up, east to the left.

The HI data

A contour plot of our total HI map is shown in the bottom panel of Fig. 2.11, overlaid on the V-band image from the top panel. Like the stellar disk, the HI disk is also slightly warped and more extended towards the NE side. This was already observed by Kregel et al. (2004). The channel maps (Fig. 2.17 later in this section) further show that the HI disk of IC 2531 does not behave perfectly like an axisymmetric, regularly rotating disk. Indeed, the approaching and the receding side behave quite differently, for example regarding the shape of the emission in the channel maps and the (projected) peak intensities. In addition, (projected) extraplanar features appear and disappear irregularly throughout the cube.

We measure a total HI flux of 42.7 Jy km s^{-1}, which corresponds to a total HI mass of 1.37 $\times 10^{10}$ M$_{\odot}$ at the assumed distance of 36.8 Mpc. Our total HI flux is remarkably higher than the flux reported by O'Brien et al. (2010d) (13.1 Jy km s^{-1}), but in relatively good agreement with the values from Kregel et al. (2004) (44.1 Jy km s^{-1}) and Peters et al. (2017a) (41.7 Jy km s^{-1}). These studies are all based on the same data as the current analysis, although Kregel et al. (2004) did not include the observations from January 2002 taken in the ATCA 750A configuration (see our Table 2.2 and their Table 1). The single-dish 21-cm fluxes reported on NED range from 33.1 Jy km s^{-1} (Koribalski et al. 2004) to 52.3 Jy km s^{-1} (Mathewson & Ford 1996).

Models

In the basic geometry, the best agreement of the *B* model with the data was achieved with an inclination of 87.5° and a scale height of 1.1 kpc. The position angle in the outer regions deviates at most 4° from the inner disk. Comparing the total HI map of the basic model of IC 2531 to the observed map (Fig. 2.12) makes it clear that the low-density contours of the model disk are too thin. An obvious explanation for this would be that the

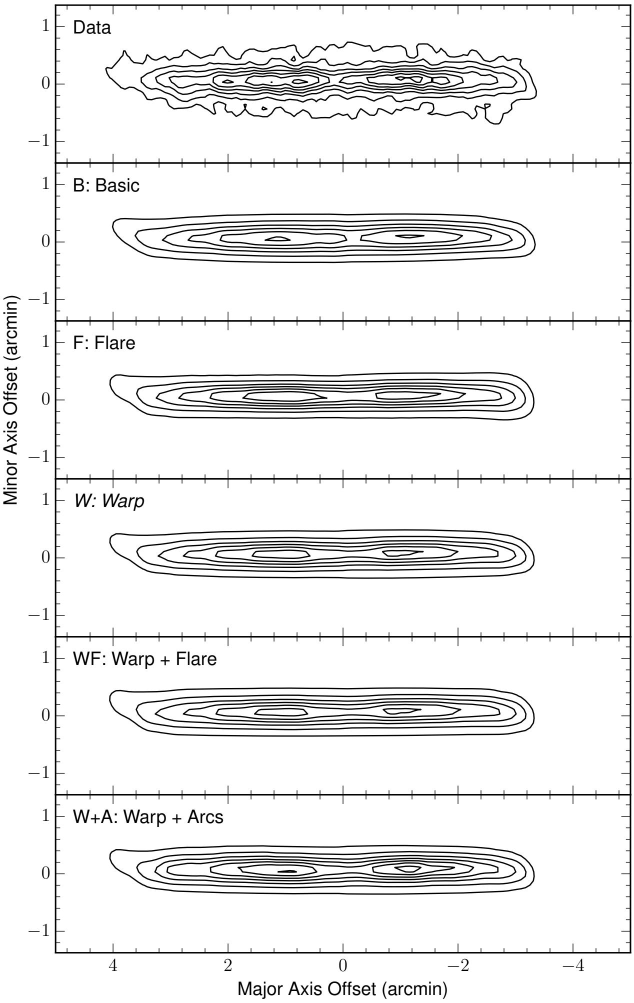

Figure 2.12: Total Hɪ maps of the various models discussed here as compared to the observed total Hɪ map of IC 2531. The *W* model is our best model. Contour levels are the same as in Fig. 2.11.

scale height is underestimated or that the inclination is overestimated, or a combination of both. In that case, the model emission (or at least a part of it) in the individual channel maps would be systematically thinner than the observed emission. Figure 2.13 shows that this is not the case. The apparent thickness of the disk in the observed moment-0 map is in fact caused by the extraplanar features indicated in the previous section. At the sensitivity of our data, these do not seem to be part of a regular structure, and it is not possible to model them in the frame of an axisymmetric disk. We therefore excluded these features in the modelling and focussed on the underlying disk. As a consequence, all models appear slightly too thin in the total HI map. Deeper observations might reveal the true nature of these irregular features and show whether they are part of an extended, low column-density structure.

Ignoring the extraplanar emission, the comparison of some key channel maps in Fig. 2.13, particularly on the receding side, shows that the geometry of the basic model is wrong. Indeed, in the observed channel maps we see that the emission has a triangular shape with the inner part (i.e. the part closest to the centre of the galaxy) a bit thinner than the outer part. In addition, the outer tip of the observed emission generally appears quite flat; i.e., it looks more like a straight vertical line than a round arc. This is illustrated in Fig. 2.13 by the blue dashed lines in the map at 2530 km s^{-1}, where the effect is most obvious. The *B* model, on the other hand, has a round shape. The difference between both might be difficult to see in Fig. 2.13, but is obvious in Fig. 2.14. The triangular shape of the observed emission indicates the presence of a LOS warp or a flare. We therefore continued by investigating these two geometries.

The best agreement with the inner parts of the observed emission in the channel maps was obtained with an inclination of 89.5° and a scale height of 1.0 kpc for the inner disk. A flaring (*F*) model was constructed by gradually increasing the scale height in the outer rings while fixing the inclination to 89.5°. The flare starts at a radius of 25 kpc on both sides of the disk and grows to a maximum scale height of 1.3 kpc on the approaching side and 1.8 kpc on the receding side. Figure 2.13 shows that the flaring model provides a better fit to the data on the inner side of the emission, but the outer edge of the model is still systematically too round on the receding side. This rounding is inherent to a flaring geometry and cannot be removed by changing the details of the flare.

A model with a warp along the LOS naturally explains these issues. The best-fitting model (*W*) has a constant scale height of 1.0 kpc, a central inclination of 89.5° and a LOS warp that reaches an inclination of 85° on the receding side and 87° on the approaching side. Figures 2.13 and 2.14 show that the triangular shape of the emission on the receding side is now nicely matched by the model. The high-density contours are a bit underestimated in some channels (e.g. at 2569 and 2609 km s^{-1} in Fig. 2.13), but this is most likely due to the presence of a spiral arm, which we discuss below. The agreement with the data on the approaching side seems less good in Fig. 2.13, although it is still better than for the previous models. However, the misalignment between the stellar disk and the dust lane, the larger extent seen in the optical and in HI, and the irregular channel maps all suggest

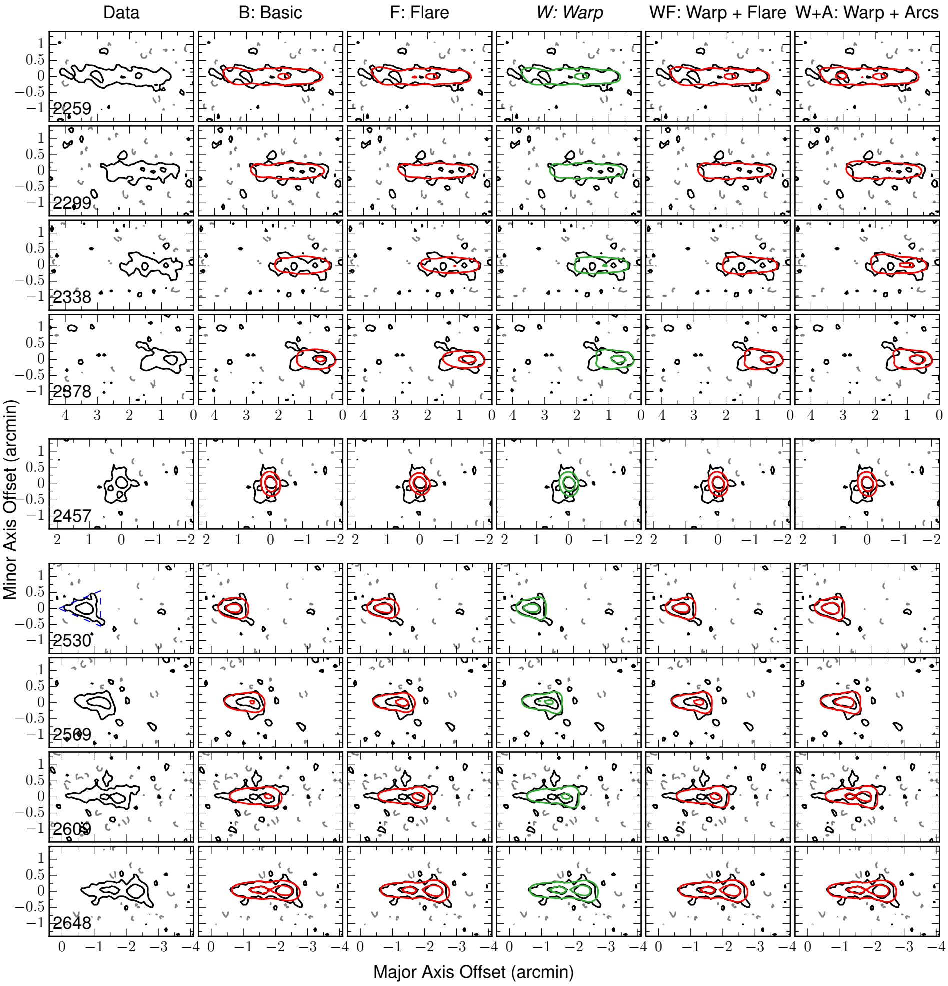

Figure 2.13: Representative channel maps from the observed data cube of IC 2531 and the different models. Contour levels are -1.6, 1.6 (1.5σ), and 6.5 mJy beam^{-1}. The black contours show the observations with negative contours as dashed grey. The green contours represent the final (*W*) model. Other models are shown as red contours. The dashed blue lines illustrate the triangular-like shape of the observed emission. The systemic velocity is 2455 ± 6 km s^{-1}.

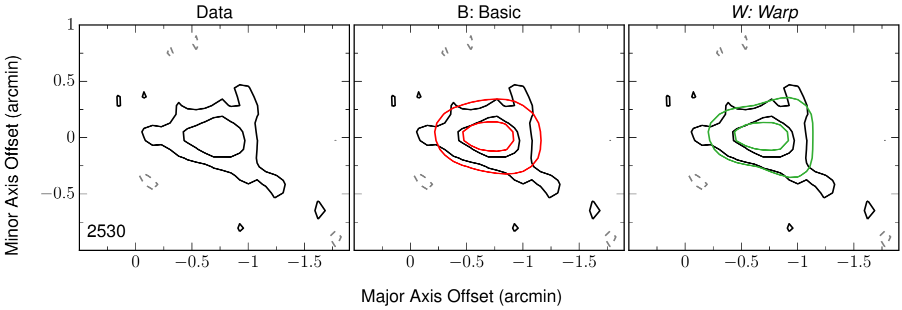

Figure 2.14: Channel map at 2530 km s^{-1} from the observed cube of IC 2531 (black and grey contours), the basic (*B*) model (red contours) and the final (*W*) model (green contours). Contour levels are -1.6, 1.6 (1.5σ), and 6.5 mJy beam^{-1}. The *B* model is clearly too round. The *W* model has a more triangular shape and provides a better fit to the data.

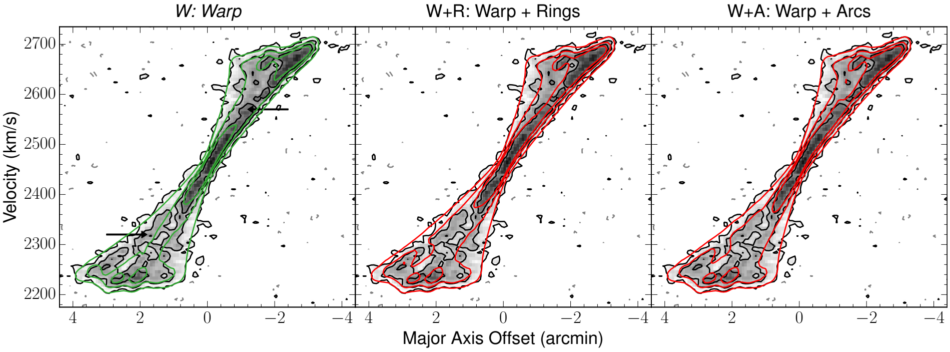

Figure 2.15: Observed major axis position-velocity diagram of IC 2531 (black and grey contours) overlaid with different models. The green contours represent the final (*W*) model. Other models are shown as red contours. Contour levels are -1.6, 1.6 (1.5σ), 4.9, and 8.1 mJy beam^{-1} and the greyscale corresponds to the observations. The high-density ridge along the low-velocity edge on both sides (indicated by the arrows) is not reproduced by the *W* model.

that this side of the galaxy is somewhat disrupted and not simply a smooth disk.

Rather than just one specific type of geometry, real galaxy disks usually contain a combination of different features. Therefore we also investigated the combination of a LOS warp with a flare. A substantial LOS warp is in any case required to reproduce the flattening of the outer edge of the emission in the channel maps. Adding to this a flare of the same order as in the *F* model makes the emission too thick in the outer channels. Adding a more modest flare does not cause significant changes compared to the *W* model. This is shown for a flare with a maximum scale height of 1.3 kpc on both sides as the *WF* model in Fig. 2.13. Since the addition of a flare does not result in a significant improvement of the model, but does introduce extra free parameters, we discard this additional feature and stick to the simple LOS warp geometry (*W* model).

Spiral arms

The terminal side of the major axis position-velocity diagram (Fig. 2.15) is nicely reproduced by the *W* model. This indicates that we recover the rotation curve and the global HI distribution of the disk very well. Not reproduced by our model is the high-density ridge that is clearly visible along the low-velocity edge of the diagram. This ridge is present on both sides of the galaxy, albeit at lower contour levels on the approaching side, and was already noticed by Kregel et al. (2004) on the receding side. After inspecting their full-resolution data cube, they conclude that the ridge is a superposition of multiple rings. On the other hand, in the next paper of this series, Kregel & van der Kruit (2004) argue that the coincidence of HII emission with the HI ridges in many galaxies could indicate the presence of spiral arms.

We tested the first hypothesis by modelling the ridge as a set of rings in different ways. A first possibility is that the ridge is in fact a projection along the major axis of some high-density rings at large radii, rotating at the normal terminal velocities. In practice, this approach requires increasing the densities of the outer rings. On the approaching side, we were unable to construct a ridge in this way, no matter how much the densities were increased. On the receding side, this strategy led to a huge overestimation of the intensities in the tip of the XV-diagram for the *W* model. For a flaring model with a constant inclination of 88°, the outer rings are more strongly projected along the major axis, so a smaller increase in the outer densities suffices to create a ridge in the XV-diagram. But even in this case, the intensities in the tip of the XV-diagram were overestimated.

A second, more artificial possibility would be that the ridge is a superposition of multiple rings at different radii, rotating at velocities considerably lower than the terminal velocities. Such a model, based on the *W* model, is shown in Fig. 2.15. Although it is indeed possible to reconstruct the observed ridge, this approach requires adding a large number of low-velocity rings on top of the main disk (see Fig. 2.16 for the details of these rings) and is highly unphysical.

Based on our modelling we thus exclude the interpretation of the high-density ridge as a superposition of rings. A prominent spiral arm provides a much more natural explanation. Unfortunately, the edge-on orientation offers few constraints, and modelling the spiral arms would be highly speculative at best. We therefore do not attempt to include spiral arms in our model. Because of this, the peak densities in the total HI map and in some channel maps are slightly underestimated by the *W* model. To prove that the latter is not in fact caused by a structural mistake in the model, we constructed a toy model (*W*+*A*) that reproduces the HI ridge in the XV-diagram by locally enhancing the density in several arcs within the disk (Fig. 2.15). Figures 2.12 and 2.13 show that with this addition the model indeed reproduces the observed peak densities.

It is interesting to note that Mosenkov et al. (2016) similarly find overdensities with respect to their radiative transfer models in the WISE *W*3 and *W*4, and PACS 100 images of the dust content of IC 2531. These overdensities are at the same projected locations as the

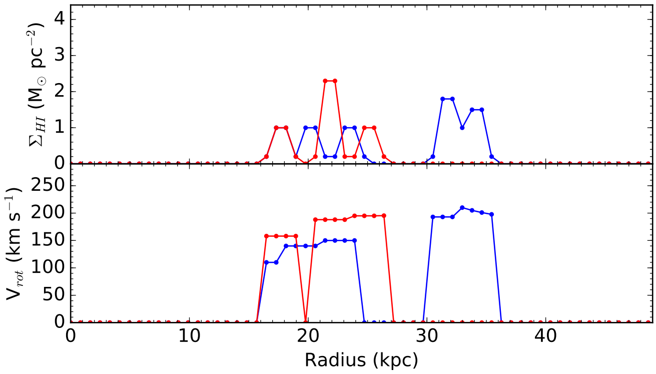

Figure 2.16: Surface densities (top) and rotational velocities (bottom) of the rings added to the *W* model of IC 2531 in order to reproduce the high-density ridge in the major axis XV-diagram. Blue indicates the approaching side, red the receding side.

arcs in the total Hɪ map of the *W+A* model. Our Hɪ modelling has helped to interpret these overdensities as spiral arms rather than flaws in the radiative transfer models.

Despite the improved agreement with the data at high column densities, adding arcs to a model without a clear physical motivation is a dangerous practice and ambiguous. The *W+A* model therefore remains a toy model, and we take the *W* model as our final model for the atomic gas disk of IC 2531. The total Hɪ map of the *W* model is compared to the observed map in Fig. 2.12. Our final model data cube is compared to the observed cube in Fig. 2.17. The main parameters of the final model are given in Fig. 2.35 and Table 2.4. The errors on the inclination, position angle, and scale height are 1.3°, 1.8°, and 0.5 kpc, respectively.

Comparison with O'Brien et al.

O'Brien et al. (2010a) used the same data set as we do to analyse the Hɪ content of IC 2531. Based on the vertically integrated XV-diagram they derived the rotation curve and the radial surface density and velocity dispersion profiles. The radial variation of the vertical FWHM of the disk was subsequently measured by fitting Gaussian profiles to vertical slices across the major axis. It is important to note that they assumed a fixed inclination for the entire disk in this process. O'Brien et al. (2010a) also state that their results within the central ~10 kpc are highly uncertain due to the low signal-to-noise ratio and "should be treated with caution". Excluding this central region, we find that the surface densities from O'Brien et al. (2010a) are generally of the same order as our values (~2-3 M$_\odot$ pc^{-2}) and have a comparable radial profile. The approaching and receding rotation curves from O'Brien et al. (2010a) are also in good agreement with our results beyond 10 kpc, although they do find a slightly lower velocity dispersion of 7 km s^{-1}. Finally, O'Brien et al. (2010a) find a vertical scale height that gradually increases from about 0.5

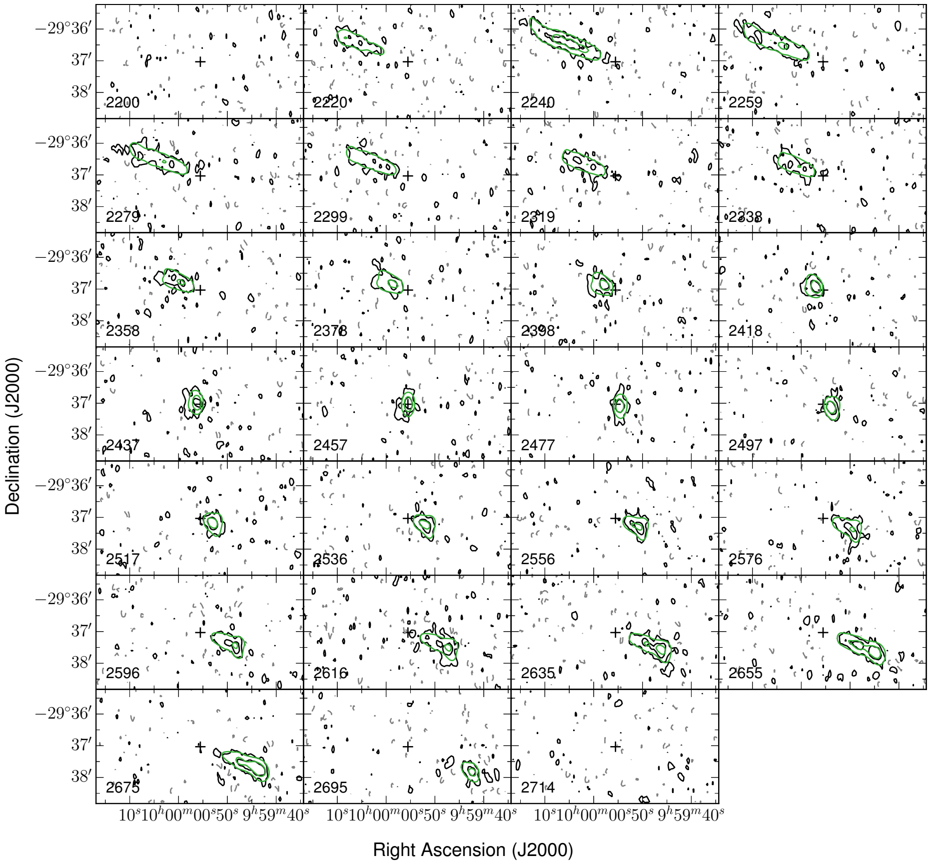

Figure 2.17: Channel maps from the observed data cube of IC 2531 (black and gray contours) and our final (W) model (green). Contour levels are -1.6, 1.6 (1.5σ) and 6.5 mJy beam^{-1}. The black cross indicates the centre of the galaxy.

kpc at a radius of 10 kpc to about 2 kpc at a distance of 37 kpc from the center (if we translate their FWHM values to our assumed sech^2 profile). This flare is stronger than what is allowed by our results, but this is in fact expected since O'Brien et al. (2010a) did not include a LOS warp.

IC 2531 was originally also part of the sample of Peters et al. (2017a,b,c), but they were unable to measure the thickness its HI disk and therefore did not include it in their final analysis.

2.4.4 NGC 4217

NGC 4217 is located at a distance of 19.6 Mpc. Its atomic gas content has previously been studied by Verheijen & Sancisi (2001) and Verheijen (2001), who used the kinematics of the atomic gas in a sample of galaxies in the Ursa Major cluster to investigate

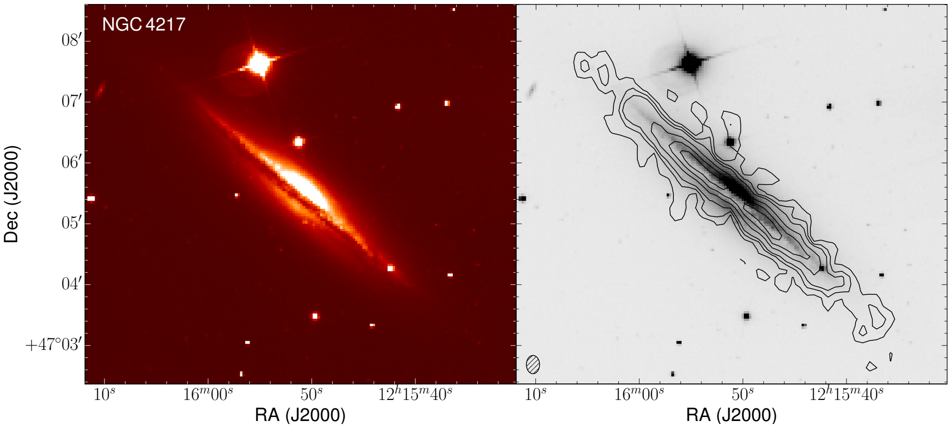

Figure 2.18: Left: False colour r-band image of NGC 4217 (SDSS J121551.51+470538.1) from the EFIGI catalogue (Baillard et al. 2011), based on data from the SDSS DR4. Right: HI contours overlaid on the same r-band image. Contours start at 3.76×10^{20} atoms cm^{-2} and increase as 2.5, 4, 8, 12, and 16 times this value. North is up, east to the left.

the statistical properties of the Tully-Fisher relations. However, their sample consisted largely of moderately inclined galaxies, and their method to derive the surface density distribution of the HI is actually not suitable for an edge-on geometry. Indeed, Verheijen and Sancisi themselves state that their "method for extracting the surface density profiles from integrated HI maps breaks down for nearly edge-on systems."

The HI data

In the total HI map of NGC 4217 (Figs. 2.18, 2.19), two blobs of gas on either side of the main disk immediately catch the eye. These suggest the presence of a ring, which, strikingly, has no optical counterpart in the r-band image in Fig. 2.18. In what follows we refer to this feature as the outer ring. Some filaments can also be seen extending out of the plane of the galaxy. The HI disk is not significantly warped, apart from a slight upward bend (i.e. towards the NW in Fig. 2.18) where it meets the outer ring. This upward bend is also visible in the stellar and dust disks.

If we separate the outer ring from the main disk in our data (see section 2.4.4 for a discussion on the nature of the outer ring), we measure a total HI flux of 27.6 Jy km s^{-1} for the main disk and 4.2 Jy km s^{-1} for the outer ring. At a distance of 19.6 Mpc, this translates to atomic hydrogen masses of $2.50{\times}10^9$ M$_\odot$ and $3.81{\times}10^8$ M$_\odot$. It should be noted that in the central channels of the data cube the emission from the outer ring and the main disk are projected on top of each other, making it very difficult to separate both components. Our estimate of the mass of the outer ring only includes the emission that unambiguously belongs to this component, so it should be regarded as a lower limit. Verheijen & Sancisi (2001) also analysed the HI content of NGC 4217, based on the same data cube as used

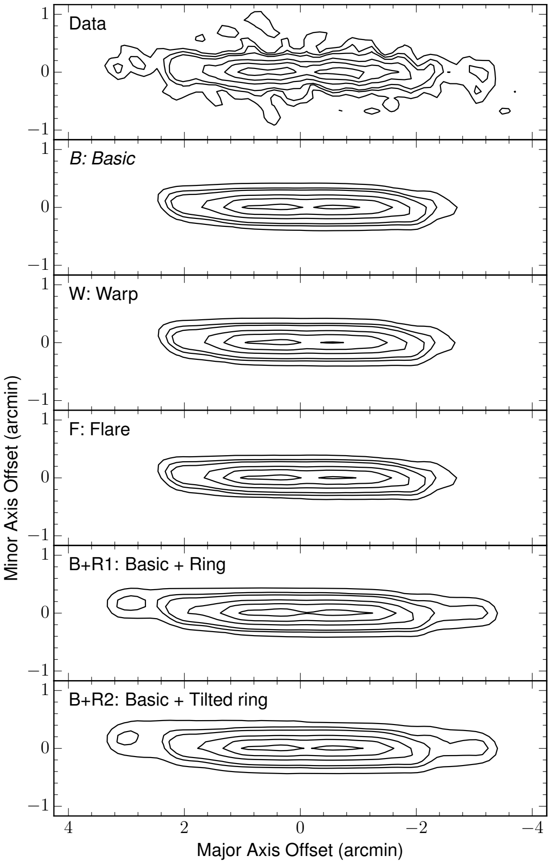

Figure 2.19: Total HI maps of the various models discussed here as compared to the observed total HI map of NGC 4217. The *B* model is our best model. Contour levels are the same as in Fig. 2.18.

here, but did not make a distinction between the main disk and the outer ring. They found a total HI flux of 33.8 Jy km s^{-1}, which is slightly higher than our total flux of 31.8 Jy km s^{-1}. The reason for this is probably that we were stricter in separating the real emission from the noise. (Corrected) single-dish fluxes of 25.8 Jy km s^{-1} and 31.0 Jy km s^{-1} are reported by Springob et al. (2005) and Huchtmeier & Richter (1989), respectively.

Models

In the major axis position-velocity diagram (see Fig. 2.21 later), the outer ring corresponds to the sudden drop in rotational velocities at major axis offsets of about ± 3 arcmin. The outer ring thus seems both spatially and kinematically separated from the main disk, indicating that it probably has an external origin. Because of this, we start by modelling only the main gas disk and add the outer ring as an extra feature in a later stage.

An initial fit (*B*) imposing the basic geometry resulted in an inclination of 86.2° and a scale height of 0.5 kpc. Figure 2.20 compares this basic model to the observations. Ignoring the outer ring, the model already provides a good fit to the data. The only exception to this are four channels on the receding side between 1059 and 1109 km s^{-1} and (to a lesser extent) two channels on the approaching side between 928 and 944 km s^{-1}, where the model is significantly thicker than the observed emission in the inner regions. Two of these channels (at 928 and 1076 km s^{-1}) are shown in Fig. 2.20 and the discrepant regions are indicated with arrows. This discrepancy could indicate a flaw in the model, but the fact that it only shows up in a few channels and that the affected channels are not symmetric around the central channel (which is at 1026 km s^{-1}) indicates that it is probably just caused by local irregularities in the disk and does not reflect a large-scale geometric feature. Nonetheless, we investigate whether a more complex geometry could provide a better fit.

With the parameters of the basic model as input, we conducted a new fit with TiRiFiC. The inclination and scale height were now allowed to vary in blocks of five rings in order to reveal a potential flare and/or LOS warp, but at the same time smooth out the unphysical jumps that TiRiFiC usually finds. Fits in blocks of three and seven rings were also performed to verify the results. The inclination on the receding side was found to roughly increase towards the centre, reaching a maximum of 89.5° in the central rings. For the inclination on the approaching side and the scale height on both sides, the radial profile found by TiRiFiC was still dominated by unphysical jumps and did not display a clear trend. In the absence of strong constraints, we constructed a model with a LOS warp by applying the rising trend of the inclination that was found for the receding side to the approaching side as well and imposing a constant global scale height. A new TiRiFiC fit found a value of 0.6 kpc for the latter. As can be seen in Fig. 2.20, the difference between this model (*W*) and the *B* model is very small, and the discrepancy mentioned in the previous paragraph is still present. Moreover, looking at the r-band image in Fig. 2.18, a central inclination of 89.5° seems too high. Indeed, the bulge is clearly a lot stronger on the NW side of the galaxy ('above' the major axis), while the dust lane is located more towards the SE, suggesting that the galaxy is not seen perfectly edge-on. For these reasons we rejected the *W* model and continue with a constant inclination.

In a final attempt to model the thinning of the disk we added a flare to the *B* model. The *F* model shown in Fig. 2.20 has a constant scale height of 0.1 kpc out to a radius of 2.6 kpc, which then linearly increases to reach a maximum value of 0.6 kpc in the outer regions of the disk. The discrepancy in the six channels mentioned earlier is still not completely resolved, although it is (slightly) less severe. However, at the same level as this flaring model improves the fit in these six channels, it is then too thin in many other channels. Adding a flare to the model therefore introduces many free and poorly constrained parameters without significantly improving the quality of the fit. We thus decided not to include a flare and to stick with the basic geometry (*B* model). It should be noted, though, that the difference between the various models we discussed here is very small, so the geometry

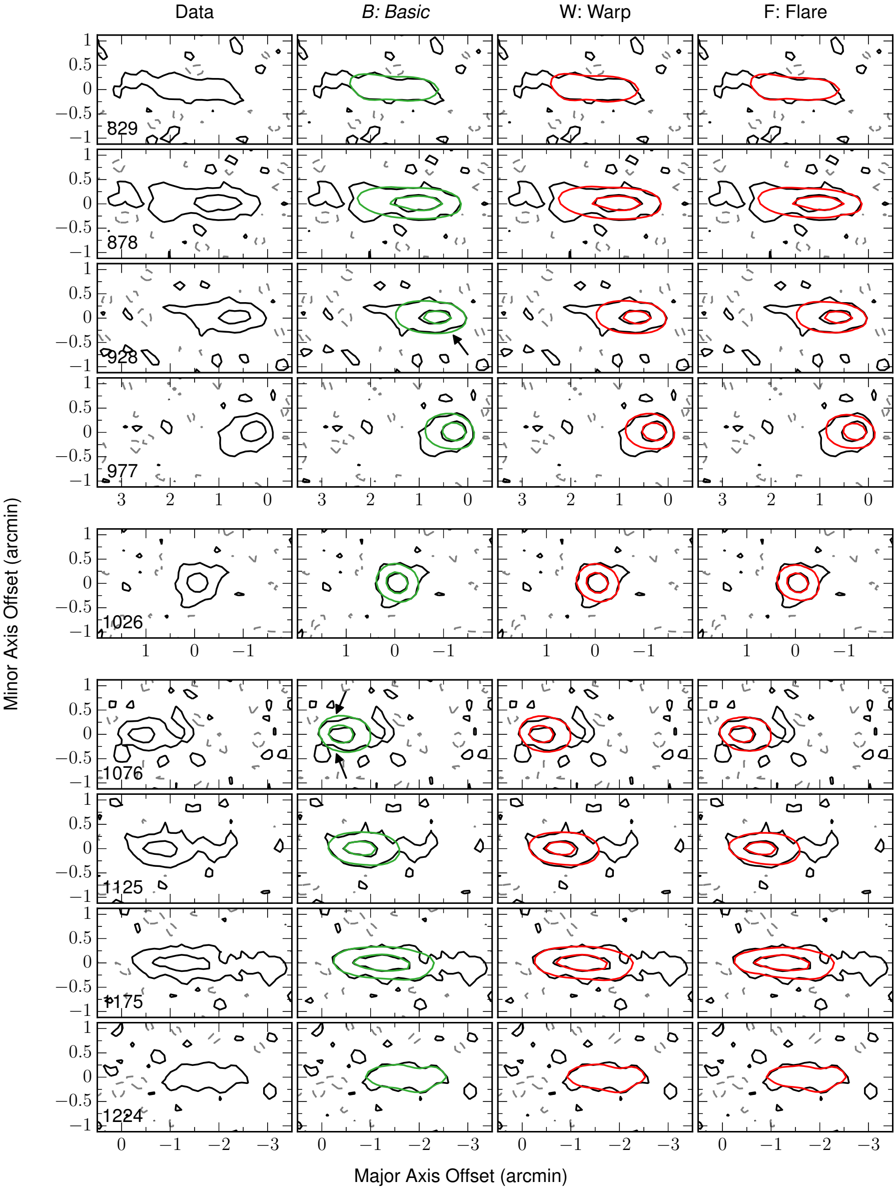

Figure 2.20: Representative channel maps from the observed data cube of NGC 4217 and the different models of the main disk. Contour levels are -1.5, 1.5 (1.5σ,) and 8.0 mJy beam^{-1}. The black contours show the observations, with negative contours as dashed grey. The green contours represent the final (*B*) model. Other models are shown as red contours. The systemic velocity is 1022 ± 6 km s^{-1}. The arrows highlight regions where the *B* model is significantly thicker than the observed emission, as explained in the text.

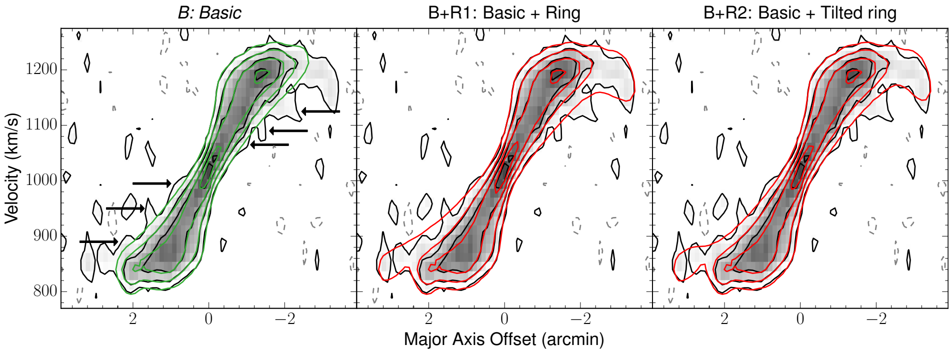

Figure 2.21: Observed major axis position-velocity diagram of NGC 4217 (black and grey contours) overlaid with different models. The green contours show the final (*B*) model. Other models are shown as red contours. Contour levels are -1.5, 1.5 (1.5σ), 4.5, 9.0, and 13.5 mJy beam^{-1}. The greyscale corresponds to the observations. We interpret the features indicated by the arrows as the projection of a clumpy ring along the major axis.

of the gas disk is not very well constrained by our modelling. However, this does not significantly affect the other parameters. Between the different geometries investigated here, only the surface brightness distribution needed slight adjustments and the changes were of the order of 10% at most.

The outer ring

The next step in the modelling process is to determine the nature of the outer ring. We start by modelling it as a simple extension of the main disk, i.e. using the same inclination and scale height as in the disk. This model (model *B+R1* in Fig. 2.22) performs well in the very outer channels, but in the other channels the projection of the outer ring along the major axis clearly disagrees with the data, especially on the approaching side. Arrows highlight this effect in the channel maps at 895, 944, and 1158 km s^{-1} in Fig. 2.22. This is also visible in the XV-diagram (Fig. 2.21) and indicates that either the outer ring is not a complete and smooth ring or that the inclination should be lower, placing less gas along the major axis. We test the latter option in the *B+R2* model, with inclinations in the outer ring of 84°on the approaching side and 83°on the receding side. Figure 2.21 shows that this model does indeed solve the aforementioned projection problem, but cannot account for the clumpy features along the low-velocity edges of the XV-diagram (indicated with arrows for the *B* model). Moreover, the lower inclination makes this model too thick, as can be seen in the moment-0 map (Fig. 2.19) and in the central channels in Fig. 2.22. Finally, both these models also require a highly unphysical rotation curve on the receding side, with a rather abrupt decrease of about 60 km s^{-1} (see Fig. 2.35). All these arguments indicate that the outer ring is not simply an extension of the main disk. A more natural interpretation would be that we are observing the accretion of a roughly coplanar satellite

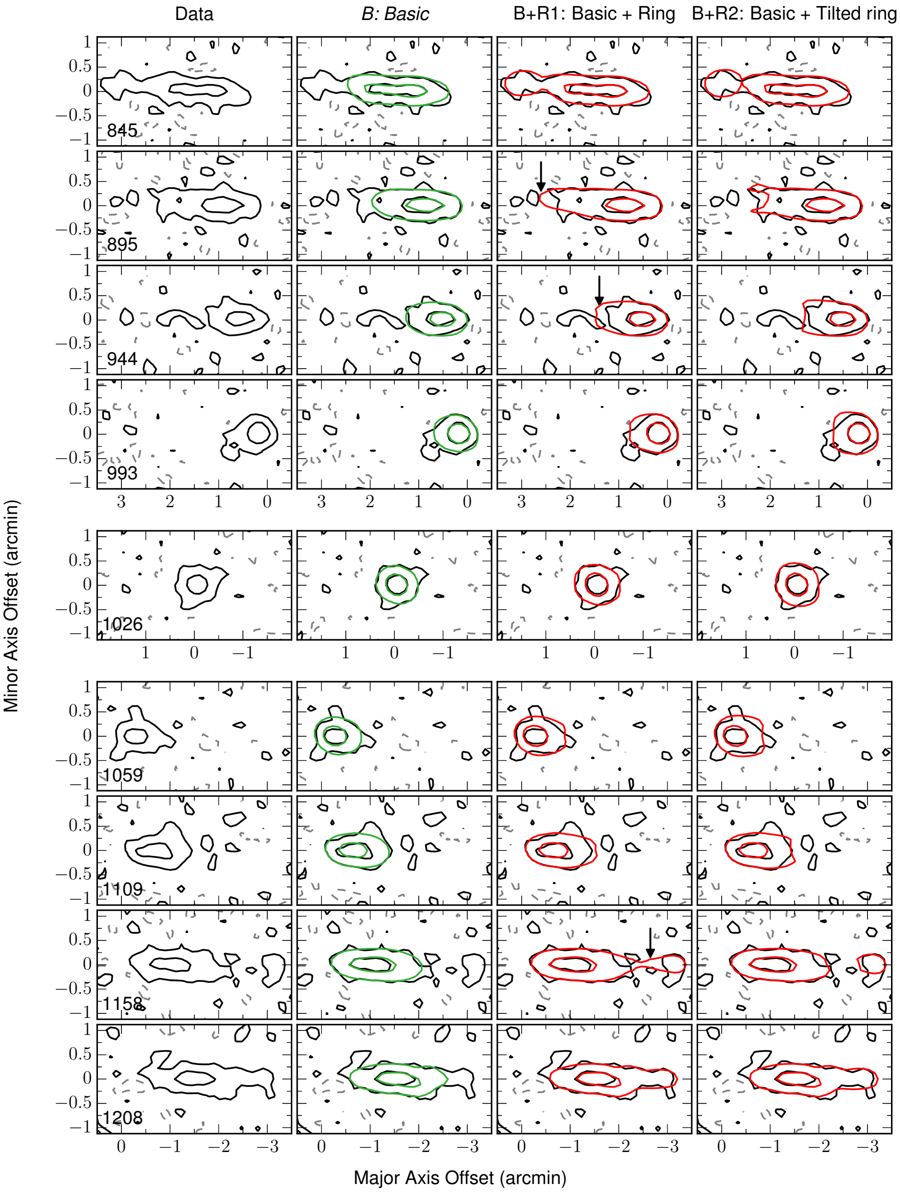

Figure 2.22: Representative channel maps from the observed data cube of NGC 4217 and the different models that include the outer ring. Contour levels are -1.5, 1.5 (1.5σ), and 8.0 mJy beam^{-1}. The black contours show the observations, with negative contours as dashed grey. The green contours represent the final (*B*) model. Other models are shown as red contours. Because we want to highlight different features, the channels shown here are different from those in Fig. 2.20. The arrows highlight the projection along the major axis of the outer ring in the *B+R1* model, which clearly disagrees with the data.

galaxy that has been gradually ripped apart, forming a clumpy arc or ring-like structure around NGC 4217. This would explain the spatial and kinematical offset with respect to the main disk and the absence of a smooth projection of the ring along the major axis.

Modelling the outer ring as a set of individual clumps is, in principle, possible with TiRiFiC, but this exercise would not contribute much to the overall quality of the model and is beyond the scope of this paper. We therefore take the *B* model as our final model for the atomic gas disk of NGC 4217 and note that a coplanar ring-like structure just outside of the disk is not included in this model. A comparison between the final model and the observed data cube is shown in Fig. 2.23. The major axis position-velocity diagrams are compared in Fig. 2.21, and the main parameters of the final model are shown in Fig. 2.35 and Table 2.4. The inclination and position angle have respective uncertainties of 1.5° and 2.0°, and the error on the scale height is 0.2 kpc.

2.4.5 NGC 5529

NGC 5529 is located at a distance of 49.5 Mpc and is part of a rich galaxy group with at least 16 other members (Irwin et al. 2007). Its stellar disk (shown in Fig. 2.24) shows a clear warp and extends out to larger (projected) radii on the NW side. Like IC 2531, NGC 5529 was also part of the sample of galaxies analysed by Kregel et al. (2004) and Kregel & van der Kruit (2004). In their study of the atomic gas in this galaxy, Kregel et al. (2004) discovered that HI bridges connect the disk of NGC 5529 to two of its companions, MGC +06-31-085a and NGC 5529 B.

The HI data

Derived from the same WSRT data as used by Kregel et al. (2004), our total HI map (Fig. 2.24) is very similar to theirs. On the approaching (NW) side, the atomic gas follows the same moderate warp as the stars. On the receding (SE) side, the HI appears more strongly warped and shows a strong upturn beyond the stellar disk. The channel maps (see Fig. 2.29 later in this section) reveal that the HI disk of NGC 5529 is surrounded by a significant volume of extraplanar gas, especially on the approaching side, as a consequence of the interaction with the satellite galaxies. This will be discussed in further detail in the next section.

It is not possible to unambiguously separate the actual HI disk of NGC 5529 from the extraplanar gas and the satellite galaxies in the channel maps. To determine the total HI mass of the galaxy, we took a conservative approach and omitted only the emission that unambiguously comes from the satellite galaxies. From the resulting moment-0 map, we measured a total HI flux of 46.5 Jy km s^{-1}. This is slightly higher than the value of 43.2 Jy km s^{-1} found by Kregel et al. (2004). The small difference between both fluxes is most probably due to the rather subjective distinction between the emission from NGC 5529

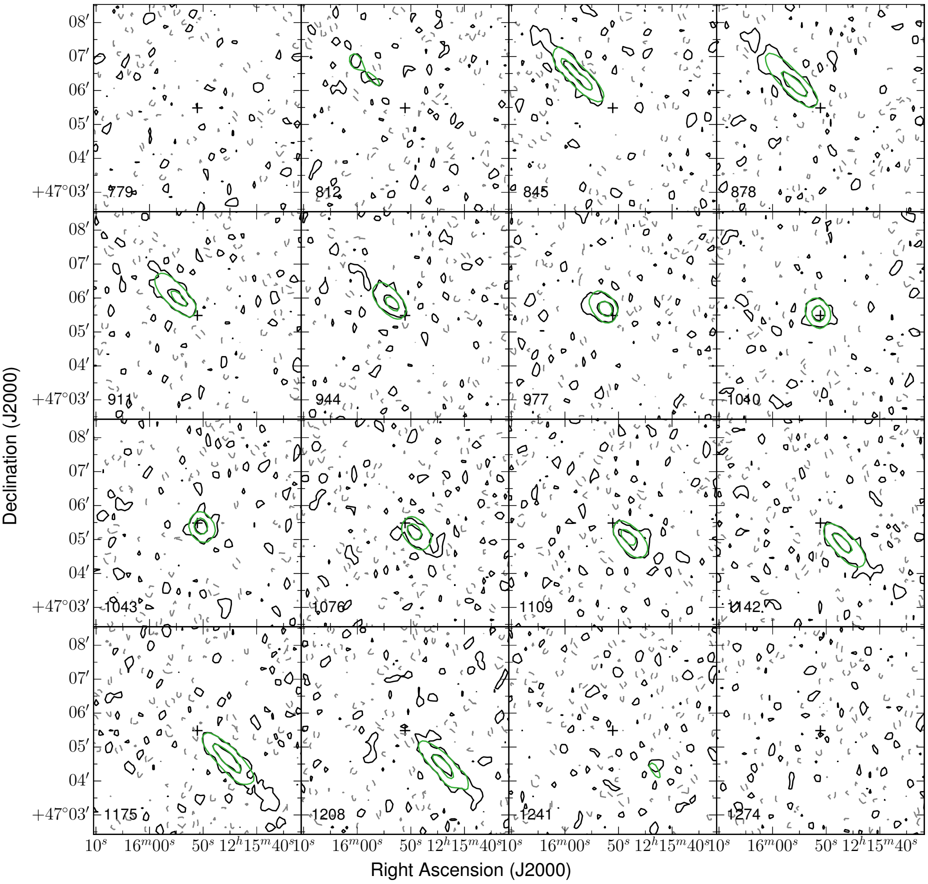

Figure 2.23: Channel maps from the observed data cube of NGC 4217 (black and gray contours) and our final (*B*) model of the main disk (green). Contour levels are -1.5, 1.5 (1.5σ) and 8.0 mJy beam^{-1}. The black cross indicates the centre of the galaxy.

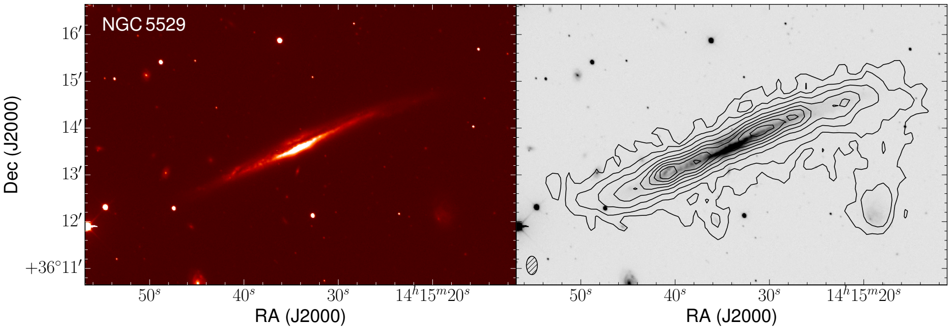

Figure 2.24: Left: False colour V-band image of NGC 5529 taken with the 1.3m telescope at the Skinakas Observatory in Crete. The data were cleaned and combined using standard data reduction techniques.. Right: HI contours overlaid on the same V-band image. Contours start at 9.94×10^{19} atoms cm^{-2} and increase as 4, 10, 20, 30, 40, 50, and 60 times this value. North is up, east to the left.

and from the satellites. At a distance of 49.5 Mpc, our HI flux corresponds to a total HI mass of 2.69×10^{10} M$_{\odot}$. Huchtmeier & Richter (1989) report total HI fluxes of 26.8, 37.1, and 40.8 Jy km s^{-1} obtained with different single-dish telescopes.

Models

After imposing a simple, one-component disk to start the modelling, the best agreement with the data was achieved with an inclination of 86.4° and a scale height of 0.4 kpc. The approaching side of the resulting *B* model is dominated by a gradual warp that starts early on in the disk, at a radius of 15 kpc, and reaches a maximum deviation of 10° with respect to the central position angle. The receding side shows a more abrupt warp, starting at a radius of 37 kpc and rapidly increasing to a maximum deviation of 16°. Comparing the *B* model to the data in the channel maps (Figs. 2.25, 2.26) and the moment-0 map (Fig. 2.27), we see that the model already provides a reasonable approximation to the data, although there are still some issues to address. Part of the observed channel maps on the approaching side contain additional emission that is trailing behind the model. This emission is indicated with arrows at 2615, 2697, and 2780 km s^{-1} in Fig. 2.25 and is also visible in Fig. 2.29 between 2598 and 2763 km s^{-1}. However, in the outermost channels, the model reproduces all the observed emission very well. In addition, the extra emission never exceeds the outer edge of the (integrated) model disk. These two arguments indicate that the model disk extends out far enough radially and is rotating at the correct velocity, and that the extra emission is not the projection of larger rings. We thus interpret this emission as extraplanar gas resulting from the interaction with MGC +06-31-085a and do not include it in our models of the main disk of NGC 5529.

A second, more subtle deficiency of the *B* model is most visible in the innermost channel maps, for example at 2780 and 2879 km s^{-1} in Fig. 2.25, and is highlighted for the

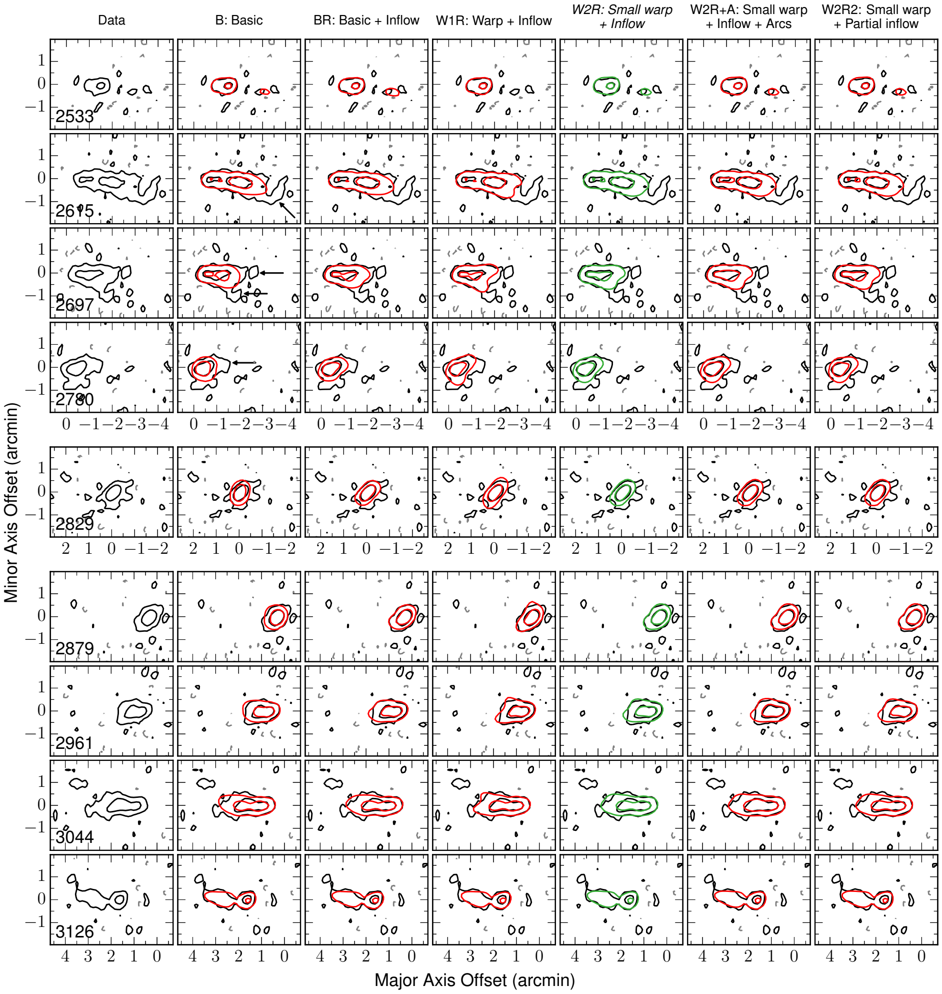

Figure 2.25: Representative channel maps from the observed data cube of NGC 5529 and the various models. Contour levels are -0.8, 0.8 (1.5σ), and 5.6 mJy beam^{-1}. The black contours show the observations, with negative contours as dashed grey. The green contours represent the final (*W2R*) model. Other models are shown as red contours. The systemic velocity is 2830 ± 6 km s^{-1}. The arrows highlight extraplanar gas that probably results from the interaction with the companions.

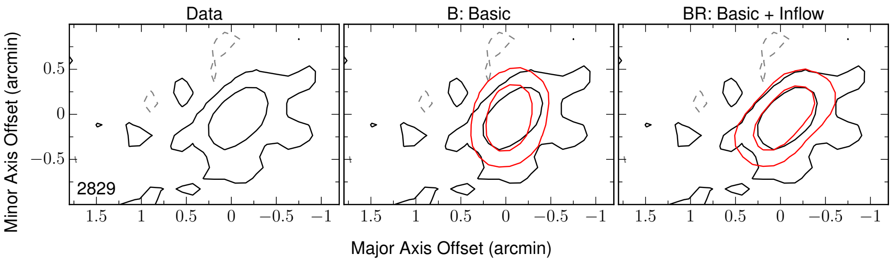

Figure 2.26: Channel map at 2829 km s^{-1} from the observed data cube of NGC 5529 (black and grey contours), the *B* model, and the *BR* model. Contour levels are -0.8, 0.8 (1.5σ), and 5.6 mJy $beam^{-1}$. The orientation of the *B* model is clearly too vertical. Adding a radial inflow significantly improves the agreement with the data.

2829 km s^{-1} channel in Fig. 2.26. While the model emission in these channels is oriented more or less perpendicular to the major axis (vertical in Figs. 2.25 and 2.26), the observed emission shows a slant and is oriented more diagonally from the top right to the bottom left. This discrepancy cannot be resolved by changing the geometry of the disk. Instead, we model the slant by introducing inward radial motions of -15 km s^{-1} in the entire disk (*BR* model). We note that from our Hɪ data alone, it is in principle not possible to determine which half of the disk (north or south of the major axis in Fig. 2.24) is the near side and which the far side. In the optical, however, we clearly see that the dust lane is mainly located north of the major axis, indicating that this is the near side. The radial motions in our model are inward under this assumption. The addition of a radial inflow significantly improves the agreement with the data, especially in the inner channels. On the other hand, this purely kinematical adjustment has no influence on the moment-0 map.

The total Hɪ map of the *BR* model is therefore identical to the map of the *B* model. In general it is in good agreement with the observed moment-0 map (Fig. 2.27), but it is too thin at the lowest contour levels (outermost contours). Adding a substantial flare to the model can immediately be ruled out as a potential solution to this problem. Indeed, in the outermost channel maps, we see that the model emission is thick enough and matches the data very well. Adding a flare would make the model significantly too thick in these channels. A second alternative consists of adding a LOS warp. We tested this option by gradually lowering the inclination from 86.4° to 82.0° between radii of 40 kpc (2.8′) and 47 kpc (3.3′) and keeping it fixed at 82.0° beyond that. The moment-0 map of the resulting *W1R* model now has the correct thickness, but in the channel maps this model does not provide a consistent improvement over the *BR* model (Fig. 2.25). In some channels the observed emission broadens on the outer side and shows a triangular shape, which is nicely reproduced by the *W1R* model (e.g. at 2615 km s^{-1} in Fig. 2.25). In other channels, however, this broadening is less strong or even absent, and the emission from the *W1R* model is too thick on the outer side (e.g. at 2879 and 2961 km s^{-1}). The absence of a

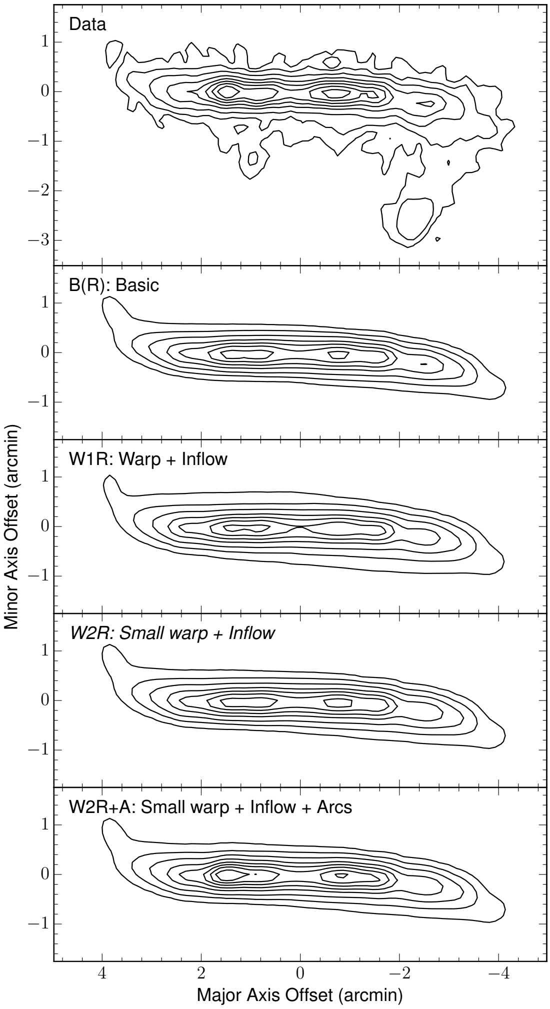

Figure 2.27: Total HI maps of the various models discussed here as compared to the observed total HI map of NGC 5529. The *W2R* model is our best model. Contour levels are the same as in Fig. 2.24.

systematic trend in the data leads us to believe that the strong broadening of the observed emission in some of the channels is not a real feature of the disk, but is rather caused by the extraplanar gas from the interaction with the satellites. As a consequence, the lowest contours in the observed moment-0 map most probably also reflect the extraplanar gas and not the real thickness of the disk.

Notwithstanding the arguments from the previous paragraph, the data do show indications of a small LOS warp. Indeed, if we compare the *BR* model to the data in the channel maps, we see that the outer tip of the model emission is generally a bit too extended and sharp.

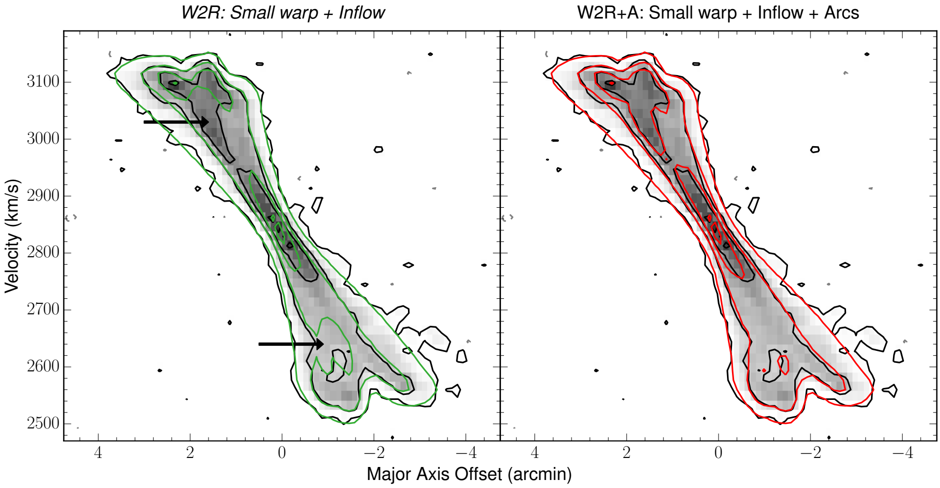

Figure 2.28: Observed major axis position-velocity diagram of NGC 5529 (black and grey contours) overlaid with different models. The green contours show the final *W2R* model, the red contours show the *W2R+A* model. Contour levels are -0.8, 0.8 (1.5σ), 5.6, 11.2 and 16.8 mJy beam^{-1}. The greyscale corresponds to the observations. The arrows indicate a HI ridge that is not reproduced by the *W2R* model.

To correct for these effects without affecting the central channels, we constructed the *W2R* model. This has a central inclination of 87.5° and a constant scale height of 1.1 kpc. The inclination then gradually decreases to 85.0° between 40 kpc and 47 kpc from the centre and stays constant beyond that. This model provides a subtle but significant improvement over the *BR* model.

Spiral arms

The terminal edges of the major axis XV-diagram (Fig. 2.28, left panel) are reproduced very well by the *W2R* model, both on the approaching and on the receding half. Similar to the case of IC 2531, however, the XV-diagram of NGC 5529 shows an additional HI ridge that is not reproduced by our model of the gas disk (indicated by arrows in the left panel of Fig. 2.28). And similar to the case of IC 2531, Kregel & van der Kruit (2004) find that this ridge coincides with a ridge of Hα emission, suggesting a spiral arm. Given the many uncertainties that are involved, we made no attempt to include spiral arms in our model, but we again constructed a toy model (*W2R+A*) that reproduces the HI ridge by locally enhancing the surface brightness in various arcs in the disk. The major axis XV-diagram of this model is shown in the right-hand panel of Fig. 2.28 and the corresponding zeroth moment map and channel maps can be seen in Figs. 2.25 and 2.27. We see that with the addition of the arcs, the peak intensities of the model indeed agree with the data.

As for IC 2531, we note that the addition of arcs to the *W2R* model is not really physical and is ambiguous. We therefore consider the *W2R+A* model as a toy model and take the *W2R* model as our final model for the atomic gas disk of NGC 5529. A comparison of this model to the full observed data cube is shown in Fig. 2.29 and the major axis position-velocity diagrams are compared in Fig. 2.28. Table 2.4 and Fig. 2.35 show the main parameters of the final model. The inclination, position angle, and scale height have errors of 2.0°, 3.0°, and 0.7 kpc, respectively.

About the radial motions

The central channel maps of the observed cube show a clear slant that indicates the presence of radial motions in the disk. To model this effect we used a global inflow in the entire gas disk. We acknowledge that such a parametrisation is most probably too simplistic, but the data do not provide sufficient constraints to model the radial motions in more detail. To reproduce the observed slant, an inflow of -15 ± 5 km s^{-1} is definitely required in the outer half of the disk. On the other hand, radial motions in the inner parts of the disk only cause very subtle changes in the channel maps. Unfortunately, these subtle changes are completely dominated by the effects of the extraplanar gas in the observed cube. It is therefore not possible to determine from the data whether an inflow is also present in the inner disk or not. In fact, even a small outflow in the inner regions is consistent with the data. As an example of this, Fig. 2.25 compares our final model to a similar model (*W2R2*) with no radial motions in the inner disk. The difference between both is indeed very small, and it is not possible to determine which model is better. To minimise the number of free parameters, we therefore opted to use global inflow in the entire disk.

The velocity of the radial motions derived in this work is comparable to the inflow of -20 km s^{-1} found by de Blok et al. (2014) in the outer part of the gas disk of NGC 4414. Zschaechner et al. (2012) report a strong, local inflow of -50 km s^{-1} in the inner part and an outflow of 10 km s^{-1} in the outer part of the gas disk of NGC 4565.

How should we interpret this radial inflow? It was already mentioned that NGC 5529 shows strong evidence of prominent spiral arms. It further has a peanut-shaped bulge, where Kregel & van der Kruit (2004) find a typical figure-of-eight pattern in their optical emission line position-velocity diagram, indicating the presence of a bar. These features are indeed known to generate non-circular flows in the disk of a galaxy. However, theory and simulations show that bars and spiral arms induce an inflow of gas inside the corotation radius and an outflow outside the corotation radius (Kenney 1994; Kormendy & Kennicutt 2004). Since corotation generally occurs at only several kpc from the centre of a galaxy (Elmegreen et al. 1992), it is unlikely that the inflow we find for NGC 5529 is driven by a bar or spiral arms. Instead it might be related to ongoing accretion of gas from the satellite galaxies. Indeed, when the accreted gas has a lower angular momentum than the gas in the disk, it can generate a radial inflow in the galaxy (Matteucci 2012).

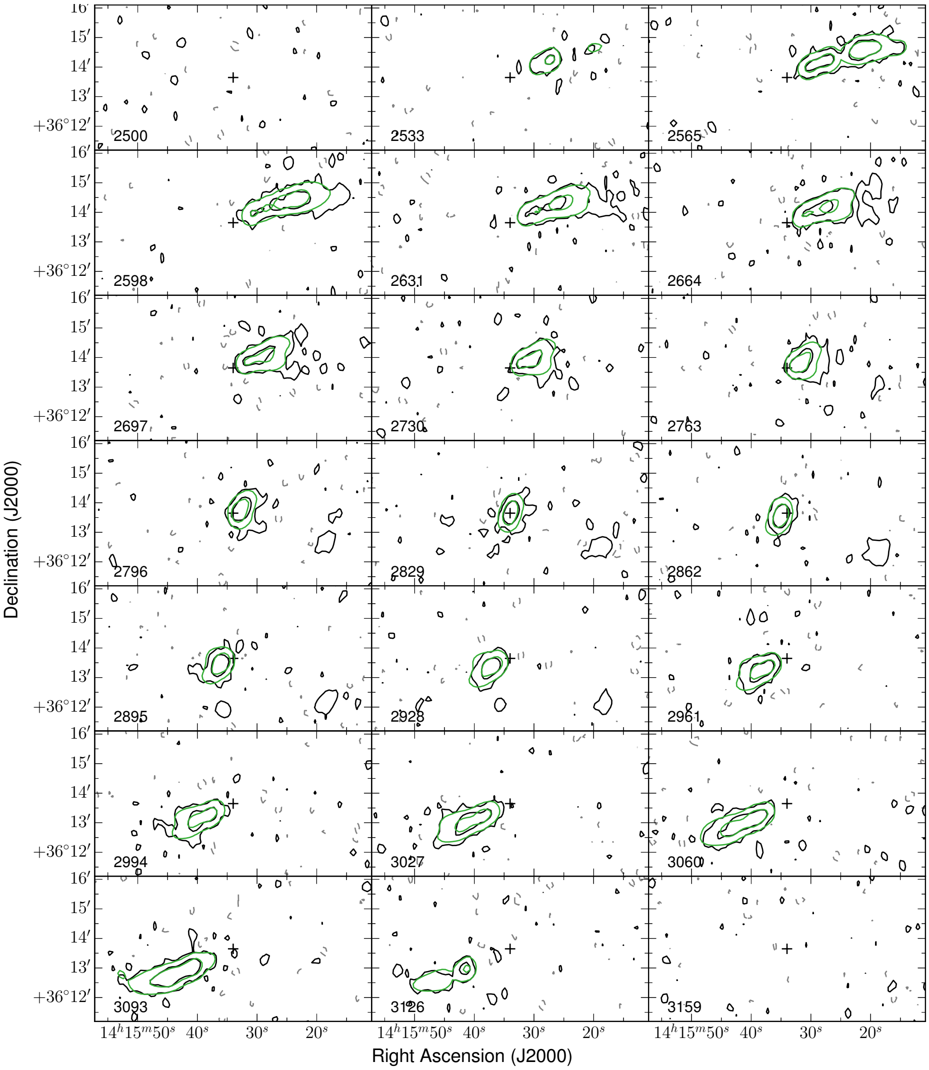

Figure 2.29: Channel maps from the observed data cube of NGC 5529 (black and gray contours) and our final (*W2R*) model (green). Contour levels are -0.8, 0.8 (1.5σ) and 5.6 mJy beam^{-1}. The black cross indicates the centre of the galaxy.

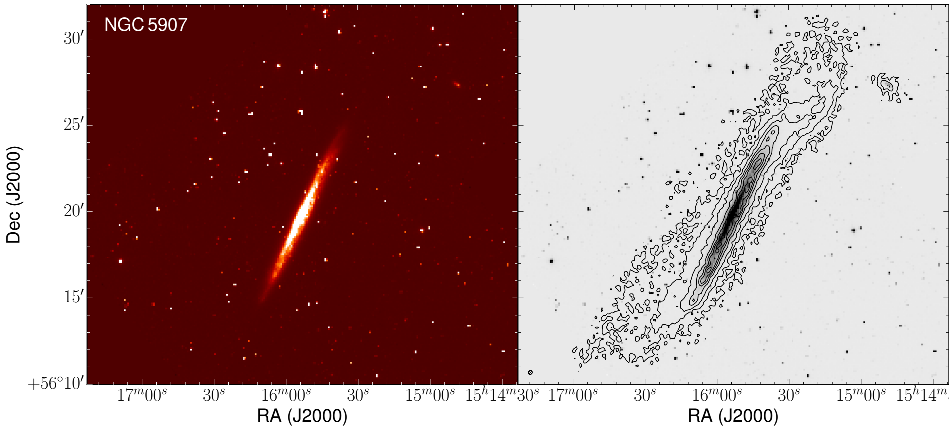

Figure 2.30: Left: False colour r-band image of NGC 5907 (SDSS J151553.77+561943.5) from the EFIGI catalogue (Baillard et al. 2011), based on data from the SDSS DR4. Right: HI contours overlaid on the same r-band image. Contours start at 1.01×10^{20} atoms cm^{-2} and increase as 5, 15, 30, 45, 60, and 75 times this value. North is up, East to the left.

2.4.6 NGC 5907

The closest member of our sample is NGC 5907, located at a distance of 16.3 Mpc. It is a disk-dominated galaxy with no significant bulge visible. Almost 40 years ago, Sancisi (1976) already noticed that the HI disk of NGC 5907 is strongly warped. This warp is also visible in the optical, although less obvious. NGC 5907 is a member of the NGC 5866 group (or LGG 396), but the three other members of this group are located at large distances. NGC 5907 was therefore long considered as the prototype of an isolated galaxy with a warped disk, until Shang et al. (1998) discovered a small companion in their VLA HI map (PGC 54419), and an extended stellar tidal stream around the galaxy in their optical observations. Deeper optical imaging by Martínez-Delgado et al. (2008) later revealed even more loops of stellar debris. The latter also conducted N-body simulations showing that most of the stellar loops they observed can be explained by the accretion of a single satellite galaxy. More recently, Yim et al. (2014) used the same VLA data to study the vertical structure of the gas disk of NGC 5907. They also derived the surface density distribution, rotation curve, inclination and vertical scale height of the HI, but followed a completely different approach.

The HI data

The total HI map of NGC 5907 as derived from our data is compared to an r-band image from the SDSS in Fig. 2.30. In the optical image we see that the dust lane is located slightly below (i.e. to the west) of the major axis. We therefore interpret that side as the front half of the disk and the east side as the back half. The HI reveals a more complex structure than would be expected from the optical image. Indeed, the main gas disk is strongly warped and slightly asymmetric, with the receding (NW) half showing a slight upturn in the outer regions. Additionally, an extended body of low-density gas seems to surround the main disk (in projection). Strikingly, this low-density gas is located almost entirely above (i.e., east of) the disk. Finally, the companion galaxy PGC 54419 is visible towards the NW of NGC 5907. We note that the atomic gas content of NGC 5907 might actually extend even farther than seen in our map since a significant amount of low-density gas is likely still hidden in the noise in our channel maps. Deeper WSRT observations with a total integration time of about 16×12 hours have recently been conducted by G. Józsa, and a detailed modelling of these data is underway.

Excluding the companion, we measure a total HI flux of 317.6 Jy km s^{-1}. This corresponds to an atomic hydrogen mass of 1.99×10^{10} $M_{\odot}$ if we assume a distance of 16.3 Mpc. NED lists a variety of single-dish fluxes, ranging from 36.6 Jy km s^{-1} (Huchtmeier & Richter 1989) to 282.5 Jy km s^{-1} (Springob et al. 2005). Shang et al. (1998) did not measure the total HI flux of NGC 5907. Somewhat surprisingly, our interferometric flux measurement is higher than all the single-dish fluxes. Keeping in mind the large angular extent of NGC 5907, the limited HPBW of many of the single-dish observations is likely part of the reason for this. In addition, uncertainties in the flux calibration generally also cause differences.

Models

The best-fitting single-component (B) model has a constant inclination of 85.4° and scale height of 1.2 kpc. The strong warp on the approaching side is reproduced with a sudden strong decrease in the position angle at a radius of 26 kpc (see e.g. Fig. 2.31). This decrease then becomes more gradual and continues out to the edge of the disk, where the position angle reaches a maximum deviation of 12.9° with respect to the centre. On the receding side the position angle initially shows similar behaviour with a maximum deviation of 12.9° with respect to the centre. However, at a radius of 45 kpc, the position angle then starts to increase again, eventually deviating only 2.8° from the central value in the outer regions of the disk (Fig. 2.31). We also note that in the best-fitting B model, the position angles in the inner, flat part of the disk differ by 1.8° between the approaching and receding sides. Comparing this model to the observed data cube we see that in the outer channels (e.g. at 424, 486, 548, 837, and 898 km s^{-1} in Fig. 2.32), the model is clearly too thick in the central regions of the disk. Additionally, the inclination in the outer regions of the model still seems too high, since the observed emission in the channel maps clearly opens up more than the model does. We address these issues one by one.

On the one hand, we note that the central parts of the model disk appear too thick primarily in the outer channels near the terminal velocities, where the inclination only has a negligible effect. This indicates that the problem is related to the scale height rather than

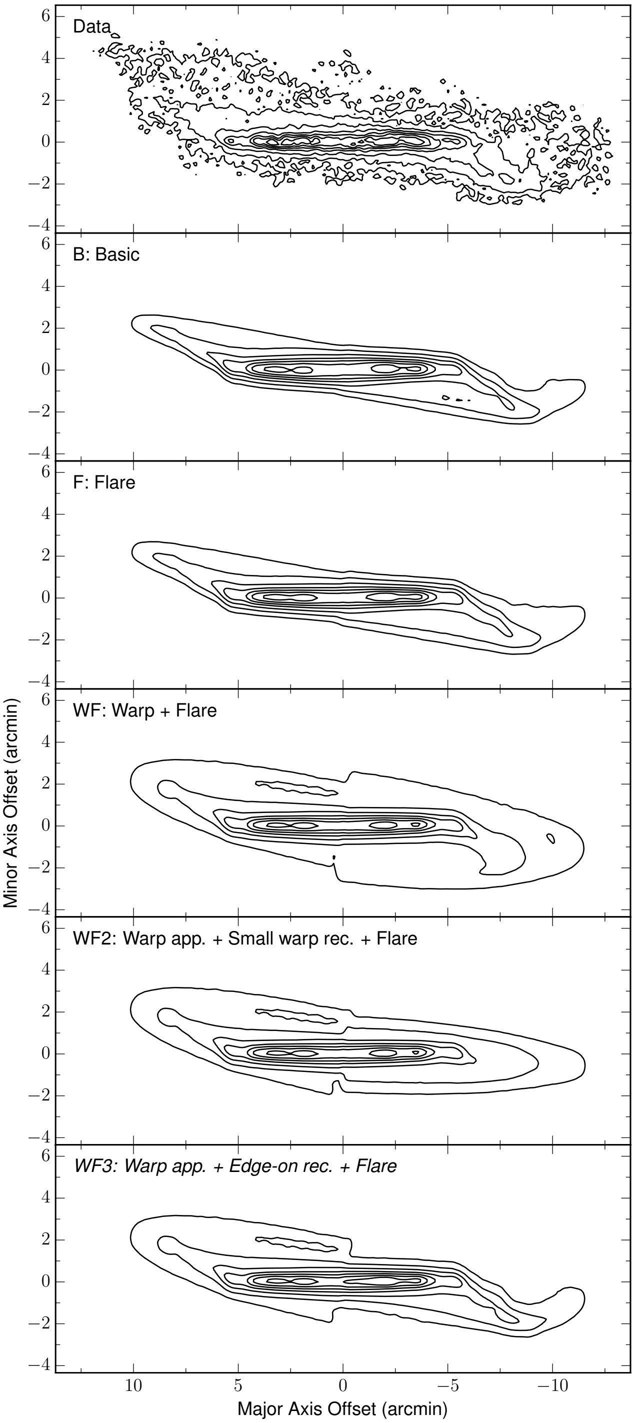

Figure 2.31: Total HI maps of the various models discussed here as compared to the observed total HI map of NGC 5907. The *WF3* model is our best model. Contour levels are the same as in Fig. 2.30.

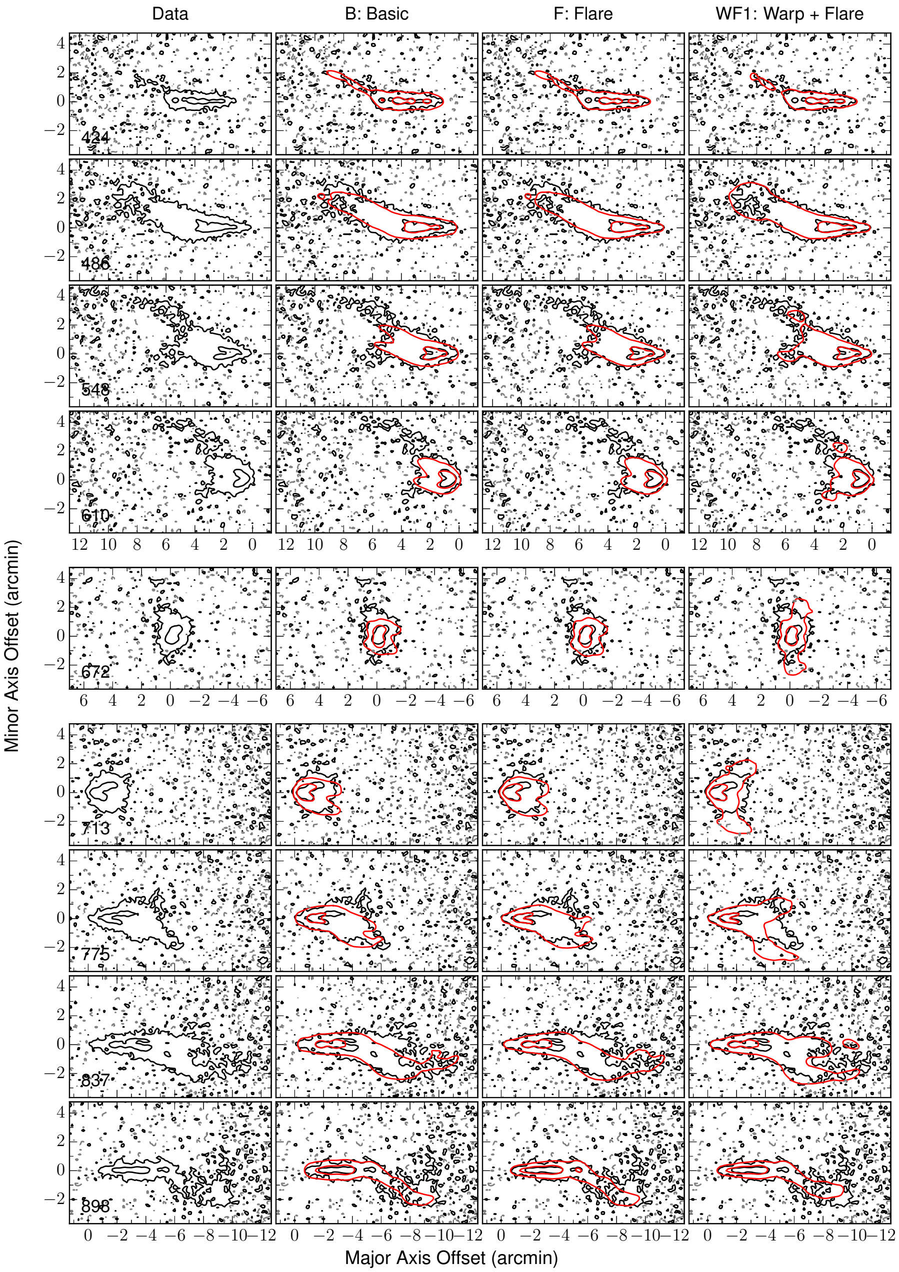

Figure 2.32: Representative channel maps from the observed data cube of NGC 5907 and the various models. Contour levels are -0.5, 0.5 (1.5σ), and 6.4 mJy beam^{-1}. The black contours show the observations with negative contours as dashed grey. The red contours represent the models. The systemic velocity is 664 ± 7 km s^{-1}.

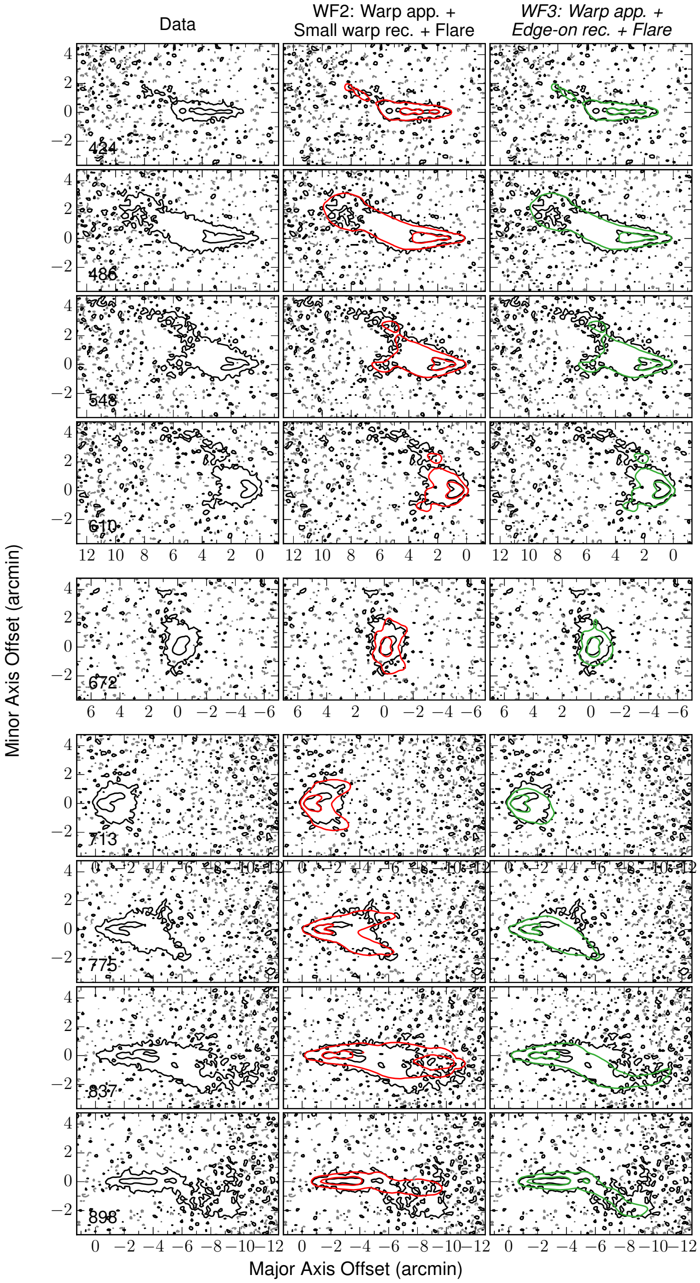

Figure 2.32: continued. The final (*WF3*) models is shown as green contours.

the inclination. We therefore added a flare to the *B* model by lowering the scale height in the central rings. The resulting *F* model has a central scale height of 0.5 kpc out to a radius of 4.2 kpc. It then linearly increases to a maximum value of 1.6 kpc at a radius of 32.7 kpc and stays constant after that. As can be seen in Fig. 2.32, the addition of a flare improves the agreement with the data in the inner regions of the disk.

On the other hand, the *F* model still does not reproduce the forked shape of the observed emission in the outer parts of the disk. This forked shape is present on both the approaching and receding halves, which seem to behave very similarly at first sight. In a first attempt to model this behaviour, we included a strong and abrupt LOS warp in the *F* model. With an inclination of 79° in the outer part of the warp, the *WF1* model broadly matches the forked shape of the observed emission on the approaching half. Indeed, although the model is slightly offset from the data in the very central channels and does not include the faint tail that is observed above (i.e. on the rear side of) the disk, it is able to reproduce the general trend very well. This is not the case on the receding half. If the position of the model matches that of the observed emission in the outer channels and if the inclination is taken to reproduce the opening of the upper arm, the lower arm of the model opens up far too strongly. This is clearly visible in Fig. 2.32, e.g. at 775 km s^{-1}. A smaller LOS warp could resolve this problem, but also requires a change in the position angles in the warp to now avoid underestimating the opening of upper arm. Although this causes a clear offset between the model and the data at terminal velocities (at 898 km s^{-1} in Fig. 2.32), we investigated this option with the *WF2* model. The agreement of this model with the data in the lower arm is still very poor. Indeed, it now underestimates the opening of the data in the outer channels while still opening up a bit too strongly in the central channels. In fact, the only way to match the observed position of the lower arm in all receding channels is with an almost edge-on orientation in the warp. This is demonstrated in Fig. 2.32 by the *WF3* model, with inclinations between 87° and 89° throughout most of the warp and dropping to 81° only in the outer tip of the disk (as shown in Fig. 2.35).

The two arms of the forked emission on the receding side thus seem to behave systematically different and cannot be modelled simultaneously with a simple, axisymmetric model. The lower arm behaves like an edge-on disk while the upper arm opens up and seems to suggest a significantly lower inclination. Unfortunately it is not possible to give a clear interpretation of this feature based on our data. Maybe only the rear side of the receding half has a LOS warp and the front side does not. On the other hand, the upper arm could also be caused by an extraplanar, arc-like feature related to the recent or ongoing interaction. Given the close companion and the stellar tidal streams that have been observed in the optical, it is indeed not unlikely that the gas disk of NGC 5907 is somewhat disturbed. Since further modelling based on our data would degrade into guessing and speculating, we take the *WF3* model as our (preliminary) final model. The much deeper WSRT data that were recently taken by G. Józsa will most probably reveal the full extent of the atomic gas disk of NGC 5907 and provide additional constraints on its

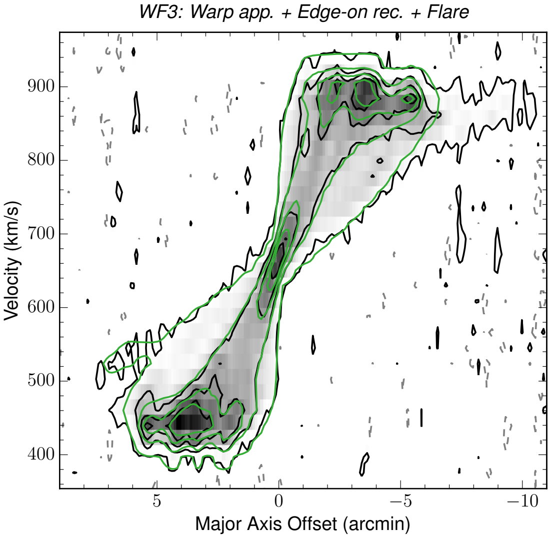

Figure 2.33: Observed major axis position-velocity diagram of NGC 5907 (black and grey contours) overlaid with the final (*WF3*) model (green contours). Contour levels are -0.5, 0.5 (1.5σ), 4.8, 9.6, and 14.4 mJy beam^{-1}. The greyscale corresponds to the observations.

structure.

The variation in the radially dependent parameters of the model is shown in Fig. 2.35. In contrast to the warped outer regions, the inner disk of NGC 5907 appears to be remarkably symmetric. The best fit values of the remaining parameters are listed in Table 2.4. The inclination, position angle, and scale height have errors of 1.0°, 1.5°, and 0.3 kpc, respectively. A full comparison of the final model to the observed data cube is given in Fig. 2.34, and the major axis position-velocity diagrams are compared in Fig. 2.33.

Comparison with Yim et al.

NGC 5907 was also part of the sample of Yim et al. (2014), who studied the vertical structure of the gas and stellar disks of three nearby edge-on galaxies, and used the same VLA data for the Hɪ content of NGC 5907 as we do. They also derived the rotation curve and the radial surface density, inclination and scale height profiles, but used a rather different approach. Instead of building one complete three-dimensional model and matching this to the entire data cube, Yim et al. (2014) derived the various quantities sequentially. The rotation curve was obtained from the major axis XV-diagram using the envelope tracing method (Sofue 1996). The surface density profile was derived from a vertically integrated XV-diagram and assuming a flat rotation curve. Based on these quantities, the inclination and vertical scale height were then derived with the method from Olling (1996). We also note that Yim et al. (2014) only considered the flat part of the disk, out to about 27 kpc

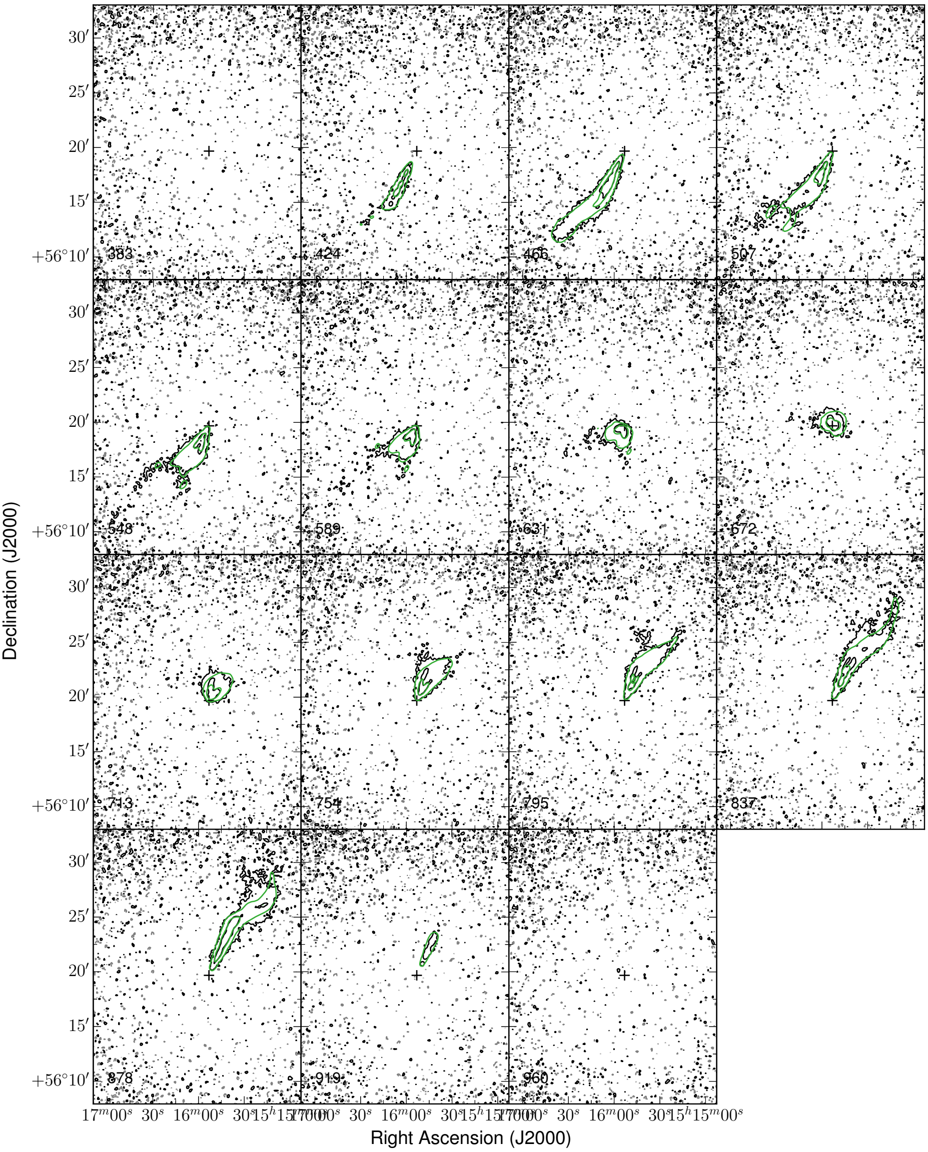

Figure 2.34: Channel maps from the observed data cube of NGC 5907 (black and gray contours) and our final (*WF3*) model (green). Contour levels are -0.6, 0.6 (for better readability we take the lowest contour at 2σ instead of 1.5σ) and 6.4 mJy beam^{-1}. The black cross indicates the centre of the galaxy.

(at our assumed distance), and neglected the warp.

Given these different approaches, we should not expect a perfect agreement between both works. Nonetheless, our results are generally comparable with theirs. Both rotation curves are approximately flat at a value of about 230 km s^{-1}, and both works find an inclination of about 86°. The surface density profiles both show a central depression at $\sim$3 $M_\odot$ pc^{-2}, but our profile peaks at a somewhat lower value ($\sim$6 $M_\odot$ pc^{-2}) than theirs ($\sim$7 $M_\odot$ pc^{-2}). This is perhaps not completely unexpected, since Yim et al. (2014) neglect the warped part of the disk, which also contributes part of the emission in their integrated XV-diagram. Finally, Yim et al. (2014) find a weakly flaring gas disk with a scale height that increases from 0.8 kpc at a radius of about 10 kpc to roughly 1 kpc at a radius of 27 kpc. Our profile is somewhat steeper, with z_0 increasing from $\sim$0.75 kpc to about 1.3 kpc over the same radial range, but the two are consistent within the uncertainty. Note that for the latter comparison we scaled all the values to our assumed distance of 16.3 Mpc, and translated the Gaussian scale heights ($z_0 = 0.42 \times \mathrm{FWHM}$) from Yim et al. (2014) to our assumed sech^2 profile ($z_0 = 0.57 \times \mathrm{FWHM}$).

2.4.7 NGC 4013

The HI content of the HEROES galaxy NGC 4013 was modelled extensively by Zschaechner & Rand (2015), according to the same strategy as followed here. To avoid overlap, we do not include this galaxy in our analysis. In summary, Zschaechner & Rand (2015) find that the gas disk of NGC 4013 has both a substantial edge-on warp and a LOS warp. In addition, the gas disk is flared, with the scale height increasing from 280 pc in the centre to about 1 kpc at radii larger than 7 kpc. Finally they report a lag (decrease in rotational velocity with increasing scale height) that becomes shallower with radius. No extraplanar HI gas is found, despite the presence of extraplanar dust and diffuse ionised gas.

Table 2.4: Radially constant parameters of the final models.

Galaxy	Centre α (J2000)	Centre δ (J2000)	V_{sys} (km s^{-1})	Velocity dispersion (km s^{-1})
NGC 973	$02^h34^m20.1^s \pm 0.4^s$	$+32°30'19.9'' \pm 4.0''$	4770 ± 8	8.2 ± 2.0
UGC 4277	$08^h13^m57.0^s \pm 0.7^s$	$+52°38'53.9'' \pm 5.0''$	5370 ± 6	10.4 ± 3.0
IC 2531	$09^h59^m55.5^s \pm 0.5^s$	$-29°37'02.4'' \pm 4.0''$	2455 ± 6	11.2 ± 1.5
NGC 4217	$12^h15^m51.1^s \pm 0.6^s$	$+49°05'29.4'' \pm 4.0''$	1022 ± 6	19.1 ± 3.0
NGC 5529	$14^h15^m34.0^s \pm 1.0^s$	$+36°13'39.0'' \pm 8.0''$	2830 ± 6	12.3 ± 3.0
NGC 5907	$15^h15^m53.2^s \pm 0.9^s$	$+56°19'42'' \pm 15''$	664 ± 7	13.3 ± 3.0

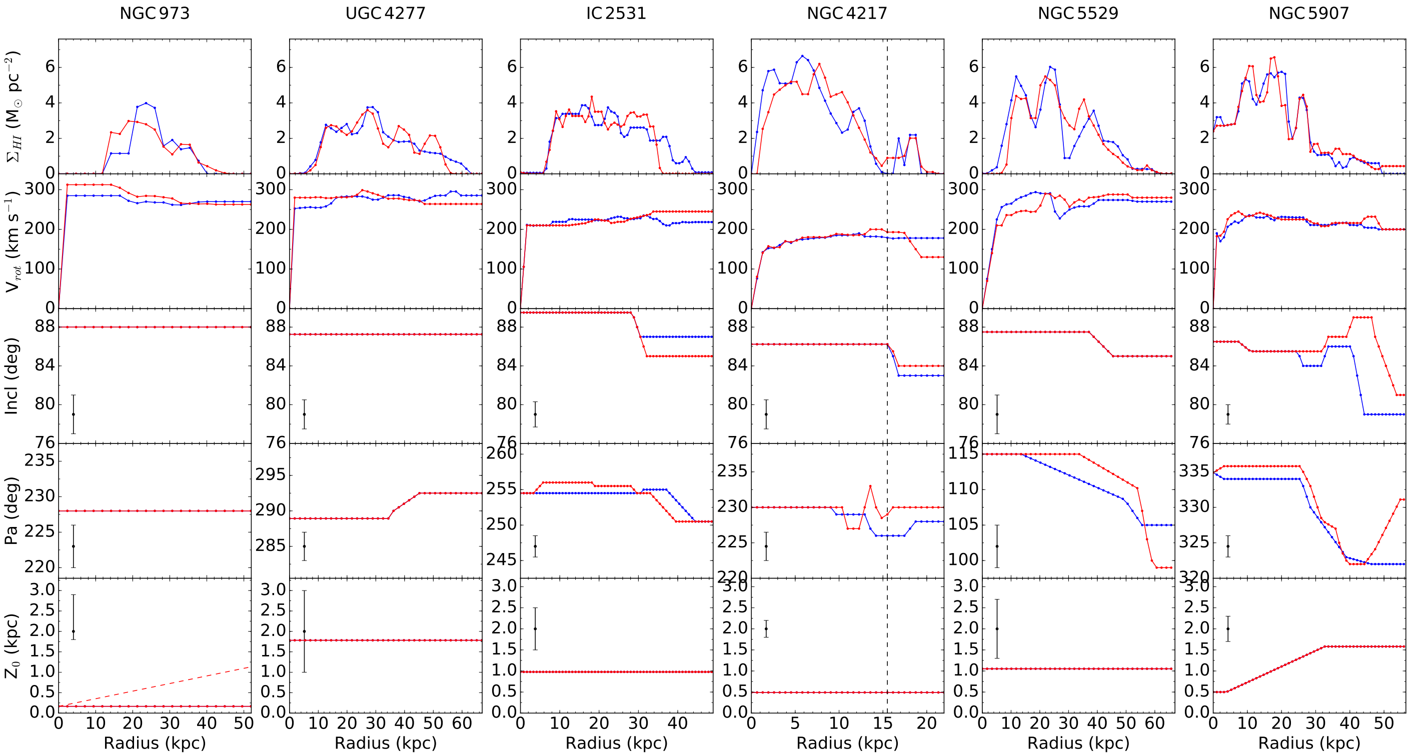

Figure 2.35: Variation in the radially dependent parameters of the final models. From top to bottom: the HI surface density, the rotation velocity, the inclination, the position angle, and the vertical scale height. Blue indicates the approaching side, red the receding side. For NGC 4217, the parameters of the *B+R2* model for the outer ring are also shown. The dashed vertical line shows (approximately) where the main disk meets the outer ring. For NGC 973, the flare from the *F* model (Section 2.5) is shown as the dashed red line. The uncertainties are represented by the error bars.

As discussed in Section 2.4, our final models generally have a constant vertical scale height throughout the entire gas disk. A flaring HI layer is only required for NGC 5907. Theoretically, however, it is expected that all spiral galaxies have a flared atomic gas disk. Indeed, in the inner regions, the gravitational potential is dominated by the stellar disk. If the vertical velocity dispersion of the gas (and hence the internal pressure in the gas disk) is independent of radius, the decreasing surface density of the stars with radius will result in an increasing scale height of the gas (e.g. van der Kruit 1981). Beyond the stellar disk, the gravitational potential is dominated by the dark matter, and the flaring of the gas disk is related directly to the shape of the DM halo (e.g. Olling 1995, 1996; Becquaert & Combes 1997; O'Brien et al. 2010d,b,a,c; Peters et al. 2017d).

We stress that these theoretical expectations are not inconsistent with our models. Indeed, as can be seen in Fig. 2.35, the uncertainties on the scale height are generally significant and, in fact, leave room for a (moderate) flare. We illustrate this point for NGC 973 by replacing the constant scale height of 0.2 kpc in the final (*B*) model with a flare. In the resulting *F* model, the scale height linearly increases from 0.2 kpc in the centre to 1 kpc at a radius of 45 kpc (dashed red line in Fig. 2.35). From Figs. 2.36 and 2.37, it is clear that the *B* and *F* models are very similar. A flaring model is thus still fully consistent with the data and would, in fact, be more realistic from a theoretical point of view. The problem is that the details of the flare are generally ill constrained. Flares with different slopes or shapes would fit the data equally well, and there is no way to tell which is best. For this reason we stick to a constant scale height in our final models, but point out that a flare is probably present within the uncertainties on the (constant) scale height. The

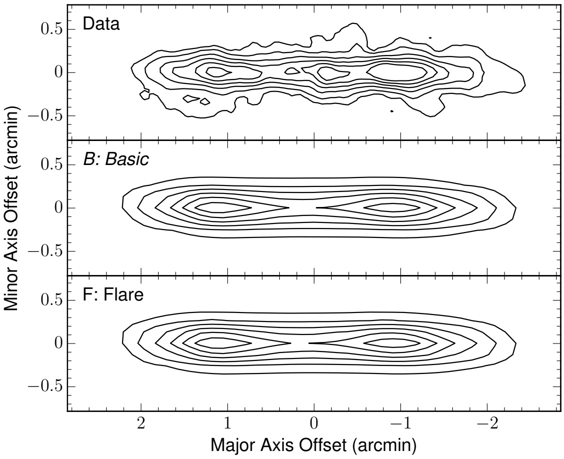

Figure 2.36: Total HI maps of the basic (*B*) and flaring (*F*) models of NGC 973 as compared to the observed total HI map. Contour levels are the same as in Fig. 2.1.

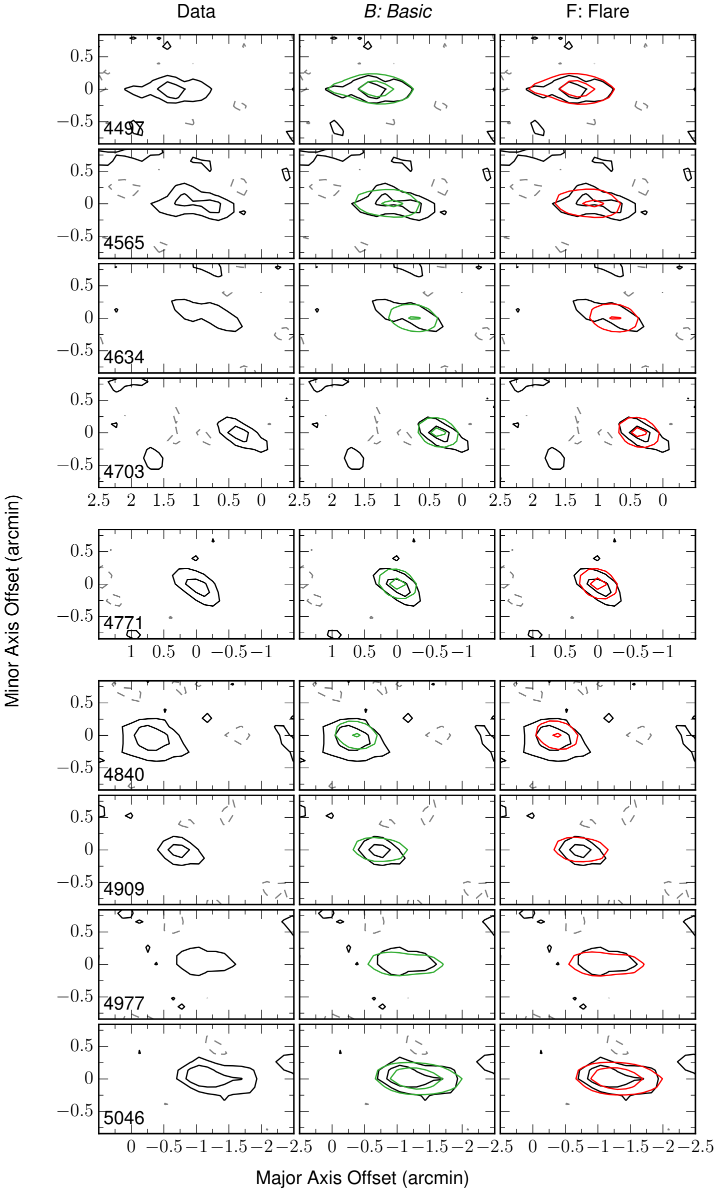

Figure 2.37: Representative channel maps from the observed data cube of NGC 973 (black and grey contours), the basic (*B*) model (green contours), and the flaring (*F*) model (red contours). Contour levels are -2.3, 2.3 (1.5σ), and 6.2 mJy beam^{-1}. The systemic velocity is 4770 ± 8 km s^{-1}.

range of scale heights allowed by our uncertainties is indeed generally of the same order of magnitude as the amplitude of the flares found in other galaxies, such as NGC 4244 (Olling 1996) or the Milky Way (Kalberla & Dedes 2008).

Finally we note that from Sections 2.4.3 and 2.4.4 it might seem like we explicitly investigated the possibility of a flare for IC 2531 and NGC 4217 and discarded it. In fact, this is not entirely true. For both galaxies, only a certain type of flare was tested to model a specific feature in the data cube. In the case of IC 2531, this flare did not significantly improve the model, but was not excluded by the data either. It was simply discarded to reduce the number of free parameters. For NGC 4217, a flare was tested to reproduce the thinning of the emission in certain channel maps. When this was achieved, the resulting model now appeared slightly too thin in other channels and was therefore discarded. It should be noted, however, that the central scale height of this model was only 0.1 kpc, which is far beyond our error bars (0.5 ± 0.2 kpc). A flare within these uncertainties agrees with the data, but does not significantly improve the model (and was therefore not discussed in Section 2.4.4). As a result, the arguments from the previous paragraph are also valid for IC 2531 and NGC 4217. Within our uncertainties on the scale height, a flare can be added to the models without affecting the quality of the fit, but its parameters are ill constrained.

2.6 Impact of the interactions

Figure 2.35 compares the radial variation of the main parameters of the final model for each galaxy. The final parameters that do not vary with radius are listed in Table 2.4, and an overview of the main features of each model is given in Table 2.5. Although there are, of course, differences between the individual galaxies, they all show normal behaviour, and there are no clear outliers in the sample.

As discussed in Section 2.4, the data cubes of NGC 4217, NGC 5529, and NGC 5907 contain a number of morphological and kinematical indications of recent or ongoing interactions with satellite galaxies. From Fig. 2.35 it appears that, apart from the radial inflow in the (outer) disk of NGC 5529, these interactions have not strongly affected the main HI disks of the galaxies in question, and their influence is mostly limited to the position angles and inclinations in the outer regions. Indeed, the radial column density profiles and rotation curves of NGC 4217, NGC 5529, and NGC 5907 do not behave systematically differently than those of the rest of the sample, and there are no strong asymmetries between the approaching and the receding halves. On the other hand, NGC 5529 and NGC 5907 do have a significantly stronger edge-on warp than the other galaxies. For NGC 4217 the edge-on warp has an unusual profile on the receding side, but its amplitude is similar to the warps of UGC 4277 and IC 2531. NGC 5907 also has a stronger LOS warp than the other galaxies, but on the other hand, NGC 4217 shows no LOS warp in its HI disk (only in the outer ring, as represented by the *B+R2* model).

Table 2.5: Main features of the final models

Galaxy	Edge-on warp	LOS warp	Flare	Signs of spiral arms	Signs of interaction
NGC 973	-	-	-	-	-
UGC 4277	✓	-	-	-	-
IC 2531	✓	✓	-	Bright ridge in XV-diagram	-
NGC 4217	✓	-	-	-	Coplanar ring outside main disk
NGC 5529	✓	✓	-	Bright ridge in XV-diagram	HI bridges to companions, extraplanar gas, radial inflow of 15 ± 5 km s^{-1}
NGC 5907	✓	✓	✓	-	Extended reservoir of low-density gas, asymmetric outer disk

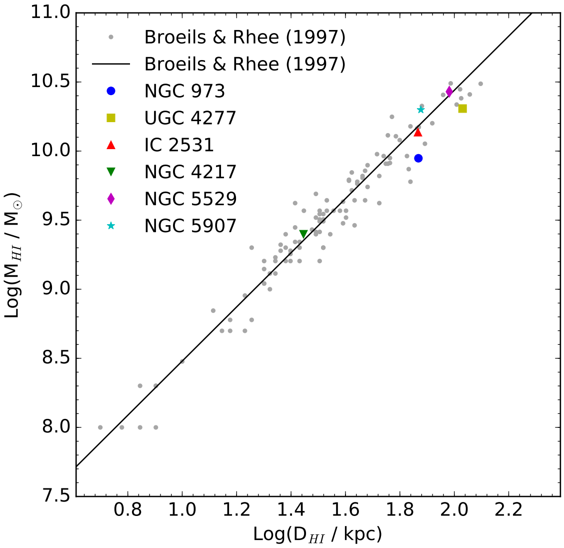

Figure 2.38: Correlation between the total HI mass and the diameter of the HI disk for our sample (coloured symbols) and the sample of Broeils & Rhee (1997) (grey dots, based on their Table 1). The black line shows the best fit linear relation from Broeils & Rhee (1997).

In addition to these arguments, the galaxies in our sample all agree with the HI mass-size relation that was found by Broeils & Rhee (1997). This can be seen in Fig. 2.38 and suggests further that the atomic gas disks of the interacting galaxies have not been strongly disrupted by the interactions. Following Broeils & Rhee (1997), we determined the HI diameter D_{HI} from our final models as the diameter where the HI column density falls below 1 M$_\odot$ pc^{-2}. Since our models cannot adequately reproduce the outer ring of NGC 4217, we excluded this structure and only used the main disk of NGC 4217 to determine the data point in Fig. 2.38. We note that with the inclusion of the outer ring, based on the *B+R2* model, NGC 4217 still agrees with the relation from Broeils & Rhee (1997).

2.7 What about HI self-absorption?

Following standard practice, we have assumed that the HI 21 cm line is optically thin, i.e. that the atomic gas does not absorb its own emission. The observed 21 cm surface brightnesses can then be translated directly into atomic gas column densities. In fact, it has been known for a fairly long time that this assumption does not always hold in the ISM of a galaxy. Observations of the absorption of continuum background emission by clouds of atomic hydrogen in the Milky Way have shown that HI gas can indeed become self-opaque at 21 cm (e.g. Hagen & McClain 1954; Radhakrishnan 1960; Gibson et al. 2005). A detailed study of HI self-opacity was carried out by Braun et al. (2009) and

Braun (2012). They analysed high-resolution HI data cubes of M31, M33, and the LMC and suggested that these galaxies contain a population of dense atomic hydrogen clouds that are self-opaque in the 21 cm line. These structures are compact with typical sizes of the order of 100 pc. Correction factors for the total atomic gas mass of 1.30, 1.36, and 1.33 were found for M31, M33, and the LMC, respectively. However, since self-opacity occurs on such small linear scales, it is very difficult to correct for this effect in a meaningful way in more distant galaxies (observed with lower spatial resolution). Studies of the atomic gas content of galaxies, both for moderately inclined systems and edge-ons, therefore generally assume that the 21 cm line is optically thin.

An important question to ask now is what the consequences of this assumption are in an edge-on galaxy. Since each sight line cuts through the entire plane of the disk, one might expect that self-absorption is strongly enhanced and that only a small fraction of the emitted HI radiation reaches the observer. Fortunately, for self-absorption to be effective, gas clouds must overlap not only in projected position, but also in radial velocity. Owing to the rotation of a galaxy, the latter is generally not the case for all the gas along a line of sight, and the problem is practically reduced to the level of the individual channel maps. In addition, warps in the disk (and in particular LOS warps) spread the emission over different sight lines and will hence further reduce the magnitude of the absorption.

The effect of HI self-absorption in edge-on galaxies was recently (and two years after this work) investigated in the series of papers by Peters et al. (2017a,b,c). They developed a new and publicly available HI modelling tool, GALACTUS[2], that takes into account self-absorption, and applied it to a set of edge-on spiral galaxies. In each channel map, GALACTUS divides every line of sight in a number of segments of at most 100 pc long, and integrates the brightness temperature along the line of sight (from back to front) based on eq. 8.22 from Draine (2011):

$$T_{\mathrm{B,self\text{-}abs}} = T_{\mathrm{bg}} \mathrm{e}^{-\tau_\nu} + T_{\mathrm{spin}} (1 - \mathrm{e}^{-\tau_\nu}), \tag{2.2}$$

where $T_{\mathrm{B,self\text{-}abs}}$ is the accumulated brightness temperature at the i'th segment of the line of sight, T_{bg} is the background temperature (i.e. the integrated brightness temperature from the gas up to the $(i-1)$'th segment), T_{spin} is a constant spin temperature of 100 K, and τ_ν is the optical depth in a certain segment. The use of a constant spin temperature is of course an approximation, since the observed HI emission comes from both the cold neutral medium (CNM, $T \sim 30 - 100$ K) and the warm neutral medium (WNM, $T \sim 6000 - 8000$ K). Peters et al. (2017b) test the validity of this constant spin temperature by making models with the gas randomly divided into warm and cold clouds for different CNM-to-WNM mass fractions. For cold clouds, a spin temperature between 50 and 100 K is randomly assigned, while warm clouds are assigned a random spin temperature between 6000 and 8000 K. It is found that the assumption of a constant spin temperature of 100 K is justified and does not introduce major errors. A downside of the approach from Peters et al. is that they fix the position angle and inclination of the galaxy and therefore

---

[2] The GALACTUS code is available at https://sourceforge.net/projects/galactus/

essentially ignore warps. We refer the reader to the original papers for more details about GALACTUS and the fitting strategy.

In summary, Peters et al. find that self-absorption hides on average about 30% of the total atomic gas mass in edge-on systems. Under the assumption of optically thin emission, the inferred face-on surface brightnesses are too low in the inner regions. On the other hand, the rotation curve is not significantly affected. The disk thickness is slightly overestimated, but the difference (scaled to z_0) is typically only of the order of 0.1 kpc, which is well within our uncertainties. Finally, the velocity dispersion profile is also affected, with the derived values overestimating the true values at some radii and underestimating the true values at other radii. Given this oscillating behaviour of the deviations, the effect will probably be less pronounced in our models that use a constant velocity dispersion.

An additional caveat in the work of Peters et al. (2017a,b,c) is that they assume a smooth gas distribution, while the work of Braun et al. (2009) and Braun (2012) showed that HI disks typically also contain a population of small and dense clumps. Because these are optically thick, an additional fraction of unseen atomic gas is hidden in their interiors. On the other hand, because they are so small, they will not contribute much to the self-absorption of the diffuse gas. As a consequence, dense HI clouds will likely add to the underestimation of the gas column densities, but have little influence on the other inferred galaxy properties.

In conclusion, the recent analysis by Peters et al. (2017a,b,c) suggests that the main consequence of our assumption of optically thin emission is that our models likely underestimate the true face-on surface brightnesses by up to a few ten percent. For the other parameters, the effects are insignificant or lie within the uncertainties of our models.

2.8 Conclusions

In this chapter we conducted a thorough analysis of the atomic gas content of six of the HEROES galaxies. This analysis is based on a combination of new GMRT HI 21-cm observations of NGC 973 and UGC 4277 and re-reduced archival data of IC 2531, NGC 4217, NGC 5529, and NGC 5907. The atomic gas content of the seventh HEROES galaxy, NGC 4013, was studied according to the same strategy by Zschaechner & Rand (2015). For each data cube we constructed a set of three-dimensional tilted-ring models with the aim to constrain the face-on column density distribution, the kinematics and the 3D geometry in an accurate and homogeneous way.

We found that the gas disks of all but one galaxy are not flat, but warped in one or more ways. Based on the kinematics, it was possible to link certain features in the total HI maps of IC 2531 and NGC 5529 to the presence of prominent spiral arms. This has helped to interpret anomalous features that were found in the analysis of the stellar and dust content of IC 2531 in the frame of the third HEROES paper. Furthermore, three galaxies in the sample show signs of recent or ongoing interactions with their environment. A clumpy and coplanar ring of atomic gas was detected just outside the main gas disk of

NGC 4217. This structure has not been reported before and we suggest that it could be the relic of a recent minor merger event. The outer part of the gas disk of NGC 5907 was found to be heavily disrupted, with unusually strong warps and large asymmetries between the approaching and receding sides. This supports earlier claims of a recent interaction based on optical observations. Finally, we identified a radial inflow of gas in the disk of NGC 5529. This is probably linked to the ongoing accretion of gas from two nearby satellite galaxies.

3 The dark matter content of the HEROES galaxies

In the previous chapter we conducted a detailed analysis of the atomic gas content of the HEROES galaxies, deriving the orientation of the disks and the radial distribution and rotational velocities of the gas. In this chapter we investigate what constraints these rotation curves put on the dark matter content of the HEROES systems, in particular on the central shape of the haloes. In section 3.1 we explain the main principle behind rotation curve decompositions. Next, the baryonic contributions to the mass models are described in section 3.2. The details and consequences of the central bars in NGC 5907 and NGC 4013 are explained in section 3.3. Section 3.4 describes the density profile used to model the dark haloes, and the fit strategy is briefly explained in section 3.5. The results of the fits are discussed in section 3.6 and the conclusions are summarised in section 3.7.

3.1 Rotation curve decomposition

In a disk galaxy the inward gravitational force that pulls a particle towards the centre is balanced by the outward centrifugal acceleration from its rotation:

$$a_{\mathrm{cfg}} = a_{\mathrm{grav}}. \tag{3.1}$$

The total gravitational potential acting on this particle is the sum of the potentials from the individual components: gas, stars and dark matter. With each of these individual potentials, we can now associate a hypothetical centrifugal acceleration that is needed to balance just that potential: a_{gas}, a_* and a_{dm}. The total centrifugal acceleration is simply the sum of these:

$$a_{\mathrm{cfg}} = a_{\mathrm{gas}} + a_{*} + a_{\mathrm{dm}}. \tag{3.2}$$

Since the centrifugal acceleration is proportional to the square of the circular velocity, this can be re-written as

$$v_{\mathrm{c}}^2 = v_{\mathrm{gas}}^2 + v_{*}^2 + v_{\mathrm{dm}}^2, \tag{3.3}$$

where v_{gas}, v_{*} and v_{dm} are the circular velocities needed to balance the gravitational force exerted by only the gas, stars or dark matter, respectively. These are of course related to the mass distributions of the individual components. For the stars, however, the conversion between the observed luminosity and the mass is uncertain. The mass-to-light ratio Υ is therefore isolated explicitly as an unknown parameter in equation 3.3. In addition, the distribution of the gas often shows a hole in the centre. Inside this hole, the net gravitational pull from the gas is directed outward, giving a negative contribution to the total circular velocity (e.g. Olling & Merrifield 1998; van Zee & Bryant 1999). A better formulation of equation 3.3 is therefore:

$$v_{\mathrm{c}}^2 = v_{\mathrm{gas}}\,|v_{\mathrm{gas}}| + \Upsilon_{*} v_{*}^2 + v_{\mathrm{dm}}^2, \tag{3.4}$$

or

$$v_{\mathrm{c}}^2 = v_{\mathrm{gas}}\,|v_{\mathrm{gas}}| + \Upsilon_{*,\mathrm{B}}\, v_{*,\mathrm{B}}^2 + \Upsilon_{*,\mathrm{D}}\, v_{*,\mathrm{D}}^2 + v_{\mathrm{dm}}^2 \tag{3.5}$$

if the stellar distribution is decomposed in bulge and disk components. v_{*} is now the circular velocity from the stars for a mass-to-light ratio of 1.

Equations 3.4 and 3.5 form the basis for the mass modelling performed here and in chapter 5. The total circular velocity v_{c} is measured by the rotation curve. The gas and stellar circular velocities v_{gas} and v_{*} are derived from their observed surface brightness profiles, with an exponential or sech^2 profile in the vertical direction. This leaves the stellar mass-to-light ratio(s) and the dark matter contribution as the only unknowns.

3.2 Baryonic contributions

3.2.1 Stars

In the frame of the third and fourth papers in the HEROES series (Mosenkov et al. 2016, Mosenkov et al., in prep.), Dr. A. Mosenkov used `IMFIT`[1] (Erwin 2015) and FitSKIRT (De Geyter et al. 2013, 2014) to determine the three-dimensional distributions of the stars (at 3.6 μm) and the interstellar dust and to study the dust energy balance problem in the HEROES galaxies. Several stellar components (thin disk, thick disk, bulge) were generally identified in a single galaxy and, depending on the case at hand, represented by a single or broken exponential disk (with an exponential profile in the vertical direction as

---

[1] http://www.mpe.mpg.de/~erwin/code/imfit/

well), or a flattened Sérsic bulge. For each of these stellar components, we calculated the associated rotational velocities assuming a mass-to-light ratio of 1. The contributions of the (broken) exponential disk components were determined using the task ROTMOD from the Groningen Image Processing System (or GIPSY[2]). For the flattened Sérsic bulges, we calculated the rotational velocities directly based on Noordermeer (2008). In order to reduce the number of free parameters, we then grouped the stellar components into a single disk and a single bulge, each with one common mass-to-light ratio.

3.2.2 Gas

For the atomic gas, we use the surface density profiles and vertical scale heights from the tilted-ring models that were presented in chapter 2. In addition to the HI, molecular gas can also have an impact on the (central) gravitational potential of massive galaxies like the HEROES systems. For NGC 5907, a fully reduced CO(1-0) data cube was kindly provided to us by Dr. Kijeong Yim, based on interferometric observations with the BIMA and CARMA telescopes (Yim et al. 2014). In section 3.3 we extract the surface density profile of the molecular gas and a higher resolution rotation curve for the inner regions of NGC 5907 from this data cube, by modelling it in a similar way as was done for the HI data. Single dish IRAM 30-m observations of the molecular gas content of NGC 4013 were presented by Gomez de Castro & Garcia-Burillo (1997), but unfortunately these data have gone lost over time (Prof. Dr. A. Gomez de Castro, private communication). Dr. S. Garcia-Burillo did kindly share his interferometric CO line observations of the nuclear region of NGC 4013, but since these only cover the projected central ~40″ (3.6 kpc), we were unable to derive the surface density distribution of the molecular gas. No CO data are available in the literature for the remaining HEROES galaxies.

For these reasons, we include molecular gas in the mass model of NGC 5907 and consider only the atomic gas for the other HEROES galaxies (which is, in fact, standard practice for rotation curve decompositions, e.g. de Blok et al. 2008; Hague & Wilkinson 2014; Katz et al. 2017). The standard Milky Way value of the CO-to-H_2 conversion factor from Bolatto et al. (2013), $\alpha_{\rm CO} = 4.3\ {\rm M}_\odot\ ({\rm K\ km\ s^{-1}\ pc^2})^{-1}$ (or equivalently $X_{\rm CO} = 2 \times 10^{20}\ {\rm cm^{-2}\ (K\ km\ s^{-1})^{-1}}$), is used to convert the observed CO surface brightnesses to molecular gas surface densities, with an additional factor of 1.36 to take into account heavier elements.

3.3 Bars

Optical images of NGC 973, IC 2531, NGC 4013 and NGC 5529 (see e.g. chapter 2) show that these galaxies have a clear box or peanut shaped bulge, indicating the presence of a bar. This is further confirmed by a typical figure-of-eight pattern in the central XV-diagram of NGC 4013 (based on interferometric CO observations, García-Burillo

---

[2] https://www.astro.rug.nl/ gipsy/

et al. 1999), and NGC 5529 (based on optical long-slit spectroscopy, Kregel & van der Kruit 2004). In both these cases, the influence of the bar was found to extend out to $\sim 40'' - 50''$. In addition, Garcia-Burillo et al. (1997) also found a figure-of-eight pattern in their CO-based XV-diagram of NGC 5907, despite its optical appearance as a disk-dominated system. Since these bars can introduce non-circular motions and severely influence the central kinematics of the galaxies, we should take them into account in our mass models.

In chapter 2 we found that the HI disks of NGC 973, IC 2531 and NGC 5529 have a significant hole in their centre. As a consequence, our tilted-ring models only sample the kinematics of these galaxies outside the bar region. For NGC 973, IC 2531 and NGC 5529, we can therefore safely use the rotation curves from chapter 2 in the current analysis. The same argument also holds for UGC 4277, although we find no record of a bar in this galaxy in the literature. The situation is different for NGC 4013 and NGC 5907, where the rotation curves do also sample the bar region.

Spekkens & Sellwood (2007) developed a formalism to model the effect of a bar on the kinematics as a bisymmetric distortion. In this formalism, the observed line-of-sight velocity at a certain position in a flat disk is given by:

$$\begin{aligned} V_{\rm obs}(r) = V_{\rm sys} + \sin(i)\Big[& V_{\rm t}(r)\cos(\theta) - V_{2,\rm t}(r)\cos(2\theta_{\rm b})\cos(\theta) \\ & - V_{2,\rm r}(r)\sin(2\theta_{\rm b})\sin(\theta)\Big]. \end{aligned} \tag{3.6}$$

In this expression, $V_{\rm sys}$ is the systemic velocity of the galaxy, i is the inclination angle and $V_{\rm t}(r)$ is the tangential (or rotational) velocity at radius r. The angle θ is the azimuthal angle in the plane of the disk, measured counterclockwise with respect to the projected major axis of the galaxy on the receding half of the disk. Similarly, the angle $\theta_{\rm b}$ is the azimuthal angle with respect to the major axis of the bar, i.e.:

$$\theta_{\rm b} = \theta - \phi_{\rm b}, \tag{3.7}$$

where $\phi_{\rm b}$ is the azimuthal angle of the bar major axis. $V_{2,\rm t}(r)$ and $V_{2,\rm r}(r)$ are the amplitudes of the tangential and radial 2$^{\rm nd}$ order harmonic distortions.

This formalism has been implemented in the software package `DiskFit`[3] (Spekkens & Sellwood 2007; Sellwood & Sánchez 2010), which takes an observed velocity field as input and can be used to to recover the orientation of the bar, the amplitude of the distortions and the true rotation curve of the galaxy. `DiskFit` works well for moderately inclined galaxies, where the velocity field is well sampled and the orientation and extent of the distortion are visible. For edge-on galaxies, however, this is not the case. Due to the strong line-of-sight projection, velocity fields of edge-ons offer only few data points and are, in fact, not very meaningful. Consequently, an attempt to model the CO velocity field of NGC 5907 with `DiskFit` produced highly unphysical results, with distortions of the order of 150 km s^{-1} and unphysical jumps with a magnitude of 200 km s^{-1} between

---

[3] http://www.physics.rutgers.edu/~spekkens/diskfit/

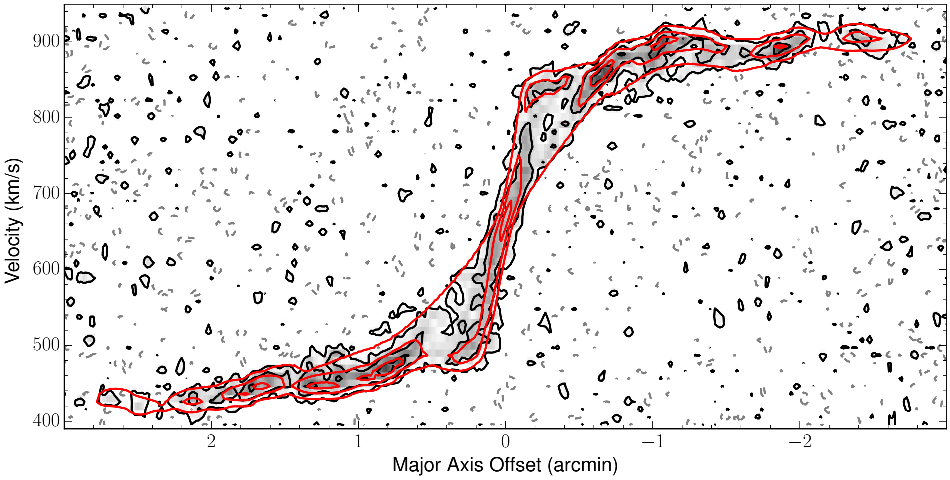

Figure 3.1: Observed major axis position-velocity diagram of the molecular gas in NGC 5907 (black and grey contours) overlaid with our initial model (red contours, see text). The rms noise in the cube is 16 mJy beam^{-1} and the contours levels are -1.5, 1.5, 5 and 10 times the noise. The greyscale corresponds to the observations.

adjacent radii.

TiRiFiC also offers the possibility to include bisymmetric distortions in a model disk using a formalism that is very similar to the one from Spekkens & Sellwood (2007). Even with this approach, however, the problem at hand is too degenerate to find good constraints on the properties of the bar or the true rotational velocities in the centre of the galaxy. We illustrate this for NGC 5907, based on the interferometric CO(1-0) data cube from Yim et al. (2014). Taking the central position, the systemic velocity and the inclination and position angles of the inner disk from our HI modelling, and the vertical scale height from Yim et al. (2014), we first constructed an initial model that includes only circular motions. The major axis position-velocity diagram of this model is compared to the data in Figure 3.1. Additionally, the central part of the XV-diagram is shown more clearly in Fig. 3.2. While the initial model agrees well with the observed XV-diagram in most of the disk, it clearly fails to reproduce the high-density contours and underestimates the width of the low-density contour in the central ±0.2′ of the XV-diagram. This disagreement in the central kinematics is also visible to some extent in the central part of the first moment map (Fig. 3.3), where the S-shape of the central contour and the asymmetry of the contour at 700 km s^{-1} are not well reproduced by the model.

The situation is already improved by adding a very simplistic bisymmetric distortion, with a bar angle $\phi_b = 120°$ and constant amplitudes of $V_{2,t} = 50$ km s^{-1} and $V_{2,r} = 30$ km s^{-1} out to a radius of 2.4 kpc (30″). This model requires corrections to the rotational velocities of the order of −35 km s^{-1} (with respect to the values from the initial model) and is shown in the middle panels of Figures 3.2 and 3.3. However, a different distortion,

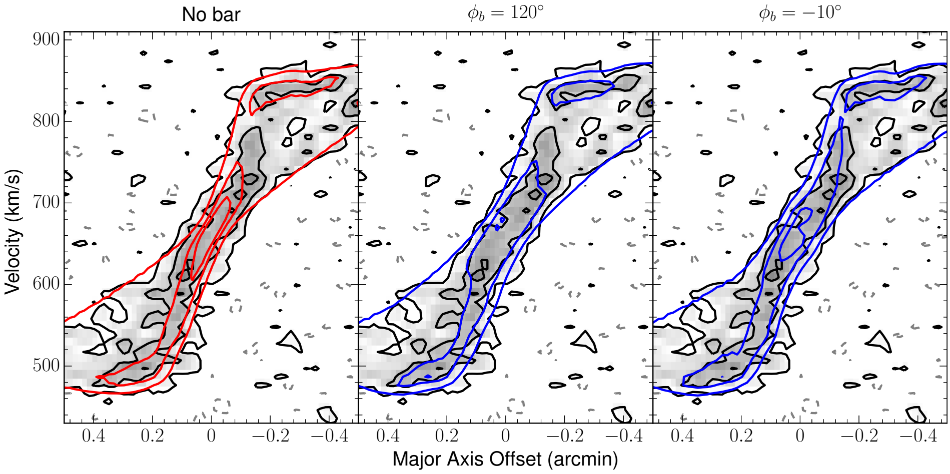

Figure 3.2: Central part of the observed major axis position-velocity diagram of NGC 5907 (black and grey contours) overlaid with our initial model (red contours) and two models with different bisymmetric distortions (blue contours) to represent the bar potential. The rms noise in the cube is 16 mJy beam^{-1} and the contours levels are -1.5, 1.5, 5 and 8 times the noise. The greyscale corresponds to the observations.

with $\phi_b = -10°$, $V_{2,t} = 30$ km s^{-1} and $V_{2,r} = 40$ km s^{-1} also improves the quality of the fit (right/bottom panels of Figs. 3.2 and 3.3), but requires corrections to the rotation curve of $\sim +45$ km s^{-1}. Other models, with e.g. $V_{2,t} = 30$ km s^{-1}, $V_{2,r} = 40$ km s^{-1} and $\phi_b = 135°$ or $150°$ also produce similar results with only small corrections to the initial rotation curve. While it is clear that none of these simplistic models fully captures the effects of the bar, this brief analysis already shows that the problem at hand is too degenerate to get firm constraints on the bar or the correct central rotation curve. Moreover, in reality, the amplitudes of the distortions are not constant with radius and can sometimes vary substantially, making the problem even more complex. We therefore do not attempt to correct the initial rotation curves of NGC 5907 and NGC 4013, but add an uncertainty of 50 km s^{-1} in the bar region.

3.4 The (α, β, γ) halo

Fitting mass models to the rotation curves of galaxies is generally not a problem with a unique solution, especially for more massive galaxies where the central gravitational potential is dominated by the stars. Ideally, one should therefore start from a physically motivated model for the dark matter halo that already limits the range of solutions. The available parameter space can be narrowed down even further by requiring that the solutions are in agreement with cosmological scaling relations such as the halo mass-concentration relation (e.g. Macciò et al. 2008; Dutton & Macciò 2014) and the stellar mass-halo mass

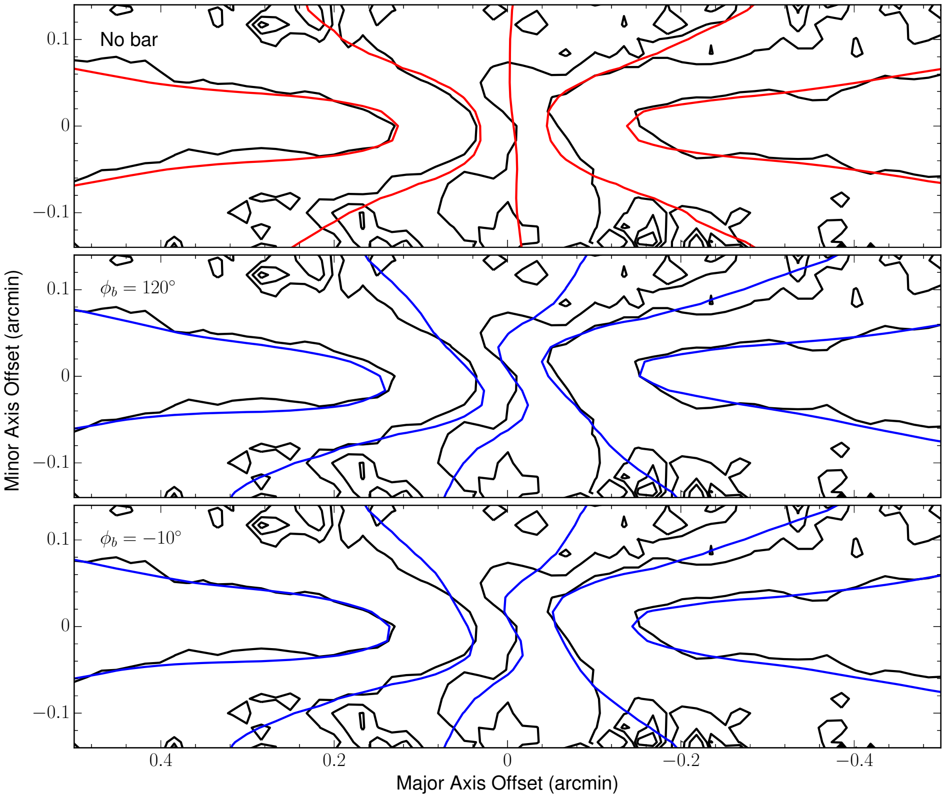

Figure 3.3: Central part of the observed first moment map of the molecular gas in NGC 5907 (black contours) overlaid with our initial model (red contours) and two models with different bisymmetric distortions (blue contours) to represent the bar potential. The contours levels are, from left to right, 570, 640, 670, 700 and 770 km s^{-1}. These maps are useful to compare different models, but do not have much physical meaning due to the strong line-of-sight projection.

relation (e.g. Conroy & Wechsler 2009; Moster et al. 2010; Behroozi et al. 2013). This strategy is used in chapter 5, where we compare two physically motivated dark matter halo models on a sample of dwarf galaxy rotation curves. These models both start from a cuspy NFW halo and include baryonic processes, in particular stellar feedback induced outflows of gas, that can transform the primordial central cusps into shallower cores. Although they were derived for complementary mass ranges ($10^7 < M_{\rm halo}/M_\odot < 10^9$ for the coreNFW model and $10^{10} < M_{\rm halo}/M_\odot < 8 \times 10^{11}$ for the DC14 halo), the combined range of these models is still limited to sub-Milky Way sized systems. At higher masses, mechanisms like AGN feedback, that are not included in the cNFW and DC14 models, start playing a role as well. For the massive spiral galaxies in the HEROES sample, we can therefore not use these physically motivated dark matter halo models.

One option would then be to resort to other pre-defined halo shapes that have been used in the past, such as the pseudo-isothermal halo (e.g. van Albada et al. 1985; Broeils 1992), the Burkert halo (Burkert 1995), the NFW halo (Navarro et al. 1996b), the Einasto halo (Einasto 1965; Merritt et al. 2006), etc. However, the cored models in this series have essentially no physical motivation, while the cuspy haloes derived from dark matter only simulations have proven to be incomplete due to the lack of baryonic physics. Rather than forcing the data in a limited and somewhat arbitrary set of artificial shapes, we aim to investigate what range of dark matter density profiles are consistent with the rotation curves.

We therefore opted to use the more general (α,β,γ) halo (Jaffe 1983; Hernquist 1990; Zhao 1996). Hague & Wilkinson (2013, 2014, 2015) have recently also used this profile to study the dark matter haloes of M33 and a sample of THINGS galaxies. In its standard form, the (α,β,γ) profile is given by:

$$\rho(r) = \frac{\rho_{\rm s}}{\left(\frac{r}{r_{\rm s}}\right)^{\gamma}\left[1+\left(\frac{r}{r_{\rm s}}\right)^{1/\alpha}\right]^{(\beta-\gamma)\alpha}}, \tag{3.8}$$

where γ and β give the power-law slope of the profile at small and large radii, respectively, and α marks the sharpness of the transition between these two regimes. $r_{\rm s}$ and $\rho_{\rm s}$ are the usual scale radius and density. The NFW and pseudo-isothermal haloes are simply special cases of this profile, with $(\alpha,\beta,\gamma) = (1,3,1)$ and $(\alpha,\beta,\gamma) = (1/2,2,0)$, respectively.

Given the strong degeneracy between $r_{\rm s}$ and $\rho_{\rm s}$, and the fact that $\rho_{\rm s}$ does not have a very clear physical interpretation, we replace this parameter by $V_{\rm vir}$ (the circular velocity associated to the dark matter potential at the virial radius of the halo). This is also more in line with the parametrisation that we will use for the DC14 halo (chapter 5), which is in fact a restricted case of the (α,β,γ) halo. We could then also define a concentration parameter as:

$$c = r_{\rm vir}/r_{\rm s}, \tag{3.9}$$

but since our general profile does not have a fixed, pre-defined shape, it is hard to interpret and compare this concentration for different haloes. We therefore stick with $r_{\rm s}$ as the fifth parameter.

As mentioned in Hague & Wilkinson (2013), the enclosed mass at a radius r of an (α,β,γ) halo is given by:

$$M(r) = \frac{4\pi\rho_{\rm s}r^3}{3-\gamma}\left(\frac{r_{\rm s}}{r}\right)^{\gamma} {}_2F_1(a,b,c,z), \tag{3.10}$$

where ${}_2F_1(a,b,c,z)$ is the Gaussian hypergeometric function and $a = \alpha(\beta-\gamma)$, $b = \alpha(3-\gamma)$, $c = 1+\alpha(3-\gamma)$ and $z = -(r/r_{\rm s})^{1/\alpha}$. From the fit parameter $V_{\rm vir}$ and the assumed cosmology, we can determine the associated virial mass $M_{\rm vir}$ and virial radius $r_{\rm vir}$. The original scale density parameter can then be recovered by filling in the virial mass and radius in eq. 3.10 and solving for $\rho_{\rm s}$.

3.5.1 `emcee`

The dynamical models were fitted to the rotation curves with `emcee`[4] (Foreman-Mackey et al. 2013), an open-source python implementation of the affine invariant Markov Chain Monte Carlo (MCMC) ensemble sampler from Goodman & Weare (2010). MCMC (e.g. Metropolis et al. 1953; Hastings 1970; Press et al. 2007) is a sampling technique that has been applied to the decomposition of rotation curves for several years (e.g. Puglielli et al. 2010; Hague & Wilkinson 2013). It is more efficient in sampling the parameter space than the fitting techniques used in earlier works and has the big advantage that it returns the full multi-dimensional probability distribution of all the parameters instead of only the best fit model. In addition, MCMC allows to include physical knowledge about the parameters in the fits via so-called priors that are combined with the likelihood function. A more elaborate discussion of the MCMC technique can be found in appendix A.

`emcee` explores the N-dimensional parameter space with different, randomly initialised 'walkers' that each make their own MCMC chain. An initial burn-in phase is used to allow the walkers to move to the relevant high-likelihood areas of the parameter space. After this, the walkers are reinitialised at their current positions and the actual MCMC chains are made. As a last step, the chains of all the walkers are combined to form the final MCMC chain. For every fit we used 500 walkers, each taking 2000 steps, of which the first 1000 were used as burn-in. These numbers are in line with the `emcee` recommendations (Foreman-Mackey et al. 2013) and with the values typically used in other works (e.g. Kirichenko et al. 2015; Katz et al. 2017; Read et al. 2017), and ensured good convergence of our fits (see below). Our likelihood function is

$$\mathcal{L} = e^{-\chi^2/2}. \tag{3.11}$$

For a multimodal posterior distribution, part of the walkers can get stuck in isolated low probability modes if they are initialised randomly over the full range of the parameter space (within the imposed boundaries). This generates numerous irrelevant peaks in the retrieved posterior distribution. We therefore performed each fit in two iterations. First the walkers were initialised randomly over the full relevant range of parameter space. The different peaks in the posterior distribution were then investigated to find the relevant mode with the highest likelihood. Next, as a second iteration, we redid the fit with the walkers now initialised in a small Gaussian ball centred on this mode and with standard deviation equal to 1 percent of the allowed range for each parameter. The parameter values that are used in the figures below and reported in Table 3.1 correspond to the maximum likelihood model for each fit.

For good performance, an MCMC sampler should be run for at least a few (about 10) au-

---

[4] http://dan.iel.fm/emcee/current/

tocorrelation times and should have an acceptance fraction between 0.2 and 0.5 (Foreman-Mackey et al. 2013). With 1000 steps taken by each walker, the first condition was well met for all the fits. Appropriately setting `emcee`'s proposal scale parameter to a value of 2 or 3 ensured that the second condition was also met. Finally we checked the convergence of the MCMC chains by performing each fit three times and evaluating the Gelman-Rubin eigenvalues (for more information, see section A.5) with the `GetDist`[5] python package. These values were well below 1 for all the fits, indicating good convergence.

3.5.2 Parameter ranges

The fits were performed with a total of 7 free parameters: α, β, γ, r_s and V_{vir} for the dark matter halo, and two stellar mass-to-light ratios, Υ_{disk} and $\Upsilon_{\mathrm{bulge}}$. Flat priors were used for all these parameters. Following Hague & Wilkinson (2013), we set $0.1 < \alpha < 2.5$, $3 < \beta < 5$ and $0 < \gamma < 2$. The virial velocity and scale radius were further constrained inside $10 < V_{\mathrm{vir}}/(\mathrm{km\ s^{-1}}) < 500$ and $0 < r_s/r_{\mathrm{outer}} < 2$, where r_{outer} is the outer point of the rotation curve. Finally, the 3.6 μm mass-to-light ratios were generally limited to the physically motivated range $0.3 < \Upsilon_{\mathrm{disk/bulge}} < 0.8$ (Meidt et al. 2014; McGaugh & Schombert 2014). For NGC 973, however, the 3.6 μm luminosity of the bulge as reported by Mosenkov et al. (in prep) seems overestimated. Indeed, even with $\Upsilon_{\mathrm{bulge}} = 0.3$, the bulge velocity curve already reaches a very large maximum of 450 km s^{-1}. For this one galaxy, we therefore used $0.01 < \Upsilon_{\mathrm{bulge}} < 0.8$.

A Planck cosmology with $h = 0.6774$, $\Delta = 102.356$ and $\rho_{\mathrm{crit}} = 127.351\, M_{\odot}\,\mathrm{kpc}^{-3}$ (Planck Collaboration et al. 2016) was assumed here, and the stellar mass-halo mass relation from Behroozi et al. (2013) was imposed as a log-normal prior. A halo mass-concentration prior could not be used in the current case, because the (α,β,γ) profile does not have a primordial halo as physical starting point. Although a concentration parameter could in principle be defined as in eq. 3.9, we can therefore not translate this concentration back to the concentration of a primordial pure dark matter halo. As such, imposing a mass-concentration relation would be meaningless.

3.5.3 Uncertainties

Using the `GetDist` package, the uncertainties for the different parameters were determined from the multi-dimensional 68% confidence region of the full posterior distribution, as the extremal values of the projection of that region onto each parameter axis. As such the error bars give a good indication of how tight the constraints are for a certain parameter, but they should not be over-interpreted as the absolute range of good models. Indeed, if the fit quality of the best-fit model is very high, models outside of the N-dimensional 68% confidence region often still provide an acceptable fit to the data. On the other hand, if we plot, for example, the halo mass versus the stellar mass, the area suggested by the two (orthogonal) error bars is often larger than the actual area to which the

---

[5] https://pypi.python.org/pypi/GetDist/

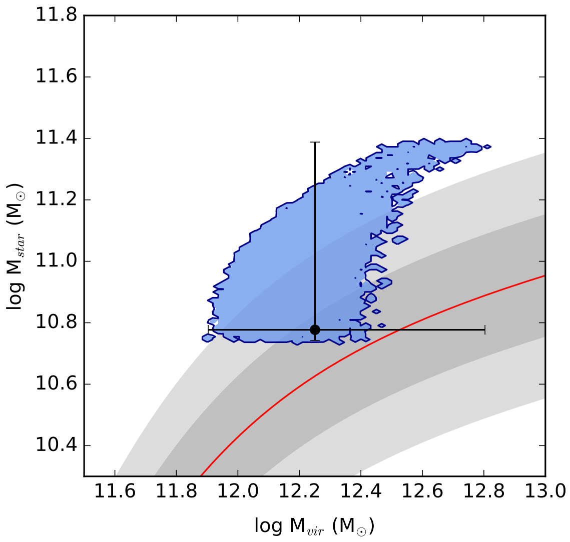

Figure 3.4: Stellar and halo mass of the best fit model of NGC 973. The projected 68% confidence region, shown as the blue shaded area, is significantly smaller than the area suggested by the two error bars. Also shown in the plot is the theoretical $M_{\rm halo} - M_*$ relation from Behroozi et al. (2013) (red line) and its 1σ and 2σ scatter (dark and light grey bands).

models from the MCMC chain are confined (i.e. the projection of the multi-dimensional confidence region onto the $M_{\rm halo}$-M_* plane). This is illustrated in Figure 3.4 for the best fit model of NGC 973.

3.6 Results

The parameters of the best-fit models from the MCMC chains are listed with their uncertainties in Table 3.1. The decomposition of the rotation curves according to these models is shown in Figure 3.5. An excellent fit is obtained for each galaxy. This is, of course, not surprising, given the flexible halo model that was used and the fact that the central kinematics of the galaxies, which are typically the most constraining and difficult to model, are generally not sampled by our rotation curves. Figure 3.6 further shows that the derived dark matter haloes are also in good agreement with the stellar mass-halo mass relation.

One of the main goals of constructing dynamical models of galaxy rotation curves (in the ΛCDM framework) is typically to investigate how the cold dark matter is distributed in the central regions of galaxies and whether this agrees with the expectations from cosmological simulations. In Figure 3.7 we plot the distribution of the log slopes of the dark matter density from the MCMC chains as a function of radius. As can be seen,

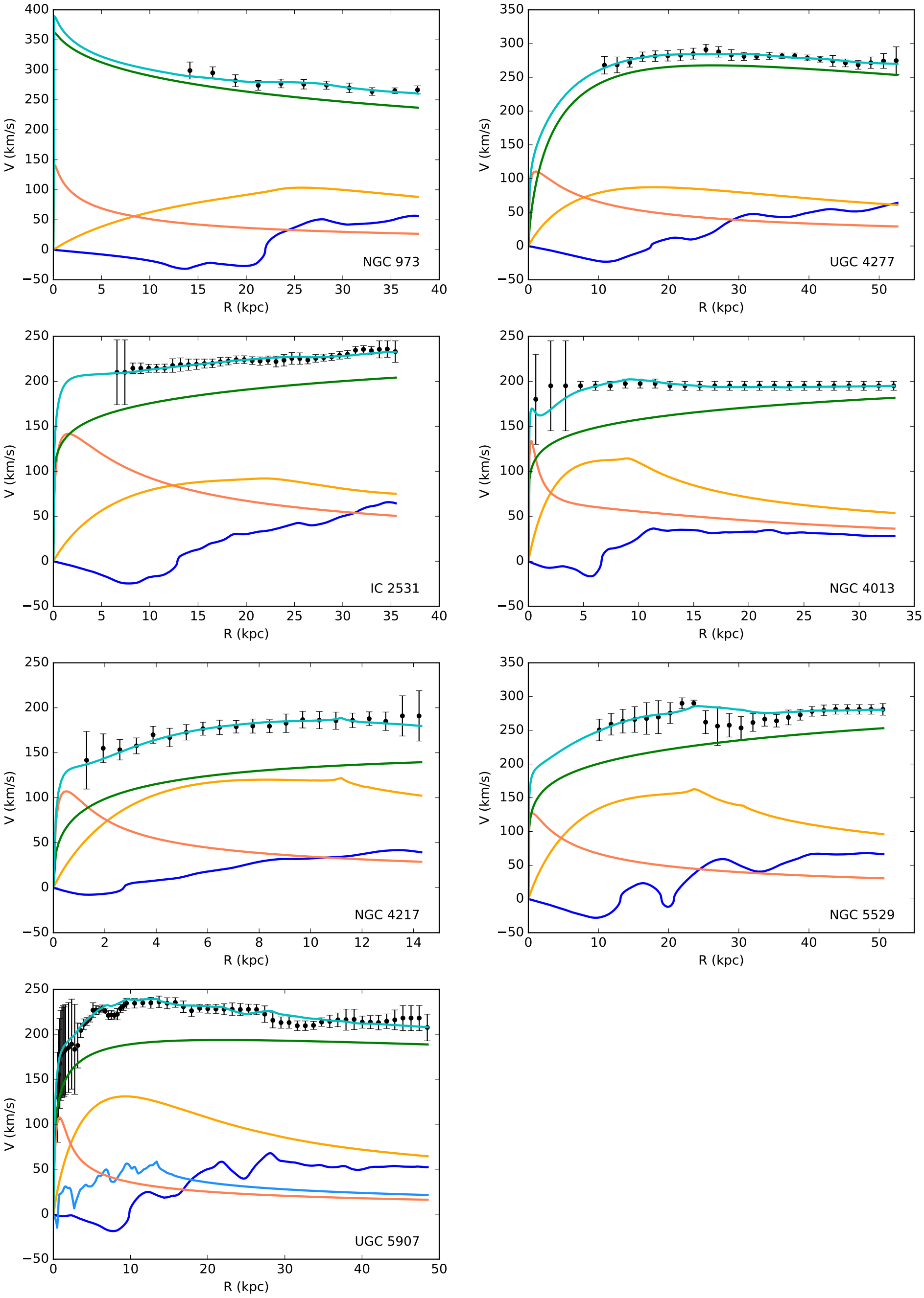

Figure 3.5: Decomposition of the rotation curves according to the maximum likelihood models. The black points show the observed rotation curves and the cyan curves represent the models. The contributions from the individual components are given by the blue (atomic gas), orange (stellar bulge and disk) and green (dark matter) curves. The lighter blue curve for NGC 5907 shows the contribution of the molecular gas.

Table 3.1: Parameters and uncertainties of the maximum likelihood models from the MCMC chains.

Galaxy	α	β	γ	r_s (kpc)	$\log_{10}(M_{\rm vir})$ $(M_\odot)$	$\log_{10}(M_*)$ $(M_\odot)$
NGC 973	$2.41^{+0.09}_{-2.29}$	$3.25^{+1.75}_{-0.25}$	$1.94^{+0.06}_{-1.93}$	$61.4^{+14.2}_{-59.8}$	$12.17^{+0.55}_{-0.35}$	$10.78^{+0.61}_{-0.03}$
UGC 4277	$1.67^{+0.83}_{-1.57}$	$4.78^{+0.22}_{-1.78}$	$0.39^{+1.55}_{-0.39}$	$31.6^{+73.3}_{-28.0}$	$12.19^{+0.48}_{-0.22}$	$10.70^{+0.40}_{-0.01}$
IC 2531	$0.18^{+2.32}_{-0.08}$	$3.02^{+1.97}_{-0.02}$	$1.75^{+0.17}_{-1.74}$	$66.6^{+4.4}_{-59.9}$	$12.35^{+0.25}_{-0.58}$	$10.78^{+0.16}_{-0.13}$
NGC 4013	$0.14^{+2.36}_{-0.04}$	$3.30^{+1.70}_{-0.30}$	$1.73^{+0.12}_{-1.73}$	$53.4^{+13.0}_{-48.5}$	$12.09^{+0.69}_{-0.46}$	$10.51^{+0.27}_{-0.08}$
NGC 4217	$2.00^{+0.50}_{-1.90}$	$3.02^{+1.57}_{-0.02}$	$1.20^{+0.63}_{-1.20}$	$27.5^{+1.1}_{-25.1}$	$11.97^{+0.42}_{-0.4}$	$10.52^{+0.2}_{-0.02}$
NGC 5529	$0.24^{+2.26}_{-0.14}$	$3.03^{+1.96}_{-0.03}$	$1.71^{+0.2}_{-1.71}$	$101.1^{+0.1}_{-93.4}$	$12.71^{+0.71}_{-0.56}$	$11.05^{+0.25}_{-0.17}$
NGC 5907	$2.13^{+0.37}_{-2.03}$	$3.04^{+1.85}_{-0.04}$	$1.54^{+0.38}_{-0.95}$	$65.7^{+30.1}_{-55.5}$	$12.24^{+0.15}_{-0.47}$	$10.68^{+0.21}_{-0.01}$

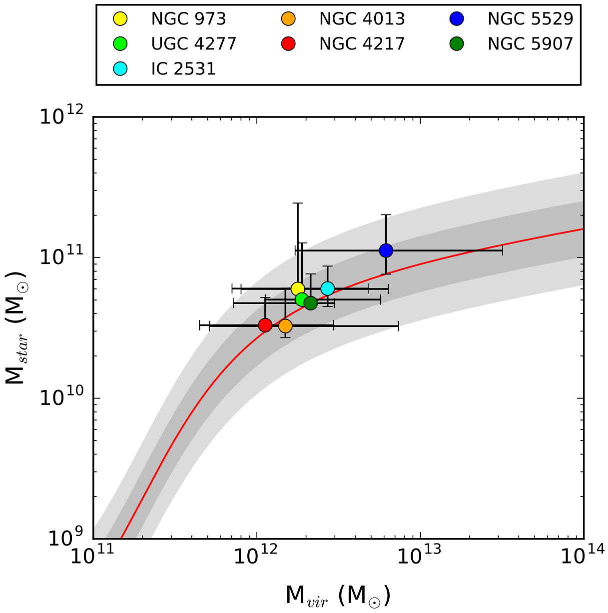

Figure 3.6: Comparison of our mass models to the stellar mass-halo mass relation from Behroozi et al. (2013). The theoretical relation is shown as the red line and its 1σ and 2σ scatter is represented by dark and light grey bands, respectively.

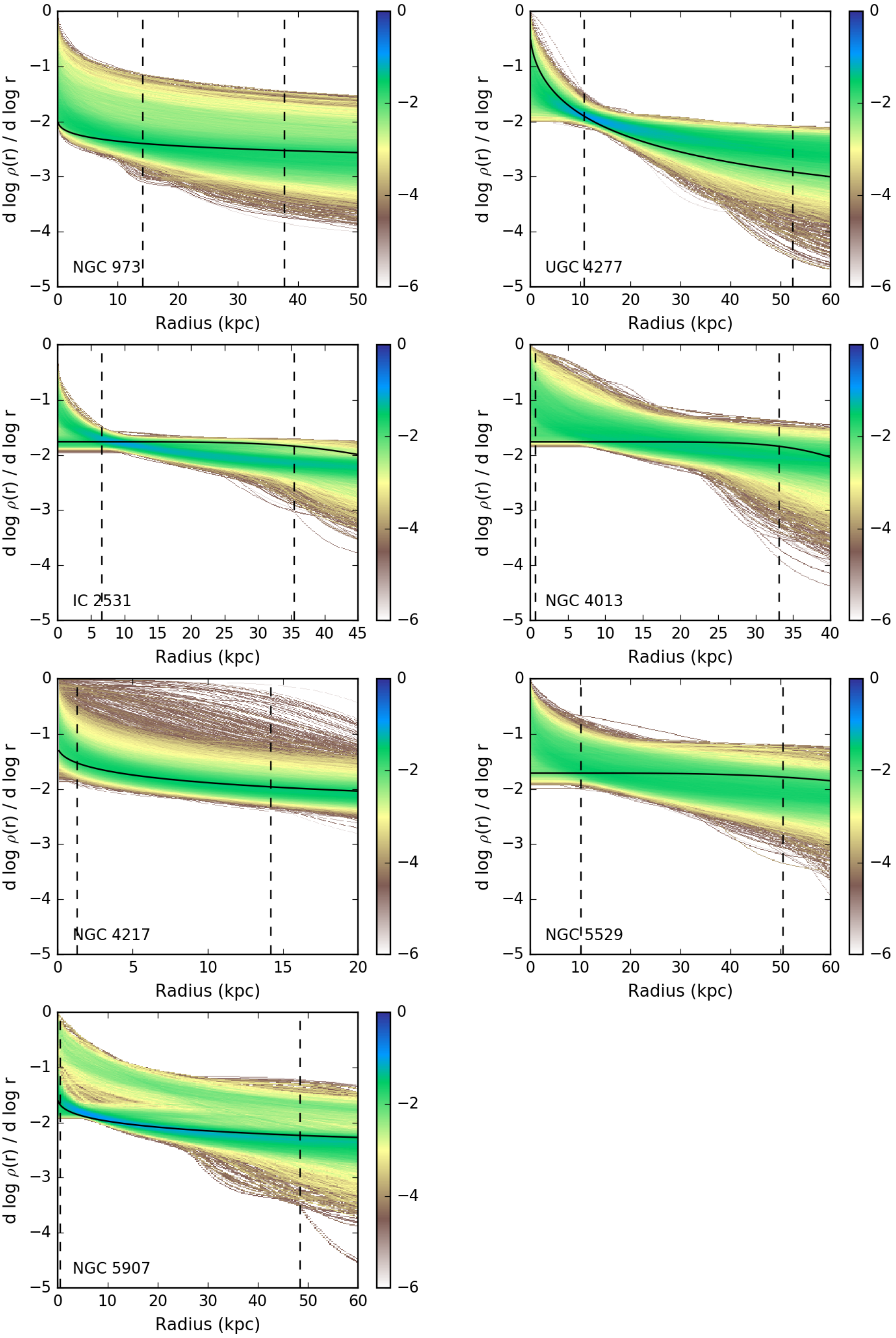

Figure 3.7: Distribution of the log slope of the dark matter density profile from the MCMC chains as a function of radius. At each radius, the colour scale represents the density of models relative to the total number of models in the chain, in log scale. The solid line shows the best fit model. The vertical dashed lines show the radial range of the rotation curve.

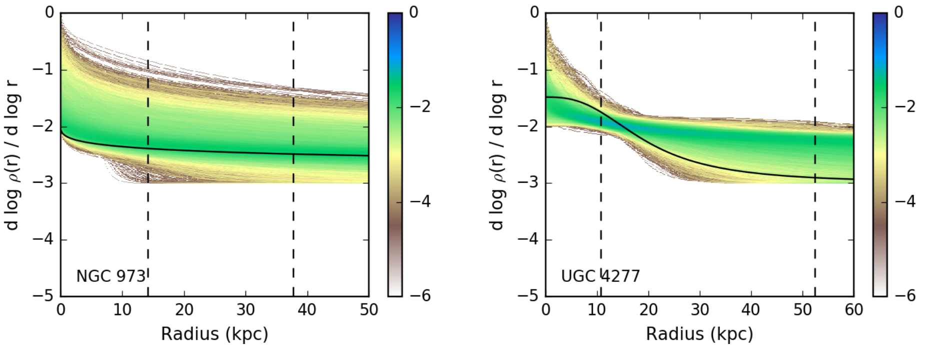

Figure 3.8: Distribution of the log slopes of the dark matter density of NGC 973 and UGC 4277 as a function of radius, with β fixed to 3. Colours and lines are as in Figure 3.7.

our limited rotation curves do not offer any constraints in this area. For each galaxy, the distribution of the central slopes covers essentially the entire range from cored haloes with γ close to zero, to strongly cuspy haloes with central slopes as high as 2. Even inside the radial ranges probed by the rotation curves, the data provide essentially no constraints on the slope of the dark matter density profiles. Since the baryonic physics associated to galaxy formation and evolution is not expected to have a strong influence on the outskirts of a dark matter halo, one way to improve this situation could be to fix β to 3, the outer slope expected from cosmological dark matter only simulations. Unfortunately, this does not offer much improvement. This is illustrated for NGC 973 and UGC 4277 in Figure 3.8, where we show the distribution of the log slopes for a fit with $\beta = 3$. The shape of the dark matter haloes remains essentially unconstrained. This result is in line with the analysis of de Blok et al. (2001a), who showed in their Figure 3 that, for typical parameter values, cored pseudo-isothermal haloes and cuspy NFW and Moore (Moore et al. 1999b) haloes have similar log slopes in the radial range $\sim 1 - 10$ kpc. As a consequence, they found that rotation curves whose innermost data point falls in this range have trouble distinguishing between cored and cuspy dark matter haloes. From Figure 3.7, it is clear that the innermost data points of our rotation curves of the HEROES galaxies also fall in this region (if we take into account the large uncertainties in the inner parts of NGC 5907 and NGC 4013). High-resolution interferometric CO or optical IFU observations, tracing the central kinematics for all the galaxies, might offer a solution, but the central bars would probably still introduce substantial uncertainties. We therefore leave this analysis as it is.

3.7 Conclusions

Based on the rotation curves and atomic gas surface density profiles from our analysis in chapter 2, we have constructed mass models of the HEROES galaxies in an attempt to gain insights in the shape of their dark matter haloes. The stellar distributions were taken from the third and fourth HEROES papers and molecular gas was included for NGC 5907 based on literature data. The central kinematics of NGC 5907 and NGC 4013, probed to some extent by our rotation curves, are affected by a bar. However, due to the edge-on orientation of these galaxies, it is not possible to correct for the bar potential in a unique way. We therefore added a large uncertainty of 50 km s^{-1} to the affected points of the rotation curves. The dark matter haloes were modelled with a general (α, β, γ) profile and the models were fitted to the rotation curves using MCMC.

Good fits to the rotation curves were found for all the galaxies and the resulting haloes are in agreement with the cosmological stellar mass-halo mass relation. Unfortunately, our HI based rotation curves generally do not probe the central regions of the galaxies. As a consequence, our models are not able to constrain the shape of the dark matter haloes, even when some of the freedom is removed by fixing the outer slope of the profile to the value expected from cosmological simulations.

4

Cold gas and dust in the FRIEDL galaxies

In this chapter we investigate the cold gas and dust content of a sample of dust lane early type galaxies (ETGs) in the frame of the FRIEDL project. Such galaxies are generally considered to be the remnants of very recent minor mergers, and their cold ISM was most probably accreted from the merging satellite. As such, dust lane ETGs are good laboratories to study minor mergers and their gas-to-dust ratios can provide some information about the progenitors. To date, there are, however, only few studies that accurately constrain both the atomic and molecular gas, and the dust content of these systems.

In section 4.1 we give a brief overview of the FRIEDL sample. Our single-dish observations of the molecular gas content of several FRIEDL galaxies are described in section 4.2, and section 4.3 gives a description of our single-dish and interferometric follow-up observations of the HI content. The Herschel observations of the FRIEDL galaxies are briefly described in section 4.4. In section 4.5 we investigate the unusually low gas-to-dust ratio found for NGC 5485, and the main conclusions of this chapter are presented in section 4.6. Parts of sections 4.4 and 4.5 were published as Baes et al. (2014).

4.1 The FRIEDL sample

The FRIEDL project targets 11 nearby lenticular galaxies with clear dust lanes. These were selected from the combined samples of Patil et al. (2007) and Finkelman et al. (2008), who conducted multi-colour optical observations and presented a structural analysis of a large set of dust lane ETGs. As for the HEROES project, one of the original goals of FRIEDL was to model the dust content of the galaxies self-consistently using radiative transfer models. Therefore, only the galaxies with a single, well-defined and

Table 4.1: Overview of the FRIEDL sample

Galaxy	RA (J2000)	Dec (J2000)	D (Mpc)	z
NGC 2534	08:12:54	+55:40:19	50.2	0.011807
NGC 2907	09:31:37	−16:44:05	28.2	0.006788
NGC 3283*	10:31:12	−46:15:05	37.8	0.009637
NGC 3497	11:07:18	−19:28:18	55.3	0.012248
NGC 3665	11:24:44	+38:45:46	33.1	0.006900
NGC 4370	12:24:55	+07:26:42	35.9	0.002595
NGC 5485	14:07:11	+55:00:06	25.2	0.006366
NGC 5525	14:15:39	+14:16:57	75.2	0.018487
NGC 5626*	14:29:49	−29:44:54	94.2	0.022859
NGC 5799*	15:05:35	−72:25:58	33.1	0.010337
NGC 5866	15:06:30	+55:45:48	14.9	0.002565

Notes. * Not treated in this chapter.

regular dust lane were retained from this combined sample. An overview of the complete FRIEDL sample is given in Table 4.1. All the FRIEDL galaxies have been observed with the PACS and SPIRE instruments of the Herschel space telescope at 100, 160, 250, 350 and 500 μm to study their dust content. Observations of the atomic and molecular gas were only available in the literature for a few galaxies. We have conducted new observations to fill in these gaps, but due to the northern location of the telescopes that were used, the southern FRIEDL galaxies (NGC 3283, NGC 5626 and NGC 5799) could not be included. Therefore, only the 8 northern and equatorial galaxies are treated in this chapter. The distances in Table 4.1 were assigned according to the strategy from the ATLAS^{3D} project. For NGC 3665, NGC 5485 and NGC 5866 we take over the distances from Cappellari et al. (2011a). For the remaining galaxies, we use the median of the redshift-independent distances reported by NED (if available), or the distance derived from the heliocentric radial velocity considering the influence of the Virgo Cluster according to Mould et al. (2000). Redshifts are generally taken from the SDSS. If no SDSS value is available, we use values based on optical spectroscopy from NED (de Vaucouleurs et al. 1991; Fairall et al. 1992).

4.2 Molecular gas

4.2.1 IRAM 30-m observations and data reduction

The molecular gas content was previously only studied for 4 of the FRIEDL galaxies. For NGC 3665 and NGC 5866, ^{12}CO was clearly detected in the J=1-0 and J=2-1 lines by

Young et al. (2011) and Alatalo et al. (2013). For NGC 2534 (Wiklind et al. 1995) and NGC 5485 (Young et al. 2011) no CO was detected and upper limits for the molecular gas mass were derived from the spectra.

We therefore used the IRAM 30-meter single-dish telescope, located in the Sierra Nevada mountains in Spain, to look for molecular gas in the remaining northern and equatorial FRIEDL systems. We also re-observed NGC 5485, which seems to contain very little gas (see section 4.5), with the aim of measuring its molecular gas mass or obtaining a tighter upper limit than the one that was found by Young et al. (2011). The observations were carried out on June 26 and 27, 2014. We simultaneously observed the CO(1-0) and (2-1) lines and used a single pointing towards the centre of each galaxy. The consequences of using only one pointing per galaxy are discussed in section 4.2.4. We used the E090 and E230 bands of the EMIR receiver in Wobbler switching mode, with a wobbler throw of $\pm 110''$ in azimuth, in combination with the WILMA backend. For each EMIR band, this gave a total bandwidth of 4 GHz and a channel spacing of 2 MHz. The latter corresponds to a velocity resolution of 5.2 km s^{-1} for the (1-0) line and 2.6 km s^{-1} for the (2-1) line. The 30 meter wide dish of the IRAM telescope gives a beam FWHM of $21.34''$ at 115 GHz (J=1-0) and $10.67''$ at 230 GHz (J=2-1).

The focus of the telescope was evaluated and corrected at the start of each observing session (by observing Venus) and after sunset (using Mars). The pointing of the telescope was checked every two hours and when the target source was changed, by observing a nearby quasar. The observations of the FRIEDL galaxies were conducted as sets of 6 minute on-off scans and the total time on source (TOS) ranged from 17.1 to 74.1 minutes (see Table 4.2). Unfortunately, due to unfavourable weather conditions, the pointing of the telescope was rather uncertain during the observations of NGC 3497 and NGC 5485. As a consequence, our data for these two galaxies might be unreliable. We still include NGC 3497 and NGC 5485 in Table 4.2, but note that the derived fluxes should be treated with caution.

For the reduction of the data, we made use of the CLASS[1] package that is part of the GILDAS[2] software. For each galaxy, we investigated the individual 6 minute scans for signs of interference or baseline ripples. If RFI was found, the affected channels were flagged, or, in bad cases, the entire scan was discarded. Baseline ripples were removed from the data based on the Fourier transform of the affected spectra. Next, the individual scans were averaged for each polarization (horizontal and vertical) and the baseline was subtracted by fitting a first order polynomial to the line free regions of each spectrum. The spectra for the different polarizations were then averaged together. Subsequently, we converted the antenna temperatures T_A^* to main beam temperatures $T_{\rm mb}$ as:

$$T_{\rm mb} = T_A^* \times F_{\rm eff} / B_{\rm eff}, \tag{4.1}$$

where $F_{\rm eff}$ is the forward efficiency and $B_{\rm eff}$ is the main beam efficiency of the telescope.

---

[1] https://www.iram.fr/IRAMFR/GILDAS/doc/html/class-html/class.html

[2] http://www.iram.fr/IRAMFR/GILDAS/

From the IRAM website[3] we find that this gives a conversion factor of 0.83 for the (1-0) line and 0.64 for the (2-1) line. Finally, the spectra were boxcar smoothed and rebinned to a resolution of $\sim$ 31 km s^{-1}.

4.2.2 The spectra

The final spectra for both CO transitions are shown in Figure 4.1. The (1-0) and (2-1) lines are clearly detected for NGC 4370 and their widths are consistent (see also Table 4.2). For NGC 5525 we also detect both lines, although the noise is already significant at 230 GHz. The (1-0) line is rather wide, with a total width of 730 km s^{-1}, and symmetric around the expected systemic velocity of the galaxy (5442 km s^{-1}). The (2-1) line, on the other hand, seems significantly narrower and extends further on the low velocity side, although it does still peak at the systemic velocity. Due to the smaller beam area at higher frequencies, it is in fact not abnormal that the CO(2-1) line is narrower than the CO(1-0) line in IRAM 30-m observations. However, since the (2-1) line in this case seems asymmetric around the systemic velocity, while the (1-0) line is symmetric, and since both lines do have a similar width on the low velocity side, the discrepancy is probably caused by a negative noise peak in the high velocity wing of the (2-1) line.

For NGC 2907, NGC 3497 and NGC 5485 no lines are detected.

4.2.3 Line intensities and H$_2$ masses

If a line was clearly detected, we measured the total intensity by summing the fluxes of all the channels in the line region (and multiplying by the channel width). The uncertainty associated with such a summation is given by (Sage et al. 2007; Young et al. 2011):

$$\sigma^2 = \sigma_{\rm rms}^2 \, (\Delta v)^2 \, N_{\rm l} \left(1 + \frac{N_{\rm l}}{N_{\rm b}}\right), \tag{4.2}$$

where $\sigma_{\rm rms}$ is the rms noise in the spectrum, Δv is the channel width, $N_{\rm l}$ is the number of channels in the line region and $N_{\rm b}$ is the number of channels that were used to fit the baseline. The last part of the above expression takes into account the uncertainty on the subtracted baseline.

If no line was evident in the spectrum, we assumed a general line width of 300 km s^{-1} (following Young et al. 2011) and determined the 3σ upper limit for the total intensity as three times the uncertainty given by equation 4.2 (but see also section 4.2.4).

The molecular gas masses were determined from the integrated intensities of the (1-0) line, since the associated beam covers a larger part of the galaxy than the CO(2-1) beam.

---

[3] http://www.iram.es/IRAMES/mainWiki/Iram30mEfficiencies

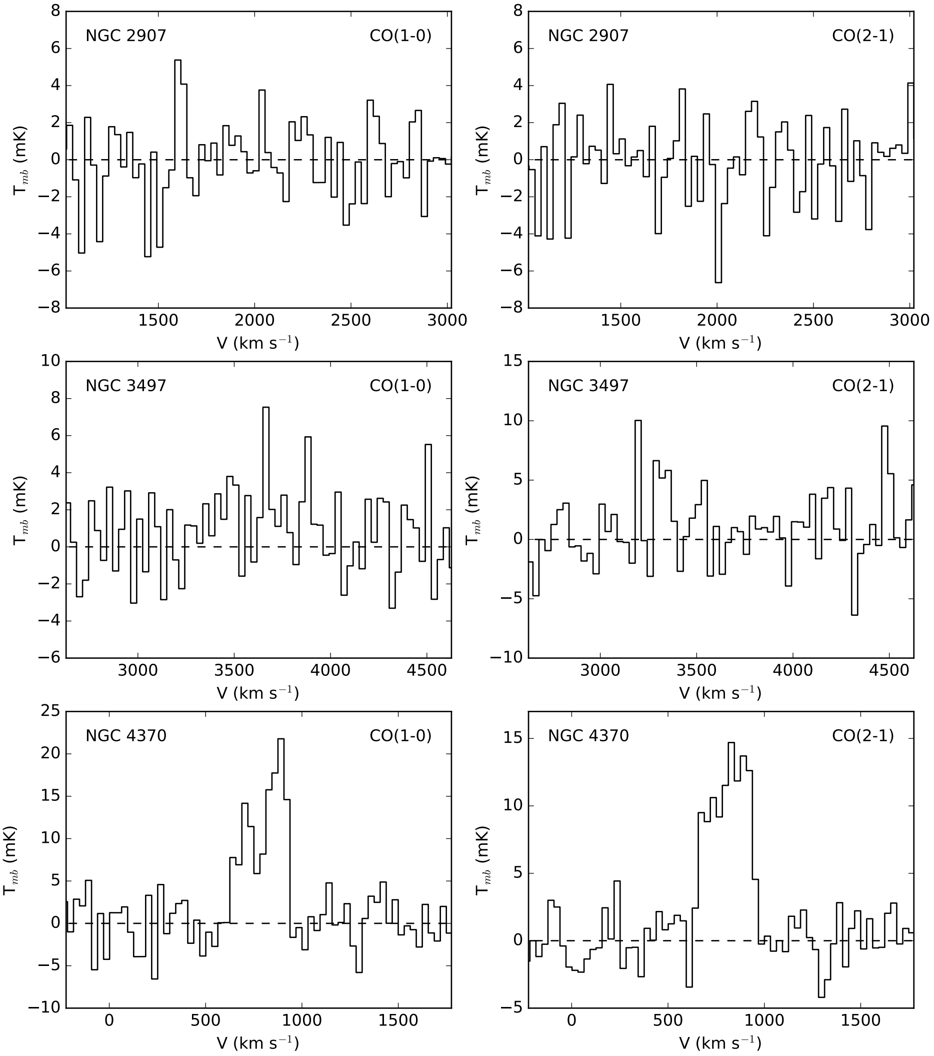

Figure 4.1: CO(1-0) and CO(2-1) spectra obtained from our IRAM 30-m observations. The velocities on the horizontal axis are barycentric radio velocities. The vertical axis shows the main beam temperature. The spectra are boxcar smoothed and binned to a resolution of 31 km s^{-1}. The dashed horizontal line shows the zero line.

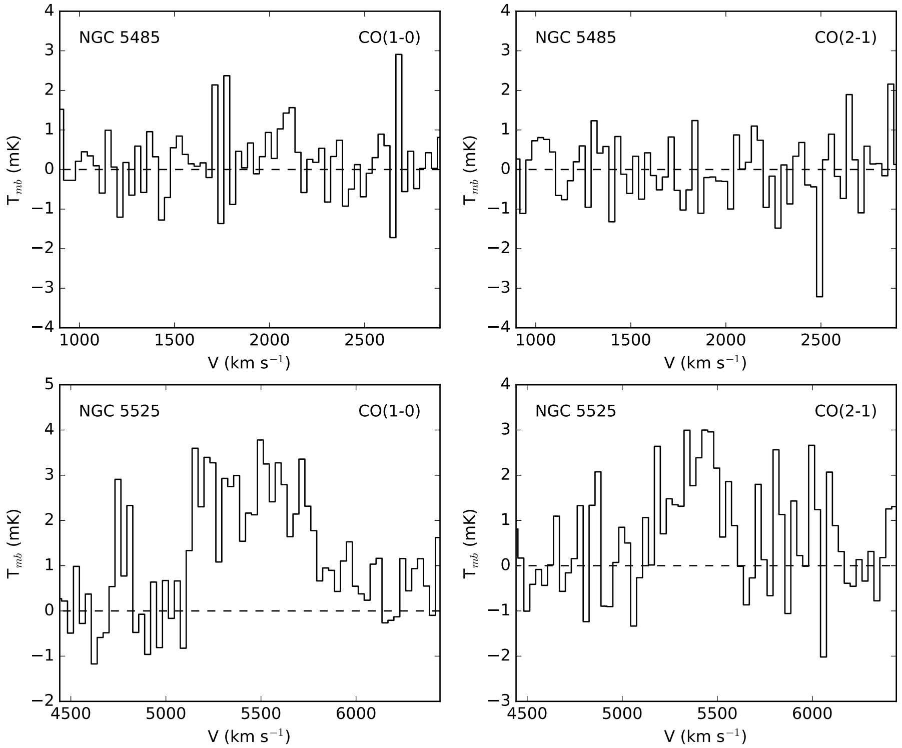

Figure 4.1: continued.

For this purpose we use equation 3 from Bolatto et al. (2013):

$$\frac{M_{\rm mol}}{M_{\odot}} = 5.25 \times 10^{-17} \left(\frac{1}{1+z}\right) \left(\frac{X_{\rm CO}}{{\rm cm}^{-2}\ ({\rm K\ km\ s})^{-1}}\right) \left(\frac{D}{\rm Mpc}\right)^{2} \left(\frac{I_{1-0}}{{\rm Jy\ km\ s}^{-1}}\right), \tag{4.3}$$

where z is the redshift, $X_{\rm CO}$ is the CO-to-H$_2$ conversion factor, D is the distance, and I_{1-0} is the integrated intensity expressed in Jy km s^{-1}. Note that equation 4.3 already includes a correction factor of 1.36 to account for the contribution of helium and heavier elements. By combining the Rayleigh-Jeans law:

$$\frac{S_{\nu}}{1.133\,\Theta^{2}_{\rm FWHM}(rad)} = 2\,k_{\rm B}\,\frac{\nu^{2}}{c^{2}}\,T_{\rm mb} \tag{4.4}$$

with the approximation for the beam FWHM of the IRAM telescope[4]:

$$\Theta_{\mathrm{FWHM}}('') \approx \frac{2460}{\nu(\mathrm{GHz})}, \tag{4.5}$$

we find that the conversion from (main beam) brightness temperatures (in K) to fluxes (in Jy) is given by

$$S_\nu(\mathrm{Jy}) = 4.9513\, T_{\mathrm{mb}}(K). \tag{4.6}$$

For consistency with the ATLAS$^{\mathrm{3D}}$ project, we assume a conversion factor of $X_{\mathrm{CO}} = 3 \times 10^{20}$ cm^{-2} (K km s^{-1})$^{-1}$. The line widths, total intensities and molecular gas masses are summarised in Table 4.2.

4.2.4 Consequences of using a single pointing

As mentioned above, our 30-m observations are limited to a single pointing towards the centre of each galaxy. This strategy offered the best compromise between a reasonable sample size on the one hand and limited observing time on the other hand. The downside of this approach is that the data only cover the central 22″ of each galaxy for the (1-0) line and 11″ for the (2-1) line. With optical diameters (D_{25}) ranging from 85″ to 154″ (de Vaucouleurs et al. 1991), it is clear that this corresponds to only the very central regions of each galaxy. On the other hand, the molecular gas in a galaxy is typically very centrally concentrated. Indeed, Davis et al. (2013) found that the extent of the molecular gas in the ATLAS$^{\mathrm{3D}}$ early type galaxies is typically only of the order of 10 percent of D_{25}, with a maximum of 40 percent. Alatalo et al. (2013) further compared their interferometric CO(1-0) fluxes to the single dish fluxes from Young et al. (2011) that were also obtained from single pointing observations with the IRAM 30-m telescope. They found that the interferometric fluxes are higher, as expected, but with a maximum difference of only a factor of 2.3. Moreover, the galaxies with discrepancies of this order typically had optical diameters of the order of 300″, which is significantly larger than the FRIEDL galaxies.

From these considerations we conclude that our IRAM data probably miss some fraction of the molecular gas content of the galaxies. The integrated intensities reported in Table 4.2 should therefore be treated as lower limits, although they probably only underestimate the true values by up to a few ten percent. For the non-detections in our sample, we take the limited beam size into account by adding an additional factor of 2 to the upper limits in Table 4.2. In this way these values can really be interpreted as upper limits.

---

[4] http://www.iram.es/IRAMES/telescope/telescopeSummary/telescope_summary.html

Table 4.2: Summary of the IRAM 30-m observations

Galaxy	TOS (min)	rms_{1-0} (mK)	rms_{2-1} (mK)	Δv_{1-0} (km s^{-1})	Δv_{2-1} (km s^{-1})	I_{1-0} (K km s^{-1})	I_{2-1} (K km s^{-1})	M_{mol} (10^7 $\mathrm{M}_\odot$)
NGC 2907	42.8	1.74	2.21	300	300	< 1.06	< 1.37	< 6.52
NGC 3497	17.1	2.05	3.09	300	300	$< 1.25^*$	$< 1.93^*$	$< 29.38^*$
NGC 4370	34.2	2.60	1.65	368	374	3.85 ± 0.29	3.37 ± 0.19	38.58
NGC 5485	74.1	0.87	0.85	300	300	$< 0.53^*$	$< 0.53^*$	$< 2.62^*$
NGC 5525	39.9	0.84	0.88	734	565	1.78 ± 0.14	0.85 ± 0.13	77.00

Notes. * Unreliable due to unstable pointing of the telescope during the observations.

4.3.1 GBT 100-m observations and data reduction

The atomic gas content of NGC 4370 was already studied by Lake & Schommer (1984), who found a total HI flux of 0.63 Jy km s^{-1} based on their Arecibo data. A much higher flux of 3.17 Jy km s^{-1} was later reported for the same galaxy by Hoffman et al. (1989), also based on Arecibo data. However, their central beam spectrum only shows a very tentative detection, so we do not attach much credibility to this value. Richter & Huchtmeier (1987) and Springob et al. (2005) both present HI data of NGC 2907 taken with the 300-ft Green Bank Telescope, and report total fluxes of 6.10 and 4.14 Jy km s^{-1}, respectively. We consider the value from Richter & Huchtmeier (1987) as more reliable, given the higher signal-to-noise ratio in their spectrum. Finally, the HI content of NGC 3665, NGC 5485 and NGC 5866 was studied with the WSRT by Serra et al. (2012). HI emission was detected for NGC 5866 and firm upper limits were derived for the atomic gas masses of the other two galaxies. The atomic gas content of the remaining three FRIEDL galaxies was not previously studied.

To fill in these blanks, we conducted HI 21-cm observations of NGC 2534, NGC 3497, NGC 3665 and NGC 5525 with the 100-m Green Bank Telescope on November 18, 2013. NGC 3665 was included in the sample with the goal of measuring its atomic gas mass or obtaining a stronger upper than the one from Serra et al. (2012). A similar strategy for NGC 5485 was not allowed because a different GBT program had proprietary rights to this source. For each galaxy we performed OnOff position switched observations using the single beam L-band Gregorian focus receiver. The offset (in declination) was chosen differently for each galaxy as to avoid any nearby companions, and varied between 28′ and 40′. With a typical beam size of 9′, a single pointing was sufficient for each galaxy. The Spectrometer backend was used in narrow band mode, with a total bandwidth of 50 MHz and a channel width of 1.526 kHz (0.32 km s^{-1}). The pointing and focus of the telescope were checked at the start of the observing run using the bright source 3C286. This source was also used as flux calibrator. The time on source varied between 17.4 and 35.4 minutes.

The reduction of the GBT data was performed using the IDL package GBTIDL[5]. The reduction steps are essentially similar to the reduction of the IRAM data, apart from the calibration. The individual 6-second scans were inspected and channels affected by RFI were flagged. The spectra were then averaged for each polarization and a first or second order baseline was subtracted. At the IRAM 30-m telescope, flux calibration is performed online after observing a calibrator source. At the GBT, this step should be performed manually during the reduction of the data. Following the advice of Dr. David Frayer[6], we derived appropriate calibration factors for both polarizations by directly comparing

---

[5] http://gbtidl.nrao.edu/

[6] see e.g. also http://www.gb.nrao.edu/GBTtraining/GB2016_obscal.pdf

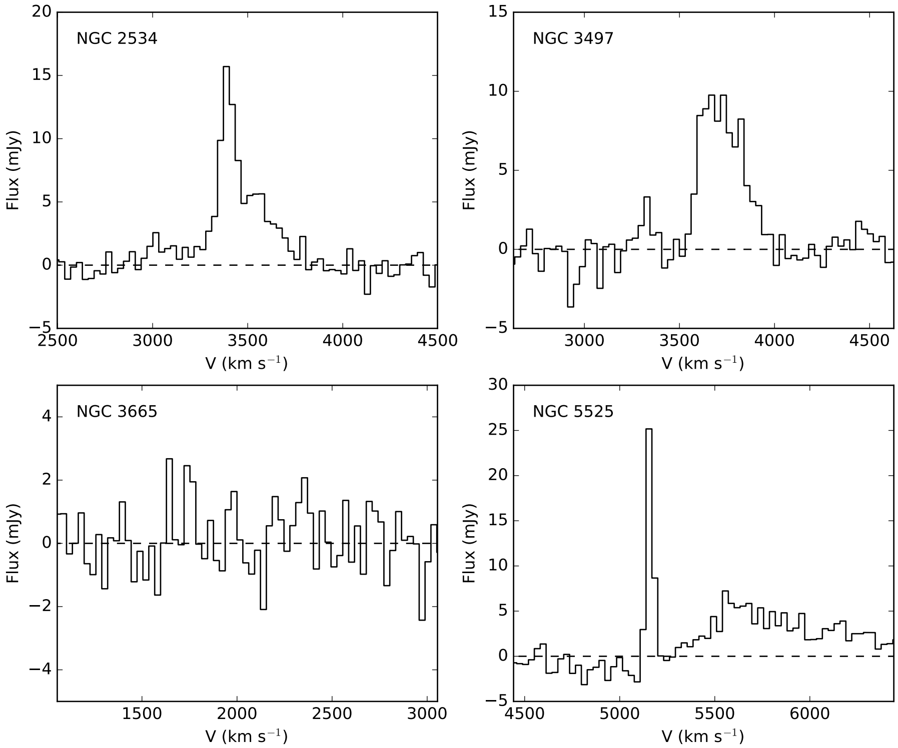

Figure 4.2: Hɪ spectra obtained from our GBT 100-m observations. The velocities on the horizontal axis are barycentric radio velocities. The spectra are boxcar smoothed and binned to a resolution of 31 km s^{-1}. The dashed horizontal line shows the zero line.

the antenna temperatures in our observations of 3C286 to the known flux of this source at the appropriate frequency. The baseline-subtracted spectra of the target sources could then directly be converted from T_A^* (in K) to flux density (in Jy) by multiplying them with these factors. After averaging both polarizations, the spectra were boxcar smoothed and rebinned to a resolution of approximately 31 km s^{-1}.

4.3.2 The spectra

The final 31 km s^{-1} resolution spectra are shown in Figure 4.2. The Hɪ 21-cm line is clearly detected in the spectrum of NGC 2534, but does appear somewhat asymmetric, with a much stronger peak on the approaching side (i.e. at LOS velocities below the expected systemic velocity of 3498 km s^{-1}). It is not clear what causes this asymmetry, but it is most likely not an artificial feature induced by the observation. With an optical diameter of only 1.38′, the observational beam of 9′ should extend well out to the outskirts of the atomic gas disk of NGC 2534. A potential error in the pointing of the telescope can therefore not have caused the observed asymmetry. In addition, NGC 2534 has no known companions that could cause confusion in the velocity range of the detected line and within (or even well outside) the observational beam area. Instead we might be observing an artefact of a recent minor merger event. Dust lane early type galaxies such as NGC 2534 are indeed considered to be the remnants of recent minor mergers.

HI is also clearly detected in the spectrum of NGC 3497, which has a systemic velocity of 3627 km s^{-1}. However, the gas-rich spiral galaxy NGC 3529 is located at an angular offset of only $5'$ from NGC 3497 (according to NED) and has a systemic velocity of 3703 km s^{-1}. Given the long high-velocity tail with respect to the systemic velocity of NGC 3497, the line profile that is observed in the spectrum is probably a combination of HI emission from both sources. The associated line width and total intensity given in Table 4.3 should therefore be treated as upper limits. Interferometric follow-up observations to resolve this degeneracy are discussed in section 4.3.4.

The prominent and narrow line at 5150 km s^{-1} in the spectrum of NGC 5525 comes from the nearby galaxy LEDA 087262. The much weaker feature at 5600 km s^{-1} can most likely be attributed to another nearby galaxy, LEDA 1455200. HI emission from our target source, NGC 5525, should be located in between these features, at 5442 km s^{-1}. The nearby galaxies and unstable baseline at these velocities unfortunately make it impossible to tell whether any signal from NGC 5525 is present in the spectrum, but the detection would be tentative in any case. We therefore restrict ourselves to giving a 3σ upper limit for the total flux.

Finally, no signal is detected for NGC 3665.

4.3.3 Line widths and integrated intensities

The total intensities of the detected HI lines were again determined by summing the fluxes of all the channels inside the line region, and the associated uncertainties are again given by equation 4.2. Upper limits for the non-detections were also calculated with this expression, but we assume a larger line width of 500 km s^{-1} for the atomic gas in NGC 3665 and use the width of the CO(1-0) line for NGC 5525, since the latter is larger than 500 km s^{-1}. We also drop the additional factor of 2 (discussed in section 4.2.4), as the GBT beam does cover the entire galaxy.

The integrated intensities were converted into atomic gas masses according to:

$$\frac{M_{\rm atom}}{M_\odot} = 3.21 \times 10^5 \left(\frac{I_{\rm HI}}{\rm Jy\ km\ s^{-1}}\right)\left(\frac{D}{\rm Mpc}\right)^2, \tag{4.7}$$

which is the same as equation 2.1, but with the correction factor of 1.36 for the contribution of heavier elements absorbed in the numeric value. With our calibration strategy, the integrated line intensities already have units of Jy km s^{-1}. The adopted line widths, the total intensities and the atomic gas masses are listed in Table 4.3. Within the limited observing time that was granted, our GBT observation of NGC 3665 unfortunately did

Table 4.3: Summary of the GBT 100-m observations

Galaxy	TOS (min)	rms (mJy)	Δv (km s^{-1})	$I_{\rm HI}$ (Jy km s^{-1})	$M_{\rm atom}$ (10^7 M$_\odot$)
NGC 2534	35.4	0.93	475	2.81 ± 0.13	227.08
NGC 3497	25.0	1.03	475*	2.62* ± 0.14	256.75*
NGC 3665	18.0	1.05	500	< 0.47	< 16.38
NGC 5525	17.4	2.20	734	< 1.10	< 199.67

Notes. * Source confusion with NGC 3529 inside the GBT beam.

not provide a stronger upper limit than the one obtained by Serra et al. (2012).

4.3.4 VLA observations and data reduction

Hɪ emission is clearly detected in our GBT spectrum of NGC 3497, but due to the large beam size of the GBT, it is not possible to determine whether this emission comes from NGC 3497, its nearby companion NGC 3529, or both. Similar confusion could also be present in the 300-ft GBT spectrum of NGC 2907 from Richter & Huchtmeier (1987). Indeed, the edge-on spiral galaxy FGC 0904 is located at a projected distance of only 5.2′ and has a systemic velocity of 2100 km s^{-1} (only 80 km s^{-1} higher than that of NGC 2907), so its atomic gas disk (or at least part of it) could well have been picked up by the large observational beam.

To resolve these degeneracies, we conducted interferometric follow-up observations of these two galaxies with the Jansky-VLA in January 2015. Since both targets have a declination below -15°, we used the CnB array. This configuration gives the same angular resolution as the C array (beam major axis of about 15″ at 1.42 GHz), but has an extended north arm to yield a more circular beam for very southern or very northern declinations. Both sources were observed with a total bandwidth of 16 MHz and a channel separation of 62.5 kHz (13 km s^{-1}). For NGC 3497 we used 3C286 as flux calibrator and J1130-1499 as phase calibrator. For NGC 2907, J0902-1415 was observed as phase calibrator and, depending on the time of day of the observation, 3C48 or 3C286 was used to calibrate the amplitudes. An overview of our JVLA observations is given in Table 4.4.

The data reduction was performed with the CASA[7] software package and followed largely the same steps as explained in section 2.2.2. One major difference, though, is that CASA does not use a channel-0 set and performs the full reduction directly on the spectral line data. As a consequence, the order of the calibration steps needs to be altered and the band-pass calibration (that takes care of the variation of the observed amplitudes and phases with frequency) should be performed at the start of the calibration process. Before this was done, however, a preliminary phase-only calibration of the data of the flux calibrator

---

[7] https://casa.nrao.edu/

Table 4.4: Summary of the JVLA observations

Galaxy	Array	Date	TOS (min)	Bandwidth (MHz)	Number of channels
NGC 2907	CnB	12 Jan 2015	36.0	16.0	256
	CnB	19 Jan 2015	36.1	16.0	256
	CnB	26 Jan 2015	92.0	16.0	256
NGC 3497	CnB	22 Jan 2015	93.3	16.0	256
	CnB	26 Jan 2015	93.2	16.0	256

(also used as bandpass calibrator) was performed, based on a selection of central channels, to correct for the strong time dependence of the observed phases. After the bandpass calibration, the gain amplitude and phase solutions were determined more thoroughly for both calibrators and the flux information from the amplitude calibrator was transferred to the phase calibrator. Finally, the solutions were interpolated to the data of the target source.

The different data sets for each source were reduced separately and were only combined after the continuum subtraction in the *uv* plane. For this purpose, the data sets were first regridded to a common velocity grid. We used the radio velocity definition to obtain a constant velocity width of the channels.

At the original angular and spectral resolution of the data, the faint and extended HI emission from NGC 2907 and NGC 3497 was essentially buried in the noise of the data cubes. We therefore smoothed the data in velocity to a resolution of 40 km s^{-1}. A Gaussian taper with FWHM of 10 kλ was further used to obtain a more circular beam. The deconvolution of the dirty beam was performed in Miriad[8], according to the same strategy as outlined in section 2.2.2. Finally, the data cubes were corrected for the primary beam pattern of the array antennas.

4.3.5 First moment maps and atomic gas masses

The channel maps of the final data cubes of NGC 2907 and NGC 3497 are shown as contour plots in Figures 4.3 and 4.4. The data cube of NGC 2907 clearly shows the atomic gas disk of the target galaxy. In addition, HI emission from its companions FGC 0904 and PGC 027031 (outside the field of view in Figure 4.3) is also detected. For NGC 3497, on the other hand, the data cube only shows emission from NGC 3529. Even with a substantial taper and at a coarse spectral resolution of 40 km s^{-1}, the target galaxy itself is not detected.

A zeroth moment map (Fig. 4.5) of the atomic gas disk of NGC 2907 was constructed by defining masks around the emission in a slightly (spatially) smoothed version of the data

---

[8] http://www.atnf.csiro.au/computing/software/miriad/

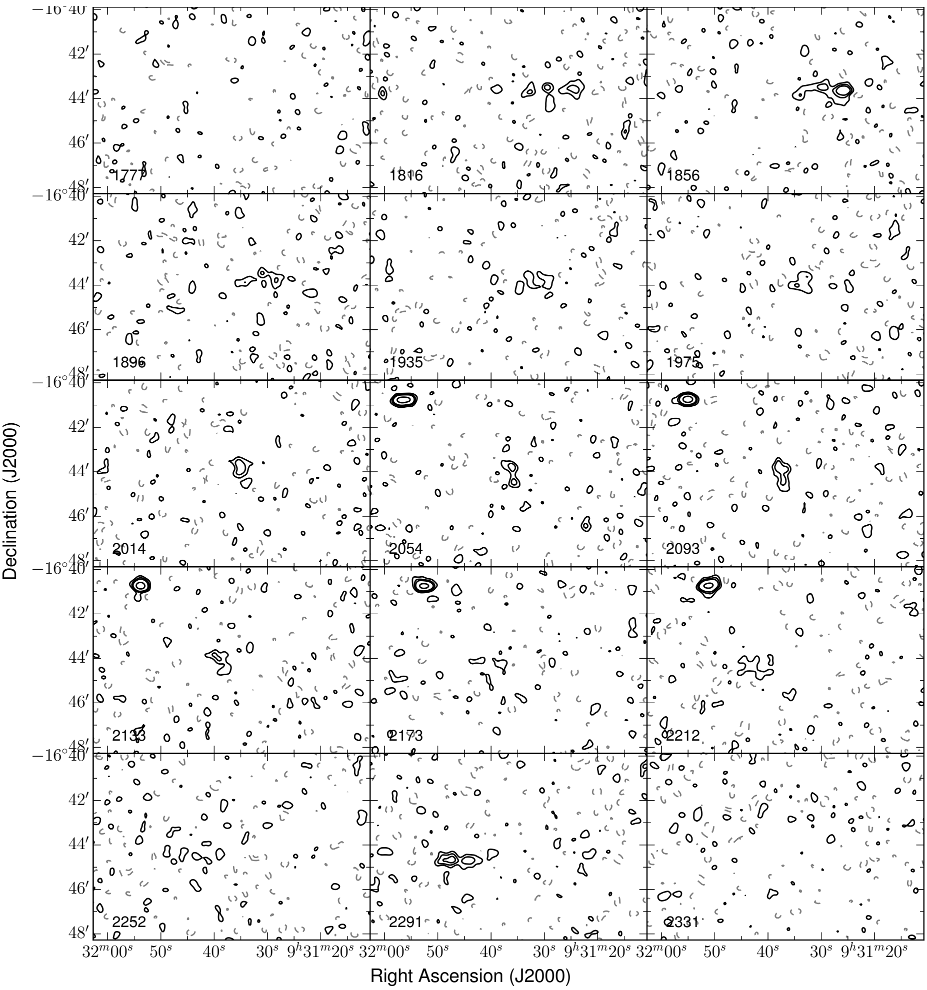

Figure 4.3: Channel maps from the JVLA data of NGC 2907. To emphasize the faint HI emission from NGC 2907, we plot a version of the data cube that was smoothed to twice the original beam size. The noise level in this cube is 0.42 mJy beam^{-1} and the contour levels are -2σ, 2σ, 4σ, 6σ and 15σ. The bright source in the top left corner of the panels at 2054 – 2212 km s^{-1} is FGC 0904.

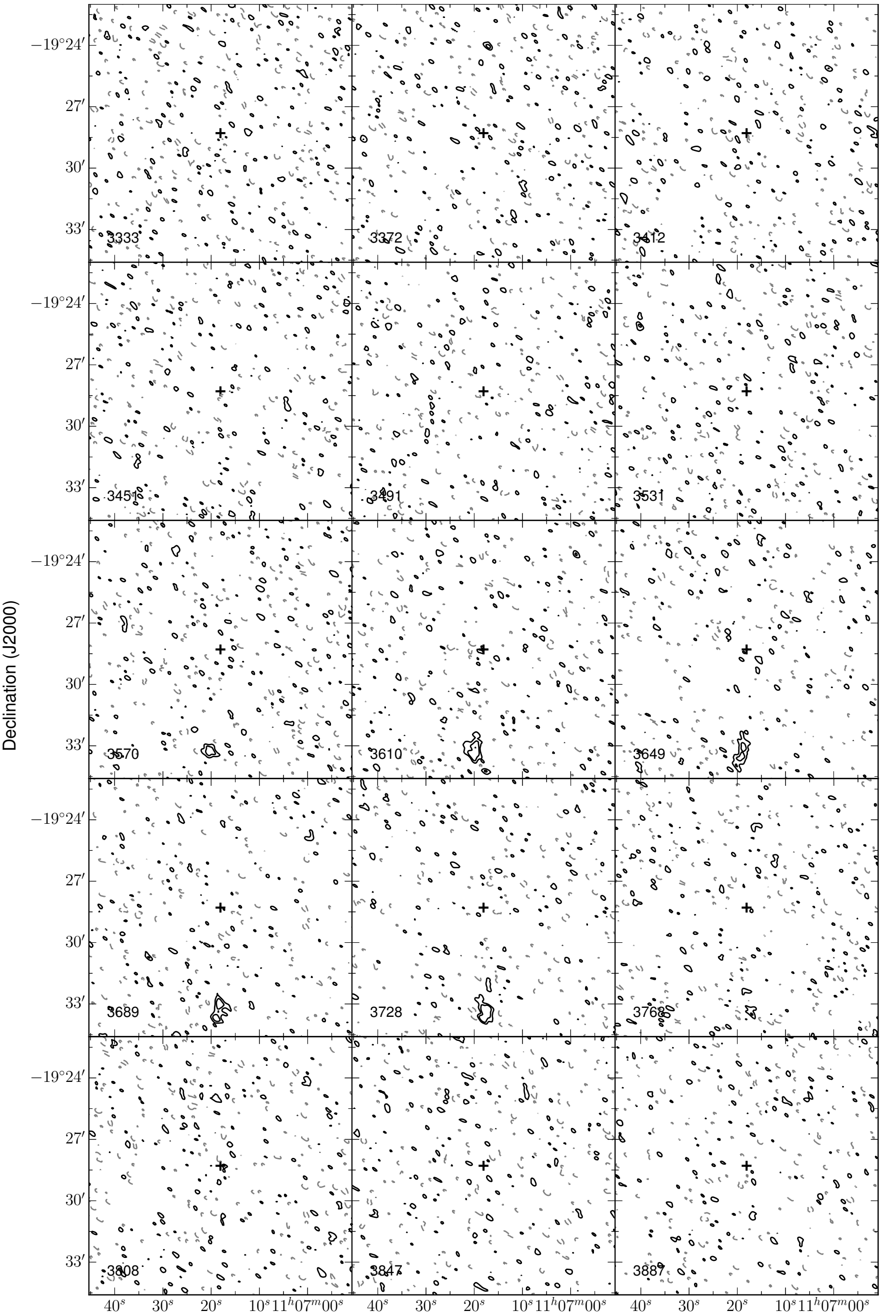

Figure 4.4: Channel maps from our full resolution JVLA data cube of NGC 3497. The noise level in this cube is 0.38 mJy beam^{-1} and the contour levels are -2σ, 2σ, 4σ, 8σ and 12σ. The source in the bottom of the panels at 3570 − 3768 km s^{-1} is NGC 3529. The black cross marks the expected central position of NGC 3497.

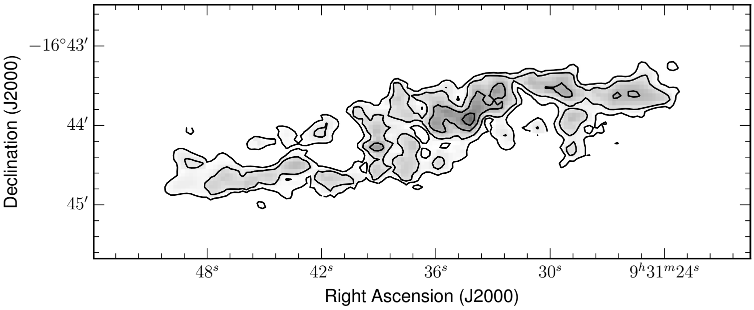

Figure 4.5: Moment-0 map of the atomic gas disk of NGC 2907. The contours start at 1.84×10^{20} atoms cm^{-2} and increase as 2, 4 and 6 times this value.

Table 4.5: Main properties of the data cubes and derived quantities

Galaxy	Synthesised beam FWHM		Δv	rms	I_{HI}	M_{atom}
	(arcsec)	(kpc)	(km/s)	(mJy/bm)	(Jy km/s)	(10^7 $M_\odot$)
NGC 2907	14.8×14.2	2.02×1.94	39.6	0.39	6.00	153.17
NGC 3497	24.4×11.9	6.53×1.41	39.6	0.38	< 0.37	< 36.00

cube and subsequently summing the masked regions from the original cube. From this map we measured the total intensity by summing all the pixels, and equation 4.7 was then used to convert the HI intensity to an atomic gas mass.

For NGC 3497 we estimated a 3σ upper limit for the atomic gas mass according to the following strategy. First, we convolved the non primary beam corrected cube to a beam size of 154″, which corresponds to the optical D_{25} diameter reported by NED. In this way, the HI emission from NGC 3497 should fall within one beam area in each channel map of the data cube. Next, we estimated the velocity range of the emission by smoothing our GBT spectrum to a channel width of 40 km s^{-1} and taking double the width of the detected line on the low velocity side (i.e. away from the companion galaxy NGC 3529). This resulted in an estimated line width of 150 km s^{-1}. After correcting the convolved data cube for the primary beam, we measured the rms noise in the channel maps that are inside the estimated line region. From this value, an upper limit was finally determined according to:

$$I_{\text{UL}} = 3 \times \sigma_{\text{rms}}\, \Delta v\, \sqrt{N_{\text{l}}}, \tag{4.8}$$

where again σ_{rms} represents the rms noise, Δv is the velocity resolution (39.57 km s^{-1}) and N_{l} is the number of channels in the estimated line range (4). The fluxes and atomic gas masses are listed in Table 4.5.

4.4 Herschel observations and dust masses

All the FRIEDL galaxies have been observed with the PACS and SPIRE photometers of the Herschel Space Observatory. Both instruments were used in scan mode with their nominal scan speed, i.e. 20 arcsec/s for PACS and 30 arcsec/s for SPIRE. The size of the maps was chosen to be 8×8 arcmin^2. For the PACS maps, four cross-scans (i.e. four nominal and four orthogonal scans) were performed, while the SPIRE maps were observed with a single cross-scan. The data reduction was performed with HIPE[9] (version 12.0.0) and includes the same steps as in Verstappen et al. (2013). For the PACS data, it includes the use of the Scanamorphos version 23 (Roussel 2013) in order to make optimal use of the redundancy in the observational data. The PACS and SPIRE maps at 100, 160 and 250 μm have a FWHM of $7''$, $11''$ and $18''$, respectively, and generally resolve the dust emission from the FRIEDL galaxies along the direction of the dust lane. In the SPIRE maps at 350 and 500 μm, where the FWHM increases to $24''$ and $36''$, the emission is typically not resolved any more.
Global flux densities were determined via aperture photometry using the DS9/Funtools[10] program FUNCNTS, following the same strategy as described in detail by Verstappen et al. (2013). The background level and uncertainty estimates were determined following the approach of Dale et al. (2012).

Dust masses were derived from the Herschel fluxes using the MAGPHYS code (da Cunha et al. 2008), which has already been used extensively to model the panchromatic SEDs of galaxies (e.g., Smith et al. 2012a; Lanz et al. 2013; Clemens et al. 2013; Viaene et al. 2014). A dust emissivity index $\beta = 2$ and $\kappa_\nu = 0.192$ m^2 kg^{-1} at 350 μm were assumed in this process. These values correspond to what is probably the most widely adopted physical dust model (Draine 2003; Draine & Li 2007), and they have been widely used to interpret Herschel SEDs (e.g., Dale et al. 2012; Auld et al. 2013; Verstappen et al. 2013; Hughes et al. 2014). The dust masses that were derived in this way are listed in Table 4.6.

4.5 The strange case of NGC 5485

In Table 4.6 we compare the final atomic and molecular gas masses to the dust masses for the full northern and equatorial FRIEDL sample. For the values from the literature, we took the reported fluxes and used equations 4.3 and 4.7 to obtain the corresponding masses. The molecular gas mass upper limit of NGC 5485 is based on the CO(1-0) flux from Young et al. (2011). Although our CO(1-0) spectrum of this galaxy is deeper and seems to provide a stronger upper limit, the unstable pointing of the IRAM telescope during our observations of this galaxy makes our value unreliable.

---

[9] http://herschel.esac.esa.int/hipe/

[10] http://hea-www.harvard.edu/saord/funtools/help.html

Table 4.6: Gas and dust masses of the FRIEDL galaxies

Galaxy	M_{H_2} (10^7 M$_\odot$)	$M_{\mathrm{H\,I}}$ (10^7 M$_\odot$)	M_d (10^6 M$_\odot$)	$M_{\mathrm{H}_2}\,/\,M_\mathrm{d}$	$M_{\mathrm{H\,I}}\,/\,M_\mathrm{d}$	$M_\mathrm{gas}\,/\,M_\mathrm{d}$
NGC 2534	$< 46.89^\mathrm{a}$	227.08	8.15	< 57.56	278.76	278.76 - 336.32
NGC 3497	$< 29.38^*$	< 36.00	26.36	$< 11.15^*$	< 13.66	$< 24.80^*$
NGC 4370	38.58	26.06^b	11.77	32.77	22.13	54.90
NGC 2907	< 6.52	153.17	10.26	< 6.36	149.36	149.36 - 155.72
NGC 5525	77.00	< 199.67	28.57	26.95	< 69.88	26.95 - 96.84
NGC 3665	161.61^c	$< 2.69^\mathrm{e}$	11.37	142.09	< 2.37	142.09 - 144.45
NGC 5485	$< 4.82^\mathrm{d}$	$< 1.48^\mathrm{e}$	3.81	< 12.66	< 3.88	< 16.54
NGC 5866	90.05^c	0.91^e	7.18	125.47	1.27	126.75

References. a) Wiklind et al. (1995); b) Lake & Schommer (1984); c) Alatalo et al. (2013); d) Young et al. (2011); e) Serra et al. (2012). **Notes.** * Unreliable due to unstable pointing of the IRAM 30-m telescope.

In our limited sample, it is striking to see that some dust lane ETGs, such as NGC 2534 and NGC 2907, are very atomic gas rich, while the ISM of NGC 3665 and NGC 5866 is completely dominated by molecular gas. Without a fresh supply of atomic gas, the molecular-to-atomic gas ratio in galaxies can indeed gradually rise. However, the extremely high values of this ratio for NGC 3665 ($M_{\mathrm{H}_2}\,/\,M_{\mathrm{H\,I}} > 60$) and NGC 5866 ($M_{\mathrm{H}_2}\,/\,M_{\mathrm{H\,I}} = 99$) indicate that most of the atomic gas must have been stripped. As it is generally more extended and less strongly bound than the molecular gas, the atomic gas is indeed more easily stripped during interactions. On the other hand, in their WSRT data cubes, Serra et al. (2012) find no HI emission in the surroundings of these two galaxies. This indicates that the atomic gas must either be located in highly diffuse tidal tails, or that it was already stripped from the progenitor in the past, before the merger. Deeper observations are needed to discern between these scenarios.
Typically, the gas-to-dust ratios (GDRs) of galaxies vary from several thousands for low-metallicity dwarfs to about 100 (or 50 in rare cases) for metal rich galaxies (Muñoz-Mateos et al. 2009; Galametz et al. 2011; Magrini et al. 2011; Rémy-Ruyer et al. 2014). From column 7 of Table 4.6, we see that the GDRs of the FRIEDL galaxies are on the low side, but still fall in the normal range in most cases. NGC 5485, however, has an extremely low cold gas-to-dust upper limit of $M_\mathrm{gas}\,/\,M_\mathrm{dust} < 16.5$. It is tempting to draw a similar conclusion for NGC 3497 as well ($M_\mathrm{gas}\,/\,M_\mathrm{dust} < 24.8$), but we note again that our CO flux for this galaxy is uncertain and could be underestimated. It would be interesting to re-observe the CO lines in this galaxy in better conditions to establish whether it too truly has an unusually low GDR.

As mentioned earlier, dust lane early-type galaxies are a particular type of ETGs that are thought to have accreted their ISM through a recent minor merger. An elaborate study of the HI content of a sample of 9 dust lane ETGs was performed by Oosterloo and collaborators (Oosterloo et al. 2002, and references therein), based on a combination of new ATCA observations and archival data. They found huge atomic gas reservoirs in 6 of their galaxies, with masses up to several times $10^9\ M_\odot$ and atomic gas-to-dust ratios of more than 1000. In the other 3 galaxies of their sample, they did not detect any HI. This implied unusually low HI-to-dust mass ratios, down to $M_{\rm HI}/M_{\rm dust} < 20$. As they did not have any constraints on the molecular gas content of these galaxies, Oosterloo et al. (2002) suggested that the cold ISM of these systems could be mainly in molecular rather than atomic form. This would bring the total gas-to-dust ratios more in line with the expected range. Additionally, an important caveat in the work of Oosterloo et al. (2002) is that they determined the dust masses solely from IRAS data. With a wavelength range going up to (only) 100 μm, IRAS does not trace the cold dust that generally makes up the bulk of the total dust mass.

More recently, Davis et al. (2015) also investigated the cold ISM of a sample of dust lane ETGs, based on Arecibo data for the HI and IRAM 30-m data for the molecular gas. The dust masses were determined from photometry at 20 different wavelengths, ranging from 0.12 to 500 μm, using MAGPHYS. Davis et al. (2015) found that their dust lane ETGs are generally very gas rich and have gas-to-dust ratios in the range ~100-750, with the exception of two systems. For 2MASX J13341710+3455455 and NGC 5233 they found GDRs of 50 and 44, respectively. It should be noted, though, that Davis et al. (2015) use a different normalisation to transform their CO(1-0) intensities to molecular gas masses than the relation from Bolatto et al. (2013) that we assume (eq. 4.3):

$$\frac{M_{\rm mol}}{M_\odot} = 3.93 \times 10^{-17} \left(\frac{X_{\rm CO}}{\rm cm^{-2}\ (K\ km\ s)^{-1}}\right) \left(\frac{D}{\rm Mpc}\right)^2 \left(\frac{I_{1-0}}{\rm Jy\ km\ s^{-1}}\right). \tag{4.9}$$

With equation 4.3 instead of the expression above, the gas-to-dust ratios of these two galaxies become 58 and 54, respectively. While these values are also on the low side, they are still consistent with the extremities of the range that was reported in earlier works.

The most complete effort to make a census of the cold gas in ETGs in the Local Universe is the ATLAS$^{\rm 3D}$ project (Cappellari et al. 2011a). This targets a volume-limited sample of 260 ETGs, of which some 17% show dust disks or filaments in optical/NIR images. Atomic and/or molecular gas is also detected in most of these dusty ETGs (Young et al. 2011; Serra et al. 2012; Alatalo et al. 2013), but unfortunately no dust masses have been determined in the frame of the ATLAS$^{\rm 3D}$ project. Many of the ATLAS$^{\rm 3D}$ galaxies have been observed with Herschel in the frame of the HErschel Among the eaRly Types (HEART) project[11], but these data are yet to be reduced and published. Since dust masses can easily vary by an order of magnitude between individual dust lane ETGs, it is not (yet) possible to draw any conclusions about the gas-to-dust ratio of the ATLAS$^{\rm 3D}$ galaxies.

From the works mentioned above, it seems that low GDRs of 50 – 100 might not be uncommon for dust lane ETGs, although we find no record of total gas-to-dust ratios as

---

[11] http://herschel.esac.esa.int/Docs/AO2/OT2_accepted.html#OT2_hgomez_3

extreme as that of NGC 5485. We investigate this low GDR in more detail in the sections below.

4.5.1 Reliability of the mass estimates

One possible explanation for the extreme gas-to-dust ratio upper limit for NGC 5485 is that the dust mass as determined from the Herschel flux densities is overestimated. There are several possible systematic effects that we should investigate in some detail.

A first observation is that the new dust mass that we have derived is a factor 3 to 4 larger than the IRAS-based dust masses of Patil et al. (2007) and Finkelman et al. (2010a). And these dust masses are themselves more than an order of magnitude higher than the dust masses the same authors derived using extinction in optical images, for which they found several times $10^4\ M_\odot$. However, we are convinced that our new dust mass based on Herschel FIR/submm data is more reliable than those based on IRAS and optical extinction. IRAS-based dust masses are most certainly an underestimate of the true dust mass, since IRAS is insensitive to cool dust at temperatures below about 25 K (e.g., Goudfrooij & de Jong 1995; Tsai & Mathews 1996). Herschel observations have decisively shown that the typical cold dust temperature in ETGs is around 20 K (Smith et al. 2012c; Rowlands et al. 2012; di Serego Alighieri et al. 2013). For NGC 5485, we find an effective dust temperature of 19 K, which indeed indicates that IRAS missed the bulk of the dust. On the other hand, inferring the amount of dust from optical extinction maps is complicated due to the complexity of the star-dust geometry and the effects of scattering (e.g., Witt et al. 1992; Baes & Dejonghe 2001). In dust lane ETGs, dust mass estimates based on simple extinction recipes applied to optical images can underestimate the true dust mass by an order of magnitude or more (Goudfrooij & de Jong 1995; Patil et al. 2007; Finkelman et al. 2008, 2010b).

We should also critically consider the possibility that the observed Herschel flux densities are overestimated. NGC 5485 has a galactic latitude of 59°, so there are no foreground subtraction issues due to strong cirrus that have plagued some other Herschel extragalactic observations (e.g., Davies et al. 2010; Fritz et al. 2012). In optical and NIR images, NGC 5485 seems to have a shell-like structure some 20 arcsec towards to SE of the nucleus (see left panel of Figure 4.6). This feature has a clear counterpart in the PACS maps, and could be an edge-on background galaxy rather than a feature linked to NGC 5485 itself. In any case, the contribution of this source to the Herschel flux densities of NGC 5485 is marginal. In the PACS 100 μm map, where the resolution is sufficient to separate this feature from the dust emission in the dust lane, we find that it contributes no more than 10% to the total flux density.

Finally, a last aspect to take into consideration is that we modelled the FIR/submm emission as a single modified black body at a single temperature, whereas in reality, the FIR/submm emission results from a complicated weighted sum of modified blackbodies at a range of temperatures. This is a systematic effect that we cannot avoid due to our lack of resolution. However, the total dust mass is typically *underestimated* when it is based on

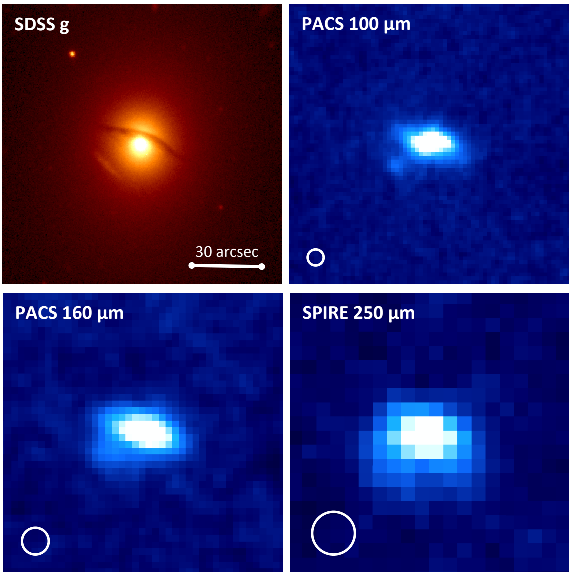

Figure 4.6: SDSS *g* band, PACS 100 and 160 μm, and SPIRE 250 μm images of NGC 5485. The field of view of each image is 2×2 arcmin^2, and the beam FWHM is indicated in the three Herschel images. In the optical image, a shell-like feature is clearly visible some 20 arcsec towards the SE of the nucleus, and its counterpart is detectable in the PACS images as well.

the integrated SED (Galliano et al. 2011; Galametz et al. 2012), so this does not help to explain the low gas-to-dust ratio.

On the other hand, the low gas-to-dust ratio might be the result of a systematic underestimate of the gas mass. In any case, there does not seem to be any reason to doubt the reliability of the HI and CO upper limits of Serra et al. (2012) and Young et al. (2011), respectively. The noise levels obtained in both observation campaigns are almost exactly the median value of the entire ATLAS^{3D} study. One source of uncertainty on the derivation of the molecular gas mass upper limit is the $X_{\rm CO}$ factor needed to convert CO(1-0) intensities to H_2 masses. This factor has been the subject of a substantial debate in the recent literature (e.g., Strong & Mattox 1996; Israel 1997; Leroy et al. 2011; Smith et al. 2012b; Sandstrom et al. 2013). The authoritative review by Bolatto et al. (2013) suggests the value $X_{\rm CO} = 2 \times 10^{20}$ cm^{-2} (K km s^{-1})$^{-1}$ for the Milky Way and other "normal galaxies". In agreement with Young et al. (2011), we used $X_{\rm CO} = 3 \times 10^{20}$ cm^{-2} (K km s^{-1})$^{-1}$ to derive the molecular gas mass upper limit of NGC 5485, i.e. 50% larger than the standard value suggested by Bolatto et al. (2013). Using the standard value would decrease the molecular gas mass upper limit by factor 1.5, and it would decrease the gas-to-dust ratio upper limit by a factor 1.34 to $M_{\rm gas}/M_{\rm d} < 12.3$. Another potential source of error is that Young et al. (2011) only used a single pointing of the IRAM telescope towards the centre of NGC 5485, with a beam size of 22″. As discussed in section 4.2.4, this likely causes their observation to miss some of the gas in the outer regions of the galaxy.

However, even with an extreme correction by a factor of two (see section 4.2.4), the total gas-to-dust ratio would still only be $M_{\text{gas}} / M_{\text{d}} < 29.2$. We furthermore stress that such a high correction is not expected for a galaxy with $D_{25} = 141''$.

In principle, most of the gas in NGC 5485 could be ionised rather than neutral. An interesting comparison case here is the study of the elliptical galaxy NGC 4125 by Wilson et al. (2013). Combining Herschel-based dust estimates with HI and CO non-detections, they also found a similar cold gas-to-dust ratio upper limit as we obtain here. However, based on a [NII]/[CII] ratio consistent with a low-density ionised medium and the (crude) assumption that the ionised gas is distributed uniformly over a 4.2 kpc diameter sphere, Wilson et al. (2013) argued that a significant fraction of the gas in NGC 4125 is warm ionised rather than cold neutral gas. For NGC 5485, this option seems excluded, though. The galaxy was imaged in Hα by Finkelman et al. (2010a). They detected an inclined disc of ionised gas that nicely follows the morphology of the dust lane, which seems to support that at least part of the dust might be associated with warm ionised gas. The total amount of ionised hydrogen gas traced in the Hα map is $M_{\text{HII}} = (2.0 \pm 0.6) \times 10^4\ M_\odot$, far too little to be a significant contributor to the total gas budget. Finkelman et al. (2010a) even warn that their HII masses are likely overestimated by a factor 2-3 due to confusion of the Hα and [NII] lines. On the other hand, Hα photons are subject to dust attenuation in the dust lane, which could cause the HII mass in NGC 5485 to be underestimated. However, in order to bring the HII mass to the level required for a typical gas-to-dust ratio of about 100, unrealistically high attenuation values $A_{\text{V}} \gg 10$ are needed (Calzetti et al. 1994).
Alternatively, a major part of the gas budget in NGC 5484 could be in the form of hot X-ray emitting ionised gas. While dust grains are expected to be destroyed through sputtering by thermal collisions with energetic ions, the coexistence of dust and a hot X-ray gas is not completely impossible (e.g., Temi et al. 2003; Kaneda et al. 2007; Leeuw et al. 2008). NGC 5485, however, was not detected in the ROSAT all-sky survey: Beuing et al. (1999) quote an upper limit of $L_{\text{X}} < 10^{39.8}$ erg s^{-1}. If we insert the K-band luminosity $L_{\text{K}} = 5.65 \times 10^{10}\ L_\odot$ from 2MASS into the calibration from Boroson et al. (2011) between the K-band luminosity of ETGs and the expected unresolved X-ray emission due to low-mass X-ray binaries (LMXBs), we find the same number, $L_{\text{X,LMXB}} = 10^{39.8}$ erg s^{-1}. This implies that any X-ray emission from NGC 5485 most probably originates from LMXBs rather than from hot ionised gas. Moreover, the fact that the dust is distributed in a well-defined dust lane makes a physical association with a potential hot diffuse halo rather unlikely, although it is not impossible that a fraction of the dust is distributed diffusely over the galaxy (Goudfrooij & de Jong 1995).

4.5.2 Accretion of an exotic companion?

A different option could be that NGC 5485 contains a reservoir of molecular gas, but that this gas is not emitting CO line emission. Both diffuse γ-ray emission (Grenier et al. 2005; Abdo et al. 2010; Ackermann et al. 2012) and combined gas and dust observations (Planck Collaboration XIX 2011; Paradis et al. 2012) have revealed the presence of a substantial amount of so-called dark gas in our own Milky Way. The presence of CO-dark gas has been found many years ago in low-metallicity dwarf galaxies. At low metallicities, most of the carbon is locked up in neutral or singly ionised carbon rather than CO, which makes [CII] a more reliable tracer of the cold H_2 reservoir (Stacey et al. 1991, 2010; Madden et al. 1997, 2013). As a relatively massive lenticular galaxy, NGC 5485 is not expected to contain copious amounts of CO-dark gas. Being a dust lane ETG, however, it has most probably acquired most of its dust and gas during a recent minor merger. The recent merger scenario is also supported by its rather exceptional kinematical structure, which shows strong minor-axis rotation (Wagner et al. 1988; Krajnović et al. 2011; Emsellem et al. 2011). In principle, it is possible that NGC 5485 has accreted a dwarf galaxy with a substantial CO-dark molecular gas reservoir. An appropriate example of such a dwarf galaxy would be the SMC, which contains a dust mass of 3×10^5 $M_\odot$, but hardly any CO-emitting molecular gas (Mizuno et al. 2001; Leroy et al. 2007, 2011). It does, however, contain about 4×10^8 $M_\odot$ of HI gas (Stanimirovic et al. 1999; Bolatto et al. 2011), while no atomic gas is seen in or around NGC 5485 in the WSRT data of Serra et al. (2012). Hence, similarly to NGC 3665 and NGC 5866, if a minor merger with an SMC-type galaxy would be the origin of the dust lane in NGC 5485, a large fraction of the atomic gas must have been stripped from the progenitor in a previous interaction, before the merger, or reside in very diffuse tidal tails that are hidden in the noise of the WSRT cube. Another argument against such a scenario is that the gas-to-dust ratios of low-metallicity dwarf galaxies are typically up to an order of magnitude higher than those of giant galaxies (Rémy-Ruyer et al. 2014), which makes the apparently low gas-to-dust ratio in NGC 5485 even more puzzling.

Finally, Merritt et al. (2016) recently discovered four ultra diffuse galaxies (UDGs) that are most likely associated with the NGC 5485 group. UDGs are extended low surface brightness systems that are as faint as dwarf galaxies, with predominantly red colors, but at the same time have sizes similar to those of luminous $L^\star$ galaxies (van Dokkum et al. 2015). Despite their low surface brightness, recent observational studies have detected many hundreds of UDGs in the local Universe, mainly in clusters (e.g. Mihos et al. 2015; Koda et al. 2015; van der Burg et al. 2016; Román & Trujillo 2017a), but with increasing detections in groups as well (e.g. Merritt et al. 2016; Román & Trujillo 2017a,b).

How such UDGs were formed is still largely a mystery. One of the potential scenarios is that they started as regular $L^\star$ galaxies, but lost their gas very early on, inhibiting them to continue to form stars (van Dokkum et al. 2015). Other scenarios propose that they are diffuse dwarf galaxies that either reside in dark matter haloes with a high spin (Amorisco & Loeb 2016), or whose stellar and dark matter content has expanded substantially as a consequence of repeated, stellar feedback driven outflows of gas (Di Cintio et al. 2017). From both observational studies (e.g. Beasley & Trujillo 2016; Román & Trujillo 2017a) and theoretical work (e.g. Rong et al. 2017), evidence is now growing that (the majority of) UDGs are puffed up dwarf galaxies.

In their study of UDGs in galaxy groups, Román & Trujillo (2017b) found that UDGs that are close to the group centre have red colors (as found earlier), but also detected a number of blue UDGs in the group outskirts. They proposed a scenario where UDGs start as gas-rich puffed up dwarfs that can subsequently be stripped of their gas when falling into a galaxy group, leaving them to evolve passively from then on. Of the four UDGs found around NGC 5485 by Merritt et al. (2016), the average color is rather red (although with large uncertainties), and one system indeed shows signs of tidal stripping. Interestingly, a recent study of the HI content of a sample of relatively isolated UDGs by Papastergis et al. (2017) revealed substantial reservoirs of atomic gas in some of the UDGs, while no gas was detected in the others, yielding much lower gas fractions than would be expected for field galaxies of the same stellar mass. The latter is surprising, given the isolation of the investigated systems, and leads Papastergis et al. (2017) to suggest that UDGs may have different formation scenarios. In any case, whatever the nature and origin of these systems may be, a significant fraction of them is expected to be gas-poor, especially in group environments. If such systems are able to retain their dust reservoir, or built up a new one through mass loss of the evolved stars, a merger of NGC 5485 with such a UDG could explain the unusually low gas-to-dust ratio. This scenario, of course, remains speculative. Deep HI and CO, and perhaps [CII], observations of NGC 5485 and its UDG companions are needed to unveil the nature and origin of the ISM in this peculiar system.

4.6 Conclusions

In this chapter we investigated the gas and dust content of the northern and equatorial dust lane early type galaxies from the FRIEDL project. For this purpose, new observations were combined with data from the literature. We presented new IRAM 30-m observations of the CO(1-0) and CO(2-1) lines for 5 galaxies to study their molecular gas content. CO emission was clearly detected and converted to molecular gas masses for NGC 5525 and NGC 4370. Upper limits were further determined for NGC 2907, NGC 3497 and NGC 5485, although the values for the latter two are uncertain due to the poor observing conditions. Additionally, we also presented new HI data for 4 galaxies, taken with the 100-m Green Bank Telescope. HI emission was detected in the spectra of NGC 2534 and NGC 3497, and upper limits were derived for NGC 5525 and NGC 3665. However, the spectrum of NGC 3497 in fact contains emission from multiple sources that are confused in the large observational beam of the GBT. A similar effect is also present in the literature HI data of NGC 2907. To resolve these degeneracies, we conducted interferometric follow-up observations of these two sources with the JVLA. These yielded a more reliable measure of the atomic gas mass of NGC 2907 and a firm upper limit for NGC 3497. The FRIEDL galaxies have also been observed with the PACS and SPIRE instruments of the Herschel telescope, and dust masses were determined using MAGPHYS.

Combining our dust and gas masses with the data from the literature, we found that the GDRs of the FRIEDL systems are generally on the low side, but not unusual, with one, possibly two, exception(s). For NGC 5485, the cold gas-to-dust ratio is extremely low:

$M_{\rm gas}/M_{\rm dust} < 16.5$. This is almost an order of magnitude lower than the canonical value of the Milky Way. The same could also be true for NGC 3497, but more reliable observations of the molecular gas content are needed to confirm this claim. Various possible explanations for this extreme gas-to-dust ratio were investigated. We critically checked the reliability of the dust mass estimate, but neither the lack of spatial resolution in the FIR/submm imaging, nor a possible contamination of background or companion sources strongly affect the dust mass. Similarly, we investigated the reliability of the cold gas mass. The main source of uncertainty here is the CO-to-H_2 conversion factor, but applying the standard value for the Milky Way rather than the slightly higher value that is assumed in the ATLAS$^{\rm 3D}$ project would result in an even lower gas-to-dust ratio upper limit of $M_{\rm gas}/M_{\rm d} < 12.3$. On the other hand, even an extreme correction by a factor of 2 for the small observational beam of the molecular gas observations would only increase the gas-to-dust ratio to $M_{\rm gas}/M_{\rm d} < 29.2$.
Less obvious scenarios to explain the lack of cold gas in NGC5485 were also investigated. Based on Hα and X-ray observations, the possibility that the bulk of the gas is in a warm or hot ionised medium could be discarded. Another option is the presence of a reservoir of CO-dark molecular gas. In principle, the extreme gas-to-dust ratio could be the result of a merger with an SMC-type metal-poor dwarf galaxy, if a substantial fraction of the HI could have been lost during the interaction, but it remains to be investigated whether such a scenario is possible. Finally, if ultra diffuse galaxies are indeed stripped of their gas when falling into group environments (as suggested by Román & Trujillo 2017b), but are able to retain their dust or form new dust, a merger with such a UDG could also explain the low gas-to-dust ratio of NGC 5485.

5

An observational comparison of the coreNFW and DC14 dark matter halo models

For about two decades, there has been a strong discrepancy between the dark matter haloes that are predicted by gravitational N-body simulations and those inferred from the rotation curves of dwarf and LSB galaxies. While the simulated haloes have steep, cuspy central density profiles, the rotation curves generally require haloes with a central core of constant density. Core formation through baryonic physics, in particular repeated outflows of gas caused by supernova feedback, offers a promising solution to this cusp-core controversy. The coreNFW and DC14 halo models take these processes into account for galaxies in different mass ranges and have individually been found to successfully reproduce the rotation curves of galaxies. For the DC14 model, however, the agreement of the predicted haloes with cosmological scaling relations was confirmed by one study, but strongly refuted by another.

In this chapter, we compare the cNFW and DC14 models for a set of galaxies in the mass range where both models should be valid, to test whether they converge to the same solution. The DC14 model is further applied to a set of rotation curves at higher halo masses, to verify its agreement with the halo mass-concentration and stellar mass-halo mass relations. In section 5.1 we explain the selection of our sample of galaxies. The details of the rotation curve decomposition and the cNFW and DC14 haloes are described in section 5.2. Our modelling strategy is described in section 5.3 and the results are presented in section 5.4. Finally, we summarise our main conclusions in section 5.5. This chapter has been published in Astronomy & Astrophysics as Allaert et al. (2017).

Our sample of rotation curves was compiled mainly from the Little THINGS (Hunter et al. 2012; Iorio et al. 2017), THINGS (Walter et al. 2008; de Blok et al. 2008) and SPARC (Lelli et al. 2016) datasets. For Little THINGS we used the publicly available rotation curve data from Iorio et al. (2017) and took the surface density and surface brightness profiles of the atomic gas and the stars from Oh et al. (2015). The latter were kindly provided to us by S.H. Oh and D. Hunter. The THINGS data, both the rotation curves and the baryonic profiles, were kindly made available by E. de Blok. Finally the SPARC data are publicly available and can be downloaded from the SPARC website[1]. For all three datasets the stellar surface brightness profiles are based on observations at 3.6 μm.

For Little THINGS we selected only the galaxies that are marked as 'clean dIrrs' by Read et al. (2017) and further eliminated NGC 6822 and DDO 210. For the former no rotation curve is presented by Iorio et al. (2017), while the rotation curve of the latter is highly uncertain and completely dominated by the asymmetric drift correction. This leaves 9 galaxies from the Little THINGS sample.
de Blok et al. (2008) present rotation curves of 19 THINGS galaxies, from which we eliminated 10 because of poor sampling of the rising part of the rotation curve or strong non-circular motions. We further also remove NGC 925, NGC 3521 and NGC 7793 from our THINGS sample. Although Hague & Wilkinson (2014) did include these galaxies in their analysis, we find that their rotation curves might be unreliable because of a substantial bar (NGC 925), poorly constrained distance (NGC 3521) and uncertain inclination in the outer half (NGC 7793).
The gap in mass between the Little THINGS and THINGS galaxies is bridged with a set of low mass systems from the SPARC dataset. These are selected according to the following criteria: a total 3.6 μm luminosity $L_{3.6} \lesssim 10^9\ L_\odot$, a rotation curve with quality label 1, a reliable distance estimate, an inclination between 40° and 80° and little beam smearing. These criteria lead to an additional 5 galaxies, of which we further eliminate UGC 8490. For this galaxy, McQuinn et al. (2015) discovered a strong increase in the star formation rate over the past 100 Myr. This indicates that UGC 8490 might be experiencing a starburst, which may severely bias its kinematics.
Finally we also included the rotation curve of M33 (taken from Corbelli et al. 2014), which is a galaxy previously claimed to have a strongly cusped dark matter halo (Corbelli et al. 2014; Hague & Wilkinson 2015). For this galaxy, Corbelli et al. (2014) do not report the stellar surface brightness profile, but immediately derive the surface *density* profile of the stars from a pixel by pixel population synthesis analysis.

Finally, Iorio et al. (2017) remark that their rotation curves of UGC 8508 and DDO 126 are unreliable up to a radius of 0.5 and 1.43 kpc, respectively, while Gentile et al. (2007) note that elliptical streaming motions could be affecting the innermost data points of their

---

[1] http://astroweb.cwru.edu/SPARC/

rotation curve of NGC 3741, up to a radius of 1.2 kpc. Blais-Ouellette et al. (2001) additionally found that the inner seven data points of the rotation curve of NGC 3109 could be slightly underestimated because of weak beam smearing. These same data points also have suspiciously small error bars. Since only the inner parts of the rotation curves are affected, we still included these galaxies in our sample, but excluded the affected data points from the fits. The rotation curves are still sampled well enough by the remaining points.

Our total sample thus comprises 20 rotation curves. An overview of this sample is given in Table 5.1. For the galaxies from the THINGS and SPARC datasets we use distances from the Cosmicflows-2 catalogue (Tully et al. 2013). For M33 we take over the distance from Corbelli et al. (2014) and for the Little THINGS galaxies we use the distances from Iorio et al. (2017).

5.2 Rotation curve decomposition and halo models

As explained in section 3.1, mass modelling of galaxy rotation curves is based on the expression:

$$v_c^2 = v_{\rm gas}\,|v_{\rm gas}| + \Upsilon_{*,\rm B}\, v_{*,\rm B}^2 + \Upsilon_{*,\rm D}\, v_{*,\rm D}^2 + v_{\rm dm}^2, \tag{5.1}$$

where the total circular velocity v_c is measured by the (corrected) rotation curve and the gas and stellar circular velocities $v_{\rm gas}$ and v_* are derived from their observed surface brightness profiles. The stellar mass-to-light ratio(s) and the dark matter contribution $v_{\rm dm}$ are the unknowns in this expression. For the latter, we use two different parametrisations: the coreNFW halo and the DC14 halo. We express both these parametrisations in terms of the virial radius and the virial mass. The former is defined as the radius inside which the average density of the dark matter halo is equal to Δ times the critical density of the Universe $\rho_{\rm crit}$, where Δ and $\rho_{\rm crit}$ depend on the assumed cosmology. The virial mass is simply the enclosed mass at the virial radius:

$$M_{\rm vir} = \frac{4}{3}\pi\, r_{\rm vir}^3\, \Delta\, \rho_{\rm crit}. \tag{5.2}$$

For consistency with Di Cintio et al. (2014a) we use a WMAP3 cosmology (Spergel et al. 2007) with $\Delta = 93.6$, $H_0 = 73.0$ km s^{-1} Mpc^{-1} and $\rho_{\rm crit} = 147.896\ M_\odot$ kpc^{-3}.

5.2.1 DC14

The DC14 profile is formulated by Di Cintio et al. (2014a) as a special case of the general (α, β, γ) profile that was already introduced in section 3.4:

$$\rho(r) = \frac{\rho_s}{\left(\frac{r}{r_s}\right)^{\gamma}\left[1+\left(\frac{r}{r_s}\right)^{\alpha}\right]^{(\beta-\gamma)/\alpha}}. \tag{5.3}$$

Table 5.1: Sample overview. Columns 1-3 represent the galaxy name and distance and an indicative inclination. Columns 4-5 give the integrated 3.6 μm luminosity of the disk and bulge (if present). Column 6 gives the stellar half-light radius. Data references are given in columns 7-8.

Galaxy	D (Mpc)	incl (°)	$\log_{10}(L^{\mathrm{D}}_{3.6})$ $(L_\odot)$	$\log_{10}(L^{\mathrm{B}}_{3.6})$ $(L_\odot)$	$R_{1/2}$ (kpc)	Reference
UGC 8508	2.6	68	6.954		0.623	1,2
CVnIdwA	3.6	49	7.199		1.784	1,2
NGC 3741	3.23	70	7.453		0.341	3
WLM	1.0	74	7.522		1.334	1,2
DDO 154	3.7	68	7.628		3.511	1,2
DDO 126	4.9	62	7.880		1.771	1,2
DDO 87	7.4	43	8.121		3.363	1,2
UGCA 442	4.37	64	8.150		1.906	3
DDO 168	4.3	47	8.168		1.562	1,2
DDO 52	10.3	55	8.300		2.278	1,2
NGC 3109	1.37	70	8.314		2.700	3
NGC 2366	3.4	65	8.548		2.899	1,2
UGC 7603	6.85	78	8.902		1.239	3
			DC14 only			
IC 2574	3.89	51	9.352		4.352	4
NGC 2976	3.63	54	9.516		1.505	4
M33	0.84	55	9.690*		3.325	5
NGC 2403	3.18	55	10.074	8.846	2.215	4
NGC 3621	6.73	62	10.536		4.471	4
NGC 3198	13.37	72	10.520	9.569	5.209	4
NGC 5055	9.04	51	11.096	10.182	4.100	4

References. (1) Little THINGS (Iorio et al. 2017); (2) Little THINGS (Oh et al. 2015); (3) SPARC (Lelli et al. 2016); (4) THINGS (de Blok et al. 2008); (5) Corbelli et al. (2014). **Notes.** * For M33 column 4 gives the stellar *mass* from Corbelli et al. (2014) (in $M_\odot$) instead of the 3.6 μm luminosity.

At small and large radii this profile follows a power law with slopes γ and β, respectively, and the sharpness of the transition between these two regimes is governed by α. Note, though, that Di Cintio et al. (2014a) take α as the reciprocal of the α parameter that was used in section 3.4 and by Hague & Wilkinson (2013). The (α, β, γ) profile reduces to a simple NFW halo for $(\alpha, \beta, \gamma) = (1, 3, 1)$.

Starting from an NFW profile, but in the general formulation of equation 5.3, Di Cintio et al. (2014a) allow supernova feedback to modify the dark matter distribution by expressing the shape parameters α, β and γ as a function of the 'integrated star formation efficiency' $(M_* / M_{\rm halo})$ as follows:

$$\begin{aligned} \alpha &= 2.94 - \log_{10}[(10^{X+2.33})^{-1.08} + (10^{X+2.33})^{2.29}] \\ \beta &= 4.23 + 1.34X + 0.26X^2 \\ \gamma &= -0.06 + \log_{10}[(10^{X+2.56})^{-0.68} + (10^{X+2.56})], \end{aligned} \tag{5.4}$$

with $X = \log_{10}(M_* / M_{\rm halo})$. It should be noted that these expressions are only valid for $-4.1 < X < -1.3$, which is the range probed by the simulations of Di Cintio et al. (2014a). At lower values of X, too few stars form to modify the dark matter halo. On the other hand, at $X > -1.3$ (corresponding to halo masses $\gtrsim 10^{12}\ M_\odot$) processes not included in the simulations, such as AGN feedback, can start to play a role as well.

The variation of α, β and γ as a function of X is shown in Fig. 5.1. The inner log slope γ first decreases with increasing X, since a higher stellar-to-halo mass ratio implies more energy input from supernova feedback. However, it reaches a minimum at $X \sim -2.6$ and goes back up at higher values of X. The reason for this turnover is the increasing gravitational potential of the stars, which at a certain point starts to dominate the feedback

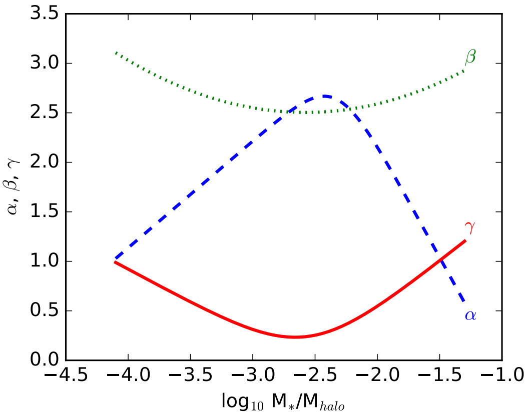

Figure 5.1: Variation of the shape parameters α, β and γ of the DC14 halo as a function of the integrated star formation efficiency.

and pulls the dark matter back towards the centre. In the DC14 formalism more star formation therefore does not monotonically result in ever stronger cores.

For an NFW halo, the concentration is defined as $c = r_{\mathrm{vir}}/r_{\mathrm{s}}$, where the scale radius r_{s} is equal to r_{-2}, the radius at which the slope of the density profile becomes -2. For the (α,β,γ) profile, the meaning of r_{s} depends on the values of α, β and γ, with

$$r_{-2} = \left(\frac{2-\gamma}{\beta-2}\right)^{1/\alpha} r_{\mathrm{s}}. \tag{5.5}$$

Di Cintio et al. (2014a) therefore define the concentration of their dark matter haloes as

$$c_{\mathrm{vir}} = \frac{r_{\mathrm{vir}}}{r_{-2}}. \tag{5.6}$$

The concentration of the original, unmodified NFW halo can be recovered from this as

$$c_{\mathrm{NFW}} = \frac{c_{\mathrm{vir}}}{1.0 + 0.00003 e^{3.4(X+4.5)}}, \tag{5.7}$$

with again $X = \log_{10}(M_*/M_{\mathrm{halo}})$. It is this concentration that should be used to compare the DC14 halo from a rotation curve fit to, for example, the cosmological mass-concentration relation.

5.2.2 CORENFW

A CORENFW halo (Read et al. 2016a) is essentially a NFW halo where the inner part is modified by a spherically symmetric function f^n that models the effects of supernova feedback. Practically, this modification is expressed at the level of the enclosed mass. For an ordinary NFW halo profile (Navarro et al. 1996b)

$$\rho_{\mathrm{NFW}}(r) = \frac{\rho_{\mathrm{s}}}{\left(\frac{r}{r_{\mathrm{s}}}\right)\left(1+\frac{r}{r_{\mathrm{s}}}\right)^2} \tag{5.8}$$

with concentration

$$c = r_{\mathrm{vir}}/r_{\mathrm{s}} \tag{5.9}$$

the enclosed mass at a radius r is given by

$$\begin{aligned} M_{\mathrm{NFW}}(<r) &= M_{\mathrm{vir}} \frac{\ln(1+r/r_{\mathrm{s}}) - (r/r_{\mathrm{s}})/(1+r/r_{\mathrm{s}})}{\ln(1+c) - c/(1+c)} \\ &= M_{\mathrm{vir}}\, g_c \left[\ln\left(1+\frac{r}{r_{\mathrm{s}}}\right) - \left(\frac{r}{r_{\mathrm{s}}}\right)\left(1+\frac{r}{r_{\mathrm{s}}}\right)^{-1}\right]. \end{aligned} \tag{5.10}$$

The cNFW profile is then defined as

$$M_{\mathrm{cNFW}}(<r) = M_{\mathrm{NFW}}(<r)\, f^{n}(r), \tag{5.11}$$

with

$$f(r) = \tanh\left(\frac{r}{r_{\mathrm{c}}}\right). \tag{5.12}$$

The radial extent of the core is determined by the core radius r_c, which Read et al. (2016a) relate to the stellar half-mass radius as $r_{\mathrm{c}} = \eta\, r_{1/2}$, with an optimal value of 1.75 for the fitting parameter η .
The strength of the core is governed by the parameter n, which ranges between $0 < n \leqslant 1$ and is defined as

$$n = \tanh\left(\kappa \frac{t_{\mathrm{SF}}}{t_{\mathrm{dyn}}}\right). \tag{5.13}$$

Here κ is again a fitting parameter and the star formation time t_{SF} is the total time that the galaxy has been forming stars. The dynamical time t_{dyn} is the duration of 1 circular orbit at the scale radius in the unmodified NFW halo

$$t_{\mathrm{dyn}} = \frac{2\pi\, r_{\mathrm{s}}}{v_{\mathrm{NFW}}(r_{\mathrm{s}})} = 2\pi \sqrt{\frac{r_s^3}{G M_{\mathrm{NFW}}(<r_{\mathrm{s}})}}. \tag{5.14}$$

The longer stars have been forming, the larger n and stronger the core. On the other hand, the bigger the original dark matter halo, the smaller n and more difficult it is to form a core. Following Read et al. (2016a), we set $\kappa = 0.04$ and choose $t_{\mathrm{SF}} = 14$ Gyrs.

5.2.3 Asymmetric drift correction

For a gas particle moving in a galaxy disk, the gravitational pull from the stars, gas and dark matter is in fact not balanced solely by its circular motion, but also for a small part by the internal pressure of the gas. The observed rotation velocity v_{rot} is therefore not exactly equal to the circular velocity v_{c} from equation 5.1. Instead, it is given by:

$$v_{\mathrm{rot}}^2 = v_{\mathrm{c}}^2 + \left[\frac{R}{\rho}\frac{\partial(\rho\sigma_{\mathrm{R}}^2)}{\partial R} + \sigma_{\mathrm{R}}^2 - \sigma_{\phi}^2 + R\frac{\partial(\overline{v_{\mathrm{R}}v_{\mathrm{z}}})}{\partial z}\right] \tag{5.15}$$

(Binney & Tremaine 2008, equation 4-227), where ρ and σ are the density and velocity dispersion of the gas. The asymmetric drift correction (term inside the square brackets) is usually simplified under the assumptions that the velocity dispersion is isotropic ($\sigma_{\mathrm{R}} = \sigma_{\phi}$), the velocity ellipsoid is aligned with the cylindrical coordinate system ($\overline{v_{\mathrm{R}}v_{\mathrm{z}}} = 0$), and the vertical scale height does not change much with radius. This leads to

$$v_{\mathrm{c}}^2 = v_{\mathrm{rot}}^2 - \frac{R}{\Sigma}\frac{\partial(\Sigma\sigma^2)}{\partial R}, \tag{5.16}$$

where Σ is the surface density of the gas. The observationally derived radial $\Sigma\sigma^2$ profile is typically rather rugged, leading to sometimes strong and unphysical fluctuations in its derivative. To avoid this, a smooth function is fitted to the profile and the derivative is determined analytically. The simplifications involved in deriving equation 5.16 do limit its accuracy. As a consequence, equation 5.16 only provides an order of magnitude estimate of the correction.

For the rotation curves taken from the Little THINGS and SPARC datasets, the asymmetric drift correction is already taken into account by the authors. On the other hand, de Blok et al. (2008) and Corbelli et al. (2014) did not consider asymmetric drift for their THINGS and M33 rotation curves. We therefore evaluated this correction based on equation 5.16. Depending on the shape of the $\Sigma\sigma^2$ profile, we used one of the following analytic 3-parameter functions:

$$\Sigma\sigma^2(R) = I_0 \frac{R_0 + 1}{R_0 + e^{\alpha R}} \tag{5.17}$$

for a profile with a central core (Oh et al. 2011), and

$$\Sigma\sigma^2(R) = I_0 \left(1 + \frac{R}{R_0}\right)^{\alpha} e^{-\frac{R}{R_0}} \tag{5.18}$$

for a profile showing a hole in the centre (Read et al. 2016b). In the inner halves of the rotation curves, the derived corrections are consistently much smaller than the error bars and generally only of the order of 1 km s^{-1} or less. For four galaxies, the corrections do become more substantial (of order 5 – 10 km s^{-1}) near the outer edge of the rotation curve. However, because these larger corrections occur far from the centre, we found that they have only little effect on our fits and don't change any of our conclusions. In addition, the agreement between the $\Sigma\sigma^2$ profile and the analytic function is often not very good in these regions, making the corrections uncertain. This is illustrated for NGC 3621 in Fig. 5.2. Because of this uncertainty, and the very limited effect the corrections have on our results, we decided to use the original, uncorrected rotation curves in our analysis.

5.3 Markov Chain Monte Carlo fitting

The dynamical models were fitted to the rotation curves using Markov Chain Monte Carlo, following essentially the same approach as outlined in section 3.5. We again used

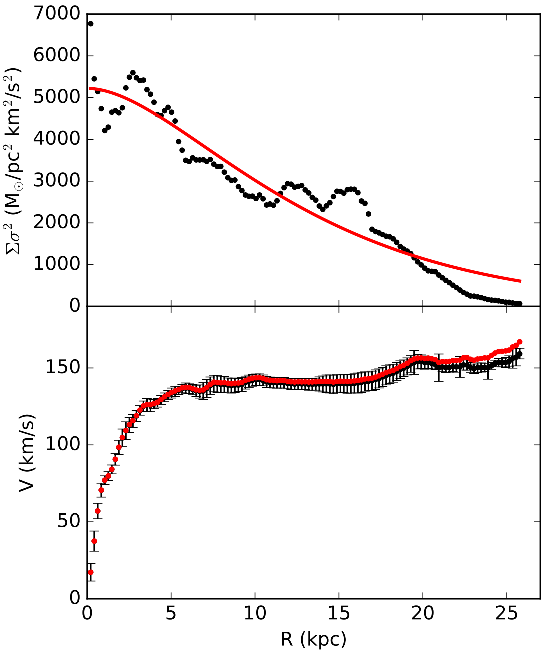

Figure 5.2: Asymmetric drift correction for NGC 3621. Top: observed $\Sigma\sigma^2$ profile (black circles) and analytic fit (red line). Bottom: original (black circles and error bars) and corrected (red circles) rotation curves.

the open-source python package `emcee` as MCMC engine and took:

$$\mathcal{L} = e^{-\chi^2/2} \tag{5.19}$$

as likelihood function. For every fit we used 100 walkers to explore the parameter space, each taking 2000 steps. The first 1000 steps served as burn-in phase to find the high likelihood areas in parameter space and were discarded. As mentioned in section 3.5, good performance of the MCMC sampler requires that the chains span at least 10 autocorrelation lengths and have acceptance fractions between 0.2 and 0.5. With 1000 steps per walker and an appropriately set proposal scale parameter of 2 or 3, this was consistently the case for all the fits. The convergence of the chains was further also checked by performing each fit 3 times and making sure that the Gelman-Rubin eigenvalues were well below 1 for all the parameters. More details on `emcee`, the fit strategy and the derivation of the uncertainties can be found in section 3.5.

5.3.1 Priors and parameter ranges

The coreNFW halo fits were performed with $\log_{10} M_{\rm vir}$, c and Υ (or $\Upsilon_{\rm d}$ and $\Upsilon_{\rm b}$) as free parameters. We use the log of $M_{\rm vir}$ instead of $M_{\rm vir}$ itself as a parameter in the fits because of the large dynamical range involved. Flat priors were assumed for all free parameters. $\mathrm{Log}_{10}\, M_{\rm vir}$ and c were loosely constrained inside $8 < \log_{10}(M_{\rm vir}/M_\odot) < 14$ and $1 < c < 100$. The 3.6 μm mass-to-light ratio was confined to the range $0.3 < \Upsilon_{3.6} < 0.8$, as motivated by the constraints from Meidt et al. (2014) and McGaugh & Schombert (2014). For M33 we allow the initial stellar mass to vary by a factor $0.758 < \Upsilon < 1.319$ based on the uncertainty that is mentioned in Section 6 of Corbelli et al. (2014). Following Read et al. (2017), η, κ and $t_{\rm SF}$ were kept fixed at 1.75, 0.04 and 14 Gyrs, respectively.

For the fits with the DC14 halo, we let $V_{\rm vir}$, $c_{\rm vir}$ and Υ (or $\Upsilon_{\rm d}$ and $\Upsilon_{\rm b}$) free and again used a flat prior for each of these. Following Katz et al. (2017) we used wide ranges of $10 < V_{\rm vir}/(\mathrm{km\,s^{-1}}) < 500$ and $1 < c_{\rm vir} < 100$ for the first two parameters, and the same range as before for the mass-to-light ratio: $0.3 < \Upsilon_{3.6} < 0.8$ (and $0.758 < \Upsilon < 1.319$ for M33).

Since our goal is to find models that fit the rotation curves well and yield physically acceptable dark matter haloes at the same time, we further imposed the cosmological halo mass-concentration and stellar mass-halo mass relations as log-normal priors in the fits. For the DC14 halo the shape parameters α, β and γ are expressed as a function of $\log_{10}(M_*/M_{\rm halo})$, where $M_{\rm halo} = M_{\rm vir}$. Hence, α, β and γ depend on the definition of the virial mass, which depends on the assumed cosmology. Since Di Cintio et al. (2014a) assume a WMAP3 cosmology, we do the same in our fits and we use the $M_{\rm halo} - c$ relation from Macciò et al. (2008) that was derived under this cosmology. The $M_* - M_{\rm halo}$ relation from Moster et al. (2010) also uses the WMAP3 values. However, this relation was derived from abundance matching using the SDSS DR3 stellar mass function for halo masses down to $\sim 3 \times 10^{10}\, M_\odot$ and is an extrapolation at lower masses. As pointed out by Read et al. (2017), this extrapolation is not consistent with the newer and deeper SDSS data, which means that the Moster et al. (2010) relation is actually not reliable for halo masses below $\sim 3 \times 10^{10}\, M_\odot$. Indeed, the stellar mass-halo mass relation from Behroozi et al. (2013), which is based on the newer SDSS data and the cosmological parameters used in the Bolshoi simulations (compatible with WMAP5 and WMAP7; Klypin et al. 2011), is much shallower and diverges significantly from the Moster et al. (2010) relation at low halo masses. Since a number of the galaxies in our sample fall in this low mass regime we opted to use the relation from Behroozi et al. (2013) rather than that from Moster et al. (2010) as a prior in our fits. For coreNFW the parametrisation is independent of the assumed cosmology and depends only on the global original NFW profile (i.e. before alteration by stellar feedback) and on the stellar half-mass radius and total star formation time.

5.3.2 χ^2_{red} and fit quality

In the discussion of our results, we express the quality of the fits to the rotation curves in terms of the reduced chi-squared statistic (χ^2_{red}). In the ideal case where the uncertainties on all the rotation curves are Gaussian and derived in a uniform way, and where all the points of a rotation curve have equal importance, this would be a good measure to compare the fit qualities for all the galaxies in our sample. In reality, however, our rotation curves are compiled from the literature, with differing data quality and techniques used to estimate the error bars. In addition, some rotation curves keep rising up to the last point, whereas others, for the more massive galaxies, include a large flat part. The latter is generally easier to reproduce and can have a large impact on the χ^2_{red} value of a fit, but is at the same time much less important in the analysis of core formation. For these reasons the χ^2_{red} values of our fits should only be used to compare the quality of different fits for the same galaxy, and not to compare fits for different galaxies.

5.4 Results

Following the procedure outlined in section 5.3, we have fitted DC14 halo models to each of the rotation curves in our sample and coreNFW models to the rotation curves of the Little THINGS and SPARC galaxies. The best-fit parameters and χ^2_{red} values of these fits are listed in Table 5.2. The results of the fits are discussed in the sections below.

5.4.1 DC14

Figure 5.3 shows the individual DC14 models for the galaxies in our sample. As can be seen, the DC14 halo generally provides excellent fits to the rotation curves, confirming the recent results from both Katz et al. (2017) and Pace (2016). The only clear exception to this is the rotation curve of DDO 168, where the model overestimates the data in the inner part. However, the inner three points of the rotation curve are in fact already well accounted for by the gravitational potential of the gas alone, so any model with a non-zero contribution of the dark matter at these radii will overestimate the data. Similar arguments also hold for the very inner regions of NGC 2366 and NGC 3198.

In Figure 5.4 we compare the best-fit parameter values from our models with the cosmological halo mass-concentration and stellar mass-halo mass relations. These relations were derived from dark matter-only simulations (in combination with abundance matching). To account for this in the comparison, we scale our inferred halo masses as $M_{\mathrm{vir}}/(1\text{-}f_{\mathrm{b}})$, where f_{b} is the Universal baryon fraction (0.176 according to WMAP3; McCarthy et al. 2007). The fits show excellent agreement with both scaling relations, although, somewhat surprisingly, our models seem to favour the M_{halo}-c relation from Dutton & Macciò (2014), that is based on the Planck cosmology, over the Macciò et al. (2008) relation that was used as prior in the fits. The only galaxy that falls significantly outside

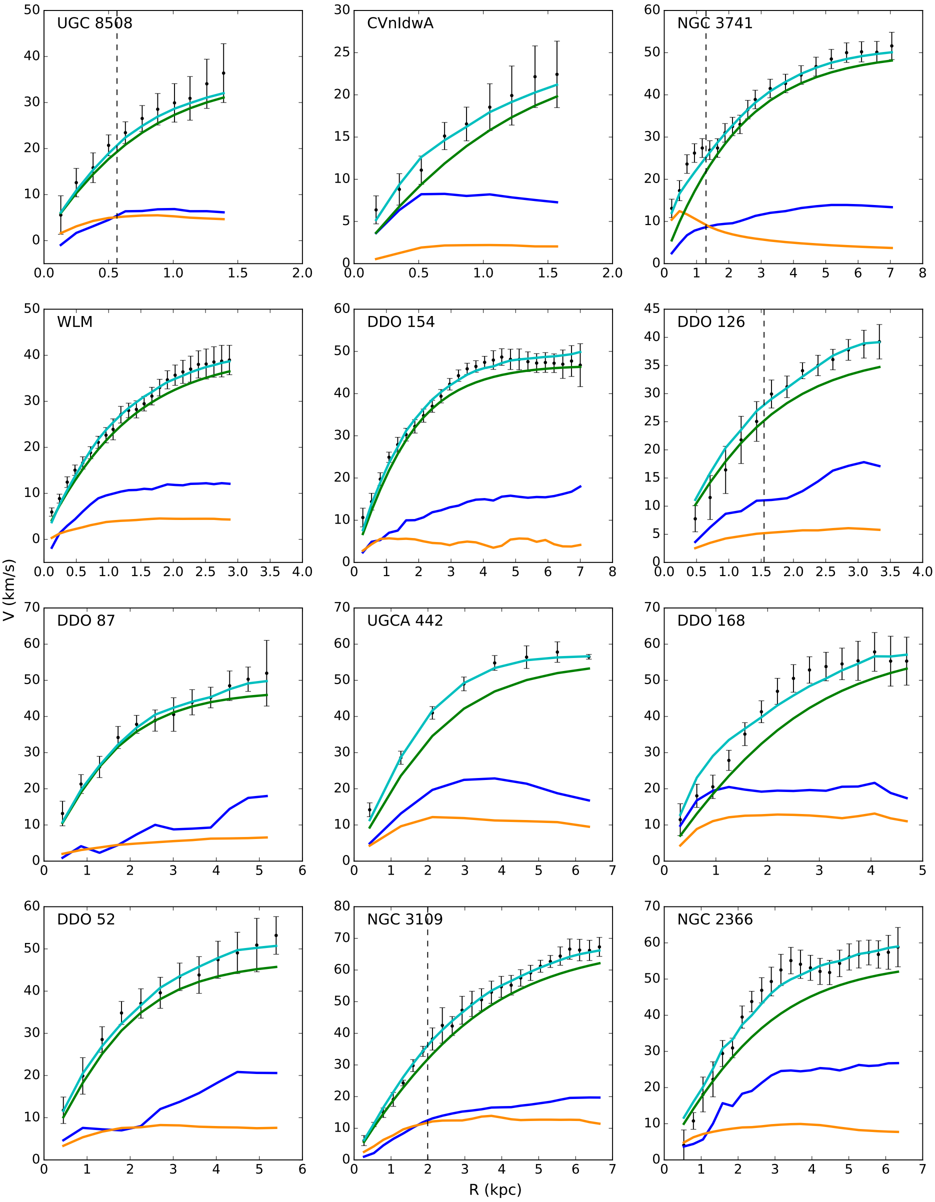

Figure 5.3: Decomposition of the rotation curves in our sample according to the maximum likelihood DC14 models. The black points show the observed rotation curves and the cyan curves represent the models. The contributions from the individual components are given by the blue (gas), yellow and red (stars) and green (dark matter) curves. The vertical dashed lines mark the central ranges that were, in some cases, excluded from the fit.

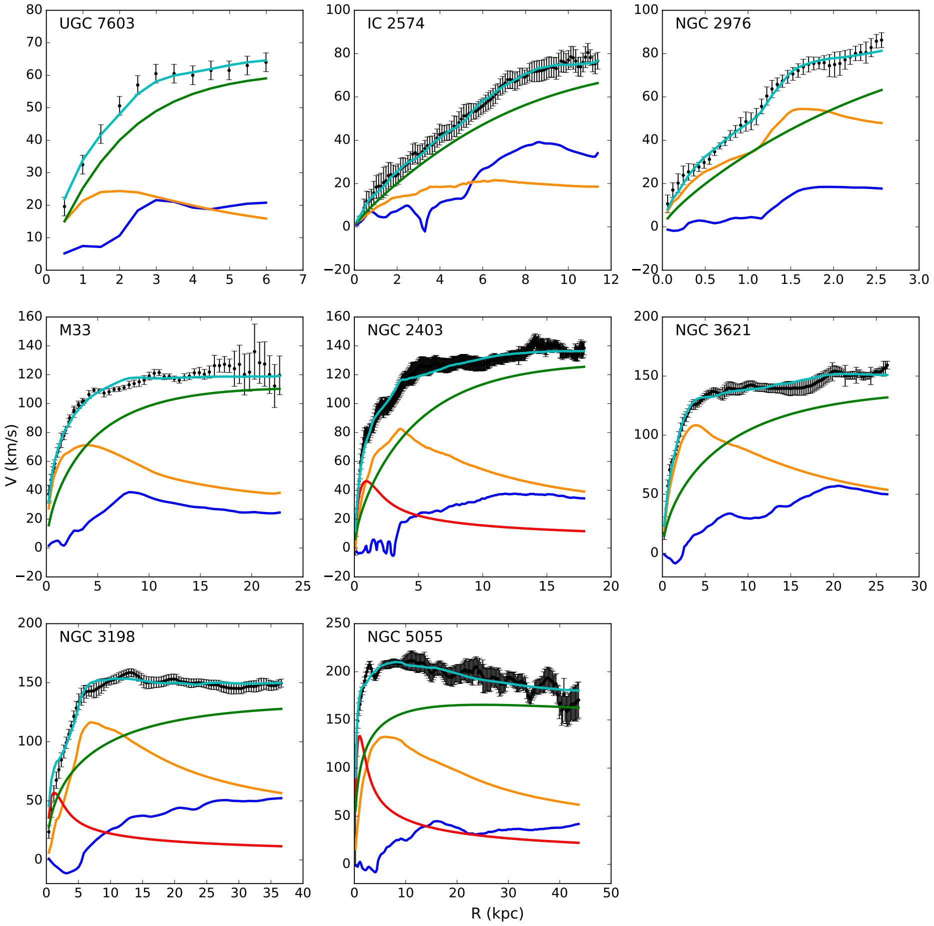

Figure 5.3: continued.

the 2σ scatter of the Dutton & Macciò (2014) relation is NGC 3198, but models with the concentration forced inside this scatter actually still provide a good fit to the data.

Although the sample size is limited, our analysis thus seems to confirm the recent conclusion by Katz et al. (2017) that the DC14 halo is in good agreement with ΛCDM and can recover the predicted mass-concentration and stellar mass-halo mass relations in a sample of observed rotation curves. The latter might seem obvious since we use priors that 'push' our fits towards these relations. The key point here, however, is that DC14 can produce dark matter haloes that *simultaneously* provide good fits to the rotation curves and agree with the scaling relations; this is something that, for example, the NFW halo cannot do. The priors do not 'make' physical solutions according to the scaling relations, but merely act as a filter to retain only the most physical solutions, if they exist. The fact that our

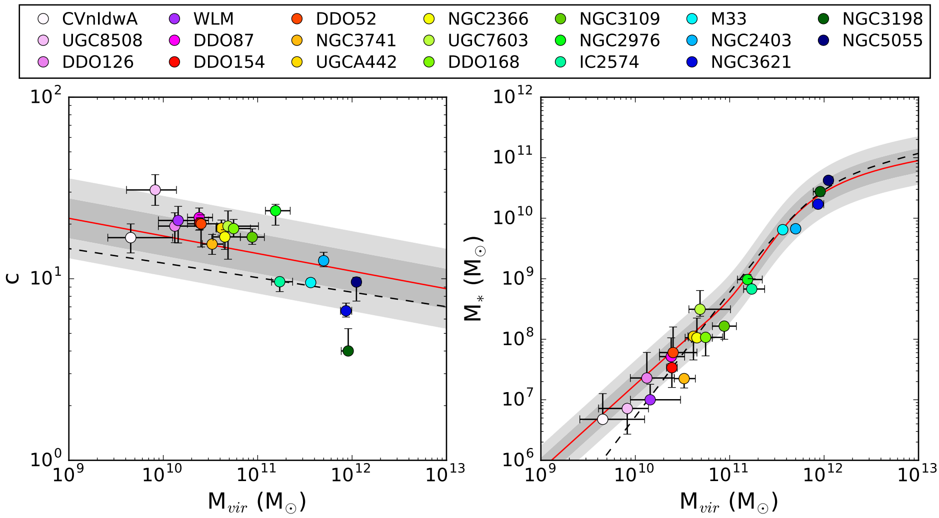

Figure 5.4: Comparison of the best-fit DC14 models to the $M_{\text{halo}} - c$ relation from Dutton & Macciò (2014) (left) and the $M_* - M_{\text{halo}}$ relation from Behroozi et al. (2013) (right). The error bars correspond to the extremal values of the multidimensional 68% confidence region for each fit. The theoretical relations are shown as red lines and their 1σ and 2σ scatter are represented by the dark and light grey bands, respectively. The mass-concentration relation from Macciò et al. (2008) and the stellar mass-halo mass relation from Moster et al. (2010) are also shown as the black dashed lines.

models prefer the Dutton & Macciò (2014) relation over the Macciò et al. (2008) relation that was used as prior is a good illustration of this.

Our analysis contradicts the results from Pace (2016). We do not recover the huge range of halo concentrations that he found and we find no evidence for his claim that galaxies with $M_* \lesssim 10^9\ M_\odot$ often reside in less massive haloes than predicted. It should be noted here, though, that the modelling strategy from Pace (2016) is somewhat different than our approach and that used by Katz et al. (2017). Pace (2016) used multi-nested sampling (e.g. Feroz & Hobson 2008) to fit his models and did not assume any physical priors between the parameters. The lack of priors results in posterior distributions that often contain multiple modes (or peaks). The mode with the lowest halo mass was selected as the final mode and galaxies for which the modes were too wide or not well separated were discarded. To investigate the effects of these differences, we performed a second set of fits without physical priors and used the criteria from Pace (2016) to select the final models. The results are shown in Fig. 5.5. CVnIdwA, UGC 8508, NGC 3741, NGC 3109, IC 2571 and NGC 2976 were discarded because their posterior distributions showed multiple blended modes; this was not the case in the original fits because the priors suppressed the additional modes. The best-fit model for WLM has shifted significantly. It is still consistent with the mass-concentration relation but now lies considerably

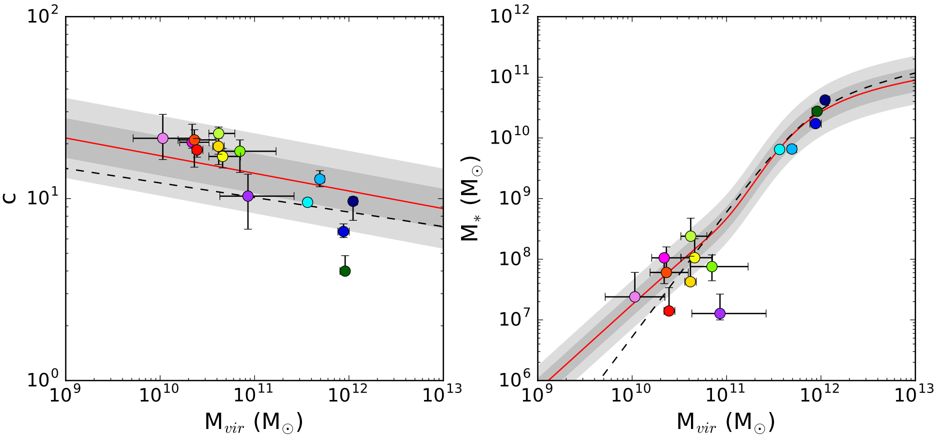

Figure 5.5: Comparison of the parameters of the DC14 fits performed according to the strategy from Pace (2016) to the $M_{\rm halo} - c$ relation from Dutton & Macciò (2014) (left) and the $M_* - M_{\rm halo}$ relation from Behroozi et al. (2013) (right). Colours are as in Figure 5.4.

below the stellar mass-halo mass relation. For the remaining galaxies, the new models are essentially similar to the previous models or consistent within the uncertainties. The agreement with the scaling relations is still remarkably good, and although the number of galaxies is limited, we still find no evidence for the strong deviations that were reported by Pace (2016).

5.4.2 coreNFW

For the coreNFW halo, we limit our analysis to the lower mass galaxies with $M_{\rm halo} \lesssim 7 \times 10^{10}\ M_\odot$. The individual cNFW fits for these galaxies are shown in Figure 5.6. The models again provide a decent description of the data, with no clearly bad fits, except for DDO 168. The fit results are compared to the cosmological scaling relations in Fig. 5.7. The agreement is very good and our models again seem to prefer the mass-concentration relation from Dutton & Macciò (2014) over that from Macciò et al. (2008).

coreNFW models were also fitted to the same rotation curves by Read et al. (2017). Their results for the individual galaxies sometimes differ significantly from what is found in this work: Read et al. (2017) generally find somewhat lower halo and stellar masses, higher concentrations and a better fit quality (lower $\chi^2_{\rm red}$). These differences are, however, not unexpected. Indeed, while we use the measured surface density profiles from Oh et al. (2015) to derive the stellar and gas contributions (v_* and $v_{\rm gas}$), Read et al. (2017) use smooth exponential surface density profiles based on the measurements of Zhang et al. (2012) and Oh et al. (2015). In addition, Read et al. (2017) use the M_{200} formalism while we use the *virial* mass M_{vir}, so the halo parameters given in their Table 2 should not be

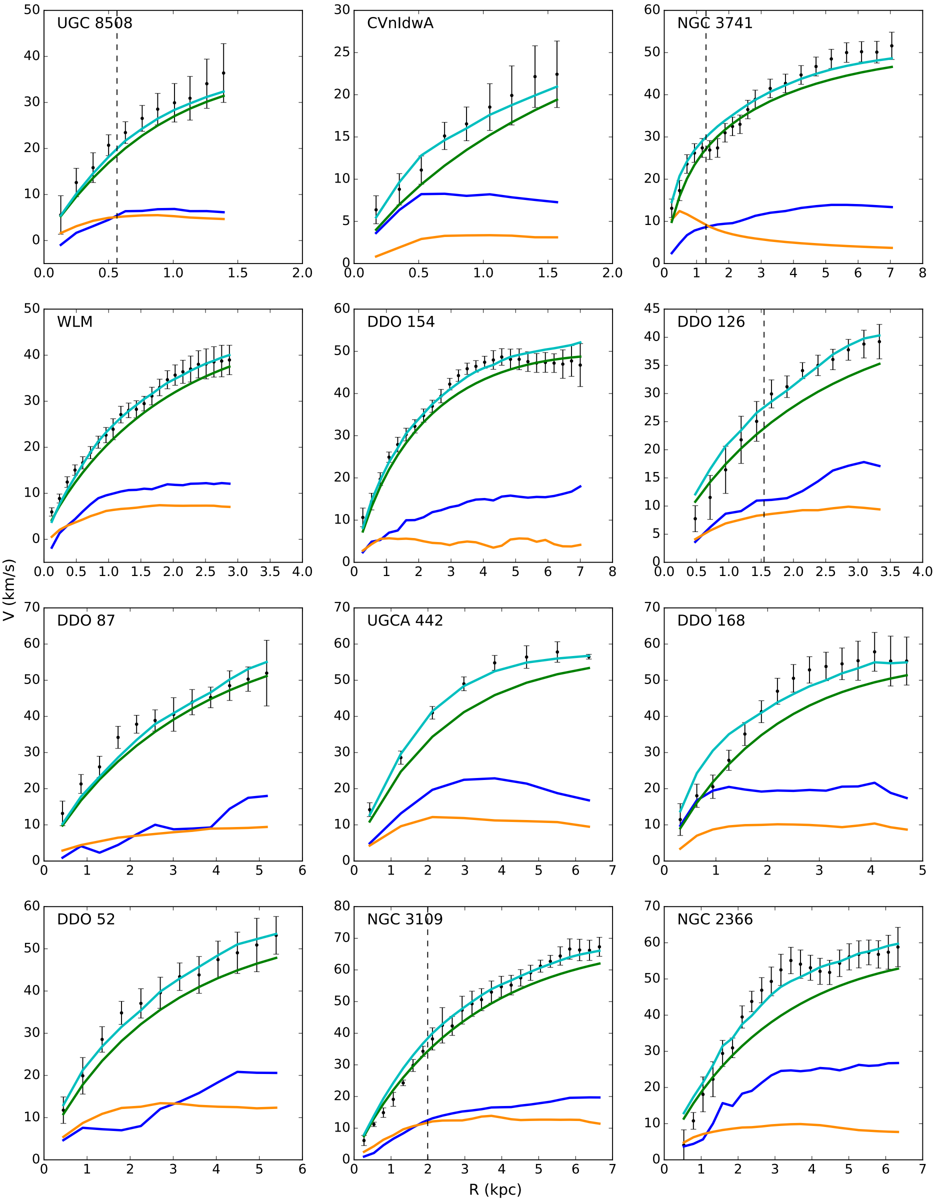

Figure 5.6: Decomposition of the rotation curves in our sample according to the maximum likelihood coreNFW models. Colours and symbols are as in Figure 5.3.

compared directly to our values in Table 5.2. For an identical dark matter halo, our virial mass and concentration should be somewhat higher than the M_{200} and c_{200} values from Read et al. (2017). The fact that we generally find lower concentrations probably comes

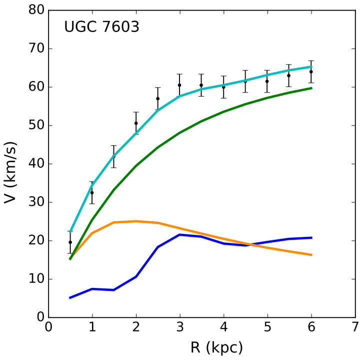

Figure 5.6: continued.

from the fact that Read et al. (2017) do not use a mass-concentration prior. Instead, they set the boundaries for the concentration range in their fits by plugging the edges of their M_{200} range in the $M_{\rm vir}$-c relation from Macciò et al. (2007). Finally, the rotation curve of NGC 2366 that is reported by Iorio et al. (2017) differs from the curve that is used by Read et al. (2017), although the latter refer to the former as data source. As already indicated by de Blok et al. (2008) and Oh et al. (2008), significant non-circular motions occur in the outer regions of the gas disk of NGC 2366, beyond radii of about 4.5 kpc. However, since the differences between the two rotation curves occur at all radii (and in particular in the central 2 kpc), a different treatment of these non-circular motions still does not fully explain the discrepancy.

Despite these individual differences, the main conclusions do remain the same. Both works generally find acceptable fits to the data and a good agreement with the stellar mass-halo mass relation.

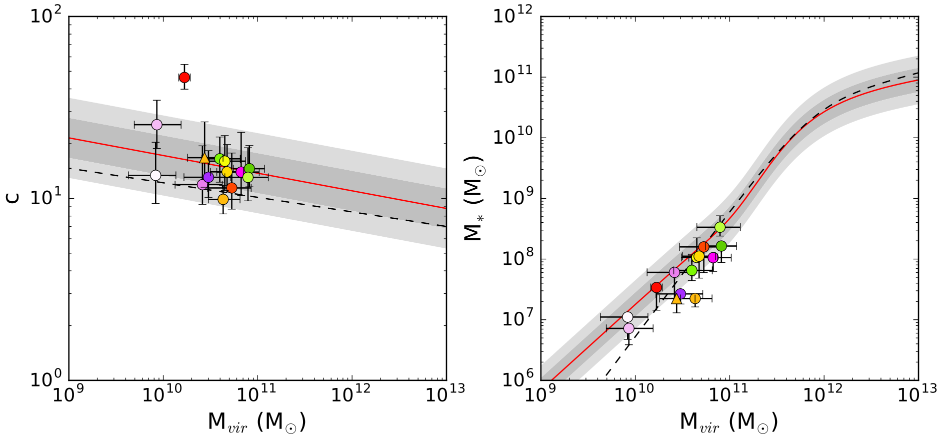

Figure 5.7: Comparison of the best-fit cNFW models to the $M_{\text{halo}} - c$ relation from Dutton & Macciò (2014) (left) and the $M_* - M_{\text{halo}}$ relation from Behroozi et al. (2013) (right). Colours are as in Figure 5.4. The triangle represents the best-fit model for NGC 3741 from a fit with the core radius as a free parameter (see section 5.4.3).

Table 5.2: Parameters and fit quality of the maximum likelihood DC14 and coreNFW models for the galaxies in our sample.

	DC14				cNFW				
Galaxy	$\log_{10}(M_{\rm vir})$ ($M_\odot$)	c	$\log_{10}(M_*)$ ($M_\odot$)	$\chi^2_{\rm red}$	$\log_{10}(M_{\rm vir})$ ($M_\odot$)	c	$\log_{10}(M_*)$ ($M_\odot$)	$r_{\rm c}$ (kpc)	$\chi^2_{\rm red}$
UGC 8508	$9.83^{+0.22}_{-0.30}$	$30.84^{+6.60}_{-5.49}$	$6.86^{+0.00}_{-0.42}$	0.42	$9.85^{+0.26}_{-0.24}$	$25.43^{+9.23}_{-6.61}$	$6.86^{+0.00}_{-0.27}$	1.09	0.61
CVnIdwA	$9.57^{+0.44}_{-0.24}$	$16.84^{+3.21}_{-2.97}$	$6.68^{+0.42}_{-0.00}$	0.34	$9.84^{+0.21}_{-0.29}$	$13.39^{+6.97}_{-4.02}$	$7.04^{+0.06}_{-0.37}$	3.12	0.41
NGC 3741	$10.43^{+0.12}_{-0.10}$	$15.52^{+2.02}_{-1.91}$	$7.35^{+0.00}_{-0.16}$	0.18	$10.55^{+0.18}_{-0.16}$	$9.88^{+1.92}_{-1.66}$	$7.35^{+0.00}_{-0.14}$	0.60	1.23
NGC 3741*					$10.35^{+0.20}_{-0.18}$	$16.75^{+9.59}_{-5.22}$	$7.35^{+0.00}_{-0.24}$	$4.06^{+1.75}_{-1.48}$	0.19
WLM	$10.07^{+0.32}_{-0.21}$	$20.94^{+4.09}_{-5.21}$	$7.00^{+0.26}_{-0.00}$	0.73	$10.39^{+0.24}_{-0.26}$	$13.07^{+5.23}_{-2.93}$	$7.43^{+0.00}_{-0.17}$	2.33	0.62
DDO 154	$10.30^{+0.06}_{-0.06}$	$20.29^{+1.36}_{-1.65}$	$7.53^{+0.00}_{-0.33}$	0.61	$10.14^{+0.06}_{-0.06}$	$46.23^{+8.30}_{-6.39}$	$7.53^{+0.00}_{-0.37}$	6.14	0.86
DDO 126	$10.04^{+0.29}_{-0.17}$	$19.50^{+3.59}_{-3.69}$	$7.36^{+0.42}_{-0.00}$	0.17	$10.33^{+0.21}_{-0.29}$	$11.91^{+7.54}_{-2.63}$	$7.78^{+0.00}_{-0.42}$	3.1	0.40
DDO 87	$10.30^{+0.14}_{-0.12}$	$21.74^{+2.78}_{-3.23}$	$7.71^{+0.31}_{-0.12}$	0.24	$10.74^{+0.19}_{-0.26}$	$13.96^{+9.13}_{-3.58}$	$8.02^{+0.00}_{-0.23}$	5.88	1.24
UGCA 442	$10.53^{+0.07}_{-0.06}$	$18.99^{+2.06}_{-1.61}$	$8.05^{+0.00}_{-0.39}$	0.65	$10.59^{+0.17}_{-0.18}$	$14.00^{+5.77}_{-3.17}$	$8.05^{+0.00}_{-0.36}$	3.34	0.63
DDO 168	$10.66^{+0.18}_{-0.18}$	$18.89^{+2.32}_{-1.89}$	$8.03^{+0.04}_{-0.31}$	1.61	$10.51^{+0.22}_{-0.19}$	$16.51^{+5.25}_{-4.23}$	$7.81^{+0.26}_{-0.17}$	2.73	2.2
DDO 52	$10.32^{+0.25}_{-0.14}$	$20.07^{+2.41}_{-5.11}$	$7.78^{+0.42}_{-0.00}$	0.20	$10.64^{+0.21}_{-0.26}$	$11.42^{+6.35}_{-2.69}$	$8.20^{+0.00}_{-0.42}$	3.99	0.30
NGC 3109	$10.86^{+0.13}_{-0.13}$	$16.96^{+1.86}_{-1.50}$	$8.22^{+0.00}_{-0.22}$	0.13	$10.83^{+0.16}_{-0.17}$	$14.57^{+4.95}_{-2.98}$	$8.22^{+0.00}_{-0.27}$	4.73	0.23
NGC 2366	$10.57^{+0.16}_{-0.12}$	$17.00^{+1.62}_{-2.50}$	$8.02^{+0.33}_{-0.00}$	0.93	$10.57^{+0.22}_{-0.16}$	$16.03^{+6.12}_{-4.98}$	$8.03^{+0.32}_{-0.00}$	5.07	1.25
UGC 7603	$10.60^{+0.32}_{-0.12}$	$19.48^{+4.16}_{-6.68}$	$8.50^{+0.31}_{-0.12}$	0.43	$10.81^{+0.22}_{-0.25}$	$13.06^{+5.93}_{-3.37}$	$8.53^{+0.19}_{-0.15}$	2.17	0.58

[*] cNFW fit with the core radius $r_{\rm c}$ as a free parameter.

Table 5.2: continued.

Galaxy	DC14			
	$\log_{10}(M_{\rm vir})$ $(M_\odot)$	c	$\log_{10}(M_*)$ $(M_\odot)$	$\chi^2_{\rm red}$
IC 2574	$11.15^{+0.14}_{-0.09}$	$9.63^{+0.29}_{-1.13}$	$8.83^{+0.17}_{-0.00}$	0.20
NGC 2976	$11.11^{+0.16}_{-0.11}$	$23.69^{+1.99}_{-3.97}$	$8.99^{+0.08}_{-0.00}$	0.43
M33	$11.48^{+0.03}_{-0.03}$	$9.53^{+0.50}_{-0.24}$	$9.81^{+0.00}_{-0.02}$	1.47
NGC 2403	$11.61^{+0.04}_{-0.04}$	$12.57^{+1.41}_{-0.93}$	$9.83^{+0.04}_{-0.05}$	0.56
NGC 3621	$11.85^{+0.06}_{-0.06}$	$6.66^{+0.69}_{-0.50}$	$10.23^{+0.03}_{-0.04}$	0.56
NGC 3198	$11.88^{+0.03}_{-0.07}$	$4.00^{+1.31}_{-0.14}$	$10.44^{+0.00}_{-0.08}$	1.04
NGC 5055	$11.96^{+0.05}_{-0.02}$	$9.59^{+0.58}_{-2.06}$	$10.63^{+0.05}_{-0.00}$	0.68

5.4.3 coreNFW versus DC14

The coreNFW halo model determines the strength of the dark matter core from the total time that the galaxy has been forming stars, while the radial extent of the core is related to the spatial distribution of the stars via the stellar half-mass radius. The stellar mass of the galaxy is not used. This is an important difference with the DC14 profile. On the one hand, DC14 uses M_* instead of $t_{\rm SF}$ as a measure of the amount of supernova feedback energy that has become available to form a core. On the other hand, this model also uses the additional gravitational potential due to M_* as a mechanism to counteract core formation.

Given these rather different approaches, it is interesting to investigate how the dark matter haloes inferred by the cNFW and DC14 halo models compare across our sample. Since the physical mechanism that drives core formation is essentially the same for both models (supernova feedback after bursts of star formation), they should in principle give similar results in the overlapping halo mass range where they are both appropriate.

Best-fit parameters

In Figure 5.8 we compare the main parameters of the best-fit DC14 and coreNFW models for the galaxies with $M_{\rm halo} \lesssim 7 \times 10^{10}\ M_\odot$. With the exception of the unphysically high concentration of the cNFW model of DDO 154, we find a fairly good agreement between the two models. The stellar and virial masses follow the identity line, albeit with some scatter, and the two models are generally consistent within the error bars. With

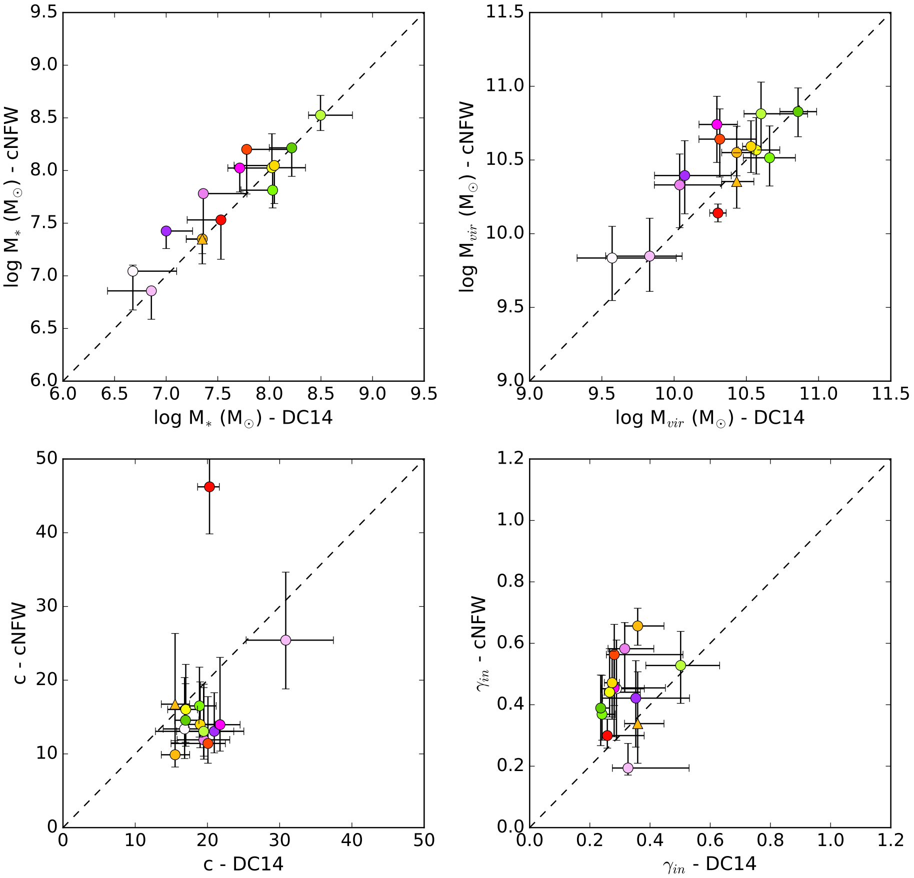

Figure 5.8: Comparison of the main parameters of the best-fit DC14 and cNFW models: stellar mass (top left), halo mass (top right), halo concentration (bottom left) and log slope of the dark matter density at the innermost point of the rotation curve (bottom right). The slopes in the latter plot were not measured in the actual centres of the galaxies and are therefore an upper limit to the real central slopes of the dark matter haloes. Colours and symbols are as in Figs 5.4 and 5.7.

the exception of DDO 154, the concentrations are also consistent within the uncertainties. The bottom right panel in Fig. 5.8 shows the log slope of the dark matter density profiles, measured at the innermost point of each rotation curve. This parameter strongly depends on the local shape of the density profile and should not be over-interpreted for the comparison between the two haloes. The main conclusion to be drawn is that both models find relatively cored dark matter haloes for all the galaxies, with inner log slopes that are generally not too far apart and often consistent within the uncertainties.

Despite the general consistency of the two models, there are some notable differences. First, there are several Little THINGS galaxies (CVnIdwA, WLM, DDO 126, DDO 87

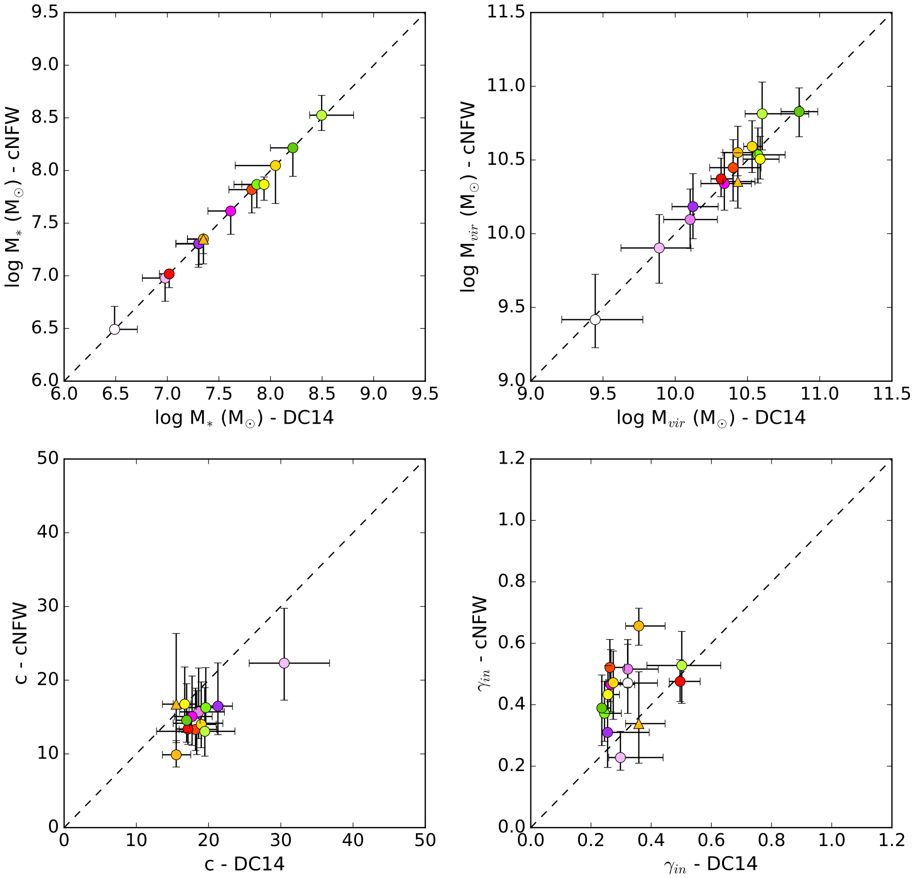

Figure 5.9: Comparison of the main parameters of the best-fit DC14 and cNFW models, using the baryonic profiles from Read et al. (2017) for the Little THINGS systems: stellar mass (top left), halo mass (top right), halo concentration (bottom left) and log slope of the dark matter density at the innermost point of the rotation curve (bottom right). Colours and symbols are as in Figure 5.8.

and DDO 52) for which cNFW finds both higher stellar masses and higher halo masses. In addition, the offset between the concentrations found by cNFW and DC14 is also highest for these same systems (and DDO 154). To investigate this consistent difference in more detail, we redid the fits of the Little THINGS galaxies with the exponential baryonic profiles from Read et al. (2017) instead of the original profiles from Oh et al. (2015). The results of these fits are listed in Table 5.3. Figures 5.10, 5.11, 5.12 and 5.13 illustrate that both models again provide excellent fits to the rotation curves and are in good agreement with the scaling relations. More interestingly, Figure 5.9 further shows that the concentration of DDO 154 and the stellar and halo masses of CVnIdwA, WLM, DDO 126, DDO 87 and DDO 52 are now in much better agreement for the two models.

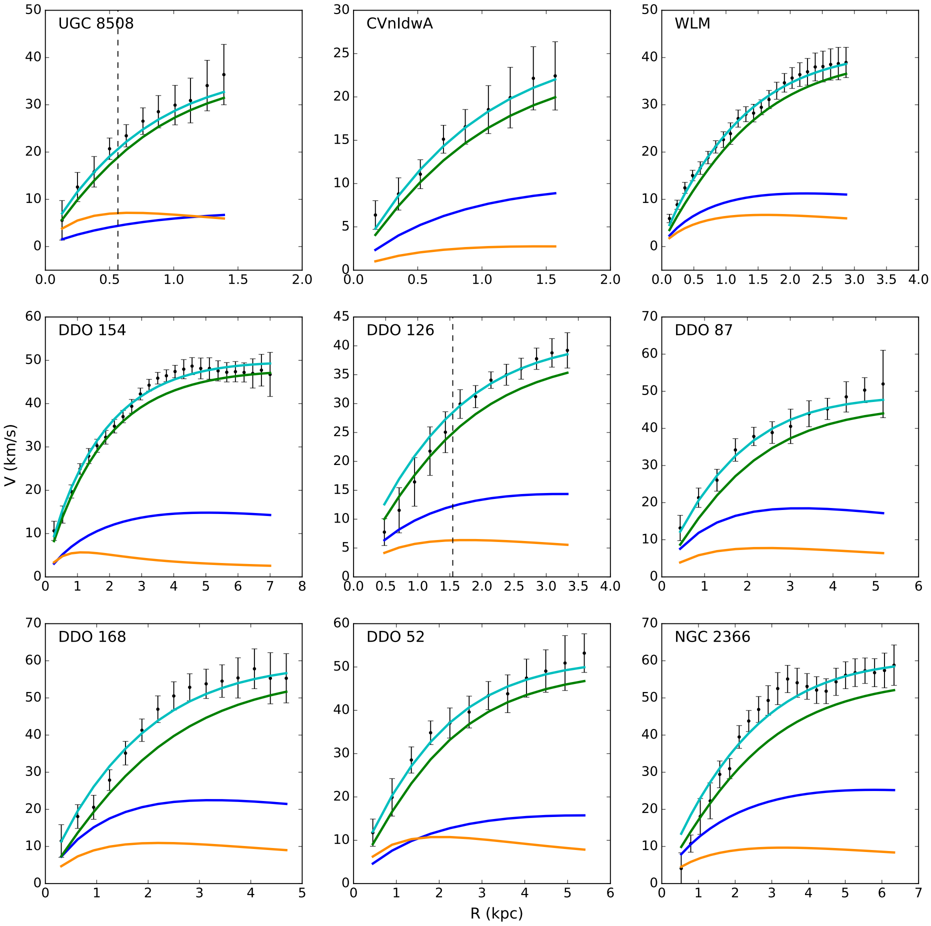

Figure 5.10: Decomposition of the Little THINGS rotation curves according to the maximum likelihood DC14 models, based on the baryonic profiles from Read et al. (2017). Colours and symbols are as in Figure 5.3.

For these same galaxies, the stellar and/or gas distributions used by Read et al. (2017) are systematically more compact than those inferred by Oh et al. (2015).

This indicates that the differences in the best-fit stellar and halo masses do not reflect fundamental differences in the core formation predicted by the simulations of Read et al. (2016a) and Di Cintio et al. (2014a), but are rather caused by the different functional form and parametrisation of the cNFW and DC14 models. Indeed, the DC14 model compensates for low central baryonic contributions with a compact dark matter core. For extended stellar distributions, the cNFW model cannot do this, because its core size is fully determined by the stellar half-mass radius. To compensate for the more extended core (giving less dark matter in the central regions), the cNFW model generally uses

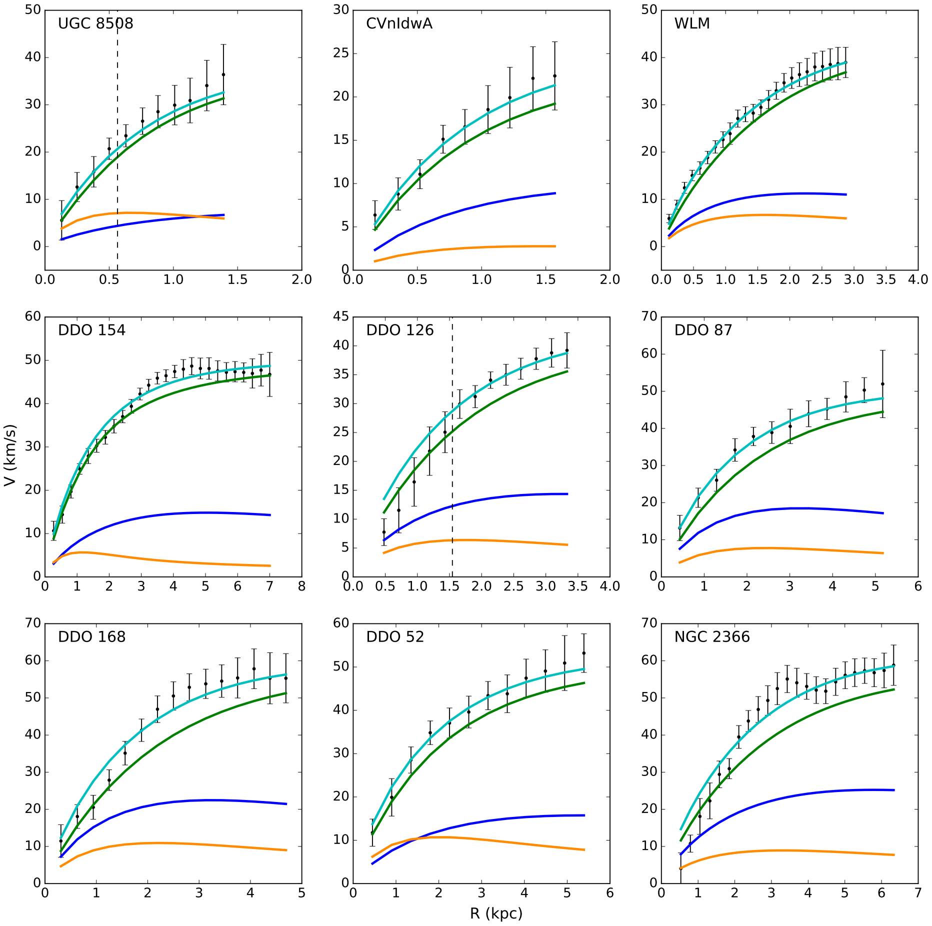

Figure 5.11: Decomposition of the Little THINGS rotation curves according to the maximum likelihood cNFW models, based on the baryonic profiles from Read et al. (2017). Colours and symbols are as in Figure 5.3.

somewhat higher stellar masses, higher halo masses and lower concentrations (i.e. less steeply falling dark matter density profiles). The less extended stellar distributions of Read et al. (2017) for CVnIdwA, DDO 154, DDO 126, DDO 87 and DDO 52 result in smaller cores and remove the need for larger stellar and halo masses.

On the other hand, the shape of the DC14 halo is fully determined by the stellar-to-halo mass ratio. As a consequence, DC14 has less freedom than cNFW to adapt these masses to optimise the fit. For WLM, the stellar half-mass radius is essentially the same in both data sets. However, the gas distribution from Oh et al. (2015) yields a considerably lower gas contribution to the central part of the rotation curve than that of Read et al. (2017). The cNFW model has more freedom to increase the stellar and halo mass in response to

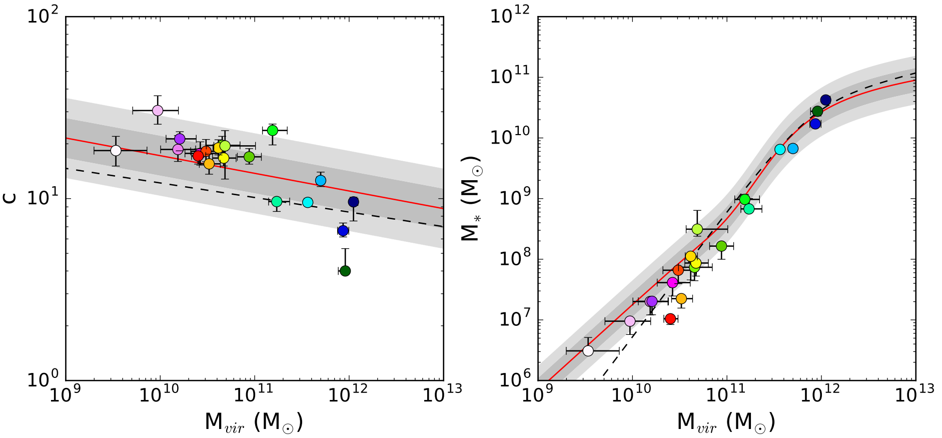

Figure 5.12: Best-fit DC14 models (based on the baryonic profiles from Read et al. (2017) for the Little THINGS systems) compared to the $M_{\mathrm{halo}} - c$ relation from Dutton & Macciò (2014) (left) and the $M_* - M_{\mathrm{halo}}$ relation from Behroozi et al. (2013) (right). Colours are as in Figure 5.4.

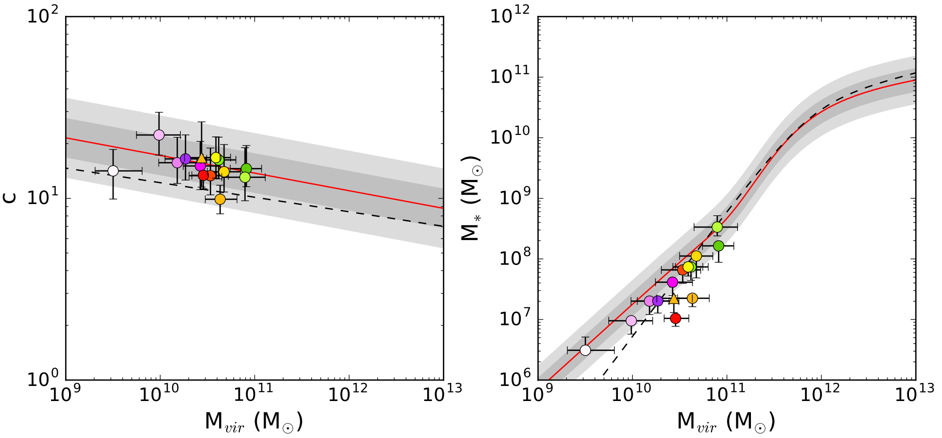

Figure 5.13: Best-fit cNFW models (based on the baryonic profiles from Read et al. (2017) for the Little THINGS systems) compared to the $M_{\mathrm{halo}} - c$ relation from Dutton & Macciò (2014) (left) and the $M_* - M_{\mathrm{halo}}$ relation from Behroozi et al. (2013) (right). Colours and symbols are as in Figure 5.4.

this.

A second difference between the two models is that DC14 consistently finds somewhat higher concentrations than coreNFW, regardless of which data set is used. This trend might be caused by the approximate conversion of the concentrations of the DC14 haloes to those of their primordial ancestors. With a modification of this factor by some 20 percent (which is not implausible, given Figure 4 from Di Cintio et al. 2014a), the agreement between the two models would already improve substantially.

Fit quality

If the gas and stellar data from Read et al. (2017) are used for the Little THINGS galaxies, we find very good agreement between the cNFW and DC14 models across the sample. As illustrated by the χ^2_{red} values in Tables 5.2 and 5.3, both models also give similar fit qualities and generally represent the data very well (more than well enough). The only exception is the rotation curve of NGC 2366, which is poorly represented by both models. As discussed in Section 5.4.1, this is probably caused by an issue with the data.
When the baryonic data from Oh et al. (2015) are used, the best-fit parameters from both models show more scatter. Generally, the fit quality does remain similar and it is not meaningful to classify one model as better than the other.

In three cases, however, the strong dependence of the cNFW core radius on the half-mass radius of the stars results in a poorer fit by the coreNFW model than by the DC14 model (for the profiles from Oh et al. 2015). For NGC 3741 and DDO 87, the rotation curves are fitted significantly better by the DC14 model than by the cNFW model. For DDO 154, the fit quality is good in both cases, but the coreNFW halo needs an unphysically high concentration to achieve this. cNFW models with a lower concentration do not fit the data well. For DDO 87 and DDO 154, the core radius derived from the stars seems too large. On the other hand, NGC 3741 has a very compact stellar distribution. This imposes a core radius for the cNFW model that seems much too small to explain the rotation curve.

At this point we should note that Read et al. (2017) do actually state that there could be some scatter in the ratio η between the core radius of the cNFW profile and the stellar half-mass radius. The value of $\eta = 1.75$ gives the best match to their simulated haloes, but is not claimed to be strictly valid for all dark matter haloes. This freedom in η is sufficient to improve the fit quality for DDO 87 and DDO 154. For NGC 3741, however, the upper limit of $\eta < 2.75$ ($r_c < 0.94$ kpc) is still far too low to explain the observed rotation curve. Indeed, a cNFW fit with η as a free parameter (Figure 5.14, and represented by the triangle in Figs 5.7, 5.8, 5.9 and 5.13) finds $\eta = 11.2$ ($r_c = 4.06$ kpc). This seems in strong contradiction with the upper limit from Read et al. (2017), but we remark that NGC 3741 is an unusual galaxy. In contrast to its compact stellar distribution, NGC 3741 does have a very extended gas disk. Since it is in fact the gravity of the outflowing gas after a supernova explosion that drives the formation of a dark matter core, we could interpret the extended gas distribution in NGC 3741 as a sign that the dark matter core radius is actually larger than inferred from the stars. This argument is further supported by the fact that the DC14 model does find sufficient stellar mass (i.e. supernova feedback energy) to form a substantial dark matter core.

In summary, we find that the works from Read et al. (2017) and Di Cintio et al. (2014a) are in agreement in the overlap of their respective mass ranges. The best-fit parameters

Table 5.3: Parameters and fit quality of the maximum likelihood DC14 and coreNFW models for the Little THINGS galaxies in our sample, based on the baryonic profiles from Read et al. (2017).

Galaxy	DC14				cNFW				
	$\log_{10}(M_{\rm vir})$ $(M_\odot)$	c	$\log_{10}(M_*)$ $(M_\odot)$	$\chi^2_{\rm red}$	$\log_{10}(M_{\rm vir})$ $(M_\odot)$	c	$\log_{10}(M_*)$ $(M_\odot)$	$r_{\rm c}$ (kpc)	$\chi^2_{\rm red}$
UGC 8508	$9.89^{+0.22}_{-0.26}$	$30.47^{+6.27}_{-4.85}$	$6.98^{+0.00}_{-0.22}$	0.39	$9.90^{+0.23}_{-0.24}$	$22.31^{+7.44}_{-5.02}$	$6.98^{+0.00}_{-0.22}$	0.91	0.40
CVnIdwA	$9.45^{+0.33}_{-0.23}$	$18.36^{+3.62}_{-3.27}$	$6.49^{+0.22}_{-0.00}$	0.23	$9.42^{+0.31}_{-0.19}$	$14.15^{+4.42}_{-4.25}$	$6.49^{+0.22}_{-0.00}$	1.14	0.21
WLM	$10.12^{+0.17}_{-0.15}$	$21.29^{+2.02}_{-3.00}$	$7.31^{+0.00}_{-0.22}$	0.36	$10.18^{+0.22}_{-0.22}$	$16.48^{+5.86}_{-3.88}$	$7.31^{+0.00}_{-0.20}$	2.21	0.24
DDO 154	$10.32^{+0.081}_{-0.07}$	$17.15^{+1.62}_{-1.67}$	$7.02^{+0.00}_{-0.10}$	0.66	$10.37^{+0.14}_{-0.12}$	$13.38^{+2.33}_{-2.08}$	$7.02^{+0.00}_{-0.13}$	1.59	1.23
DDO 126	$10.10^{+0.19}_{-0.18}$	$18.62^{+3.58}_{-2.63}$	$7.30^{+0.00}_{-0.22}$	0.12	$10.10^{+0.21}_{-0.20}$	$15.70^{+5.95}_{-3.63}$	$7.30^{+0.00}_{-0.22}$	2.41	0.10
DDO 87	$10.34^{+0.19}_{-0.16}$	$17.72^{+2.79}_{-2.44}$	$7.61^{+0.00}_{-0.22}$	0.27	$10.34^{+0.21}_{-0.18}$	$15.07^{+5.50}_{-3.91}$	$7.62^{+0.00}_{-0.22}$	3.32	0.25
DDO 168	$10.57^{+0.19}_{-0.17}$	$19.61^{+2.37}_{-2.31}$	$7.87^{+0.00}_{-0.22}$	0.76	$10.53^{+0.18}_{-0.19}$	$16.27^{+5.43}_{-3.48}$	$7.87^{+0.00}_{-0.22}$	3.02	1.09
DDO 52	$10.40^{+0.19}_{-0.16}$	$18.19^{+2.94}_{-2.27}$	$7.82^{+0.00}_{-0.22}$	0.19	$10.45^{+0.19}_{-0.23}$	$13.32^{+5.60}_{-2.87}$	$7.82^{+0.00}_{-0.22}$	2.76	0.22
NGC 2366	$10.59^{+0.13}_{-0.12}$	$16.70^{+1.65}_{-1.60}$	$7.94^{+0.00}_{-0.22}$	1.50	$10.51^{+0.15}_{-0.13}$	$16.75^{+5.04}_{-3.84}$	$7.87^{+0.07}_{-0.15}$	4.53	1.91

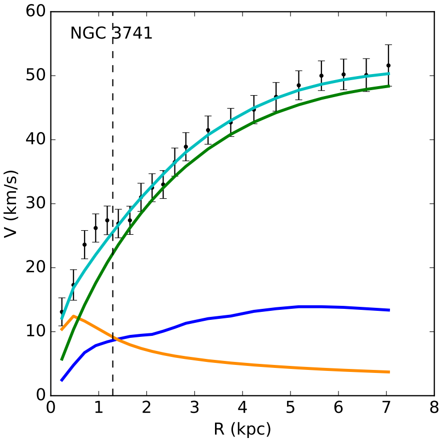

Figure 5.14: Decomposition of the rotation curve of NGC 3741 according to the best-fit coreNFW model from a fit with the core radius as a free parameter. Colours and symbols are as in Figure 5.3.

from the cNFW and DC14 models can show some minor differences, but are generally still consistent within the uncertainties. Furthermore, these differences do not reflect fundamental differences between the core formation predicted by both works, but are caused by the details of the parametrisations of the cNFW and DC14 models. In particular, if both are used as 3-parameter models, we find that the tight connection of the core radius to the stellar half-mass radius in the cNFW model is probably too strict to account for the full variety of galaxies in our sample.

Baryonic profiles

The difference between the baryonic profiles from Oh et al. (2015) and Read et al. (2017) is remarkable in some cases, such as for DDO 154 and DDO 87. It is, however, not straightforward, and beyond the scope of this work, to judge which source is more correct. On the one hand, the stellar data from Read et al. (2017) are based on the work of Zhang et al. (2012), who derived surface density profiles from SED models of the full stellar content. These are probably more accurate than 3.6 μm based profiles, since they also take the (small) contribution from the young stars into account. On the other hand, for DDO 154 and CVnIdwA, the data used by Zhang et al. (2012) only extend out half as far as the observations from Oh et al. (2015), missing an important part of the stellar mass. In addition, it is well known that the gas and stars in galaxies often show significant deviations from the simple exponential distributions that are assumed by Read et al. (2017).

In any case, the choice of the baryonic data does not strongly influence our conclusions.

5.4.4 Comparison to earlier results

Finally, it is interesting to compare our new physically motivated mass models to previous dynamical analyses of our target galaxies. Given the strong heterogeneity of these earlier studies (different halo profiles with different shapes and different parameters, different cosmologies, different assumed distances, different baryonic profiles, sometimes different rotation curves, etc.) a full quantitative comparison is not possible, and we focus on different aspects for different galaxies.

In addition to the study of Read et al. (2017), for which we already compared the results to our new cNFW models in section 5.4.2, Oh et al. (2015) also constructed mass models of the Little THINGS galaxies using their own rotation curves and baryonic profiles. First, they fitted cored pseudo-isothermal and cuspy NFW halo models to all the rotation curves, with fixed stellar mass-to-light ratios derived from population synthesis models. With the exception of DDO 154, they found that an NFW halo is not consistent with the data, giving bad fits to the rotation curves and/or unphysical parameter values. In a next part of their analysis, Oh et al. (2015) derived the dark matter density profiles directly by inverting the observed rotation curves (under the assumption of negligible baryonic masses) and estimated the inner log slopes from a power-law fit to these profiles. In agreement with their previous conclusion, they generally found inner slopes well below 1. Despite the somewhat different rotation curves, the inner slopes found by Oh et al. (2015) are generally consistent with our results within the uncertainties. The only deviations occur for WLM and DDO 168, where Oh et al. (2015) found inner slopes of $\gamma_{\text{in}} = 0.02 \pm 0.01$ and $\gamma_{\text{in}} = -0.97 \pm 0.18$ (i.e. a *rising* central density profile), respectively. Both these values seem rather extreme, so deviations are not unexpected.
For the SPARC galaxies in our sample, previous studies (Jobin & Carignan 1990; Côté et al. 2000; Blais-Ouellette et al. 2001; van den Bosch & Swaters 2001; Gentile et al. 2007) were essentially restricted to comparing cuspy (NFW) and cored (pseudo-isothermal, Burkert) dark matter models, with the general conclusion that the NFW halo provides a bad or unphysical fit. The cored models of both the SPARC and the Little THINGS galaxies also yielded a value for the core radius, i.e. the radius where the log slope of the dark matter density profile reaches a value of 1 (for the pseudo-isothermal halo) or 1.5 (for the Burkert halo). For the cNFW halo, the core radius does not have such a consistent interpretation, because the log slope profile also depends on the properties of the original NFW halo and on the value of the core radius itself (instead of only r/r_{c}). Hence, one should not compare the core radii of the previous studies to our values too strictly. On the other hand, the outliers in this comparison are interesting. While the old and new core radii generally differ by up to a factor of $2-3$, two galaxies clearly stand out. For DDO 154, the cNFW core radius is 6.5 times larger than the value from a pseudo-isothermal fit, while for NGC 3741 it is 5.3 times smaller than the Burkert value. These large differences are well in line with our conclusion from section 5.4.3, where we argued that the core radii derived from the stellar distribution are respectively significantly too large and too small for DDO 154 and NGC 3741.

de Blok et al. (2008) and Corbelli et al. (2014) also fitted pseudo-isothermal and NFW halo models to their rotation curves of the THINGS galaxies and M33, respectively. For the study of de Blok et al. (2008), we focus our comparison on the fits with free mass-to-light ratios, as these are closest to our fit strategy. For IC 2574 and NGC 2976, de Blok et al. (2008) found that a NFW halo could not explain the rotation curves. In contrast, the rotation curves of M33 and the other THINGS galaxies in our sample were fit equally well or even better by a NFW halo than by a pseudo-isothermal halo, although NGC 5055 requires an unphysically high concentration. This is in excellent agreement with the central slopes of our new mass models. Indeed, for IC 2574 and NGC 2976 we find shallow inner slopes of $\gamma_{\rm in} = 0.33$ and 0.45, respectively. For M33, NGC 2403, NGC 3621 and NGC 3198, the inner slopes range from 0.73 to 1.11. Finally, For NGC 5055, we find a rather steep inner slope of $\gamma_{\rm in} = 1.28$, which might explain the high concentration that was found by de Blok et al. (2008) for a NFW fit. The halo mass and concentration of M33 as retrieved by Corbelli et al. (2014) are also in excellent agreement with our values. For the THINGS galaxies, the comparison is less straightforward, because of the different parametrisation. Converting the c_{200} and V_{200} values from de Blok et al. (2008) to c and $M_{\rm vir}$ according to Coe (2010), we find that our halo masses and concentrations are systematically lower than the pure NFW values. It will be interesting to redo the NFW fits of these galaxies in the context of our analysis (with our assumed distances, parameter ranges and parametrisation) to see whether this result is truly intrinsic. However, such an analysis is beyond the scope of this work.

5.5 Conclusions

For a sample of 13 galaxies, spanning the mass range $M_{\rm halo} \sim 4 \times 10^9 - 7 \times 10^{10} M_\odot$, we modelled the rotation curves to compare two recently proposed dark matter density profiles: the DC14 halo and the coreNFW halo. We further applied the DC14 halo to an additional set of higher mass galaxies with $M_{\rm halo} \sim 10^{11} - 9 \times 10^{11} M_\odot$.

We found that both models generally provide acceptable fits to the rotation curves in our sample and find dark matter haloes that are in good agreement with the cosmological $M_{\rm halo} - c$ and $M_* - M_{\rm halo}$ relations. This confirms the results from Read et al. (2017) for coreNFW and from Katz et al. (2017) for DC14. On the other hand we found no evidence of the huge scatter in concentrations or the disagreement of the DC14 predictions with the $M_* - M_{\rm halo}$ relation that were recently claimed by Pace (2016), even if a similar modelling strategy is used.

The DC14 and coreNFW models furthermore converge to the same solutions. Some scatter in the best-fit parameters can be present, but this generally remains within the uncertainties of the fits. The small differences seem caused by the different parametrisations used to represent the simulated haloes, rather than true differences in the predicted core formation. In particular, in its original 3-parameter form, the cNFW model has less freedom to set the extent of the dark matter core. In some cases, this causes the cNFW model to represent the data less well than the DC14 model. NGC 3741, with its unusually compact stellar distribution, is a prime example of this.

Despite these minor differences, we conclude that the cNFW and DC14 haloes are generally consistent. Hence, the combined works of Di Cintio et al. (2014b) and Read et al. (2016a) give a coherent picture of baryon-induced dark matter core formation over a large mass range. This alleviates the cusp-core controversy and brings ΛCDM in agreement with observed rotation curves.

Summary and outlook

6

6.1 Summary

Galaxies are vibrant systems and we are only beginning to understand how they work. The stars, gas and dust constantly interact with each other and each play their own crucial role in the complex play that is galaxy evolution. Even the dark matter appears to get swept up by these baryonic processes. Given the large variety of galaxy types and environments, the only way to gain insights in their internal household is to observe and link the various components in many galaxies, both globally and on spatially resolved scales. In this work, we have conducted a number of observational studies to better understand several aspects of this interplay. The focus was in particular on observations in the radio domain, tracing both the distribution and the kinematics of the cold interstellar gas.

At the onset of this work, Herschel FIR/submm observations of a number of nearby edge-on spiral and dust lane early-type galaxies had just been completed in the frame of the HEROES and FRIEDL projects. The goal of these observations was to measure the total dust mass and to map the 3D distributions of the dust and stars with radiative transfer models. In chapter 2 we have presented a complementary analysis of the atomic gas content of 6 of the 7 the HEROES spirals. For this purpose, new 21-cm observations taken with the GMRT were combined with archival interferometric data. Tilted-ring models of the full HI data cubes were constructed to recover the radial and vertical distribution of the gas, the orientation and geometry of the disks and the rotation curves of the galaxies. From our models, we find that the disks of all but one galaxy are not flat and show warps in one or multiple directions. For IC 2531 and NGC 5529, unmodelled peaks in the total HI maps are found to coincide with bright ridges in the position-velocity diagrams. This indicates the presence of prominent, projected spiral arms and helps to interpret similar features in the stellar and dust distributions. For three galaxies in the HEROES sample, we further find clear indications that they are currently interacting, or have recently interacted with neighbouring satellite galaxies. A clumpy coplanar ring of atomic gas is discovered just beyond the main disk of NGC 4217. To our knowledge, this ring has no optical counterpart and has not been reported before. Given its spatial and kinematical offset from the main gas disk, we suggest it could be the relic of a recent minor merger. For NGC 5529, Kregel et al. (2004) already noted HI bridges connecting this galaxy to two nearby companions. We further identify a radial inflow in the disk of this galaxy, which is probably linked to an ongoing accretion of gas from the companions. Shang et al. (1998) further reported the detection of a companion galaxy close to, and a giant stellar stream around NGC 5907. Our models reveal that the outer gas disk of this galaxy is heavily disrupted, with very strong warps and large asymmetries between both sides. Finally, we also detect a new satellite galaxy of NGC 973 in our GMRT data cube.

Based on the rotation curves and atomic gas surface density profiles from this analysis, we have subsequently constructed mass models of the HEROES galaxies in chapter 3. The dynamical contributions of the stars were derived from preliminary bulge-disk decompositions of 3.6 μm images from Mosenkov et al. (2016) and Mosenkov et al. (in prep). Molecular gas was further also included for NGC 5907 based on literature data. For NGC 5907 and NGC 4013, the central parts of our rotation curves are likely affected by a central bar potential. To quantify this effect, we have attempted to model the bar in NGC 5907 by means of a bisymmetric distortion. Unfortunately, due to the edge-on orientation, the data do not offer sufficient constraints to find a unique representation of the bar or the associated corrections to the rotation curve. A general uncertainty of 50 km s^{-1} is therefore assigned to the rotation curves in the central regions of NGC 5907 and NGC 4013.
Using an MCMC approach to perform the fits and a general (α,β,γ) profile to represent the dark matter, we find good fits to the rotation curves of all the HEROES systems, with dark matter haloes that are in good agreement with the cosmological stellar mass-halo mass relation. Unfortunately, these solutions are far from unique, because our rotation curves do not (or not accurately) probe the central regions of the galaxies. Even when the outer slope of the dark matter density profile is fixed to the NFW value (3), our mass modelling provides very little constraints on the shape of the dark matter haloes.

In chapter 4 we turned our attention to the gas content of the northern and equatorial galaxies from the FRIEDL sample. An observing campaign was set up to supplement the sparse literature data for these systems. IRAM 30-m observations of the CO(1-0) and CO(2-1) lines were performed for five galaxies to trace their molecular gas content. This resulted in clear detections for two galaxies and upper limits to the molecular gas mass for the other three systems. In two cases (NGC 5485 and NGC 3497), however, these upper limits are uncertain because of the unfavourable weather conditions during the observations. The atomic gas content of four FRIEDL systems was further observed with the 100-m GBT telescope. HI emission is detected for two of these galaxies (NGC 2534 and NGC 3497) and atomic gas mass upper limits are obtained for the remaining two systems. For NGC 3497, however, the large observational beam of the GBT also includes its nearby companion NGC 3529. Similar source confusion is also present in the GBT HI data of NGC 2907 from Richter & Huchtmeier (1987). To resolve this confusion, we used the JVLA to conduct higher resolution interferometric observations of these two systems. NGC 2907 is clearly detected in these new data, with a total flux close to that reported by Richter & Huchtmeier (1987). In the data cube of NGC 3497, on the other hand, we only detect HI emission from NGC 3529. For NGC 3497 itself we can only derive an upper limit to the atomic gas mass.

Combining our gas masses or upper limits with the data from the literature and the dust masses based on Herschel data, we find that the cold gas-to-dust ratios of most of the galaxies in the sample are on the low side, but not abnormal. For NGC 5485, however, an extremely low GDR of $M_{\rm gas}/M_{\rm dust} < 16.5$ is found. Similarly, a value of $M_{\rm gas}/M_{\rm dust} < 24.8$ is obtained for NGC 3497, although the molecular gas mass of this system is uncertain and might be severely underestimated. Only a few other reliable studies of the GDR of dust lane ETGs are available in the literature. From these, it seems that GDRs of 50 – 100 might not be uncommon for dust lane ETGs, although values as low as that of NGC 5485 are not reported. Several potential explanations for this low gas-to-dust ratio are investigated. We find no evidence that the dust and cold gas masses are severely over- or underestimated. In addition, Hα and X-ray fluxes from the literature exclude the possibility that the bulk of the gas is in a warm or hot ionised state.

One option that remains is that NGC 5485 contains a large reservoir of CO-dark molecular gas, which was accreted through a merger with a very metal-poor dwarf galaxy. However, such systems do usually contain a significant amount of atomic gas. This must then have been stripped during the merger. Another exotic scenario is a merger with an ultra diffuse galaxy, if the latter was stripped of its gas when falling in the NGC 5485 group, but managed to retain a significant dust reservoir.

Finally, in chapter 5 we have used a similar mass modelling approach as in chapter 3 to test and compare two recently proposed models of supernova-driven core formation in dark matter haloes. The rotation curves of 13 dwarf galaxies, with halo masses in the range $4 \times 10^9 < M_{\rm halo}/M_\odot < 7 \times 10^{10}$, were modelled with both a coreNFW and a DC14 halo. Although they were actually derived for complementary mass ranges, both halo models should be valid in the mass range of this sample. The DC14 model was also applied to the rotation curves of an additional set of higher mass systems to verify its agreement with cosmological scaling relations.

We find that both the coreNFW and the DC14 halo generally give acceptable fits to the rotation curves and are in good agreement with the $M_{\rm halo} - c$ and $M_* - M_{\rm halo}$ relations. This is in contradiction with the results from Pace (2016), who claimed strong disagreements between these scaling relations and the DC14 haloes obtained from rotation curve fits. Interestingly, our conclusion remains valid even if we use a similar modelling ap-

proach as in Pace (2016).
The cNFW and DC14 models are generally also consistent with each other, as they should be, although minor differences between the best-fit parameters from both models sometimes occur. By repeating some of the fits based on a different baryonic data set, we find that these offsets are most likely caused by the different functional form and parametrisation used by the cNFW and the DC14 model, and not by actual differences in the predicted core formation. We can therefore conclude that the works from Read et al. (2016a) and Di Cintio et al. (2014b) give a coherent picture of supernova-driven core formation over a large mass range and bring ΛCDM in agreement with observed rotation curves.

6.2 Outlook

The recent radiative transfer models of the face-on galaxies M51 (De Looze et al. 2014) and M31 (Viaene et al. 2017) have shown that resolving the details and asymmetries of the stellar and dust distributions is very important in radiative transfer studies. Although this is not possible for edge-on galaxies, these systems remain crucial to understand the vertical structure of spiral galaxies. The radiative transfer models of Mosenkov et al. (2016) and Mosenkov et al. (in prep) will still provide strong constraints on the vertical structure of the dust and the stars in the HEROES galaxies. It will be interesting to investigate how these are related to the vertical structure of the atomic gas from our tilted-ring models. In addition, we can look for correlations with the total HI mass or the maximum circular velocity. Indeed, Dalcanton et al. (2004) found that the vertical structure of the ISM might depend strongly on the disk mass. With the NHEMESES project covering the lower mass late-type spirals, we will be able to investigate this dependence in detail.

Our analysis of the FRIEDL galaxies has revealed that the cold gas-to-dust ratio of NGC 5485 must be extremely low, but we still don't know how low exactly. A similarly low value was also tentatively found for NGC 3497, although our molecular gas mass upper limit might be flawed. As a first step, it will be interesting to conduct deeper interferometric HI and CO line observations of these two galaxies, to measure exactly how much atomic and (CO-bright) molecular gas they contain and to look for diffuse tidal tails. Additionally, deep [CII] line observations with the SOFIA infrared telescope should tell whether a significant reservoir of CO-dark molecular gas is indeed present in NGC 5485 (and perhaps NGC 3497).
Minor mergers are a crucial ingredient in galaxy evolution and are considered as an important driver of star formation and source of fresh gas in the local Universe (e.g. Kaviraj et al. 2011; Kaviraj 2014b,a). The FRIEDL sample has revealed a large variety in the gas and dust properties of the relics of such minor mergers, and hence also in their progenitors or the merger process itself. In particular, the extremely low HI masses of several of the FRIEDL systems suggest that essentially the entire atomic gas reservoir could go lost (or perhaps became ionised) during the merger. With the increased capabilities and sensitivity of (future) observatories such as ALMA and the SKA, it will become feasible

to perform deep interferometric observations of the cold atomic and molecular gas in and around a much larger, statistically significant sample of dusty ETGs. This will allow us to investigate whether such massive gas loss is indeed an important side effect of the minor merger process and whether the low GDR of NGC 5485 is truly unusual, or in fact common among dusty ETGs. Combining these gas observations with measurements of the star formation rate will further provide better insights in how minor mergers drive cosmic star formation. Indeed, contrary to what is generally considered, Davis et al. (2015) found very low star formation efficiencies in their limited sample of dust lane ETGs, suggesting that minor mergers can also suppress star formation.

In chapter 5 we have found that the simulated dark matter haloes from Di Cintio et al. (2014b) and Read et al. (2016a) are consistent with each other and agree with observed rotation curves. As such, baryonic physics indeed offers an attractive solution to the cusp-core problem. In addition, plausible solutions for two other small-scale problems of ΛCDM, the missing satellites problem and the too big to fail problem, have also been found. Several authors have pointed out that very low mass haloes are efficiently stripped of their gas via e.g. tidal stripping or supernova feedback. This process is further facilitated by the UV-background that heats the gas. As a consequence, they are unable to form stars and remain undetected in observational surveys (e.g. Hambrick et al. 2011). Verbeke et al. (2017) further showed that for turbulent low-mass galaxies, basic HI rotation curves can significantly underestimate the true circular velocities. As a consequence, the true halo masses are higher than inferred observationally, alleviating the too big to fail problem. As Read et al. (2016a) pointed out, dark matter core formation also helps to solve these problems, because cored haloes are more easily stripped of their gas and have, for the same halo mass, lower central stellar velocity dispersions than cuspy haloes.

This, however, does not mean that all the problems of ΛCDM cosmology or the cold dark matter hypothesis are solved. On small scales, several observations, such as the rotation curves of tidal dwarf galaxies or the baryonic Tully-Fisher relation, are still better explained by modified gravity than by dark matter. In addition, recent studies have also encountered tensions with the Planck 2015 CMB measurements if a ΛCDM cosmology is assumed. Riess et al. (2016), for example, found a 3.4σ discrepancy between the Hubble constant H_0 that they measured directly from local redshifts and distances, and the value obtained from ΛCDM fits to the Planck 2015 data. Likewise, assuming a ΛCDM cosmology, Hildebrandt et al. (2017) found a 2.3σ tension between the value of the S_8 parameter inferred from the Planck data and the value that they obtained from a weak lensing analysis of a large part of the sky.

Hence, the search for a correct description of the Universe, be it as a modification or extension of ΛCDM or a radically new theory based on modified gravity, continues.

7

Samenvatting

Melkwegstelsels zijn ingewikkelde en dynamische systemen waarvan we de werking nog maar net beginnen te begrijpen. De sterren, het interstellaire gas en het interstellaire stof zijn voortdurend met elkaar in interactie en spelen elk hun eigen cruciale rol in het complexe spel dat galaxie evolutie heet. Zelfs de ‘passieve’ donkere materie blijkt meegesleurd en beïnvloed te worden door deze baryonische processen. Om melkwegstelsels echt te doorgronden moeten we dus al deze componenten samen beschouwen. Aangezien er ook veel verschillende types van melkwegstelsels bestaan en er een grote verscheidenheid is aan omgevingen waarin deze zich kunnen bevinden, dienen we dit bovendien te doen voor veel verschillende melkwegstelsels, zowel globaal als op kleinere schalen. In dit werk presenteren we enkele observationele studies die verschillende aspecten van de wisselwerkingen binnen en tussen galaxieën belichten. Daarbij ligt de focus voornamelijk op waarnemingen in het radio domein die zowel de verdeling als de bewegingen van het koude gas in melkwegstelsels traceren.

Het eerste deel van deze thesis kadert in twee onderzoeksprojecten die opgericht werden door de sterrenkunde groep van de UGent: HEROES en FRIEDL. Deze richten zich op twee verschillende sets van sterrenstelsels ‘op hun kant’ (ook wel ‘edge-on’ stelsels genoemd). HEROES onderzoekt massieve spiraalgalaxieën, terwijl FRIEDL zich richt op vroeg-type (elliptische) stelsels met een stofband. Bij de aanvang van het werk in deze thesis was een reeks ver-infrarood waarnemingen van deze stelsels met de Herschel satelliet net voltooid. Doel van deze waarnemingen was om de totale stofmassa te bepalen en de driedimensionale verdeling van het stof en de sterren nauwkeurig te achterhalen aan de hand van stralingsoverdracht modellen.
In hoofdstuk 2 presenteren we aanvullend hierop een gedetailleerde analyse van het atomaire gas in de HEROES stelsels. Hiertoe werden observaties uit de literatuur aangevuld

met nieuwe interferometrische waarnemingen van de Hı 21-cm lijn, uitgevoerd met de GMRT telescoop in India. Aangezien we de HEROES stelsels op hun kant waarnemen, zien we eigenlijk de projectie van de volledige schijven op het hemelvlak. Om desondanks toch de geometrie van de galaxie-schijven, de radiale en verticale distributie van het gas en de rotatiecurves van de stelsels te kunnen achterhalen, werd voor elk HEROES stelsel een zogenaamd driedimensionaal 'tilted-ring' model gemaakt, dat zowel de verdeling als de bewegingen van het gas representeert. Uit deze modellen vinden we dat de gasschijven van op één na alle HEROES stelsels afgebogen zijn in een of meerdere richtingen. Voor IC 2531 en NGC 5529 slagen we er verder in om pieken in de geprojecteerde densiteitsverdeling van het gas te identificeren met prominente spiraalarmen in de schijf. Deze vondst is belangrijk voor de correcte interpretatie van gelijkaardige pieken in de geprojecteerde verdeling van de sterren en het stof, waar geen kinematische informatie beschikbaar is.

Voor drie HEROES stelsels vinden we ook duidelijke aanwijzingen van recente of nog steeds voortdurende interacties met naburige satellietstelsels. Zo detecteren we net buiten de schijf van NGC 4217 een bijkomende klonterige ring van atomair gas. Deze werd, voor zover wij weten, nooit eerder door iemand opgemerkt. Aangezien deze ring zowel ruimtelijk als kinematisch afgescheiden is van NGC 4217, is het waarschijnlijk een overblijfsel van een satellietstelsel dat recent werd opgepeuzeld door NGC 4217. In de gasschijf van NGC 5529 detecteren we dan weer een inwaartse stroombeweging. Deze is hoogstwaarschijnlijk het gevolg van gas dat door NGC 5529 uit twee naburige stelsels wordt aangezogen. Verder vinden we dat de gasschijf van NGC 5907 sterk gebogen en zeer asymmetrisch is in de buitenste regionen. Dit versterkt eerdere vermoedens van een recente interactie op basis van optische waarnemingen van de sterren. Tenslotte melden we ook nog de ontdekking van een nieuw, klein satellietstelseltje bij NGC 973.

Op basis van de rotatiecurves en de atomaire gasprofielen uit de bovenstaande analyse construeren we in hoofdstuk 3 vervolgens massamodellen van de HEROES stelsels. Hierbij wordt de gemeten rotatiesnelheid, die gelinkt is aan de totale gravitationele aantrekkingskracht in een melkwegstelsel, ontbonden in de bijdragen van de verschillende componenten, om uiteindelijk de massaverdeling van de donkere materie te kunnen achterhalen. De dynamische bijdrage van de sterren in elk HEROES stelsel werd afgeleid van voorlopige stellaire lichtprofielen uit het werk van Mosenkov et al. (2016) en Mosenkov et al. (in prep.). Op basis van waarnemingen uit de literatuur werd voor NGC 5907 ook het moleculaire gas in rekening gebracht.

Voor NGC 5907 en NGC 4013 worden de binnenste delen van onze rotatiecurves hoogstwaarschijnlijk beïnvloed door de aanwezigheid van een centrale balk. Om de correctie voor dit effect te bepalen, hebben we de centrale balk in NGC 5907 gemodelleerd door middel van een zogeheten bisymmetrische distorsie. Wegens de edge-on oriëntatie bieden de waarnemingen echter vrij weinig informatie. Verschillende representaties van de centrale balk blijken de data dan ook even goed te beschrijven, waardoor het niet mogelijk is om een unieke correctie voor de rotatiesnelheden te bepalen. Daarom werd in de centrale gedeeltes van de rotatiecurves van NGC 5907 en NGC 4013 een algemene onzekerheid van 50 km s^{-1} in acht genomen.

Gebruik makend van een algemeen (α,β,γ) profiel om de a priori onbekende donkere materie halo's te parametriseren, vinden we voor elk van de HEROES stelsels massamodellen die de rotatiecurves uitstekend reproduceren. De geassocieerde donkere materie halo's zijn bovendien in goede overeenstemming met de $M_* - M_{\rm halo}$ relatie die voorspeld wordt door de ΛCDM kosmologie. Helaas zijn deze modellen verre van uniek. Voor elk stelsel blijkt er een grote variëteit aan halo's te zijn die allen een gelijkwaardige fit aan de rotatiecurve geven. Zelfs wanneer we voor de buitenste regionen een vast NFW profiel aannemen, geven onze rotatiecurves helaas weinig uitsluitsel over de vorm van de donkere materie halo's.

In hoofdstuk 4 richten we onze aandacht op het koude gas in de vroeg-type stelsels van het FRIEDL project. Bij de aanvang van dit werk waren voor enkele van deze stelsels reeds waarnemingen van het atomaire en moleculaire gas beschikbaar in de literatuur, maar niet voor allemaal. Om de dataset voor het moleculaire gas te vervolledigen, werden voor vijf FRIEDL stelsels waarnemingen van de CO(1-0) en CO(2-1) lijnen uitgevoerd met de IRAM 30-m telescoop in Granada, Spanje. Moleculair gas werd hierbij duidelijk gedetecteerd voor twee stelsels en bovenlimieten voor de moleculaire gasmassa werden afgeleid voor de andere drie. Voor NGC 5485 en NGC 3497 zijn deze limieten echter onzeker wegens ongunstige weersomstandigheden tijdens het waarnemen. Verder werd het atomaire gas in vier FRIEDL stelsels geobserveerd met de GBT 100-m telescoop in Green Bank, West-Virginia. HI emissie werd hierbij gedetecteerd voor NGC 2534 and NGC 3497. Wegens de lage ruimtelijke resolutie van de waarnemingen, is het voor NGC 3497 echter niet duidelijk of de waargenomen emissie daadwerkelijk afkomstig is van dit stelsel, of (ook deels) van het nabijgelegen stelsel NGC 3529. Dergelijke 'source confusion' is ook aanwezig in de HI waarnemingen van NGC 2907 van Richter & Huchtmeier (1987), die met dezelfde telescoop werden uitgevoerd. Om de verwarring voor deze twee stelsels weg te werken, werden bijkomende, interferometrische waarnemingen uitgevoerd met de JVLA telescoop in New Mexico. Hierbij werd NGC 2907 duidelijk gedetecteerd, terwijl voor NGC 3497 bleek dat het signaal uit de GBT waarnemingen eigenlijk voornamelijk afkomstig is van NGC 3529.

Uit de combinatie van onze nieuwe gasmassa's (of bovenlimieten) met deze uit de literatuur en met de stofmassa's op basis van de Herschel data, werd vervolgens de totale gas-stof verhouding (gas-to-dust ratio of GDR) van de FRIEDL stelsels bepaald. Voor de meeste van deze stelsels vinden we GDR waarden die aan de lage kant zijn, maar niet abnormaal. Voor NGC 5485, echter, blijkt de gas-stof verhouding extreem laag te zijn ($M_{\rm gas}/M_{\rm stof} < 16.5$), veel lager dan wat tot nu toe voor andere stelsels is waargenomen. Analoog vinden we voor NGC 3497 ook een zeer lage waarde ($M_{\rm gas}/M_{\rm stof} < 24.8$), al dienen we hier op te merken dat onze bovenlimiet voor het moleculaire gas erg onzeker is.

Verschillende mogelijke verklaringen voor de extreem lage gas-stof verhouding van NGC

5485 werden onderzocht. Vooreerst vinden we na kritische evaluatie geen aanwijzingen voor een significante fout in de gas- of stofmassa. Verder kunnen we op basis van Hα en X-stralen waarnemingen ook de mogelijkheid uitsluiten dat een groot deel van het gas zich in een warme of hete geïoniseerde toestand bevindt. Een mogelijke verklaring die overblijft is dat NGC 5485 een grote hoeveelheid moleculair gas bevat met een zeer lage concentratie aan CO moleculen. Dergelijk gas werd inderdaad al aangetroffen in dwergstelsels met een lage metalliciteit. Zulke stelsels bevatten echter typisch ook een grote hoeveelheid atomair gas. Als het gas in NGC 5485 inderdaad afkomstig is uit de samensmelting met een dergelijk dwergstelsel, zou het atomair gas bij dit proces dus grotendeels verloren moeten gegaan zijn. Een andere mogelijke verklaring is de samensmelting met een zogenaamd ultra diffuus melkwegstelsel, dat het grootste deel van z'n gas verloor bij het binnenkomen van de galaxiegroep waartoe NGC 5485 behoort.

Tenslotte richten we onze aandacht op het cusp-core probleem, waarbij gravitationele simulaties van structuurvorming donkere materie halo's voorspellen die veel denser zijn in het centrum dan wat uit observationele rotatiecurves wordt afgeleid. Een aantrekkelijke oplossing voor dit probleem is dat de centrale delen van deze donkere materie halo's door opeenvolgende uitbarstingen van stervorming in melkwegstelsels geleidelijk aan uitzetten en minder dens worden. In hoofdstuk 5 testen en vergelijken we observationeel twee donkere materie profielen die dit proces in rekening brengen: de coreNFW halo (Read et al. 2016a) en de DC14 halo (Di Cintio et al. 2014a). Hiertoe construeren we, op basis van elk van deze profielen, massamodellen voor een set van rotatiecurves uit de literatuur. Deze rotatiecurves werden zo gekozen dat ze in het massagebied vallen waar beide modellen geldig zijn en dus dezelfde resultaten zouden moeten geven.
Uit onze analyse vinden we dat beide halo modellen een goede beschrijving geven van de observationele rotatiecurves en in goede overeenkomst zijn met de kosmologische $M_{\mathrm{halo}} - c$ en $M_{*} - M_{\mathrm{halo}}$ relaties. Dit resultaat weerlegt de eerdere bevindingen van Pace (2016), die voor DC14 een uitermate slechte overeenkomst vond met de kosmologische schalingsrelaties, maar is in overeenstemming de resultaten van Read et al. (2017) en Katz et al. (2017).
Verder vinden we dat de cNFW en DC14 modellen in het algemeen ook in overeenkomst zijn met elkaar. De exacte waarden van de parameters van beide modellen vertonen soms kleine verschillen, maar deze zijn het gevolg van de verschillende functionele vorm en parametrisatie van de twee profielen en niet van fundamentele verschillen in de voorspelde vorming van 'cores' in de donkere materie. We kunnen dus besluiten dat de simulaties van Read et al. (2016a) en Di Cintio et al. (2014b) consistent zijn en samen een coherent beeld geven van de vorming van donkere materie cores over een groot massabereik. Baryonische processen bieden dus inderdaad een realistische oplossing voor het cusp-core probleem.

Markov Chain Monte Carlo

A

A.1 Bayes' theorem

Ideally, when we decompose the rotation curve of a galaxy, we want to know the full (multi-dimensional) probability distribution function (pdf) of the parameters, rather than only the set of values that produces the best fit. In addition, instead of doing 'ignorant' fits, we would also like to incorporate physical knowledge about the parameters in the final pdf.

In the fitting process, a set of parameters is first translated to a model rotation curve, which is subsequently compared to the observed data points. In what follows, we will not explicitly mention this translation to a model curve any more, as it is the same in every iteration. For a certain set of observed data points d, the probability distribution function of the parameters x is typically noted as $P(x\,|\,d)$. According to Bayes' theorem, this can be decomposed as:

$$P(x\,|\,d) = \frac{P(d\,|\,x)\,P(x)}{P(d)}. \tag{A.1}$$

In this context, $P(x\,|\,d)$ is also known as the *posterior* probability. $P(d|x)$ is called the *likelihood*. It is the probability of measuring the data points d if the model curve based on the parameter values x is true. $P(x)$ is the *prior* and specifies our a priori physical knowledge about the parameters. Finally, $P(d)$ is called the *evidence*. It is a constant throughout the fitting process and will prove to be irrelevant in most cases.

In general, an analytic solution for the posterior pdf does not exist. Instead, we can only approximate it by sampling from it in large numbers. Markov Chain Monte Carlo or MCMC is the general name of a collection of algorithms that do this by constructing

Markov chains whose equilibrium or stationary distribution is exactly the desired pdf. MCMC is an extremely powerful technique that is widely used in astronomy and many other fields. Numerous books have been devoted to it. In this appendix, we restrict ourselves to a brief introduction.

A.2 Markov chains

A (discrete-time) Markov chain is a sequence of random variables (or random vectors) $X_1, X_2, ..., X_\mathrm{n}$, where the next value $X_\mathrm{n+1}$ depends only on the current state X_n, and not on the past. Or, more formally:

$$P(X_\mathrm{n+1} = x_\mathrm{n+1} \mid X_1 = x_1, X_2 = x_2, ..., X_\mathrm{n} = x_\mathrm{n}) = P(X_\mathrm{n+1} = x_\mathrm{n+1} \mid X_\mathrm{n} = x_\mathrm{n}). \tag{A.2}$$

Such a chain is fully defined by its transition kernel and can have either a continuous or a discrete state space. In the former case, the elements of the chain follow a continuous distribution and the transition kernel is given by:

$$K(x_\mathrm{n}, x_\mathrm{n+1}) = P(x_\mathrm{n+1} \mid x_\mathrm{n}). \tag{A.3}$$

In the case of a discrete state space, the elements of the chain can only take discrete values and the transition kernel is a matrix K_{xy}. A Markov chain is called irreducible if all the states communicate, i.e. if, for a discrete state space, every state is accessible from every other state in a finite number of steps.
An important property of a Markov chain is that it can have a stationary distribution of its elements $\pi(x)$ that is conserved by the transition kernel, such that (for a continuous state space):

$$\int \pi(x)\, K(x, y)\, dx = \pi(y). \tag{A.4}$$

If a Markov chain with a stationary distribution is irreducible, this stationary distribution is unique. If the chain is furthermore aperiodic (does not return to the same state after a fixed period), its final distribution after a large number of steps will always approach the stationary distribution, regardless of the initial distribution of the elements. The proof of these properties is beyond the scope of this appendix, but can for example be found in Levin et al. (2008).

The properties mentioned above are very important and imply that, with an appropriate choice of the transition kernel, we can build a Markov chain that samples a certain distribution of choice. If we wish to do that, however, we must make sure that the chain we build indeed has a stationary distribution. A way to guarantee this is via the *detailed balance* condition, which states that, for every pair of states (x, y), the transition between x and y is reversible. In other words, the probability of being in state x and going to state

y is exactly equal to the probability of being in state y and going to state x:

$$\pi(x)\, K(x, y) = \pi(y)\, K(y, x). \tag{A.5}$$

If this condition is met, the chain certainly has a stationary distribution, although the reverse is not necessarily true. Once again, we refer to Levin et al. (2008) for a formal proof of this property.

Since the 1950s, many algorithms have been devised to efficiently build Markov chains that sample a certain desired distribution. In the following sections, we discuss two of these.

A.3 Metropolis-Hastings

The Metropolis-Hastings (MH) algorithm is the oldest and most widely used MCMC algorithm. It was originally proposed by Metropolis et al. (1953) and later significantly improved by Hastings (1970). Suppose we have a dataset d, a model with parameters x and we are interested in sampling the multi-dimensional probability distribution function $P(x\,|\,d)$. The MH algorithm does this by constructing a Markov chain with a stationary distribution $\pi(x)$ that is proportional to $P(x\,|\,d)$. To find an appropriate transition kernel, the algorithm starts from the detailed balance condition:

$$\pi(x)\, K(x, y) = \pi(y)\, K(y, x). \tag{A.6}$$

The transition probability $K(x, y)$ is then split into a proposal distribution $g(x, y)$, used to propose a new state y based on the current state x, and an acceptance probability $A(x, y)$ which determines whether the proposed state y is accepted or not. Plugging this in the expression above gives:

$$\pi(x)\, g(x, y)\, A(x, y) = \pi(y)\ g(y, x)\, A(y, x), \tag{A.7}$$

which can be re-written as:

$$\frac{A(x, y)}{A(y, x)} = \frac{\pi(y)}{\pi(x)}\, \frac{g(y, x)}{g(x, y)}. \tag{A.8}$$

The above criterion still allows some freedom in the choice of the acceptance probability $A(x, y)$ (Barker 1965). The MH algorithm uses:

$$A(x, y) = \min\left[1, \frac{\pi(y)\, g(y, x)}{\pi(x)\, g(x, y)}\right], \tag{A.9}$$

which has been shown to be the most efficient choice (Peskun 1973).
In the original algorithm by Metropolis et al. (1953), the proposal distribution $g(x, y)$ was

taken symmetric (e.g. a Gaussian), such that the $g(y,x)$ and $g(x,y)$ terms cancel in the expression above. However, other choices also exist (for a brief but good overview, see e.g. Sharma 2017).
The desired stationary distribution $\pi(x)$ of the chain is of course unknown, as studying it is the whole purpose of constructing the Markov chain. At first sight, this poses a fundamental problem in equation A.9. However, for every set of parameter values x_i, we can rewrite it as (eq. A.1):

$$\pi(x_i) = P(d\,|x_i)\,P(x_i), \tag{A.10}$$

which we can calculate from the prior knowledge on the parameters and by comparing the data points d and their uncertainties with the model rotation curve that corresponds to x_i. The evidence term ($P(d)$) does not need to be specified, since it cancels out in the quotient in eq. A.9 anyway.

In practice, the MH algorithm is then executed as follows. Based on the current state of the chain x_n, a new point y in parameter space is randomly drawn from the proposal distribution g. From these two points, the ratio

$$a = \frac{\pi(y)\,g(y,x_\mathrm{n})}{\pi(x_\mathrm{n})\,g(x_\mathrm{n},y)} \tag{A.11}$$

is calculated. Subsequently, a uniform random number between 0 and 1 is drawn. If this number is smaller than a, the new point is accepted ($x_\mathrm{n+1} = y$). If not, the previous point is copied ($x_\mathrm{n+1} = x_\mathrm{n}$). This procedure is repeated until the desired length of the chain is reached.

The MH algorithm works well, but has the drawback that the efficiency of the algorithm depends strongly on the choice of the proposal distribution $g(x,y)$. Indeed, we want the Markov chain to have a high mixing rate (i.e. cover all the relevant areas of the unknown pdf in a limited number of steps). However, if the proposal distribution is too narrow, only nearby points are explored. Since these generally have similar probabilities, the acceptance rate of the chain is very high and the chain will need a lot of time to move to a different area of parameter space. On the other hand, if the proposal distribution is too wide, only distant points are proposed. Once the chain lands in or near a peak of the pdf, the proposed points will generally have much lower likelihoods and will hence not be accepted. The result is again that the chain will remain in the same location for a long time.
Various alterations of the MH algorithm have been derived that scale the proposal distribution on the fly. In addition, alternative schemes that do not involve an independent proposal distribution also exist. An example of such a scheme is the Gibbs sampler (Geman & Geman 1984). For an overview, we again refer the reader to Sharma (2017).

Even with an adaptive step size (width of the proposal distribution), MH-like algorithms have difficulties dealing with strongly skewed and anisotropic distributions. This can be illustrated with a two-dimensional pdf of the form:

$$p(x) = \frac{1}{\pi\sqrt{\beta}} \exp\left(-\frac{(x_1 + x_2)^2}{2\beta} - \frac{(x_1 - x_2)^2}{2} \right), \tag{A.12}$$

which is plotted in Figure A.1 for $\beta = 100$. The distribution has very different scales along the major and minor axes, but because it is skewed, this cannot be addressed by using different step sizes for x_1 and x_2. For both variables, a large step size results in good sampling of the pdf along the major axis, but poor sampling along the minor axis. A small step size has the opposite effect. Hence, MH-like algorithms are very inefficient for such distributions.

This problem does not occur for so-called affine invariant algorithms. An affine transformation is an $\mathbb{R}^n - \mathbb{R}^n$ transformation of the form $y = ax + b$, with a and b constant. If x is distributed according to $p(x)$, the distribution $p'(y)$ of y has the property:

$$p'(y) \propto p(x). \tag{A.13}$$

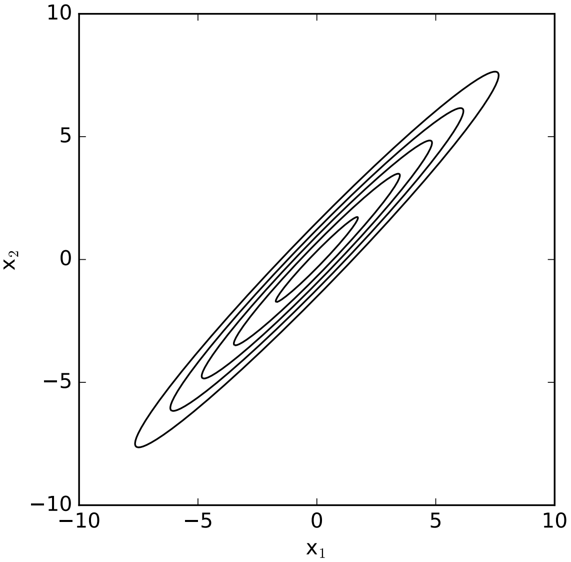

Figure A.1: Contour plot of the skewed distribution defined in eq. A.12 with $\beta = 100$.

Let us now consider a general MCMC sampler $x(t+1) = S\left(x(t), \pi\right)$, with $x(t)$ the t'th element of the chain and π the stationary distribution. Such a sampler is called *affine invariant* if, for any affine transformation $x \rightarrow ax + b$, $\pi \rightarrow \pi'$ (and a fixed random seed):

$$S\left(ax(t) + b, \pi'\right) = a\,S\left(x(t), \pi\right) + b. \tag{A.14}$$

In other words, for an affine invariant sampler (and a fixed random seed), the affine transformation $ax(t) + b$ of the t'th element of a chain with distribution π and starting point $x(0)$ will be equal to the t'th element of the chain with distribution π' and starting point $ax(0) + b$, for any t.

In the case of our example, the affine transformation

$$y_1 = \frac{x_1 + x_2}{\sqrt{\beta}} \qquad y_2 = x_1 - x_2 \tag{A.15}$$

yields a pdf

$$p'(y) \propto \exp\left(-\frac{y_1^2}{2} - \frac{y_2^2}{2}\right) \tag{A.16}$$

that no longer involves different scales and is thus much easier to handle for an MH sampler. For affine invariant samplers, on the other hand, the performance does not change under affine transformations and is thus the same for $p(x)$ as it is for $p'(x)$. This is a big advantage over MH samplers.

Goodman & Weare (2010) proposed a family of such affine invariant samplers that run multiple chains (called 'walkers') in parallel. These walkers are allowed to communicate with each other in such a way that the advancement of each walker is determined by the current state of the other walkers. The collection of these walkers is called an ensemble. Let us now consider an ensemble of L walkers $x_k \in \mathbb{R}^{\mathrm{n}}$: $X = (x_1, x_2, ..., x_{\mathrm{L}})$. While an MH sampler constructs a Markov chain on the $\mathbb{R}^{\mathrm{n}}$ state space, the ensemble samplers of Goodman & Weare (2010) can be considered to construct a Markov chain on the $\mathbb{R}^{\mathrm{Ln}}$ state space of ensembles. If the desired distribution of the individual walkers is $\pi(x)$, the target distribution for the ensemble Markov chain is:

$$\Pi(X) = \pi(x_1)\pi(x_2)\ldots\pi(x_{\mathrm{L}}), \tag{A.17}$$

where the individual walkers are independent.
An affine transformation is applied to such an ensemble by applying it to each of the individual walkers:

$$X = (x_1, x_2, ..., x_{\mathrm{L}}) \rightarrow Y = (ax_1 + b, ax_2 + b, ..., ax_{\mathrm{L}} + b). \tag{A.18}$$

If for a certain starting point $X(0) \rightarrow Y(0)$, an ensemble sampler is affine invariant if the t'th element of an ensemble chain with stationary distribution Π' and starting point $Y(0)$

is equal to the affine transformation of the t'th element of the chain with distribution Π and starting point $X(0)$.

In the ensemble samplers of Goodman & Weare (2010), an ensemble X is evolved from $X(t)$ to $X(t+1)$ by separately moving each walker x_k one step, based on the current state of all the other walkers

$$x_{[-k]}(t) = \left\{x_1(t+1),\, x_2(t+1),\, ...,\, x_{k-1}(t+1),\, x_{k+1}(t),\, ...,\, x_L(t)\right\} \tag{A.19}$$

(also called the complementary ensemble). The reason for doing this is that the position of the walkers in the complementary ensemble holds information about the desired distribution (π) that can be used to improve the proposed step for x_k. A consequence of this procedure is that the individual chains are no longer independent and Markovian. At first sight, this poses a serious problem. However, according to the idea of partial resampling (Sokal 1997; Liu 2008), the distribution $\Pi(X)$ of the ensemble chain will be preserved nonetheless, as long as the conditional transition $K(x_k,\, y_k \,|\, x_{[-k]})$ of the individual walkers conserves the conditional distribution $\pi(x_k \,|\, x_{[-k]})$ for each walker. This is easily shown:

$$\begin{aligned}\int \Pi(X) K(x_k,\, y_k \,|\, x_{[-k]}) dx_k &= \int \Pi(x_k,\, x_{[-k]}) K(x_k,\, y_k \,|\, x_{[-k]}) dx_k \\ &= \Pi(x_{[-k]}) \int \pi(x_k \,|\, x_{[-k]}) K(x_k,\, y_k \,|\, x_{[-k]}) dx_k \\ &= \Pi(x_{[-k]}) \pi(y_k \,|\, x_{[-k]}) \\ &= \Pi(Y),\end{aligned}$$

where we note the joint distribution of the complementary ensemble $x_{[-k]}$ as $\Pi(x_{[-k]})$ and Y is the ensemble with walker x_k updated to y_k. Like in the MH algorithm, the conservation of the conditional distribution $\pi(x_k \,|\, x_{[-k]})$ can be guaranteed by requiring detailed balance. This then means that the ensemble chain as a whole can still be considered to be made up of independent Markov chains with distribution π.

Goodman & Weare (2010) proposed several affine invariant ways to achieve this. The simplest one (and the one implemented in the `emcee` software package) is called the *stretch move*. In this scheme, the proposed step for the walker x_k is based on the position of one (randomly chosen) walker x_j from the complementary ensemble as:

$$y_k = x_j + z(x_k(t) - x_j). \tag{A.20}$$

In this expression, z is a scalar with distribution $g(z)$. The inverse step is given by:

$$x_k(t) = x_j + \frac{1}{z}(y_k - x_j). \tag{A.21}$$

Hence, the proposal is symmetric if the distribution $g(z)$ satisfies:

$$g(1/z) = zg(z). \tag{A.22}$$

The specific choice of $g(z)$ from Goodman & Weare (2010) is

$$g(z) \propto \begin{cases} \frac{1}{\sqrt{z}} & \text{for } z \in \left[\frac{1}{a}, a\right] (a > 0), \\ 0 & \text{otherwise.} \end{cases}$$

The a parameter is usually set to 2, but can be changed to improve performance in certain cases.

From the detailed balance condition, we get a similar constraint for the acceptance probability $A(x_k(t), y_k)$ as in eq. A.8, where the proposal distribution cancels out because it is symmetric. To find an appropriate acceptance probability, we first note that the proposal y_k is limited to a single line

$$\left\{ y \in \mathbb{R}^{\mathrm{n}} : \ y - x_j = \zeta(x_k(t) - x_j),\ \zeta > 0 \right\} \tag{A.23}$$

instead of the full n-dimensional hypersphere. The probability distribution along this line is proportional to

$$||y - x_j||^{\mathrm{n\text{-}1}}\, \pi(y). \tag{A.24}$$

(Goodman & Weare 2010). As a consequence, detailed balance is satisfied for an acceptance probability

$$A(x_k(t), y_k) = \min\left[1, \frac{||y_k - x_j||^{\mathrm{n\text{-}1}}\, \pi(y_k)}{||x_k(t) - x_j||^{\mathrm{n\text{-}1}}\, \pi(x_k(t))}\right] = \min\left[1, z^{\mathrm{n\text{-}1}} \frac{\pi(y_k)}{\pi(x_k(t))}\right]. \tag{A.25}$$

Other moves were also proposed by Goodman & Weare (2010), but we will not cover these here, as they are not used by the `emcee` package.

The stretch move algorithm is affine invariant and is executed in practice as follows. For each walker x_k (sequentially), a random scalar z is drawn from the distribution $g(z)$ and a walker x_j ($j \neq k$) is randomly selected from the complementary ensemble. From the current positions of the two walkers, a new position is then proposed as

$$y_k = x_j + z(x_k(t) - x_j). \tag{A.26}$$

A uniform random number is subsequently drawn between 0 and 1. If this number is smaller than the ratio

$$z^{\mathrm{n\text{-}1}} \frac{\pi(y_k)}{\pi(x_k(t))}, \tag{A.27}$$

the proposed position is accepted ($x_k(t+1) = y_k$). If it is larger, the previous position is copied ($x_k(t+1) = x_k(t)$). This procedure is performed sequentially for each individual walker, and repeated until the desired number of steps is reached. As a final step, the different walkers of the ensemble are combined into one large Markov chain (on the $\mathbb{R}^n$ state space) that samples the desired distribution $\pi(x)$.

A.5 Conversion diagnostics

When run for a sufficiently long time, the distribution of the elements of a Markov chain will converge to its stationary distribution (as mentioned in section A.2). This convergence is what we aim to achieve. However, it is a priori not possible to predict how many steps a given MCMC algorithm should take before convergence is achieved. After each MCMC run, it is therefore crucial to monitor whether the produced Markov chain has indeed converged. Various diagnostics have been proposed for this purpose. As the derivation of these diagnostics can be rather complex, we restrict ourselves to a brief description of the diagnostics that are used in chapters 3 and 5 of this work. For a complete overview, we refer the reader to Cowles & Carlin (1996), Brooks & Gelman (1998), or Robert & Casella (2005).

The MCMC work in this thesis is performed with the `emcee` python package, which uses the affine invariant stretch move sampler from Goodman & Weare (2010). For each fit, multiple chains are therefore run in parallel. A first diagnostic that we use to check the reliability of the fits is the overall acceptance rate r_{acc} for each walker, i.e. the fraction of the proposed steps that are accepted. This does not actually measure the convergence of the Markov chain, but it is a good indicator of the general performance of the algorithm. Indeed, as mentioned at the end of section A.3, both a high and a very low acceptance rate for a walker indicate that it moved slowly through parameter space and probably did not investigate the full posterior distribution. Gelman et al. (1996) showed that the optimal acceptance rate in a chain depends on the dimension D of the parameter space (i.e. the number of parameters), with values $r_{\mathrm{acc}} = [0.441, 0.352, 0.316, 0.279, 0.275]$ for $D = [1, 2, 3, 4, 5]$, and ultimately converging to $r_{\mathrm{acc}} \rightarrow 0.23$ for $D \rightarrow \infty$. In practice, we use the rule of thumb that the acceptance rate for each walker should lie between 0.2 and 0.5 (Foreman-Mackey et al. 2013). This can be guaranteed by appropriately setting `emcee`'s a parameter, which controls the step size in the stretch move (eq. A.4). In essentially all cases, a value of 2 or 3 is optimal.

A second diagnostic that we use is the autocorrelation time (or length) for each parameter. In a Markov chain, the next position depends on the current position. As such, adjacent elements of the chain are not independent. The autocorrelation time measures the number of steps that should be taken in a chain to draw independent samples from the target distribution. `emcee` measures the so-called integrated autocorrelation time of the chain using the `acor`[1] python package. For a formal definition and extensive discussion of

---

[1] https://pypi.python.org/pypi/acor/1.1.1

the integrated autocorrelation time, we happily refer the reader to e.g. Berg (2004) or Goodman & Weare (2010). In practice, for good convergence, the total chain length should be at least ~ 10 autocorrelation times (Foreman-Mackey et al. 2013).

As a last diagnostic, we evaluate the Gelman-Rubin eigenvalues (Brooks & Gelman 1998) for the different parameters. Suppose we have m chains of length n for p parameters, and let us denote the t'th instance of the parameter vector in the j'th chain as θ_{jt}. The covariance matrix of the j'th chain is then given by:

$$W_j = \frac{1}{n-1}\sum_{t=1}^{n}(\theta_{jt}-\bar{\theta}_j)(\theta_{jt}-\bar{\theta}_j)^T, \tag{A.28}$$

and the mean 'within-chain' covariance matrix of all the chains is:

$$W = \frac{1}{m}\sum_{j=1}^{m}W_j = \frac{1}{m(n-1)}\sum_{j=1}^{m}\sum_{t=1}^{n}(\theta_{jt}-\bar{\theta}_j)(\theta_{jt}-\bar{\theta}_j)^T. \tag{A.29}$$

The 'between-chain' covariance matrix is defined as:

$$B = \frac{1}{m-1}\sum_{j=1}^{m}n(\bar{\theta}_j-\bar{\theta})(\bar{\theta}_j-\bar{\theta})^T. \tag{A.30}$$

In these expressions, $\bar{\theta}_j$ and $\bar{\theta}$ represent

$$\bar{\theta}_j = \frac{1}{n}\sum_{t=1}^{n}\theta_{jt} \quad \text{and} \quad \bar{\theta} = \frac{1}{m}\sum_{j=1}^{m}\bar{\theta}_j. \tag{A.31}$$

If the starting positions of the chains would be drawn from the target distribution, the true variance-covariance matrix of this distribution could be estimated as a weighted sum of the within and between-sequence covariances:

$$\hat{\Sigma} = \frac{n-1}{n}W + \frac{B}{n} \tag{A.32}$$

(Brooks & Gelman 1998). However, in reality, the starting distribution is usually overdispersed, i.e. the starting positions are drawn from a distribution that is wider than the target distribution. Taking this effect into account yields a pooled variance-covariance estimate:

$$\hat{V} = \hat{\Sigma} + \frac{B}{mn} \tag{A.33}$$

(Brooks & Gelman 1998). In case of convergence, the distribution of the elements of each chain approaches the target distribution, and hence the average within-chain covariance should approach the estimated covariance of the target distribution:

$$W \to \hat{V}. \tag{A.34}$$

As a scalar measure of the (fractional) distance between W and $\hat{V}$, that approaches 1 if the chains have converged, Brooks & Gelman (1998) propose:

$$\hat{R} = \max_a \frac{a^T \hat{V} a}{a^T W a}. \tag{A.35}$$

They furthermore show that this can be re-written as:

$$\hat{R} = \frac{n-1}{n} + \left(\frac{m+1}{m}\right)\lambda_1, \tag{A.36}$$

where λ_1 is the largest eigenvalue of the matrix $W^{-1}\,B/n$. If convergence is achieved, the between-chain variance B should disappear and $\lambda_1 \to 0$, which results in $\hat{R} \to 1$ for large n.

To use this diagnostic in practice, we perform each fit three times and use the `GetDist` python package to calculate the eigenvalues λ of the $W^{-1}\,B/n$ matrix for the different parameters. For good convergence, these should all be $\ll 1$.

Bibliography

Abdo, A. A., Ackermann, M., Ajello, M., et al. 2010, ApJ, 710, 133

Ackermann, M., Ajello, M., Atwood, W. B., et al. 2012, ApJ, 750, 3

Alatalo, K., Blitz, L., Young, L. M., et al. 2011, ApJ, 735, 88

Alatalo, K., Davis, T. A., Bureau, M., et al. 2013, MNRAS, 432, 1796

Albrecht, A. & Steinhardt, P. J. 1982, Physical Review Letters, 48, 1220

Allaert, F., Gentile, G., & Baes, M. 2017, A&A, 605, A55

Allaert, F., Gentile, G., Baes, M., et al. 2015, A&A, 582, A18

Alpher, R. A., Bethe, H., & Gamow, G. 1948, Physical Review, 73, 803

Alpher, R. A. & Herman, R. 1948a, Nature, 162, 774

Alpher, R. A. & Herman, R. C. 1948b, Physical Review, 74, 1737

Alton, P. B., Xilouris, E. M., Misiriotis, A., Dasyra, K. M., & Dumke, M. 2004, A&A, 425, 109

Amorisco, N. C. 2017, ArXiv e-prints

Amorisco, N. C. & Loeb, A. 2016, MNRAS, 459, L51

André, P., Men'shchikov, A., Bontemps, S., et al. 2010, A&A, 518, L102

Athanassoula, E., Bosma, A., & Papaioannou, S. 1987, A&A, 179, 23

Auld, R., Bianchi, S., Smith, M. W. L., et al. 2013, MNRAS, 428, 1880

Babcock, H. W. 1939, Lick Observatory Bulletin, 19, 41

Baes, M., Allaert, F., Sarzi, M., et al. 2014, MNRAS, 444, L90

Baes, M. & Dejonghe, H. 2001, MNRAS, 326, 733

Baes, M., Fritz, J., Gadotti, D. A., et al. 2010, A&A, 518, L39

Baes, M., Verstappen, J., De Looze, I., et al. 2011, ApJS, 196, 22

Bahcall, J. N. 1984, ApJ, 276, 169

Bahcall, J. N. & Soneira, R. M. 1980, ApJS, 44, 73

Baillard, A., Bertin, E., de Lapparent, V., et al. 2011, A&A, 532, A74

Barker, A. A. 1965, Australian Journal of Physics, 18, 119

Baushev, A. N., del Valle, L., Campusano, L. E., et al. 2016, ArXiv e-prints

Beasley, M. A. & Trujillo, I. 2016, ApJ, 830, 23

Becquaert, J.-F. & Combes, F. 1997, A&A, 325, 41

Begeman, K. G. 1987, PhD thesis, , Kapteyn Institute, (1987)

Begeman, K. G., Broeils, A. H., & Sanders, R. H. 1991, MNRAS, 249, 523

Behroozi, P. S., Wechsler, R. H., & Conroy, C. 2013, ApJ, 770, 57

Bekenstein, J. D. 2004, Phys. Rev. D, 70, 083509

Berg, B. A. 2004, eprint arXiv:cond-mat/0410490

Beuing, J., Dobereiner, S., Bohringer, H., & Bender, R. 1999, MNRAS, 302, 209

Bianchi, S. 2007, A&A, 471, 765

Bianchi, S. 2008, A&A, 490, 461

Binney, J. & Tremaine, S. 2008, Galactic Dynamics: Second Edition (Princeton University Press)

Blais-Ouellette, S., Amram, P., & Carignan, C. 2001, AJ, 121, 1952

Blumenthal, G. R., Faber, S. M., Flores, R., & Primack, J. R. 1986, ApJ, 301, 27

Blumenthal, G. R., Faber, S. M., Primack, J. R., & Rees, M. J. 1984, Nature, 311, 517

Bocchio, M., Micelotta, E. R., Gautier, A.-L., & Jones, A. P. 2012, A&A, 545, A124

Bolatto, A. D., Leroy, A. K., Jameson, K., et al. 2011, ApJ, 741, 12

Bolatto, A. D., Wolfire, M., & Leroy, A. K. 2013, ARA&A, 51, 207

Borgani, S., Moscardini, L., Plionis, M., et al. 1997, New A, 1, 321

Boroson, B., Kim, D.-W., & Fabbiano, G. 2011, ApJ, 729, 12

Bosma, A. 1978, PhD thesis, PhD Thesis, Groningen Univ., (1978)

Bottema, R. & Pestaña, J. L. G. 2015, MNRAS, 448, 2566

Bournaud, F., Duc, P.-A., Brinks, E., et al. 2007, Science, 316, 1166

Boylan-Kolchin, M., Bullock, J. S., & Kaplinghat, M. 2011, MNRAS, 415, L40

Boylan-Kolchin, M., Bullock, J. S., & Kaplinghat, M. 2012, MNRAS, 422, 1203

Braun, R. 2012, ApJ, 749, 87

Braun, R., Thilker, D. A., Walterbos, R. A. M., & Corbelli, E. 2009, ApJ, 695, 937

Broeils, A. H. 1992, A&A, 256, 19

Broeils, A. H. & Rhee, M.-H. 1997, A&A, 324, 877

Brooks, S. P. & Gelman, A. 1998, Journal of Computational and Graphical Statistics, 7, 434

Buitrago, F., Trujillo, I., Conselice, C. J., et al. 2008, ApJ, 687, L61

Bureau, M. & Freeman, K. C. 1997, PASA, 14, 146

Burkert, A. 1995, ApJ, 447, L25

Byun, Y. I., Freeman, K. C., & Kylafis, N. D. 1994, ApJ, 432, 114

Calzetti, D., Kinney, A. L., & Storchi-Bergmann, T. 1994, ApJ, 429, 582

Camps, P. & Baes, M. 2015, Astronomy and Computing, 9, 20

Camps, P., Trayford, J. W., Baes, M., et al. 2016, MNRAS, 462, 1057

Cappellari, M., Emsellem, E., Krajnović, D., et al. 2011a, MNRAS, 413, 813

Cappellari, M., Emsellem, E., Krajnović, D., et al. 2011b, MNRAS, 416, 1680

Cazaux, S. & Tielens, A. G. G. M. 2002, ApJ, 575, L29

Chakrabarti, S., Cox, T. J., Hernquist, L., et al. 2007, ApJ, 658, 840

Clark, B. G. 1980, A&A, 89, 377

Clemens, M. S., Negrello, M., De Zotti, G., et al. 2013, MNRAS, 433, 695

Cloet-Osselaer, A., De Rijcke, S., Schroyen, J., & Dury, V. 2012, MNRAS, 423, 735

Coe, D. 2010, ArXiv e-prints

Colín, P., Klypin, A., Valenzuela, O., & Gottlöber, S. 2004, ApJ, 612, 50

Conroy, C. & Wechsler, R. H. 2009, ApJ, 696, 620

Conselice, C. J., Wilkinson, A., Duncan, K., & Mortlock, A. 2016, ApJ, 830, 83

Corbelli, E., Thilker, D., Zibetti, S., Giovanardi, C., & Salucci, P. 2014, A&A, 572, A23

Cortese, L., Ciesla, L., Boselli, A., et al. 2012, A&A, 540, A52

Côté, S., Carignan, C., & Freeman, K. C. 2000, AJ, 120, 3027

Cowles, M. & Carlin, B. 1996, Journal of the American Statistical Association, 91, 883

da Cunha, E., Charlot, S., & Elbaz, D. 2008, MNRAS, 388, 1595

Dalcanton, J. J., Spergel, D. N., & Summers, F. J. 1997, ApJ, 482, 659

Dalcanton, J. J., Yoachim, P., & Bernstein, R. A. 2004, ApJ, 608, 189

Dale, D. A., Aniano, G., Engelbracht, C. W., et al. 2012, ApJ, 745, 95

Dalgarno, A. & McCray, R. A. 1972, ARA&A, 10, 375

Dasyra, K. M., Xilouris, E. M., Misiriotis, A., & Kylafis, N. D. 2005, A&A, 437, 447

Davies, J. I., Wilson, C. D., Auld, R., et al. 2010, MNRAS, 409, 102

Davis, M., Efstathiou, G., Frenk, C. S., & White, S. D. M. 1985, ApJ, 292, 371

Davis, T. A., Alatalo, K., Bureau, M., et al. 2013, MNRAS, 429, 534

Davis, T. A., Rowlands, K., Allison, J. R., et al. 2015, MNRAS, 449, 3503

de Blok, W. J. G. 2010, Advances in Astronomy, 2010, 789293

de Blok, W. J. G., Józsa, G. I. G., Patterson, M., et al. 2014, A&A, 566, A80

de Blok, W. J. G., McGaugh, S. S., Bosma, A., & Rubin, V. C. 2001a, ApJ, 552, L23

de Blok, W. J. G., McGaugh, S. S., & Rubin, V. C. 2001b, AJ, 122, 2396

de Blok, W. J. G., Walter, F., Brinks, E., et al. 2008, AJ, 136, 2648

De Geyter, G., Baes, M., Camps, P., et al. 2014, MNRAS, 441, 869

De Geyter, G., Baes, M., De Looze, I., et al. 2015, MNRAS, 451, 1728

De Geyter, G., Baes, M., Fritz, J., & Camps, P. 2013, A&A, 550, A74

De Looze, I., Baes, M., Bendo, G. J., et al. 2012a, MNRAS, 427, 2797

De Looze, I., Baes, M., Fritz, J., & Verstappen, J. 2012b, MNRAS, 419, 895

De Looze, I., Fritz, J., Baes, M., et al. 2014, A&A, 571, A69

De Lucia, G., Springel, V., White, S. D. M., Croton, D., & Kauffmann, G. 2006, MNRAS, 366, 499

de Vaucouleurs, G., de Vaucouleurs, A., Corwin, Jr., H. G., et al. 1991, Third Reference Catalogue of Bright Galaxies. Volume I: Explanations and references. Volume II: Data for galaxies between 0^h and 12^h. Volume III: Data for galaxies between 12^h and 24^h.

Di Cintio, A., Brook, C. B., Dutton, A. A., et al. 2017, MNRAS, 466, L1

Di Cintio, A., Brook, C. B., Dutton, A. A., et al. 2014a, MNRAS, 441, 2986

Di Cintio, A., Brook, C. B., Macciò, A. V., et al. 2014b, MNRAS, 437, 415

di Serego Alighieri, S., Bianchi, S., Pappalardo, C., et al. 2013, A&A, 552, A8

Di Teodoro, E. M. & Fraternali, F. 2014, A&A, 567, A68

Diemand, J., Kuhlen, M., Madau, P., et al. 2008, Nature, 454, 735

Dodelson, S. 2011, International Journal of Modern Physics D, 20, 2749

Domínguez-Tenreiro, R., Obreja, A., Granato, G. L., et al. 2014, MNRAS, 439, 3868

Draine, B. T. 2003, ARA&A, 41, 241

Draine, B. T. 2011, Physics of the Interstellar and Intergalactic Medium

Draine, B. T. & Li, A. 2007, ApJ, 657, 810

Dubinski, J. & Carlberg, R. G. 1991, ApJ, 378, 496

Dutton, A. A. & Macciò, A. V. 2014, MNRAS, 441, 3359

Dwek, E. 1998, ApJ, 501, 643

Dwek, E. & Scalo, J. M. 1980, ApJ, 239, 193

Efstathiou, G., Davis, M., White, S. D. M., & Frenk, C. S. 1985, ApJS, 57, 241

Einasto, J. 1965, Trudy Astrofizicheskogo Instituta Alma-Ata, 5, 87

Einasto, J. & Lynden-Bell, D. 1982, MNRAS, 199, 67

El-Zant, A., Shlosman, I., & Hoffman, Y. 2001, ApJ, 560, 636

Elmegreen, B. G., Elmegreen, D. M., & Montenegro, L. 1992, ApJS, 79, 37

Emsellem, E., Cappellari, M., Krajnović, D., et al. 2011, MNRAS, 414, 888

Erwin, P. 2015, ApJ, 799, 226

Fairall, A. P., Willmer, C. N. A., Calderon, J. H., et al. 1992, AJ, 103, 11

Fall, S. M. & Efstathiou, G. 1980, MNRAS, 193, 189

Famaey, B. & McGaugh, S. 2013, in Journal of Physics Conference Series, Vol. 437, Journal of Physics Conference Series, 012001

Feroz, F. & Hobson, M. P. 2008, MNRAS, 384, 449

Ferrero, I., Abadi, M. G., Navarro, J. F., Sales, L. V., & Gurovich, S. 2012, MNRAS, 425, 2817

Finkelman, I., Brosch, N., Funes, J. G., Kniazev, A. Y., & Väisänen, P. 2010a, MNRAS, 407, 2475

Finkelman, I., Brosch, N., Kniazev, A. Y., et al. 2008, MNRAS, 390, 969

Finkelman, I., Brosch, N., Kniazev, A. Y., et al. 2010b, MNRAS, 409, 727

Foreman-Mackey, D., Hogg, D. W., Lang, D., & Goodman, J. 2013, PASP, 125, 306

Freeman, K. C. 1970, ApJ, 160, 811

Friedmann, A. 1922, Zeitschrift fur Physik, 10, 377

Fritz, J., Gentile, G., Smith, M. W. L., et al. 2012, A&A, 546, A34

Fukushige, T. & Makino, J. 2001, ApJ, 557, 533

Gadotti, D. A., Baes, M., & Falony, S. 2010, MNRAS, 403, 2053

Galametz, M., Kennicutt, R. C., Albrecht, M., et al. 2012, MNRAS, 425, 763

Galametz, M., Madden, S. C., Galliano, F., et al. 2011, A&A, 532, A56

Galliano, F., Hony, S., Bernard, J.-P., et al. 2011, A&A, 536, A88

Gao, L., Navarro, J. F., Cole, S., et al. 2008, MNRAS, 387, 536

García-Burillo, S., Combes, F., & Neri, R. 1999, A&A, 343, 740

Garcia-Burillo, S., Guelin, M., & Neininger, N. 1997, A&A, 319, 450

Gelman, A., Roberts, G. O., Gilks, W. R., et al. 1996, Bayesian statistics, 5, 42

Geman, S. & Geman, D. 1984, IEEE Trans. Pattern Anal. Mach. Intell., 6, 721

Gentile, G., Józsa, G. I. G., Serra, P., et al. 2013, A&A, 554, A125

Gentile, G., Salucci, P., Klein, U., & Granato, G. L. 2007, MNRAS, 375, 199

Gentile, G., Salucci, P., Klein, U., Vergani, D., & Kalberla, P. 2004, MNRAS, 351, 903

Gibson, S. J., Taylor, A. R., Higgs, L. A., Brunt, C. M., & Dewdney, P. E. 2005, ApJ, 626, 195

Gnedin, O. Y., Kravtsov, A. V., Klypin, A. A., & Nagai, D. 2004, ApJ, 616, 16

Gomez de Castro, A. I. & Garcia-Burillo, S. 1997, A&A, 322, 381

Goodman, J. & Weare, J. 2010, Commun. Appl. Math. Comput. Sci., 5, 65

Gordon, K. D., Misselt, K. A., Witt, A. N., & Clayton, G. C. 2001, ApJ, 551, 269

Goudfrooij, P. & de Jong, T. 1995, A&A, 298, 784

Gould, R. J. & Salpeter, E. E. 1963, ApJ, 138, 393

Governato, F., Brook, C., Mayer, L., et al. 2010, Nature, 463, 203

Governato, F., Zolotov, A., Pontzen, A., et al. 2012, MNRAS, 422, 1231

Greisen, E. W. 2003, Information Handling in Astronomy - Historical Vistas, 285, 109

Greisen, E. W., Spekkens, K., & van Moorsel, G. A. 2009, AJ, 137, 4718

Grenier, I. A., Casandjian, J.-M., & Terrier, R. 2005, Science, 307, 1292

Guth, A. H. 1981, Phys. Rev. D, 23, 347

Hagen, J. P. & McClain, E. F. 1954, ApJ, 120, 368

Hague, P. R. & Wilkinson, M. I. 2013, MNRAS, 433, 2314

Hague, P. R. & Wilkinson, M. I. 2014, MNRAS, 443, 3712

Hague, P. R. & Wilkinson, M. I. 2015, ApJ, 800, 15

Hambrick, D. C., Ostriker, J. P., Johansson, P. H., & Naab, T. 2011, MNRAS, 413, 2421

Hastings, W. K. 1970, Biometrika, 57, 97

Hernquist, L. 1990, ApJ, 356, 359

Hildebrandt, H., Viola, M., Heymans, C., et al. 2017, MNRAS, 465, 1454

Hoffman, G. L., Williams, B. M., Lewis, B. M., Helou, G., & Salpeter, E. E. 1989, ApJS, 69, 65

Högbom, J. A. 1974, A&AS, 15, 417

Hollenbach, D. & Salpeter, E. E. 1971, ApJ, 163, 155

Holwerda, B. W., Bianchi, S., Baes, M., et al. 2012a, in IAU Symposium, Vol. 284, The Spectral Energy Distribution of Galaxies - SED 2011, ed. R. J. Tuffs & C. C. Popescu, 128–131

Holwerda, B. W., Bianchi, S., Böker, T., et al. 2012b, A&A, 541, L5

Hubble, E. 1929, Proceedings of the National Academy of Science, 15, 168

Hubble, E. P. 1925, Popular Astronomy, 33

Hubble, E. P. 1926, ApJ, 64

Hubble, E. P. 1927, The Observatory, 50, 276

Huchtmeier, W. K. & Richter, O.-G. 1989, A General Catalog of HI Observations of Galaxies. The Reference Catalog.

Hughes, T. M., Baes, M., Fritz, J., et al. 2014, A&A, 565, A4

Hunter, D. A., Ficut-Vicas, D., Ashley, T., et al. 2012, AJ, 144, 134

Iorio, G., Fraternali, F., Nipoti, C., et al. 2017, MNRAS, 466, 4159

Irwin, J. A., Kennedy, H., Parkin, T., & Madden, S. 2007, A&A, 474, 461

Israel, F. P. 1997, A&A, 328, 471

Jõeveer, M. 1972, Tartu Astrofuusika Observatoorium Teated, 37, 3

Jõeveer, M. 1974, Tartu Astrofuusika Observatoorium Teated, 46, 35

Jaffe, W. 1983, MNRAS, 202, 995

Jardel, J. R. & Sellwood, J. A. 2009, ApJ, 691, 1300

Jeans, J. H. 1922, MNRAS, 82, 122

Jesseit, R., Naab, T., & Burkert, A. 2002, ApJ, 571, L89

Jobin, M. & Carignan, C. 1990, AJ, 100, 648

Jones, A. P. 2004, in Astronomical Society of the Pacific Conference Series, Vol. 309, Astrophysics of Dust, ed. A. N. Witt, G. C. Clayton, & B. T. Draine, 347

Jones, A. P., Fanciullo, L., Köhler, M., et al. 2013, A&A, 558, A62

Jones, A. P. & Nuth, J. A. 2011, A&A, 530, A44

Jonsson, P. 2006, MNRAS, 372, 2

Joseph, R. D., Meikle, W. P. S., Robertson, N. A., & Wright, G. S. 1984, MNRAS, 209, 111

Józsa, G. I. G., Kenn, F., Klein, U., & Oosterloo, T. A. 2007, A&A, 468, 731

Kahn, F. D. & Woltjer, L. 1959, ApJ, 130, 705

Kalberla, P. M. W. & Dedes, L. 2008, A&A, 487, 951

Kamphuis, P., Rand, R. J., Józsa, G. I. G., et al. 2013, MNRAS, 434, 2069

Kaneda, H., Onaka, T., Kitayama, T., Okada, Y., & Sakon, I. 2007, PASJ, 59, 107

Kapteyn, J. C. 1922, ApJ, 55, 302

Karukes, E. V. & Salucci, P. 2017, MNRAS, 465, 4703

Katz, H., Lelli, F., McGaugh, S. S., et al. 2017, MNRAS, 466, 1648

Katz, H., McGaugh, S. S., Sellwood, J. A., & de Blok, W. J. G. 2014, MNRAS, 439, 1897

Kaufmann, T., Mayer, L., Wadsley, J., Stadel, J., & Moore, B. 2006, MNRAS, 370, 1612

Kaviraj, S. 2014a, MNRAS, 440, 2944

Kaviraj, S. 2014b, MNRAS, 437, L41

Kaviraj, S., Tan, K.-M., Ellis, R. S., & Silk, J. 2011, MNRAS, 411, 2148

Kenney, J. D. P. 1994, in Mass-Transfer Induced Activity in Galaxies, ed. I. Shlosman, 78

Kereš, D., Katz, N., Davé, R., Fardal, M., & Weinberg, D. H. 2009a, MNRAS, 396, 2332

Kereš, D., Katz, N., Fardal, M., Davé, R., & Weinberg, D. H. 2009b, MNRAS, 395, 160

Kessler, M. F., Steinz, J. A., Anderegg, M. E., et al. 1996, A&A, 315, L27

Kirichenko, A., Danilenko, A., Shternin, P., et al. 2015, ApJ, 802, 17

Klypin, A., Gottlöber, S., Kravtsov, A. V., & Khokhlov, A. M. 1999a, ApJ, 516, 530

Klypin, A., Kravtsov, A. V., Bullock, J. S., & Primack, J. R. 2001, ApJ, 554, 903

Klypin, A., Kravtsov, A. V., Valenzuela, O., & Prada, F. 1999b, ApJ, 522, 82

Klypin, A. A., Trujillo-Gomez, S., & Primack, J. 2011, ApJ, 740, 102

Knapen, J. H., Hes, R., Beckman, J. E., & Peletier, R. F. 1991, A&A, 241, 42

Koda, J., Yagi, M., Yamanoi, H., & Komiyama, Y. 2015, ApJ, 807, L2

Köhler, M., Jones, A., & Ysard, N. 2014, A&A, 565, L9

Köhler, M., Ysard, N., & Jones, A. P. 2015, A&A, 579, A15

Koribalski, B. S., Staveley-Smith, L., Kilborn, V. A., et al. 2004, AJ, 128, 16

Kormendy, J. & Kennicutt, Jr., R. C. 2004, ARA&A, 42, 603

Kozasa, T., Hasegawa, H., & Nomoto, K. 1991, A&A, 249, 474

Krajnović, D., Emsellem, E., Cappellari, M., et al. 2011, MNRAS, 414, 2923

Kregel, M. & van der Kruit, P. C. 2004, MNRAS, 352, 787

Kregel, M., van der Kruit, P. C., & de Blok, W. J. G. 2004, MNRAS, 352, 768

Krumholz, M. R. 2012, ApJ, 759, 9

Kuzio de Naray, R., McGaugh, S. S., & de Blok, W. J. G. 2008, ApJ, 676, 920

Kuzmin, G. G. 1952, Publications of the Tartu Astrofizica Observatory, 32, 5

Kuzmin, G. G. 1955, Publications of the Tartu Astrofizica Observatory, 33, 3

Kylafis, N. D. & Bahcall, J. N. 1987, ApJ, 317, 637

Lagos, C. d. P., Lacey, C. G., & Baugh, C. M. 2013, MNRAS, 436, 1787

Lake, G. & Schommer, R. A. 1984, ApJ, 280, 107

Lambas, D. G., Alonso, S., Mesa, V., & O'Mill, A. L. 2012, A&A, 539, A45

Lanz, L., Zezas, A., Brassington, N., et al. 2013, ApJ, 768, 90

Leeuw, L. L., Davidson, J., Dowell, C. D., & Matthews, H. E. 2008, ApJ, 677, 249

Lelli, F., McGaugh, S. S., & Schombert, J. M. 2016, ArXiv e-prints

Lemaître, G. 1927, Annales de la Société Scientifique de Bruxelles, 47, 49

Leroy, A., Bolatto, A., Stanimirovic, S., et al. 2007, ApJ, 658, 1027

Leroy, A. K., Bolatto, A., Gordon, K., et al. 2011, ApJ, 737, 12

Leroy, A. K., Walter, F., Brinks, E., et al. 2008, AJ, 136, 2782

Levin, D. A., Peres, Y., & Wilmer, E. L. 2008, Markov Chains and Mixing Times (American Mathematical Society)

Linde, A. D. 1982, Physics Letters B, 108, 389

Lintott, C. J., Schawinski, K., Slosar, A., et al. 2008, MNRAS, 389, 1179

Liu, J. S. 2008, Monte Carlo Strategies in Scientific Computing (Springer Publishing Company, Incorporated)

Lofthouse, E. K., Kaviraj, S., Conselice, C. J., Mortlock, A., & Hartley, W. 2017, MNRAS, 465, 2895

Lucy, L. B. 1974, AJ, 79, 745

Macciò, A. V., Dutton, A. A., & van den Bosch, F. C. 2008, MNRAS, 391, 1940

Macciò, A. V., Dutton, A. A., van den Bosch, F. C., et al. 2007, MNRAS, 378, 55

Macciò, A. V., Stinson, G., Brook, C. B., et al. 2012, ApJ, 744, L9

Madden, S. C., Poglitsch, A., Geis, N., Stacey, G. J., & Townes, C. H. 1997, ApJ, 483, 200

Madden, S. C., Rémy-Ruyer, A., Galametz, M., et al. 2013, PASP, 125, 600

Magrini, L., Bianchi, S., Corbelli, E., et al. 2011, A&A, 535, A13

Martínez-Delgado, D., Peñarrubia, J., Gabany, R. J., et al. 2008, ApJ, 689, 184

Mathewson, D. S. & Ford, V. L. 1996, ApJS, 107, 97

Matteucci, F. 2012, Chemical Evolution of Galaxies

McCarthy, I. G., Bower, R. G., & Balogh, M. L. 2007, MNRAS, 377, 1457

McGaugh, S. S. 2012, AJ, 143, 40

McGaugh, S. S. & Schombert, J. M. 2014, AJ, 148, 77

McQuinn, K. B. W., Lelli, F., Skillman, E. D., et al. 2015, ArXiv e-prints

Meidt, S. E., Schinnerer, E., van de Ven, G., et al. 2014, ApJ, 788, 144

Merritt, A., van Dokkum, P., Danieli, S., et al. 2016, ApJ, 833, 168

Merritt, D., Graham, A. W., Moore, B., Diemand, J., & Terzić, B. 2006, AJ, 132, 2685

Metropolis, N., Rosenbluth, A., Rosenbluth, M., Teller, A., & Teller, E. 1953, J. Chem. Phys., 21, 1087

Micelotta, E. R., Jones, A. P., & Tielens, A. G. G. M. 2010, A&A, 510, A37

Mihos, J. C., Durrell, P. R., Ferrarese, L., et al. 2015, ApJ, 809, L21

Mihos, J. C. & Hernquist, L. 1996, ApJ, 464, 641

Milgrom, M. 1983, ApJ, 270, 365

Misiriotis, A. & Bianchi, S. 2002, A&A, 384, 866

Misiriotis, A., Popescu, C. C., Tuffs, R., & Kylafis, N. D. 2001, A&A, 372, 775

Mizuno, N., Rubio, M., Mizuno, A., et al. 2001, PASJ, 53, L45

Moffat, J. W. 2006, J. Cosmology Astropart. Phys., 3, 004

Moore, B., Ghigna, S., Governato, F., et al. 1999a, ApJ, 524, L19

Moore, B., Quinn, T., Governato, F., Stadel, J., & Lake, G. 1999b, MNRAS, 310, 1147

Mosenkov, A. V., Allaert, F., Baes, M., et al. 2016, A&A, 592, A71

Moster, B. P., Macciò, A. V., Somerville, R. S., Johansson, P. H., & Naab, T. 2010, MNRAS, 403, 1009

Mould, J. R., Huchra, J. P., Freedman, W. L., et al. 2000, ApJ, 529, 786

Muñoz-Mateos, J. C., Gil de Paz, A., Boissier, S., et al. 2009, ApJ, 701, 1965

Murakami, H., Baba, H., Barthel, P., et al. 2007, PASJ, 59, 369

Naab, T., Jesseit, R., & Burkert, A. 2006, MNRAS, 372, 839

Natale, G., Popescu, C. C., Tuffs, R. J., & Semionov, D. 2014, MNRAS, 438, 3137

Navarro, J. F., Eke, V. R., & Frenk, C. S. 1996a, MNRAS, 283, L72

Navarro, J. F., Frenk, C. S., & White, S. D. M. 1996b, ApJ, 462, 563

Navarro, J. F., Hayashi, E., Power, C., et al. 2004, MNRAS, 349, 1039

Navarro, J. F., Ludlow, A., Springel, V., et al. 2010, MNRAS, 402, 21

Negroponte, J. & White, S. D. M. 1983, MNRAS, 205, 1009

Neugebauer, G., Habing, H. J., van Duinen, R., et al. 1984, ApJ, 278, L1

Newman, A. B., Ellis, R. S., Bundy, K., & Treu, T. 2012, ApJ, 746, 162

Newton, R. D. A. & Kay, S. T. 2013, MNRAS, 434, 3606

Nierenberg, A. M., Treu, T., Menci, N., et al. 2016, MNRAS, 462, 4473

Noll, S., Burgarella, D., Giovannoli, E., et al. 2009, A&A, 507, 1793

Noordermeer, E. 2008, MNRAS, 385, 1359

Oñorbe, J., Boylan-Kolchin, M., Bullock, J. S., et al. 2015, MNRAS, 454, 2092

O'Brien, J. C., Freeman, K. C., & van der Kruit, P. C. 2010a, A&A, 515, A62

O'Brien, J. C., Freeman, K. C., & van der Kruit, P. C. 2010b, A&A, 515, A61

O'Brien, J. C., Freeman, K. C., & van der Kruit, P. C. 2010c, A&A, 515, A63

O'Brien, J. C., Freeman, K. C., van der Kruit, P. C., & Bosma, A. 2010d, A&A, 515, A60

Ocvirk, P., Pichon, C., & Teyssier, R. 2008, MNRAS, 390, 1326

Oh, S.-H., de Blok, W. J. G., Brinks, E., Walter, F., & Kennicutt, Jr., R. C. 2011, AJ, 141, 193

Oh, S.-H., de Blok, W. J. G., Walter, F., Brinks, E., & Kennicutt, Jr., R. C. 2008, AJ, 136, 2761

Oh, S.-H., Hunter, D. A., Brinks, E., et al. 2015, AJ, 149, 180

Olivier, S. S., Primack, J. R., Blumenthal, G. R., & Dekel, A. 1993, ApJ, 408, 17

Olling, R. P. 1995, AJ, 110, 591

Olling, R. P. 1996, AJ, 112, 457

Olling, R. P. & Merrifield, M. R. 1998, MNRAS, 297, 943

Oort, J. H. 1932, Bull. Astron. Inst. Netherlands, 6, 249

Oort, J. H. 1940, ApJ, 91, 273

Oort, J. H. 1960, Bull. Astron. Inst. Netherlands, 15, 45

Oosterloo, T. A., Morganti, R., Sadler, E. M., Vergani, D., & Caldwell, N. 2002, AJ, 123, 729

Öpic, E. 1915, Bull. de la Soc. Astr. de Russie, 21, 150

Oser, L., Naab, T., Ostriker, J. P., & Johansson, P. H. 2012, ApJ, 744, 63

Ostriker, J. & Silk, J. 1973, ApJ, 184, L113

Pace, A. B. 2016, ArXiv e-prints

Papastergis, E., Adams, E. A. K., & Romanowsky, A. J. 2017, ArXiv e-prints

Papastergis, E., Giovanelli, R., Haynes, M. P., & Shankar, F. 2015, A&A, 574, A113

Paradis, D., Dobashi, K., Shimoikura, T., et al. 2012, A&A, 543, A103

Pastrav, B. A., Popescu, C. C., Tuffs, R. J., & Sansom, A. E. 2013a, A&A, 553, A80

Pastrav, B. A., Popescu, C. C., Tuffs, R. J., & Sansom, A. E. 2013b, A&A, 557, A137

Patil, M. K., Pandey, S. K., Sahu, D. K., & Kembhavi, A. 2007, A&A, 461, 103

Penzias, A. A. & Wilson, R. W. 1965, ApJ, 142, 419

Persic, M., Salucci, P., & Stel, F. 1996, MNRAS, 281, 27

Peskun, P. H. 1973, Biometrika, 60, 607

Peters, S. P. C., van der Kruit, P. C., Allen, R. J., & Freeman, K. C. 2013, ArXiv e-prints

Peters, S. P. C., van der Kruit, P. C., Allen, R. J., & Freeman, K. C. 2017a, MNRAS, 464, 2

Peters, S. P. C., van der Kruit, P. C., Allen, R. J., & Freeman, K. C. 2017b, MNRAS, 464, 21

Peters, S. P. C., van der Kruit, P. C., Allen, R. J., & Freeman, K. C. 2017c, MNRAS, 464, 32

Peters, S. P. C., van der Kruit, P. C., Allen, R. J., & Freeman, K. C. 2017d, MNRAS, 464, 65

Pilbratt, G. L., Riedinger, J. R., Passvogel, T., et al. 2010, A&A, 518, L1

Pineda, J. C. B., Hayward, C. C., Springel, V., & Mendes de Oliveira, C. 2017, MNRAS, 466, 63

Planck Collaboration, Ade, P. A. R., Aghanim, N., et al. 2016, A&A, 594, A13

Planck Collaboration XIX. 2011, A&A, 536, A19

Popescu, C. C., Misiriotis, A., Kylafis, N. D., Tuffs, R. J., & Fischera, J. 2000, A&A, 362, 138

Press, W. H., Teukolsky, S. A., Vetterling, W. T., & Flannery, B. P. 2007, Numerical Recipes 3rd Edition: The Art of Scientific Computing, 3rd edn. (New York, NY, USA: Cambridge University Press)

Primack, J. R., Holtzman, J., Klypin, A., & Caldwell, D. O. 1995, Physical Review Letters, 74, 2160

Puglielli, D., Widrow, L. M., & Courteau, S. 2010, ApJ, 715, 1152

Querejeta, M., Meidt, S. E., Schinnerer, E., et al. 2015, ApJS, 219, 5

Radhakrishnan, V. 1960, PASP, 72, 296

Read, J. I., Agertz, O., & Collins, M. L. M. 2016a, MNRAS, 459, 2573

Read, J. I. & Gilmore, G. 2005, MNRAS, 356, 107

Read, J. I., Iorio, G., Agertz, O., & Fraternali, F. 2016b, MNRAS, 462, 3628

Read, J. I., Iorio, G., Agertz, O., & Fraternali, F. 2017, MNRAS, 467, 2019

Rémy-Ruyer, A., Madden, S. C., Galliano, F., et al. 2014, A&A, 563, A31

Richter, O.-G. & Huchtmeier, W. K. 1987, A&AS, 68, 427

Riess, A. G., Filippenko, A. V., Challis, P., et al. 1998, AJ, 116, 1009

Riess, A. G., Macri, L. M., Hoffmann, S. L., et al. 2016, ApJ, 826, 56

Robert, C. & Casella, G. 2005, Monte Carlo Statistical Methods, Springer Texts in Statistics (Springer New York)

Roberts, M. S. & Whitehurst, R. N. 1975, ApJ, 201, 327

Rodrigues, D. C., del Popolo, A., Marra, V., & de Oliveira, P. L. C. 2017, ArXiv e-prints

Rohlfs, K. & Wilson, T. 2013, Tools of Radio Astronomy, Astronomy and Astrophysics Library (Springer Berlin Heidelberg)

Román, J. & Trujillo, I. 2017a, MNRAS, 468, 703

Román, J. & Trujillo, I. 2017b, MNRAS, 468, 4039

Rong, Y., Guo, Q., Gao, L., et al. 2017, ArXiv e-prints

Roussel, H. 2013, PASP, 125, 1126

Rowlands, K., Dunne, L., Maddox, S., et al. 2012, MNRAS, 419, 2545

Rowlands, K., Gomez, H. L., Dunne, L., et al. 2014, MNRAS, 441, 1040

Rubin, V. C., Burstein, D., Ford, Jr., W. K., & Thonnard, N. 1985, ApJ, 289, 81

Rubin, V. C. & Ford, Jr., W. K. 1970, ApJ, 159, 379

Rubin, V. C., Ford, Jr., W. K., & Thonnard, N. 1980, ApJ, 238, 471

Rubin, V. C., Thonnard, N., & Ford, Jr., W. K. 1978, ApJ, 225, L107

Saftly, W., Baes, M., De Geyter, G., et al. 2015, A&A, 576, A31

Sage, L. J., Welch, G. A., & Young, L. M. 2007, ApJ, 657, 232

Sancisi, R. 1976, A&A, 53, 159

Sancisi, R., Fraternali, F., Oosterloo, T., & van der Hulst, T. 2008, A&A Rev., 15, 189

Sandstrom, K. M., Leroy, A. K., Walter, F., et al. 2013, ApJ, 777, 5

Sault, R. J., Teuben, P. J., & Wright, M. C. H. 1995, in Astronomical Society of the Pacific Conference Series, Vol. 77, Astronomical Data Analysis Software and Systems IV, ed. R. A. Shaw, H. E. Payne, & J. J. E. Hayes, 433

Schruba, A., Leroy, A. K., Walter, F., et al. 2012, AJ, 143, 138

Schwab, F. R. 1984, AJ, 89, 1076

Sellwood, J. A. & Sánchez, R. Z. 2010, MNRAS, 404, 1733

Serra, P., Amblard, A., Temi, P., et al. 2011, ApJ, 740, 22

Serra, P., Oosterloo, T., Morganti, R., et al. 2012, MNRAS, 422, 1835

Shabala, S. S., Ting, Y.-S., Kaviraj, S., et al. 2012, MNRAS, 423, 59

Shafieloo, A. & Hazra, D. K. 2017, J. Cosmology Astropart. Phys., 4, 012

Shang, Z., Zheng, Z., Brinks, E., et al. 1998, ApJ, 504, L23

Sharma, S. 2017, ArXiv e-prints

Silva, L., Granato, G. L., Bressan, A., & Danese, L. 1998, ApJ, 509, 103

Silva, L., Schurer, A., Granato, G. L., et al. 2011, MNRAS, 410, 2043

Slavin, J. D., Dwek, E., & Jones, A. P. 2015, ApJ, 803, 7

Smith, D. J. B., Dunne, L., da Cunha, E., et al. 2012a, MNRAS, 427, 703

Smith, M. W. L., Eales, S. A., Gomez, H. L., et al. 2012b, ApJ, 756, 40

Smith, M. W. L., Gomez, H. L., Eales, S. A., et al. 2012c, ApJ, 748, 123

Smoot, G. F., Bennett, C. L., Kogut, A., et al. 1992, ApJ, 396, L1

Sofue, Y. 1996, ApJ, 458, 120

Sokal, A. 1997, Monte Carlo Methods in Statistical Mechanics: Foundations and New Algorithms, ed. C. DeWitt-Morette, P. Cartier, & A. Folacci (Boston, MA: Springer US), 131–192

Spano, M., Marcelin, M., Amram, P., et al. 2008, MNRAS, 383, 297

Spekkens, K. & Sellwood, J. A. 2007, ApJ, 664, 204

Spergel, D. N., Bean, R., Doré, O., et al. 2007, ApJS, 170, 377

Spitzer, Jr., L. 1942, ApJ, 95, 329

Springel, V., Wang, J., Vogelsberger, M., et al. 2008, MNRAS, 391, 1685

Springel, V., White, S. D. M., Jenkins, A., et al. 2005, Nature, 435, 629

Springob, C. M., Haynes, M. P., Giovanelli, R., & Kent, B. R. 2005, ApJS, 160, 149

Stacey, G. J., Geis, N., Genzel, R., et al. 1991, ApJ, 373, 423

Stacey, G. J., Hailey-Dunsheath, S., Ferkinhoff, C., et al. 2010, ApJ, 724, 957

Stadel, J., Potter, D., Moore, B., et al. 2009, MNRAS, 398, L21

Stanimirovic, S., Staveley-Smith, L., Dickey, J. M., Sault, R. J., & Snowden, S. L. 1999, MNRAS, 302, 417

Steer, D. G., Dewdney, P. E., & Ito, M. R. 1984, A&A, 137, 159

Steinacker, J., Bacmann, A., & Henning, T. 2006, ApJ, 645, 920

Strong, A. W. & Mattox, J. R. 1996, A&A, 308, L21

Taylor, G. B., Carilli, C. L., & Perley, R. A., eds. 1999, Astronomical Society of the Pacific Conference Series, Vol. 180, Synthesis Imaging in Radio Astronomy II

Taylor, J. E. & Navarro, J. F. 2001, ApJ, 563, 483

Temi, P., Mathews, W. G., Brighenti, F., & Bregman, J. D. 2003, ApJ, 585, L121

Teyssier, R., Pontzen, A., Dubois, Y., & Read, J. I. 2013, MNRAS, 429, 3068

Thronson, Jr., H. A. & Shull, J. M., eds. 1990, Astrophysics and Space Science Library, Vol. 161, The interstellar medium in galaxies; Proceedings of the 2nd Teton Conference, Grand Teton National Park, WY, July 3-7, 1989

Tielens, A. G. G. M. & Allamandola, L. J. 1986, Composition, structure and chemistry of interstellar dust, Tech. rep.

Tollerud, E. J., Boylan-Kolchin, M., & Bullock, J. S. 2014, MNRAS, 440, 3511

Toomre, A. & Toomre, J. 1972, ApJ, 178, 623

Trayford, J. W., Camps, P., Theuns, T., et al. 2017, MNRAS, 470, 771

Trujillo, I., Förster Schreiber, N. M., Rudnick, G., et al. 2006, ApJ, 650, 18

Trumpler, R. J. 1930a, PASP, 42, 214

Trumpler, R. J. 1930b, PASP, 42, 267

Tsai, J. C. & Mathews, W. G. 1996, ApJ, 468, 571

Tully, R. B., Courtois, H. M., Dolphin, A. E., et al. 2013, AJ, 146, 86

Valenzuela, O., Hernandez-Toledo, H., Cano, M., et al. 2014, AJ, 147, 27

van Albada, T. S., Bahcall, J. N., Begeman, K., & Sancisi, R. 1985, ApJ, 295, 305

van den Bosch, F. C. & Swaters, R. A. 2001, MNRAS, 325, 1017

van der Burg, R. F. J., Muzzin, A., & Hoekstra, H. 2016, A&A, 590, A20

van der Hulst, J. M., Terlouw, J. P., Begeman, K. G., Zwitser, W., & Roelfsema, P. R. 1992, in Astronomical Society of the Pacific Conference Series, Vol. 25, Astronomical Data Analysis Software and Systems I, ed. D. M. Worrall, C. Biemesderfer, & J. Barnes, 131

van der Kruit, P. C. 1981, A&A, 99, 298

van Dokkum, P. G., Abraham, R., Merritt, A., et al. 2015, ApJ, 798, L45

van Zee, L. & Bryant, J. 1999, AJ, 118, 2172

Vandenbroucke, B., Verbeke, R., & De Rijcke, S. 2016, MNRAS, 458, 912

Verbeke, R., Papastergis, E., Ponomareva, A. A., Rathi, S., & De Rijcke, S. 2017, ArXiv e-prints

Verbeke, R., Vandenbroucke, B., & De Rijcke, S. 2015, ApJ, 815, 85

Verheijen, M. A. W. 2001, ApJ, 563, 694

Verheijen, M. A. W. & Sancisi, R. 2001, A&A, 370, 765

Verlinde, E. 2011, Journal of High Energy Physics, 4, 29

Verlinde, E. P. 2016, ArXiv e-prints

Verstappen, J., Fritz, J., Baes, M., et al. 2013, A&A, 556, A54

Viaene, S., Baes, M., Tamm, A., et al. 2017, A&A, 599, A64

Viaene, S., Fritz, J., Baes, M., et al. 2014, ArXiv e-prints

Wagner, S. J., Bender, R., & Moellenhoff, C. 1988, A&A, 195, L5

Walter, F., Brinks, E., de Blok, W. J. G., et al. 2008, AJ, 136, 2563

Warmels, R. H. 1988, A&AS, 72, 427

Werner, M. W., Roellig, T. L., Low, F. J., et al. 2004, ApJS, 154, 1

White, S. D. M., Efstathiou, G., & Frenk, C. S. 1993, MNRAS, 262, 1023

Wiklind, T., Combes, F., & Henkel, C. 1995, A&A, 297, 643

Wilson, C. D., Cridland, A., Foyle, K., et al. 2013, ApJ, 776, L30

Wilson, T. L., Rohlfs, K., & Hüttemeister, S. 2009, Tools of Radio Astronomy (Berlin, Heidelberg :: Springer Berlin Heidelberg,)

Witt, A. N., Thronson, Jr., H. A., & Capuano, Jr., J. M. 1992, ApJ, 393, 611

Woods, D. F. & Geller, M. J. 2007, AJ, 134, 527

Wright, E. L., Meyer, S. S., Bennett, C. L., et al. 1992, ApJ, 396, L13

Xilouris, E. M., Alton, P. B., Davies, J. I., et al. 1998, A&A, 331, 894

Xilouris, E. M., Byun, Y. I., Kylafis, N. D., Paleologou, E. V., & Papamastorakis, J. 1999, A&A, 344, 868

Xilouris, E. M., Kylafis, N. D., Papamastorakis, J., Paleologou, E. V., & Haerendel, G. 1997, A&A, 325, 135

Yim, K., Wong, T., Xue, R., et al. 2014, AJ, 148, 127

Young, L. M., Bureau, M., Davis, T. A., et al. 2011, MNRAS, 414, 940

Zhang, H.-X., Hunter, D. A., Elmegreen, B. G., Gao, Y., & Schruba, A. 2012, AJ, 143, 47

Zhao, H. 1996, MNRAS, 278, 488

Zhukovska, S. 2014, A&A, 562, A76

Zhukovska, S. & Henning, T. 2013, A&A, 555, A99

Zschaechner, L. K. & Rand, R. J. 2015, ArXiv e-prints

Zschaechner, L. K., Rand, R. J., Heald, G. H., Gentile, G., & Józsa, G. 2012, ApJ, 760, 37

Zubko, V., Dwek, E., & Arendt, R. G. 2004, ApJS, 152, 211

Zwicky, F. 1937, ApJ, 86, 217